CONJUGATED MOLECULES, MACROMOLECULES, AND NANOPARTICLES WITH LADDER-TYPE BACKBONES

A Dissertation

by

ALEXANDER JAMES KALIN

Submitted to the Office of Graduate and Professional Studies of
Texas A&M University
in partial fulfillment of the requirements for the degree of

DOCTOR OF PHILOSOPHY

Chair of Committee,	Lei Fang
Committee Members,	John A. Gladysz
	Karen L. Wooley
	Micah J. Green
Head of Department,	Simon W. North

May 2020

Major Subject: Chemistry

ABSTRACT

Conjugated ladder polymers consist of π-conjugated, fused-ring repeating units, linked together by multiple strands of bonds. Such structural feature rigidifies the backbone and imparts unique chemical, optical, and electronic properties into ladder polymers. These valuable properties create an urgent incentive for solving the challenges associated with these materials: synthetic and processing challenges arise from the rigid, multiple-stranded backbones, and characterization of the solid-state morphology of these materials is limited.

To overcome the synthetic challenges, ring-closing olefin metathesis (RCM) was applied to two model synthetic targets. RCM annulation can construct extended fused-ring structures in a highly efficient manner due to the strong thermodynamic driving force towards aromatization. We therefore applied RCM to create the fused-ring backbone in previously challenging systems: a donor–acceptor ladder polymer and a crosslinked porous ladder polymer network. Historically, the former had been limited by inefficient annulation reactions with electron-deficient backbone units, and the latter requires an annulation which can take place within the pores of the network. The employment of RCM led to successful synthesis in both cases due to its lessened dependence on backbone electronics and the catalyst's ability to diffuse through the network pores, respectively. The network was made dispersible in organic solvents using a miniemulsion polymerization, affording nanoparticles that remained highly porous. Chemical, optical, and physical properties of these polymers were studied and reported, with emphasis on the importance of the rigidified backbone for various processes, including optical properties, gas adsorption, and fabrication into composite materials.

In order to accelerate the use of conjugated ladder polymers in practical applications, a stronger understanding of solid-state morphology is required, especially due to the strong effect of molecular orientation on their properties. However, such morphological studies are lacking for ladder-type macromolecules compared to non-ladder analogues. To this end, ladder-type molecules and molecules were studied using grazing incidence X-ray scattering (GIXS), demonstrating controllable morphology using thermal annealing and solvent vapor exposure. By studying a variety of molecular sizes and structures, size-dependent and structure-dependent effects were identified and correlated to morphological changes.

Overall, using RCM as a synthetic method and GIXS as an analytical technique both contributed to the advance of the research field of conjugated ladder polymers. These results provide valuable strategies for design, synthesis, and characterization of conjugated ladder polymers in order to improve the understanding of these materials in the pursuit of next-generation functional organic materials.

ACKNOWLEDGEMENTS

I would like to express my appreciation for my advisor, Professor Lei Fang, for giving me the opportunity to perform research in his group, and for the years of advice and mentorship during my graduate studies. Thanks also to my committee members, Professors John Gladysz, Karen Wooley, and Micah Green for their continued support, as well as Professor Sarbajit Banerjee for standing in on short notice.

I am incredibly grateful to all the present and past group members that have taught me the ins and outs of research and helped advance my skills as a chemist, as well as being phenomenally friendly people that made the group's culture such a pleasure to be a part of. Dr. Yang Zou, Dr. Zi-Hao Guo, Dr. Yun-Hyuk Choi, Dr. Yen-Hao Lin, Dr. Jongbok Lee, Dr. Congzhi Zhu, Dr. Tianyu Yuan, Sai Che, Xiaozhou Ji, Chenxu Wang, Mariela Vazquez, Anthony Mu, Bailey Phillips, Che-Hsuan Chang, Yirui Cao, Bo-Ji Peng, Chenxuan Li, Meir Duka, and many others were integral parts of my time in graduate school.

I am also very thankful for the support of my family and friends, especially outside the program, for the support with only very little understanding of what the PhD process entails. Their optimism kept me going, no matter how daunting the challenge of finishing my degree seemed.

Robin and Oliver Baumgarten are perhaps most deserving of my thanks, as they provided me daily support, no matter what part of the world we found ourselves in or how busy our work schedules were at any given time of the year. They were always understanding of the rigors and requirements of graduate school, and only asked me to make time for a good meal every now and then.

Lastly, this university has provided me opportunities I could have never found elsewhere. I have always felt at home here, part of a family whose values mirror my own and which always pushes me to better myself in every facet of life. I am eternally grateful to everyone who contributes to the welcoming and excellence-driven culture of Texas A&M, whose efforts ensure that the spirit of Aggieland will never die.

CONTRIBUTORS AND FUNDING SOURCES

This work was supervised by a committee consisting of Lei Fang [advisor] of the Departments of Chemistry and Materials Science & Engineering; John Gladysz [committee member] of the Department of Chemistry, and Karen Wooley [committee member] of the Departments of Chemistry, Chemical Engineering, and Materials Science & Engineering; and Micah Green [committee member] of the Department of Chemical Engineering.

Dr. Jongbok Lee performed the polymer synthesis and characterization in Chapter 2, with my contributions primarily in the monomer synthesis and X-ray scattering sections. Sai Che contributed to monomer synthesis in Chapter 3 and performed BET measurements for Chapter 4. ^{13}C NMR spectra in Chapter 4 were obtained by Dr. Vladimir Bakhmoutov. Chenxu Wang provided SEM images for Chapter 4. Mr. Justin Smolen aided in performing confocal microscopy measurements in Chapter 4. Dr. Joseph Strzalka at Argonne National Laboratory provided beamline support for GIXS measurements in Chapter 5. Synthesis of some molecules for GIXS measurements was performed by Dr. Jongbok Lee and Yirui Cao. Bailey Phillips and Anthony Mu aided with various GIXS measurements as well as with carbon nanotube films and conductivity measurements, respectively.

This work was funded by the Texas A&M College of Science Strategic Transformative Research Program, the National Priorities Research Program (NPRP7-285-1-045) from the Qatar National Research Fund, the Welch Foundation (A-1898), the

National Science Foundation (DMR-1654029), and the Texas A&M Energy Institute. Use of the Advanced Photon Source at Argonne National Laboratory was supported by the U. S. Department of Energy, Office of Science, Office of Basic Energy Sciences, under Contract No. DEAC02-06CH11357.

NOMENCLATURE

a_c	Critical angle of reflectance
AFM	Atomic force microscopy
a_i	Incident angle
AIBN	2,2′-azobis(2-methylpropionitrile)
ANG	Adsorbed natural gas
APCI	Atmospheric-pressure chemical ionization mass spectrometry
APS	Advanced Photon Source
BBL	Poly(benzimidazole benzophenanthroline)
BET	Brunauer–Emmett–Teller
BHT	2,6-di-*t*-butyl-4-methylphenol
Boc	*t*-butoxycarbonyl
Bpin	Pinacolatoboron
BPO	Benzoyl peroxide
BTD	Benzothiadiazole
BTBT	Benzothieno[3,2-*b*]benzothiophene
BTp	Benzo[*k*]tetraphene
cLP	Conjugated ladder polymer
CMC	Critical micelle concentration
CNT	Carbon nanotubes
COF	Covalent organic framework

CP-MAS	Cross polarization magic-angle spinning
CPN	Conjugated polymer nanoparticle
CTC	Charge Transfer Complex
D–A	Donor–acceptor
DACP	Donor–acceptor conjugated polymer
DALP	Donor–acceptor ladder polymer
DCE	1,2-dichloroethane
DLS	Dynamic light scattering
DMAP	4-(dimethylamino)pyridine
DMSO	Dimethylsulfoxide
DP	Degree of polymerization
DRIFTS	Diffuse reflectance infrared Fourier transform spectroscopy
EL	Electroluminescence
Et	Ethyl
F_4TCNQ	2,3,5,6-tetrafluoro-7,7,8,8-tetracyanoquinodimethane
FTIR	Fourier transform infrared spectroscopy
GISAXS	Grazing-incidence small-angle X-ray scattering
GIWAXS	Grazing-incidence wide-angle X-ray scattering
GIXS	Grazing-incidence X-ray scattering
GUI	Graphical user interface
HCP	Hypercrosslinked polymer
LUMO	Lowest unoccupied molecular orbital

HMBC	Heteronuclear multiple bond correlation
HOMO	Highest occupied molecular orbital
HOPG	Highly oriented pyrolytic graphite
HPLC	High-performance liquid chromatography
HRMS	High-resolution mass spectrometry
HSQC	Heteronuclear single quantum coherence
ICT	Intramolecular charge transfer
IR	Infrared
LPPP	Ladder-type poly(*p*-phenylene)
MALDI	Matrix-assisted laser desorption/ionization
Me	Methyl
M_n	Number average molecular weight
mp	Melting point
MSA	Methanesulfonic acid
M_w	Weight average molecular weight
MWCNT	Multiwalled carbon nanotube
NBS	N-bromosuccinimide
NDI	Naphthalenediimide
NIR	Near-infrared
NMR	Nuclear magnetic resonance
OAc	Acetate
OFET	Organic field-effect transistor

OLED	Organic light-emitting diode
OTS	Octadecyltrichlorosilane
PAN	Poly(acrylonitrile)
PDI/PdI	Polydispersity index
Ph	Phenyl
PL	Photoluminescence
PLAN	Porous ladder polymer network
PPA	Polyphosphoric acid
PPN	Porous polymer network
PTFE	Polytetrafluoroethylene
RCM	Ring-closing olefin metathesis
RT	Room temperature
SDS	Sodium dodecylsulfate
SEC	Size exclusion chromotography
SEM	Scanning electron microscopy
STM	Scanning tunneling microscopy
Sphos	2-dicyclohexylphosphino-2′,6′-dimethoxybiphenyl
TFA	Trifluoroacetic acid
TGA	Thermogravimetric Analysis
TLC	Analytical thin-layer chromatography
THF	Tetrahydrofuran
UV-Vis	Ultraviolet–visible spectroscopy

XPS	X-ray photoelectron spectroscopy

TABLE OF CONTENTS

Page

LIST OF FIGURES

Page

LIST OF SCHEMES

LIST OF TABLES

CHAPTER I

INTRODUCTION[*]

1.1 Fully Conjugated Linear Ladder Polymers

1.1.1 Introduction

Fully conjugated ladder polymers (cLPs) are an intriguing subset of macromolecules. Their development has relied on a wide scope of synthetic strategies to obtain a host of unique structures and materials useful for their physical, optical, and chemical properties.[1-3] In general, ladder polymers are multiple stranded polymers with periodic linkages connecting the strands, resembling the rails and rungs of a ladder, and giving an uninterrupted sequence of adjacent rings that share two or more atoms.[4] *Conjugated* ladder polymers (cLPs) are a specific subtype of ladder polymers in which all the fused rings in the backbone are π-conjugated. In addition, they are distinct from conventional conjugated polymers in that the fused-ring constitution restricts the free torsional motion in between the aromatic units along the backbone.

Stemming from the fused backbone, cLPs exhibit extraordinary thermal, chemical, and mechanical stability.[3, 5-7] Because of the diminished torsional defects, cLPs with fully coplanar backbones promise coherent π-conjugation,[8] fast intra-chain charge transport,[9] and long exciton diffusion length.[10] In contrast, the aromatic repeating units of conventional conjugated polymers tend to adopt non-zero dihedral angles either because

---

[*] Adapted with permission from "Fully Conjugated Ladder Polymers" by Jongbok Lee, Alexander J. Kalin, Tianyu Yuan, Mohammed Al-Hashimi, and Lei Fang, *Chem. Sci.*, **2017**, *8*, 2503-2521. Copyright 2017 The Royal Society of Chemistry.

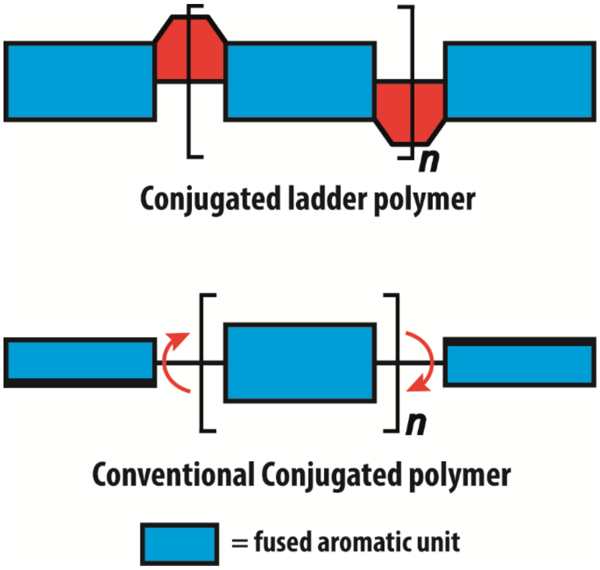

Figure 1.1. Graphical representation of conjugated ladder polymer (cLP) and conventional conjugated polymer with free torsional motions.

of torsional strain or thermal fluctuation (Figure 1.1). Such torsional defects partially break the conjugation along the polymer backbone, resulting in decreased electronic delocalization, widened band gaps, increased numbers of trapped charges, and less effective intermolecular coupling.[8, 11] Since the synthesis of poly(benzimidazole benzophenanthroline) (BBL) **1** in the 1960s,[12] many different cLPs have been prepared and investigated for various applications.[2, 3] Despite numerous reported syntheses of cLPs, the field has seen inherent synthetic challenges limiting the scope of usable precursors and reaction designs. Limitations are mainly related to several issues; (*i*) there are relatively few synthetic strategies available to efficiently construct defect-free structures; and (*ii*) poorly soluble products caused by backbone rigidity and coplanarity. In order to construct a well-defined cLP, the conversion of the ring annulation reaction must be nearly quantitative without undesired side reactions such as intermolecular cross-linking. Due to the lack of backbone rotation, at least one of the building blocks' reaction sites should possess C_{2h} symmetry in order for the rigid backbone to extend linearly. Furthermore, adequate solubilizing groups on the backbone of the cLPs are required to allow the reaction to complete while still obtaining soluble products for the subsequent characterization and processing.

From initial synthesis, through to characterization, analysis, and finally as potential end-user applications, cLPs face a number of unique challenges not found in other organic materials, originating from their rigid ribbon-like structures.[3, 13] The low solubility and backbone rigidity of the polymers limits the effectiveness of common polymer analysis techniques such as structural elucidation by NMR or molecular weight estimation by size exclusion chromatography (SEC). The low solubility also impedes simple solution processing methods in some cases. In this context, unique methods have been developed to circumvent these barriers, leading to more straightforward syntheses and widespread uses of cLPs.

Despite the aforementioned challenges in cLPs, their exceptional stability and promising electronic properties have prompted exploration in various optical and electronic applications, such as OLEDs[2, 5, 14-16] and OFETs,[17-21] among others. In many examples, cLP optoelectronic properties surpassed that of their non-ladder type counterparts.

In this perspective, the focus will center on the general synthetic strategies and specific examples of cLPs followed by discussion of chemical and engineering challenges associated with these materials. Annulation reactions of conjugated ladder oligomers will also be discussed to demonstrate the scope of reactions available for creation of ladder-type backbones. The demonstrated functions and potential applications of cLPs on multiple fronts are also discussed and outlined. Please note that conjugated step-ladder polymers[3] (conjugated polymers composed of oligomeric ladder-type building blocks connected by single-stranded σ bonds) are not included in this discussion.

1.1.2 General Synthetic Strategies

The synthesis of a well-defined cLP must fulfill several criteria; (*i*) reasonable solubility and (*ii*) quantitative conversion in the ring-closing reactions. In addition, the issues impacting the degree of polymerization and polydispersity must also be taken into consideration. Therefore, the development of an efficient and versatile synthetic strategy is indispensable to explore the potential for a functional cLP. In general, two distinct approaches can be employed to construct a fully conjugated ladder-type structure (Figure 1.2). One is single-step “ladderization” that constructs two strands of bonds simultaneously, such as polycondensation of tetra-functional monomers or repetitive Diels-Alder cycloaddition. The other approach relies on post-polymerization annulation. In this two-step approach, a pre-functionalized single-stranded conjugated polymer is first prepared, followed by the ladderization steps in which the functional groups cyclize to form the second strand of bonds. This stepwise approach provides a wider scope of applicable synthetic methods and monomeric building blocks. For this strategy, however, it is essential to ensure high conversion of the post-polymerization annulation reaction, while keeping good solubility of the reaction intermediate to achieve a well-defined ladder polymer with minimum levels of structural defects. Herein, we introduce the backgrounds and features of important cLP syntheses, discuss developments in the last decade, and offer synthetic perspective on cLPs.

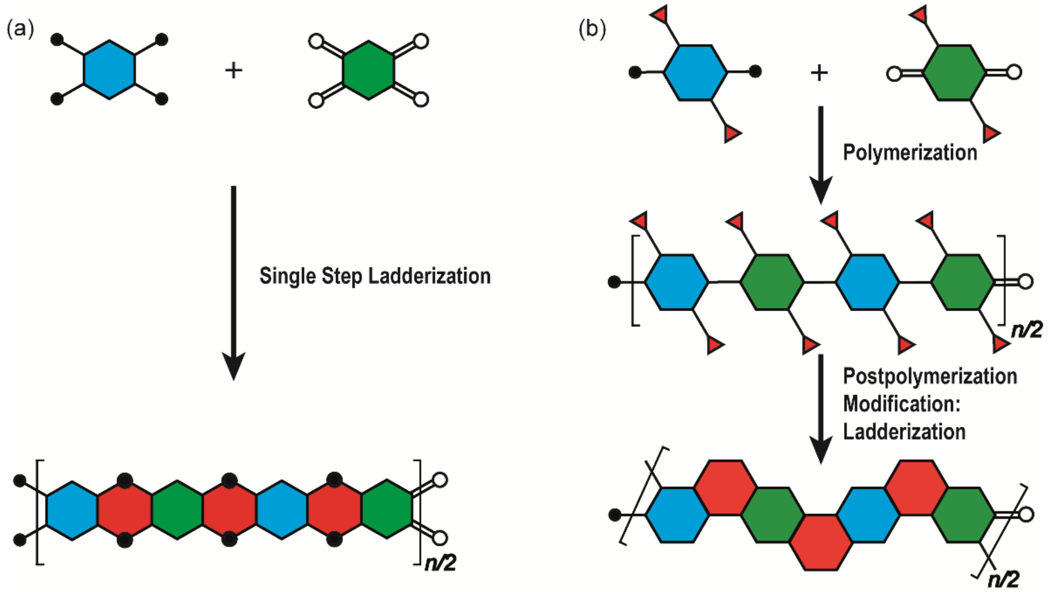

Figure 1.2. Graphical synthetic approaches to construct a ladder polymer. (a) Single-step ladderization and (b) post-polymerization modification: ladderization.

1.1.2.1 Single-Step Ladderization

In the late 1960s, Van Deusen reported the synthesis of BBL **1** for the purpose of thermally stable organic materials.[12] BBL **1** now represents one of the most extensively studied cLPs to date. The synthesis of BBL **1** was achieved by a single-step polycondensation of two tetrafunctional monomers (1,2,4,5-tetraaminobenzene and 1,4,5,8-tetracarboxynaphthalene) in polyphosphoric acid (PPA) solution. It can be viewed as a statistical copolymer of *cis* and *trans* isomeric repeating units. In parallel, one of these tetrafunctional monomers, 1,2,4,5-tetraaminobenzene, was also used in the construction of other cLPs with different comonomers by Stille *et al.*[22, 23] Their first trial to prepare a polyquinoxaline (PQL) ladder polymer **2** with hydroxylketone and tetraamine monomers provided incomplete ladder formation resulting in low thermal stability due to the low reactivity of the hydroxyl group.[22] By replacing the hydroxyketone monomer with a tetraketone monomer, *e.g.* 1,2,6,7-tetraketopyrene, where tautomerization is restricted, thermally stable PQL **2** was afforded in hexamethylphosphoramide (HMPA) solution at 180 °C.[23] It is noteworthy to mention that the key monomer (tetraaminobenzene) for the synthesis of BBL **1** and PQL **2**, is not stable to air oxidation. Therefore, oxidative side-reactions may cause structural defects of the cLP product if the reaction was not handled in a rigorously oxygen free condition. A similar synthetic strategy was employed in exploring the synthesis of poly(phenthiazine) (PTL) **3** and poly(phenooxazine) (POL) **4** by Kim in the 1980s.[24] These single-step polycondensed cLPs, however, can usually only be suspended in strong acids such as PPA or sulfuric acid, and are insoluble in common organic solvents. As a result, common solution phase characterization techniques (NMR and SEC) were not feasible to fully elucidate these structures.

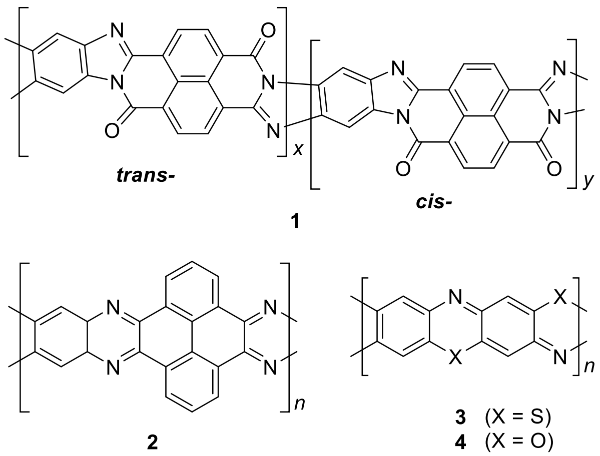

1

2

3 (X = S)
4 (X = O)

Figure 1.3. Chemical structures of *trans* and *cis* poly(benzimidazole benzophenanthroline) (BBL) **1**, polyquinoxaline (PQL) **2**, poly(phenthiazine) (PTL) **3**, and poly(phenooxazine) (POL) **4**.

Nonetheless, a promising synthetic approach was reported by Schlüter and coworkers in the mid-1990s.[25, 26] The fully unsaturated ladder polymer backbone was achieved by using Diels-Alder reaction followed by dehydrogenation (Scheme 1.1). These two reactions both gave high conversions on small molecule model compounds. cLP **7a** was synthesized through an AB+AB step growth polymerization using one single monomer containing both diene and dienophile functionalities. The product was analyzed by elemental analysis, UV-vis spectroscopy, and cross polarization magic-angle spinning (CP-MAS) ^{13}C NMR spectroscopy.[25] The carbon resonance peak corresponding to saturated carbons in the backbone of **7a** disappeared after dehydrogenation. Compound **7a** was insoluble in common organic solvents even with a long looped alkyl solubilizing group. Furthermore, film formation was not possible even when using the low molecular weight fraction (M_n = 2 - 7 kg/mol by SEC). A different solubilizing group was also installed to improve the molecular weight of intermediate **6**.[26] When an ester-linked dodecyl alkyl chain was used as the solubilizing group and the reaction was performed in

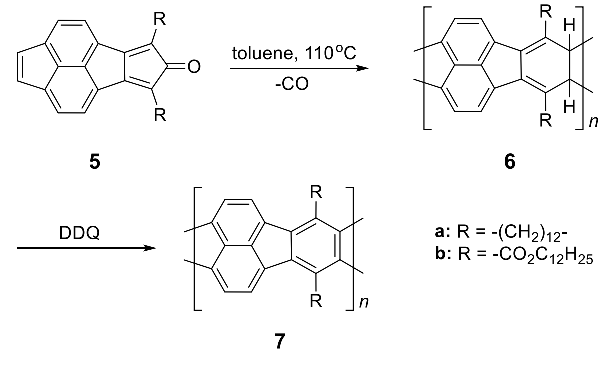

Scheme 1.1. Synthesis of ladder polymer **7** by Diels-Alder reaction followed by dehydrogenation.

an airtight ampoule, M_n of **6b** was relatively improved (34 kg/mol by SEC and 85 kg/mol by osmometry). After dehydrogenation, CP-MAS ^{13}C NMR spectrum of product **3b** showed complete disappearance of the sp^3 carbon on the polymer backbone. Product **3b**, however, was still insoluble in several organic solvents, preventing its analysis by solution-phase ^{1}H NMR spectroscopy. Although single-step ladderization has been investigated for over 50 years, the methods have not been widely adopted as a general approach for cLP synthesis due to the limited availability of ideal multifunctional monomers and their related solubility issues.

By using intramolecular non-covalent bonds, ladder-like conjugated backbones can be constructed through the formation of only one strand of covalent bonds. This strategy could also be considered as an interesting one-step approach to cLP-mimicking polymers. Through this approach, one strand of covalent bonds is formed through polymerization while another strand of non-covalent bonds can be generated simultaneously because of the dynamic and spontaneous nature of the non-covalent bonds. This approach was demonstrated in 1996, when Meijer and coworkers synthesized[27] a ladder-like polymer using intramolecular hydrogen bonding between the nitrogen on 2,5-dibromopyrazine and an adjacently attached amide functionality (Scheme 1.2). In this case, although the intramolecular hydrogen bonding feature was observed by ^{1}H NMR and IR spectroscopy, the synthesized polymer **8** was not able to adopt a fully coplanar structure along the backbone, due to the 2,2' H–H steric repulsion on the neighboring benzene and pyrazine units.[28] It is imperative that no steric effect should be present between neighboring rings in order to approach backbone coplanarity by using non-covalent

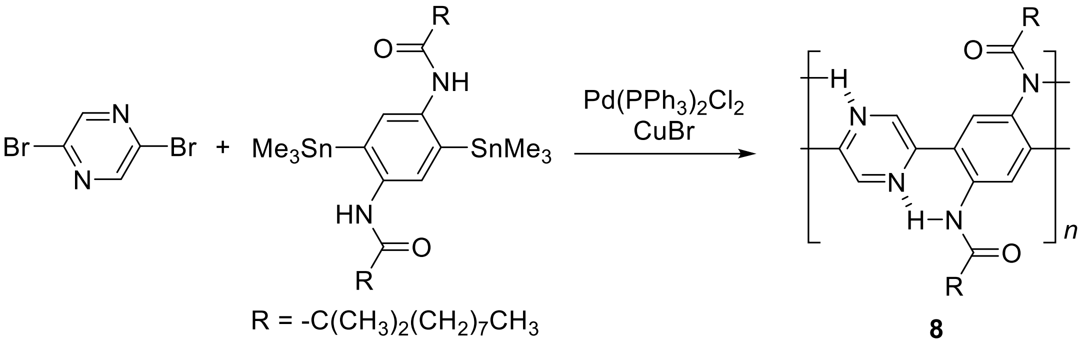

Scheme 1.2. Synthesis of ladder polymer **8** by self-assembled intramolecular N-H interaction.

interactions. Intramolecular dynamic bond-assisted coplanarization has been also reported using various kinds of non-covalent/coordination interactions such as N–H, S–N, and B–N interactions.[29-33] In principle, these dynamic yet simultaneous bonding could be used in the future for a one step construction of cLPs. In general, pre-organized non-covalent interactions could provide an alternative method to construct a coplanar ladder-like polymer without the concerns of the ladderization efficiency or intermolecular cross-linking during a ladderization step. Furthermore, the dynamic nature of intramolecular bonding could allow a simple approach to actively control the torsional conformation and intermolecular packing while processing these polymers into the solid-state.

1.1.2.2 Two Step Approach: Polymerization Followed by Annulation

1.1.2.2.1 Kinetic Ring Annulation

A widely used, Friedel-Crafts method to construct ladder-type poly(para-phenylene) structures was reported by Müllen and coworker in 1991.[34] The fused-ring backbones are achieved by transition metal-mediated polymerization followed by electrophilic cyclization. The synthesis of ladder-type poly(para-phenylene)s (LPPPs) started with Suzuki polymerization of benzenebisboronic ester and aromatic ketone-functionalized dibromobenzene (Scheme 1.3). The ketone functional groups on the single-stranded intermediate **9** were reduced by lithium aluminum hydride or alkyllithium reagents. Eventually, Lewis acid-mediated Friedel-Crafts ring annulation afforded the double-stranded LPPP products. Due to the rigid coplanar backbone of LPPPs, their UV-vis spectra possess a well-resolved vibronic progression with a very small Stokes shift (4 nm).[35, 36] In addition, MeLPPP (R^3 = Me) **12** showed identical photoluminescence (PL) spectra in solution and the thin film state, indicating that the molecular conformation does not change from the solvated state into the solid state.[2] The key factor in this synthetic strategy is the steric hindrance on the bridgehead. It is essential that substituents on -CR^2R^3OH possess moderate steric hindrance (*i.e.*, R^3 = H or alkyl).[2] Less hindered substituents can lead to intermolecular cross-linking during the reaction, resulting in insoluble by-products. On the other hand, a bulkier substituent could prevent the ring annulation from completing. Later, this synthetic strategy was expanded to prepare a number of different types of ladder polymers.[37-41]

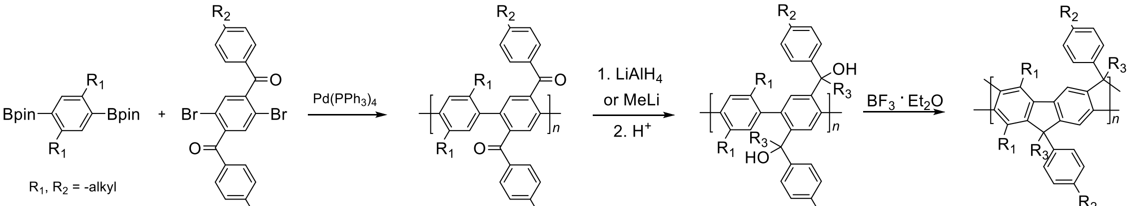

Scheme 1.3. Synthesis of poly(p-phenylene) ladder polymers (LPPPs) **11** and **12** by Friedel-Craft ring annulation.

Although ^{1}H NMR and FT-IR spectroscopy detected no defect in LPPP polymers, careful investigations on the structure-property relationship of these polymers were performed to reveal small amounts of structural defects on their backbones which can be detrimental to the properties of the desired cLP materials.[42] These defects were mainly caused by incomplete reduction of ketones that afforded monoalkylated fluorene backbones.[43, 44] As a result, these defect sites can be subsequently oxidized into fluorenones. The synthetic method was modified by Ma and coworkers to give a lower level of structural defects and thus better thermal stability.[45] This method was further improved by Bo and coworkers[5] who introduced methoxy functional groups, replacing the hydroxyl groups to avoid keto defects (Scheme 1.4). In this case, a spiro-bridged solubilizing group was installed to minimize aggregation between the polymer chains. The bromide end groups of the conjugated polymer were end-capped using the monoboronic ester of **13** to afford a well-defined ladder-type structure. As a result, the synthesized spiro-bridged LPPP **14** showed typical properties of a rigid cLP – no obvious chromatic shift in the UV-Vis and PL spectra between solution and the solid state was seen. In addition, the

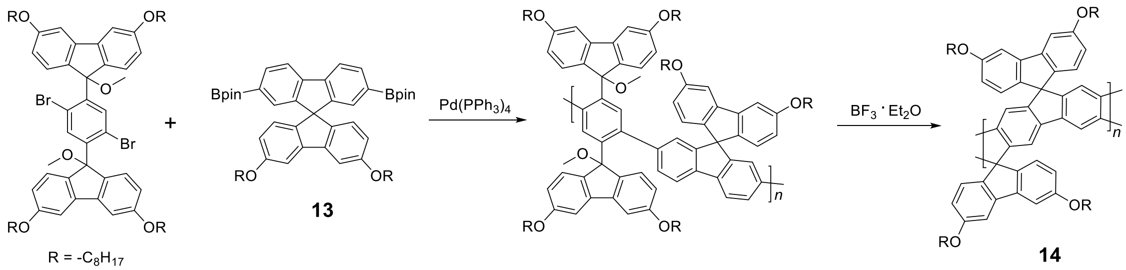

Scheme 1.4. Synthesis of spiro-bridged LPPP **14** by Friedel-Craft ring annulation.

polymer exhibited a small Stokes shift of 2 nm, and excellent thermal and optical stability. The remarkable thermal stability was also demonstrated by the unchanged PL spectrum after annealing at 110 °C for 24 h in air. Bo and coworkers. also reported the synthesis of a soluble imine-bridged ladder polymer **15** by Bischler-Napieralski cyclization (Scheme 1.5).[46] The carbazole-fluorene conjugated polymer with dodecanamides was cyclized by $POCl_3$ in the presence of P_2O_5 to form the imine bridge. It is interesting to note that the repeating units of the synthesized ladder polymer **15** lack a C_{2h} symmetry, resulting in a backbone which possesses an angular structure and does not extend in a straight manner.

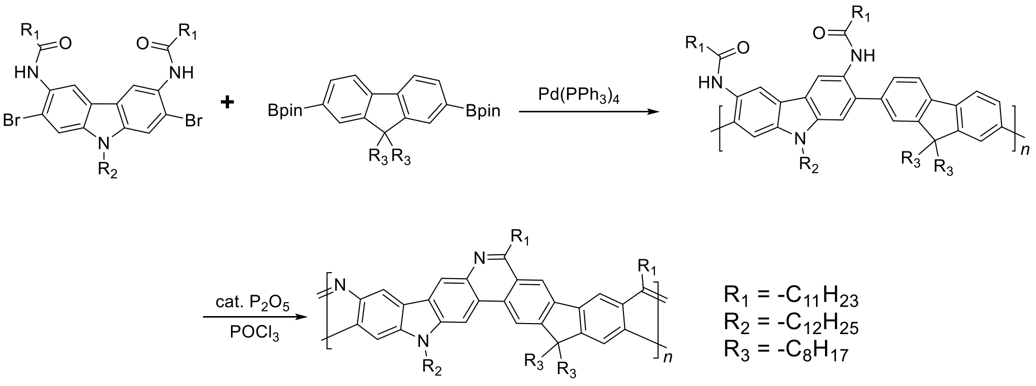

15

Scheme 1.5. Synthesis of carbazole-fluorene-based ladder polymer **15** by Bischler-Napieralski cyclization.

More recently, Scherf and coworkers. reported a donor-acceptor (D-A) alternating ladder polymer **16**, fusing electron rich thiophene units and electron deficient benzothiadiazole (BTD) units in the backbone. The synthesis was achieved by reduction of the ketones followed by the ring-closing reaction in the presence of boron trifluoride (Scheme 1.6).[36] The key to this successful synthetic design was the ability to pre-fuse the electron-deficient BTD unit with thiophene, which avoided electrophilic cyclization on an already electron deficient aromatic unit.

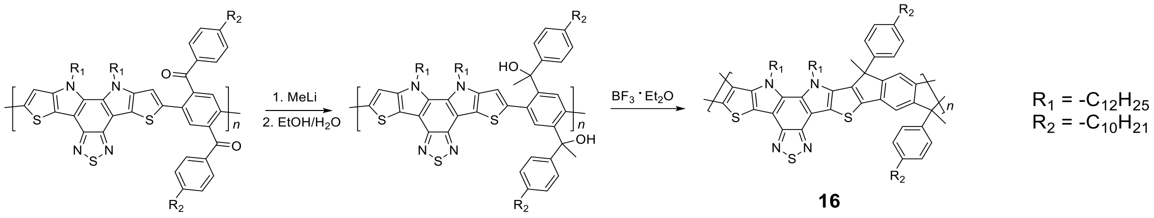

Scheme 1.6. Synthesis of D-A type ladder polymer **16** by Friedel-Craft ring annulation.

Scherf and coworkers also reported[47] the synthesis of ladder type poly(*p*-phenacene) derivatives by using Yamamoto coupling of a diketo-functionalized monomer, followed by carbonyl olefination in the presence of B_2S_3. Alternatively, the ladderization step could be also carried out by the McMurry reaction. In this report, polymer **17** with a linear side chain (4-decyloxyphenyl) resulted in a polymer which was marginally soluble, so that the product was soluble only at a low molecular weight (*ca.* 4 kg/mol). The solubility and molecular weight of ladder type poly(*p*-phenacene) derivative **17** was improved by replacing the linear side chain with bulkier (3,4-dihexyloxy)phenyl units.[48] A similar ladder-type backbone was also prepared by Swager and coworkers using electrophile-induced cyclization (Scheme 1.7).[49] The acetylenic functional group on the conjugated polymer was cyclized in the presence of trifluoroacetic acid (TFA) to form aromatic rings to afford the ladder polymer **18**.

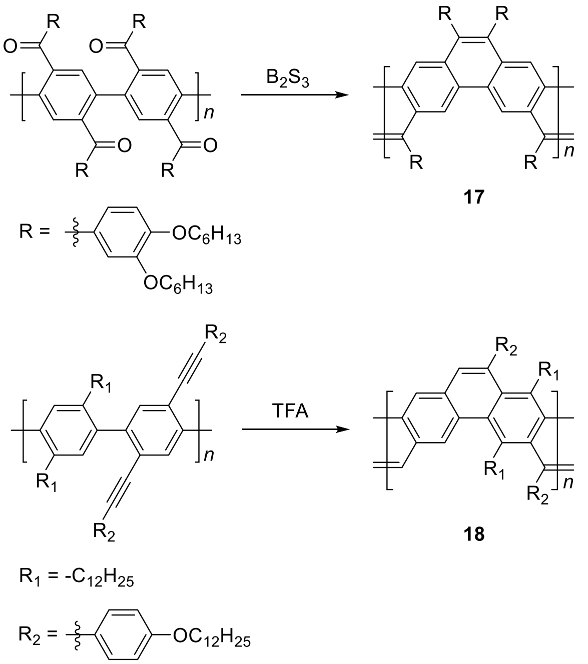

Scheme 1.7. Synthesis of poly(*p*-phenacene)s **17** and **18** by carbonyl olefination and electrophile-induced cyclization, respectively.

Electrochemical and photochemical oxidation reactions could also be employed to prepare cLPs (Scheme 1.8). Bard and coworkers described an electrochemical oxidation polymerization of precursor **19** to afford the postulated ladder polymer **20** deposited on the electrode surface. Because of the uncertain regioselectivity of the oxidative coupling process and the insolubility of **20**, the precise structure cannot be characterized by solution-phase analysis.[50] Xiong and coworkers reported photocyclization of a conjugated polymer precursor under sunlight,[35] to afford D-A ladder polymer **21** with a highly rigid and coplanar aromatic core. Due to the electron deficient nature of its perylene diimide components, **21** exhibited a low LUMO energy level of -3.98 eV, promising good *n*-type semiconducting behavior. Although the ladder polymer **21** had moderate solubility in common organic solvents at room temperature, structural characterization of the ladder backbone proved to be difficult.

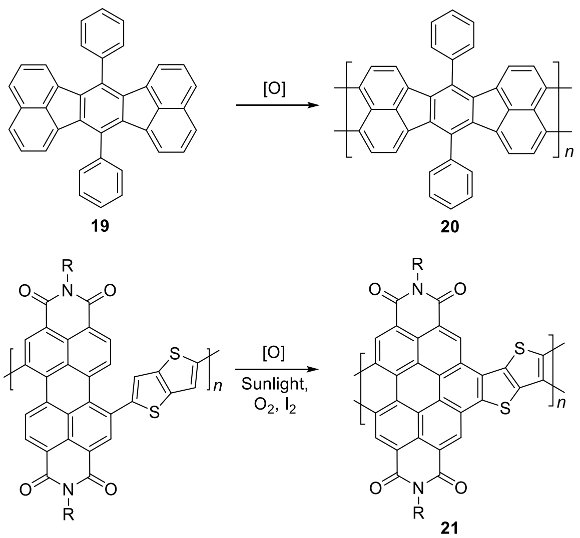

Scheme 1.8. Synthesis of ladder polymer **20** by electrochemical oxidation and D-A type ladder polymer **21** by photochemical oxidation.

In the cases discussed above, metal catalyzed cross-coupling reactions were employed prevalently to construct the conjugated polymer precursors. A synthetic method free of precious metal catalyst, however, would suit better for scalable production of cLPs. Recently, Fang and coworkers reported a 3-step, metal-free synthesis of conjugated ladder polymer **22** derived from quinacridone (Scheme 1.9).[51] Relying on imine polycondensation and a subsequent *in situ* oxidation in air, a conjugate backbone was constructed. The ring annulation was achieved through a kinetic process mediated by methanesulfonic acid. Although **22** was not soluble in common organic solvent, the structural elucidation was achieved indirectly by characterizing its soluble derivative **23**, which is functionalized with *t*-butoxycarbonyl (Boc) groups.

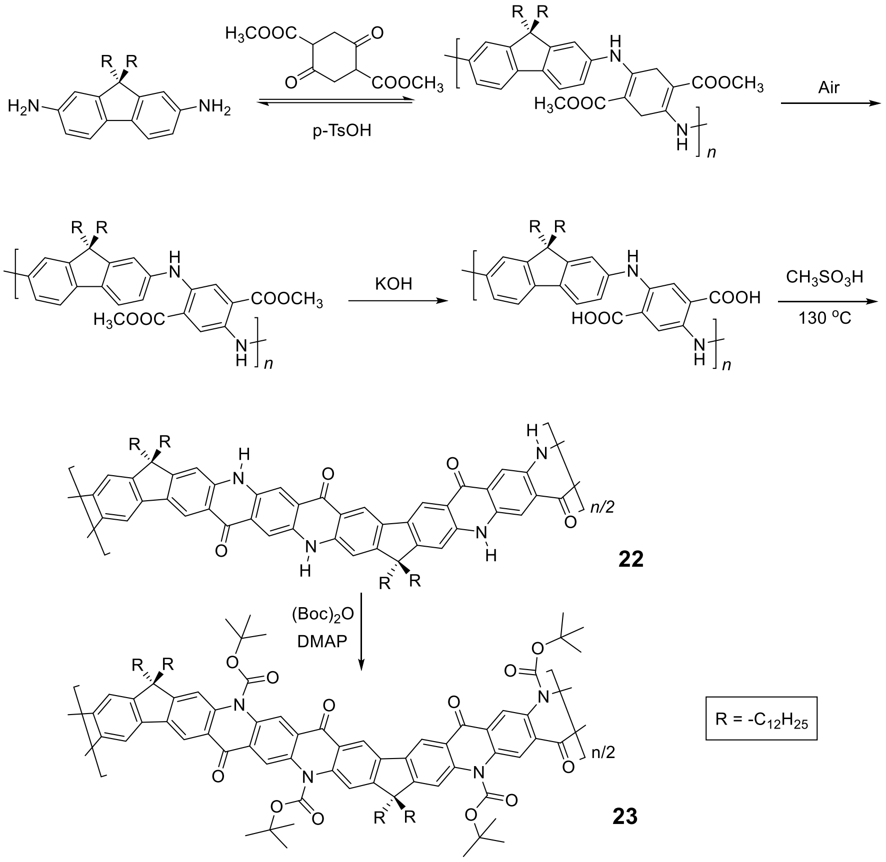

Scheme 1.9. Metal catalyst-free synthesis of quinacridone derived ladder polymers **22** and **23**.

1.1.2.2.2 Thermodynamic Ring Annulation

Distinct from kinetically controlled annulations, which require a careful selection of reagents and conditions for the efficient production of a single product due to the irreversibility of the reactions, thermodynamically controlled annulations, in principle, allow "error-checking" and "proof-reading" to push the reversible equilibrium to the most stable state.[52] Because the goal in the synthesis of cLPs is usually to construct stable aromatic rings, thermodynamically controlled reactions should afford the desired product with higher yield and fewer structural defects such as unreacted sites or inter-chain crosslinking.

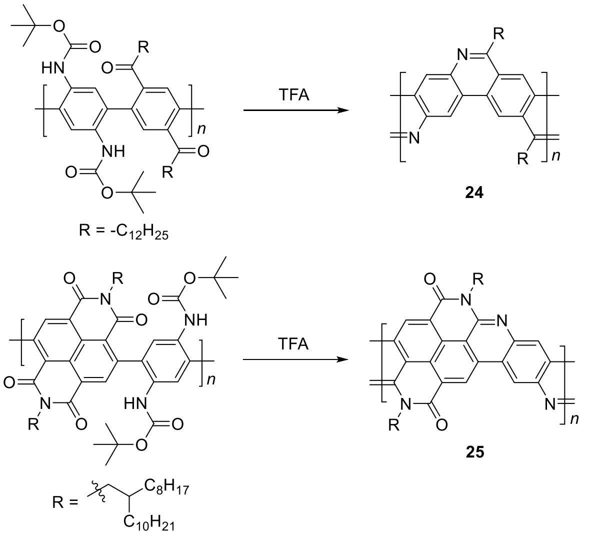

Scheme 1.10. Synthesis of imine-bridged LPPP **24** and D-A type ladder polymer **25** by thermodynamically controlled imine condensation.

In the 1990s, Tour *et al.* reported a thermodynamically controlled reaction for post-polymerization modification that afforded cLP **24**.[53] Imine-bridged LPPP **24** was synthesized by imine condensation of a conjugated polymer precursor (Scheme 1.10). To avoid unwanted imine condensation between free amines and ketones during the polymerization step, the amino group was protected by Boc group before the polymerization. In several small molecule model reactions, this method afforded fused aromatic ring formation and showed nearly quantitative conversions. The conjugated polymer was converted into imine-bridged cLP **24** by deprotection of the Boc group in the presence of TFA. However, **24** was only soluble in TFA, which can result in the protonation of the nitrogen atoms along the polymer chains and could partially dissociate the C=N bond; therefore, the structural analysis of unmodified **24** remained unclear. Luscombe and coworkers also reported solution processable imine-bridged ladder polymer **25** containing naphthalene diimide (NDI) building blocks, synthesized using the same method as **24** (Scheme 1.10).[17] The β-branched 2-octyldodecyl alkyl side chain on the NDI nitrogens provided sufficient solubility for ladder polymer **25** in common organic solvents, though there was no discussion of the effects of the side chain stereocenter on the properties of the polymers. It is worthy to note that the SEC-measured molecular weight of **25** (M_n = 14 kg/mol) was overestimated due to the increased hydrodynamic radius of the rigid, ribbon-like backbone, giving a higher M_n than the precursor conjugated polymer (7.2 kg/mol).

Another method that has recently been recognized as an efficient strategy to construct fused-ring aromatic systems is the thermodynamically controlled ring-closing olefin metathesis (RCM) method.[54] The dynamic nature of the RCM reaction can avoid the formation of cross-metathesis side-products and drives the reaction equilibrium to the desired fused-ring product, which sits in a deep energy sink because of additional aromaticity. Fang and coworkers reported the synthesis of carbazole-derived ladder polymer **27** by RCM from vinyl pendant precursor polymer **26** (Scheme 1.11).[7] The single-stranded conjugated polymer **26** was prepared by Suzuki polymerization and endcapped using styrene derivatives. The reaction was conducted in the presence of a catalytic amount of butylated hydroxytoluene (BHT) as a radical scavenger, to avoid radical crosslinking of the styrene-like derivatives. Because of the strong solubilizing effect of the α-branched 1-octylnonyl group on carbazole, cLP **27** showed good solubility in common organic solvents at room temperature, allowing for solution analysis and processing. ^{13}C NMR analysis of ^{13}C isotope-enriched **27** revealed that the average number of possible unreacted vinyl groups in a single polymer chain was less than one (Defect < 1% and DP^{SEC} = 23-27). Due to the minimum levels of unreacted defects, the polymer conformation was maintained in solution and the solid state giving nearly identical UV-Vis spectra in both states with Stokes shift of only 1 nm.

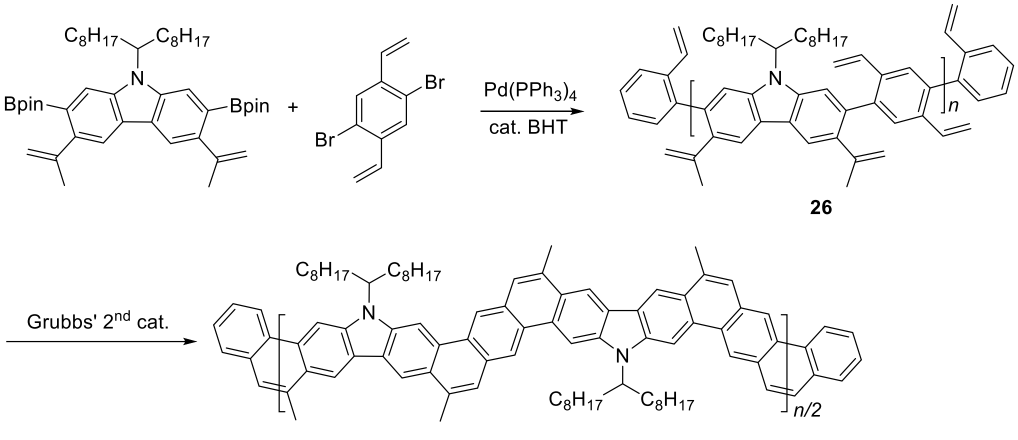

27

Scheme 1.11. Synthesis of carbazole-based ladder polymer **27** by thermodynamically controlled ring-closing olefin metathesis.

Overall, the development of both single-step ladderization and stepwise polymerization followed by ladderization methods has steadily progressed in the past decade. Although the single-step approach is limited in reaction scope, the strategy of using simultaneous dynamic bonds should provide promising advancement for cLP synthesis. For the stepwise approach, various synthetic methods have been explored to expand the selection of kinetic ring annulation. Furthermore, recent examples of thermodynamic ring annulation have widened the scope of the synthesis of well-defined cLPs. As synthetic methods to develop a wider range of cLPs have improved, similar progress has occurred in their analytical and characterization techniques. Though the challenges originating from cLPs' highly rigid structures have prompted the rise of many new techniques, continued innovation of more advanced approaches is still a potentially impactful opportunity.

1.1.3 Challenges and Issues

1.1.3.1. Structural Defects

In conventional conjugated polymers, the planar aromatic repeating units tend to adopt non-zero dihedral angles between each building block due to torsional strain and thermodynamic fluctuation.[55] Such torsional defects partially break the coherent π-conjugation of the backbone, shorten the effective conjugated lengths along the polymer chain, and decrease carrier mobilities.[8, 56] The torsional defects also perturb the intermolecular packing of the polymer materials, resulting in a higher energy barrier for the charge carriers and excitons to transport throughout the bulk material.[11, 57] These combined factors cause a much lower electronic performance of polymers compared to the theoretical value of a conjugated polymer chain.[9] Unlike conventional conjugated polymers, ideal conjugated ladder polymers are torsional defect-free, maximizing π-electron delocalization. As a result, cLPs with a perfect structure should show increased electronic performance over conventional conjugated polymers. Such a defect-free cLP, however, is challenging to synthesize and characterize, as described above. Most of the reported cLPs are likely decorated with structural defects resulting from unreacted sites or side-reactions.

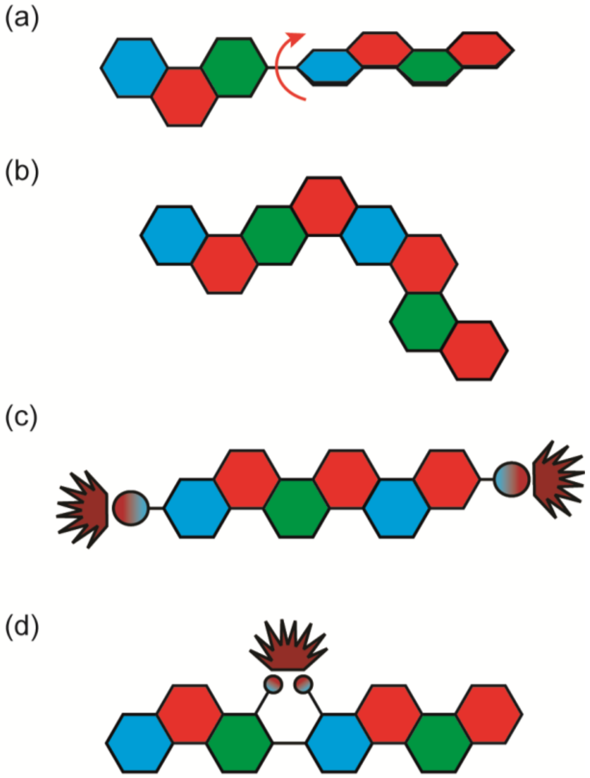

Figure 1.4. Defects common in cLPs. (a) Conjugation breaking torsional defects formed by incomplete ladderization or postsynthetic degradation, (b) regioisomeric structures created during nonregioselective syntheses, and non-conjugation breaking emissive defects (c) as a result of non-ladderized chain end groups, and (d) internally in the polymer chain.

Because of the significant impacts that polymer defects could impose on the material's properties, methods to remove or prevent these defects on cLPs are valuable. There are multiple ways in which defects can occur in a ladder polymer, including impurities in starting materials, incomplete or inefficient ladderization reactions, or a loss of solubility en route to the desired product (Figure 1.4a and b). This leads to the demand of quantitative ladderization reactions, because even a small decrease in conversion from single-stranded conjugated polymer to cLP can cause multiple defects per strand if the molecular weight is high.

An alternative way to achieve low levels of defect in cLPs is to remove defect-containing macromolecules. In the case of cLP **27**, the small amount of polymer chains containing unreacted pendant vinyl groups was reacted in solution with azobisisobutyronitrile (AIBN) to initiate the free radical cross-linking of these vinyl groups. This reaction only takes place on the polymers containing vinyl defects, giving insoluble products that can be easily removed by filtration, leaving behind the pure defect free macromolecules in solution. In general, the defect removal process depends heavily on identifying reactions that selectively react with defect sites. For soluble cLPs, cross-linking the unwanted polymer chains through defect site reactions may be developed into a useful method for purification.

The end groups are also considered defects, because undesired end groups can affect the properties of the polymer by both acting as a charge trap as well as affecting long range packing in some conjugated polymers (Figure 1.4c).[58-60] In this context, end-capping a cLP during synthesis is sometimes necessary to lower the defect level for a better material performance.

In addition, some cLPs may develop defects after synthesis. The defect-property correlations have been investigated thoroughly in LPPP derived cLPs, by taking advantage of the large difference in emission characteristics between the pristine polymer and those with defects. For example, LPPPs **11** and **12** undergo oxidative degradation that can either break one of the strands of bonds and create a torsional defect or be oxidized into an emissive ketone defect. Both LPPPs **11** and **12** and alkylated polyfluorenes, which are photooxidized into fluorenones, have been studied to illustrate the effects of these emissive defects (Figure 1.4d).[61] After these oxidative defects are formed, both systems show a broad, low energy emission, sometimes called the Green Band. Though originally thought to be caused by excimers or other intermolecular interactions, more recent research has shown that it was solely the effect of ketonic defects acting as emissive traps.[62] Such oxidation is much more likely to take place if the bridgehead carbon contains a hydrogen, as illustrated in HLPPP ($R^3 = H$) **11**, which has a much stronger low-energy band than MeLPPP **12**. It is also possible for residual impurities to play a significant role in the degradation of cLPs. Ma's group showed that $Pd(PPh_3)_4$, a common aryl coupling catalyst, could trigger the oxidation of fluorene moieties into their fluorenone forms as well, demonstrating the critical role residual impurities could play in defect formation.[63] PL lifetime measurements of defect formation were recently investigated by Lupton and coworkers using poly(9,9-dioctylfluorene) as a model system,[64] showing evidence that the Green Band is not a single broad band but instead consists of multiple emitters, each at a discrete wavelength. Scherf and coworkers showed that these emissive properties are still maintained in the absence of any intermolecular interactions, further suggesting the lack of excimer involvement in emissions.[65] To rectify this problem, the previously discussed spiro-LPPP **14** was synthesized through a slightly different, but defect-resistant synthetic scheme, and consequently showed a stable emission.[5, 66] These studies illustrated that defects can often impose significant impacts on the optical properties of cLPs.

1.1.3.2. Solubility and Processing

The features of rigid backbones enhance the strong π-π interactions of cLPs and often result in their limited solubility caused by these strong intermolecular attractions.[1, [67, 68] A notable example of a fully fused aromatic system is graphite, which is composed of π-stacked graphene layers and is apparently insoluble in any organic solvent. In addition, the presence of heteroaromatic repeating units may cause other interchain attractive interactions, *e.g.* hydrogen bonds and dipole-dipole interactions. Limited solubility of many cLPs due to these properties imposes challenges in processability and therefore in many practical applications.

A typical method to improve the solubility of cLPs is to introduce to the backbone flexible yet bulky side chains, which cause enough steric hindrance between chains to disrupt interchain aggregation.[17] For example, in LPPPs **11** and **12**, the two alkyl groups installed on the quaternary sp^3 carbon center can be viewed as a branched alkyl group. As the branching point is moved farther from the polymer chain, interchain π-π distance decreases, leading to a general trend of decreasing solubility but increasing charge carrier mobility in bulk.[69, 70] In addition, as alkyl chains grow longer, the amount of space taken up by nonconductive hydrocarbons increases, further separating conductive pathways. Therefore, a balance must be struck between solubility and device performance for a cLP that is designed for applications associated with electronic performances.[69, 71-74] In order to address this dilemma, side-chain engineering in terms of chemical structures, linkages to the backbone, and conformations need to be investigated extensively to best achieve the desired processability and properties of the cLP materials.

A promising strategy to address the aforementioned challenge is the employment of cleavable side-chains. Cleavable solubilizing groups enable solution processability of the cLP materials and can also be easily removed after processing to potentially allow for efficient packing in the solid state (Figure 1.5a). In addition, these polymers should possess significant solvent resistance after processing and side-chain cleavage,[75, 76] providing additional advantages for processing and operation in harsh conditions. In the example reported by Fang and coworkers, quinacridone derived ladder polymer **22** was rendered soluble by the incorporation of bulky Boc protecting groups that inhibit intermolecular hydrogen bonds (Figure 1.5b).[77] These Boc groups were then thermally cleaved to regenerate the hydrogen bonds and to produce thin films with remarkable solvent resistance. Grazing incidence X-ray diffraction (GIXD) measurements of the thermally annealed polymer thin films showed a decrease in the π-π stacking distance as a result of removal of the bulky Boc group (Figure 1.5c).

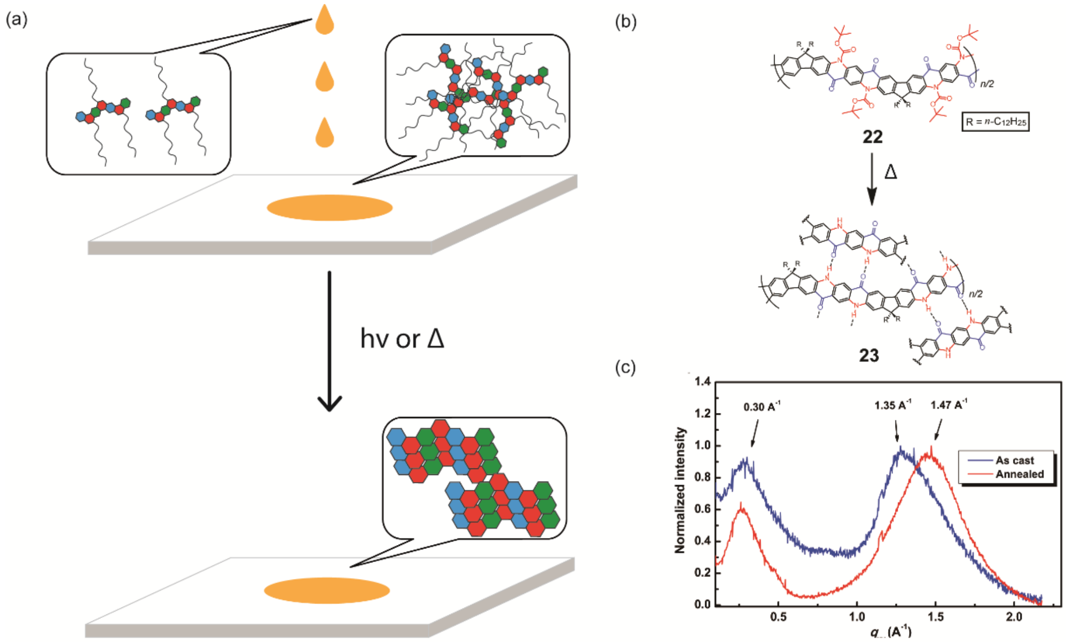

Figure 1.5. (a) Proposed illustration using cleavable side chains in cLPs processing to obtain a well-ordered, solvent resistant film from an easily processed material. (b) Schematic representation of Boc cleavage of **22** by thermal annealing in the solid state. (c) GIXD of the as-cast film of **22** (blue) in comparison with that of the annealed thin film (red). Reproduced from ref. 77 with permission from Elsevier.

1.1.3.3. Characterization of Conformation and Molecular Weight

Because of the inherent rigid nature of cLPs, their conformations and dynamics in solution are expected to differ from prevailing non-rigid polymers significantly. Quantitatively, this difference should give a much higher Mark-Houwink exponent ($0.8 < a < 2.0$) for cLPs than that of flexible polymers ($0.5 < a < 0.8$). Correlation between hydrodynamic volumes and molecular weights for cLPs is therefore also drastically different from that of flexible polymers. As a result, traditional solution characterization techniques, such as SEC calibrated by polystyrene standards, cannot provide accurate depictions of the conformation and molecular weight for cLPs. Research has illustrated that when using multiple methods of analyzing molecular weights,[78-80] the measured values vary between the different methods used. To date, a number of different methods have been applied to solve these issues, with varying levels of effectiveness.

Small angle X-ray and neutron scattering (SAXS and SANS) have been applied to characterize the conformations and gain accurate molecular weights of rigid polymers. X-rays interact with the electron cloud of the molecule, while neutrons are scattered by elastic collisions with the nuclei of the material. The scattering intensity for various values of concentration (c) and scattering angle (θ) is plotted in a Zimm plot. Upon extrapolation to $c=0$ and $\theta=0$, the intersection of the two lines is equal to $1/M_w$ and can therefore be used to determine accurate molecular weights. In addition, the slope of the $\theta=0$ line is proportional to the 2nd virial coefficient. SANS in particular provides a unique method of characterization on partially deuterated samples in order to provide a higher contrast variation without largely changing the sample itself, due to the differences of neutron scattering between hydrogen and deuterium.[81] Alternatively, a hydrogenated sample in deuterated solvent can also provide the needed contrast. These techniques were used, for example, to study the conformation of LPPP **12** in solution.[79] The use of both methods showed a persistence length of approximately 6.5 nm, indicative of a 3D ribbon-like structure instead of a one-dimensional rigid rod. However, the complexity of the instrumentation and radiation sources necessary for these forms of measurement make it challenging to perform routine measurements on other cLP systems.

Simpler light scattering methods have also been utilized to characterize rigid polymers, including dynamic light scattering (DLS), which measures the anisotropic diffusion coefficients of the materials in solution and can be used to estimate the length of an idealized rigid rod.[82] Because of the simplicity and accuracy of measurement, DLS has been used for other rod-like structures and represents an accessible method for the conformational analysis of cLPs.[83, 84]

Other methods to characterize molecular weights of rigid ladder polymers include the use of osmometry or viscometry.[85, 86] These methods rely on the change in chemical potential of a solution of ladder polymers compared to a pure, non-theta solvent. Osmometry measures the osmotic pressure of a solution by change in volume through a semipermeable membrane (membrane osmometry) or of vapor pressure in a closed system (vapor phase osmometry). Viscometry measures the change in viscosity of varying concentrations of a polymer solution in order to find the polymer's intrinsic viscosity, and via the Mark-Houwink equation, the polymer's molecular weight. However, unreliable results may be obtained at either sufficiently high or low molecular weights depending on the method used. In addition, diffusion across the membrane of the osmometer can take extended time to reach an equilibrium.

In order to calculate the molecular weight and polydispersity index (PDI) of cLPs in a more rigorous manner, several advanced methods can be used. These include SEC with viscometer-assisted universal calibration[87, 88] or SEC coupled with multi-angle light scattering detectors.[89, 90] The employment of these methods for the characterization of cLPs, however, has not yet been well-established.

Structural elucidation has been another major challenge for the investigation of rigid cLPs. Both ^{1}H and ^{13}C NMR spectroscopy suffer from broad and low intensity signals, due largely to the limited solubility of the cLP samples and aggregation. This problem can be circumvented by the use of isotope labeling or alternative isotope measurements,[7] in particular ^{13}C or ^{19}F, although the drawback for this method is sometimes tedious chemical synthesis. NMR analysis at higher temperature could also be employed to improve data quality by increasing the solubility and breaking up any aggregation. The incorporation of distinctive side chain or end-capping groups is another simple method to facilitate easier characterization. Alternatively, using the effects that rigid macromolecules have on NMR linewidths can also offer unique information of the polymers, such as the nature of solution aggregation or solid-state crystallinity.[91-93]

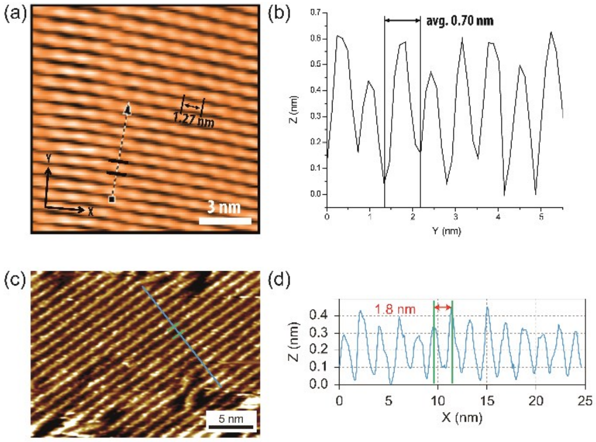

Figure 1.6. (a) STM images of cLP **27** on HOPG. (b) section profile along the arrow line drawn in (a). (c) STM images of the graphene nanoribbon on HOPG from ref. 68. (d) section profile along the blue line in (c). Reproduced from refs. 7 and 68 with permission from The Royal Society of Chemistry and Nature Publishing Group, respectively.

Surface probe microscopy can also be used to visualize the conformation of cLPs. In particular, due to the conjugated and semiconducting nature of the backbones, individual polymer chains of some cLPs can be visualized by scanning tunneling microscopy (STM). STM analysis of cLP **27** on highly-ordered pyrolytic graphite (HOPG) showed the rigid and linear shape of the polymers with repeating units that aligned well with calculated dimensions of an oligomeric model (Figure 1.6).[7] In addition, STM has found extended use in the visualization of graphene nanoribbons with improved resolution due to the extended conjugated system's favorable interaction with graphite substrates.[68, 94]

In general, though many accurate techniques have been adopted for cLP characterization, the most common method remains the use of non-rigid SEC standards. Therefore, the widespread application of a universally accurate method would help standardize measurements across the breadth of the field, increasing the quality and efficiency of related research.

1.1.4 Applications of cLPs

As discussed in the previous sections, cLPs possess rigid and planar backbones with optimum π-electron delocalization and are free of torsional defects. From this perspective, cLPs are analogous to graphene nanoribbons, which combine the excellent charge transport property of graphene with opened band gaps as high-performance semiconducting materials.[95] In addition, the rigid and planar backbones of cLPs also render extremely small Stokes shifts and high photoluminescence quantum yields.[96] Furthermore, cLPs display potentially high thermal and optical stability as well as high resistance to chemical degradation.[2] Such combination of unique properties of cLPs make them promising candidates for a wide range of applications.

1.1.4.1. Optical applications

Early examples have demonstrated that the superior optical properties of cLPs could lead to high performance in OLEDs.[2] One area of focus has been the use of LPPPs as the active layer for OLEDs, taking advantage of the highly efficient yellow-green electroluminescence (EL).[1414] OLED devices fabricated using spiro-LPPP **14** as the active layer exhibited almost identical EL and PL spectra due to the minimal ketonic defects.[5] This result indicated again the significant impact of defects on opto-electronic properties of cLPs and the importance of a low level of defects in these materials. Blue-green emitting derivative MeLPPP **12** showed EL efficiency up to 4%.[15] To improve its processability, nanoparticles of MeLPPP **12** have also been prepared via miniemulsion and employed in an OLED device.[16] Although the device showed a similar maximum brightness with that of the device fabricated from homogeneous solution, the turn-on voltage for the EL was reduced by 7 V. This improvement based on the nano-particulated ladder polymer was attributed to a better electron injection from the nanoparticles to the electrode.

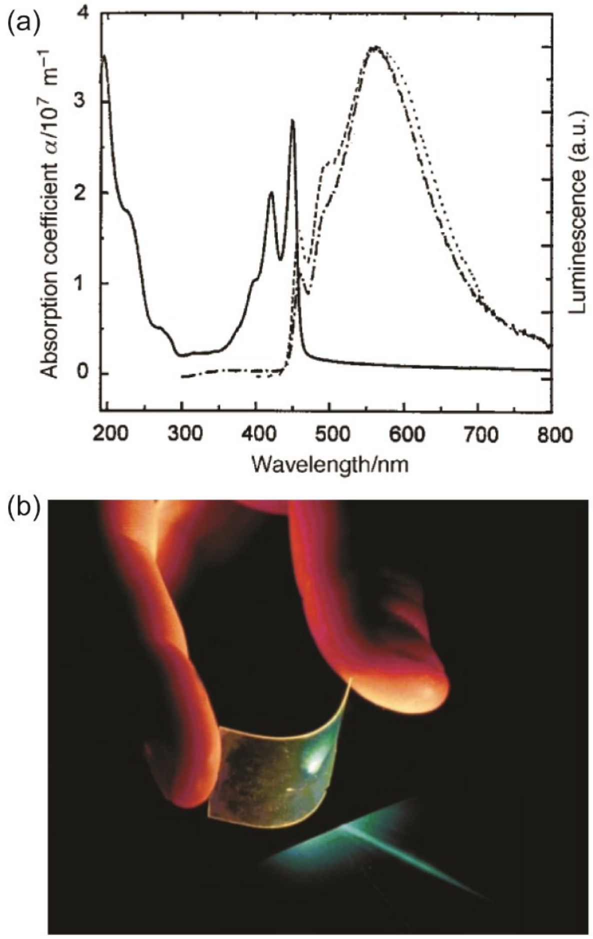

Figure 1.7. Optical properties of ladder polymers. (a) Absorption (—) and PL spectra (---) of a thin film of MeLPPP **12**. (b) A photo of a blue, flexible laser made from MeLPPP **12**. Reproduced from ref. 2 with permission from The Royal Society of Chemistry.

Besides OLED applications, MeLPPP **12** has also been spin-cast onto a poly(ethylene terephthalate) substrate[97] to afford a low-cost flexible distributed feedback laser. The laser emitted blue light centered at 487 nm with a linewidth of less than 0.4 nm (Figure 1.7b). Another optically interesting example of cLPs is ladder-type triply fused porphyrin tapes (**28a - f**), which show a remarkably red-shifted absorption band in the IR region (Figure 1.8).[98] This IR absorption band was a result of the strong intramolecular electronic coupling and coplanar geometry of the molecule. The IR absorption maximum increases linearly with the number of porphyrin units, demonstrating the large increase in effective conjugation length. The porphyrin polymer **28f** with the highest number of repeating units showed an absorption peak around 3500 cm^{-1}, making it a good candidate as an IR sensor. It is likely that **28f** has not yet reached the maximum effective conjugation length. Such a unique photophysical property of **28** was originated from the large coherent π-conjugation through triply fused backbone. As a result, the porphyrin tapes exhibited much faster internal conversion processes and energy relaxation dynamics of the lowest excited states compared to that of monomer and the non-ladder type porphyrin oligomers.[99]

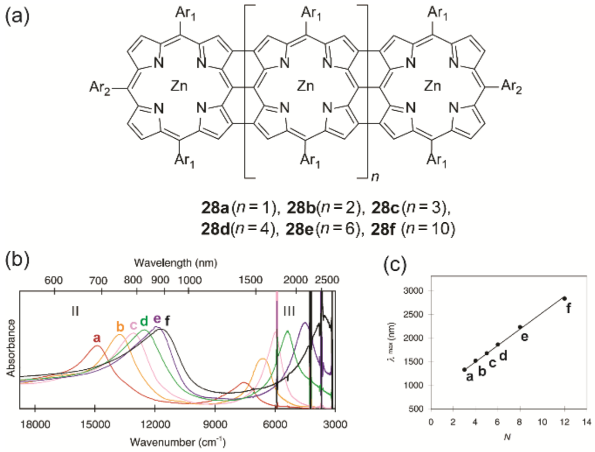

Figure 1.8. (a) Chemical structures of ladder-type porphyrins **28a**–**f**. (b) UV-vis-IR absorption spectra of porphyrins **28a**–**f**. (c) Plot of IR absorption maximum (band III) versus the number of porphyrins (N). Modified and reproduced from ref. 98 with permission from The American Association for the Advancement of Science.

1.1.4.2. Electronic Applications

cLPs show promise to reach a high charge carrier mobility compared to conventional conjugated polymers owing to a low level of torsional defects and a long effective conjugation length. Siebbeles and coworkers studied the intrachain mobility of

LPPPs using time resolved microwave conductivity.[9] With an average repeating unit of 54, the hole mobility along the MeLPPP **12** chain reached a remarkable value of 600 cm^2 V^{-1} s^{-1}. This high intrachain charge carrier mobility suggested that the bottleneck for the charge transport in bulk cLP materials is interchain charge transport.

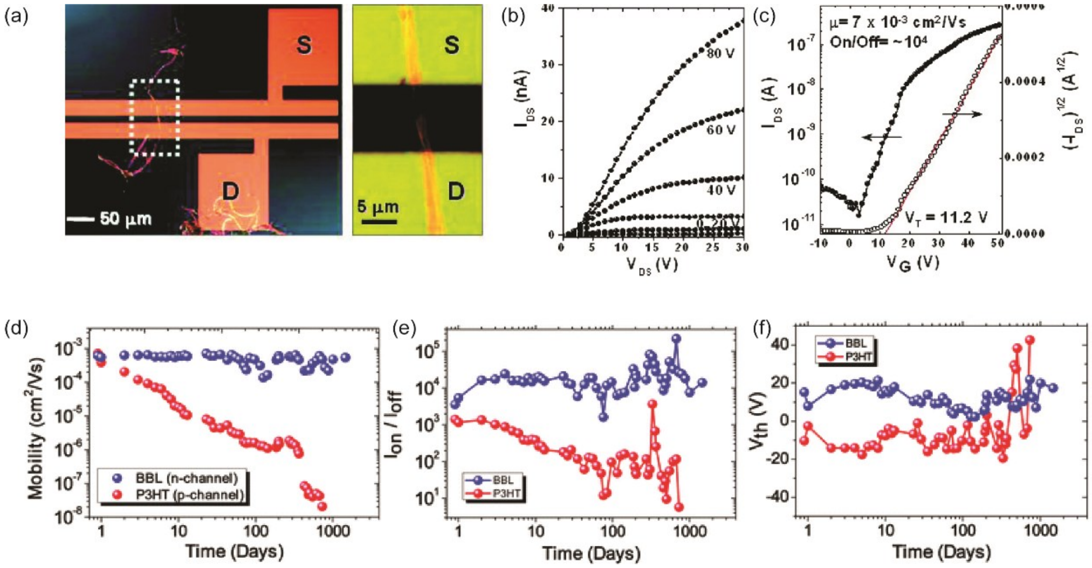

Figure 1.9. Performance of BBL **1** based OFETs. (a) A single BBL nanobelt bridging the source-drain electrode to generate a transistor. (b) Output curve of a typical BBL nanobelt transistor. (c) Transfer curve of the corresponding transistor. (d-f) Air stability analysis of P3HT and BBL transistors. Plot of (d) mobility, (e)current on/off ratio, and (f) threshold voltage as a function of time for both BBL and P3HT transistors. Reproduced from refs. 21 and 102 with permission from American Chemical Society and The Royal Society of Chemistry, respectively.

In terms of bulk electronic properties in OFETs, BBL **1** has been investigated extensively since the late 1980s.[100] A series of improvement on charge transport properties were achieved by doping the BBL thin films with Lewis acid, but the overall mobility of fabricated devices was relatively low (10^{-6} to 10^{-4} cm^2 V^{-1} s^{-1}).[19, 20] In 2003, Jenekhe and coworkers achieved a record high electron mobility of BBL **1** up to 0.1 cm^2 V^{-1} s^{-1} by doping and processing it with methanesulfonic acid (MSA).[18] This value was 5 orders of magnitude higher than that obtained from a non-ladder type control polymer. Electron diffraction studies demonstrated a higher degree of crystallinity of the MSA-processed BBL film. This result also represented one of the highest electron transport mobilities achieved on an *n*-type polymer OFET at that time. Later on, Xia and Jenekhe and coworkers developed a high-yield solution-phase processing method to prepare BBL nanobelts with a good ambient stability.[21] The BBL nanobelt was prepared by adding BBL in MSA solution dropwise to a $CHCl_3$ and MeOH mixture with rapid stirring. These nanobelts can be suspended in water and used to fabricate OFET device via solution deposition. The *n*-type OFET device showed a mobility up to 7×10^{-3} cm^2 V^{-1} s^{-1} and the on/off current ratios ($I_{on/off}$) of 10^4 (Figure 1.9a-c). Moreover, in contrast with many *n*-type organic semiconductors which are sensitive to oxygen during operation,[101] the BBL-based devices demonstrated exceptionally good stability in air for more than 4 years, even better than *p*-type polythiophene devices (Figure 1.9d-f).[102] The remarkable stability of BBL devices was attributed to its high degree of crystallinity and compact packing, which serves as a kinetic barrier to prevent oxygen from diffusing into the thin film.

Because of its excellent electronic properties and stability, BBL **1** has been used as a photoanode for the direct light-driven water oxidation reaction.[103] The BBL photoanode showed good photoelectrochemical stability with no sign of degradation after 3 hours of water oxidation reaction. The electrical and thermoelectrical properties of a solution-processed BBL thin film was also studied very recently.[104] After *n*-doping, the BBL thin film exhibited an electrical conductivity as high as 1.7 ± 0.6 S^{-1}, three orders higher than that of NDI-based conventional conjugated polymer P(NDI2OD-T2). Density functional theory (DFT) calculation indicated that BBL possesses a much more delocalized polaron along its backbone than P(NDI2OD-T2), due to its coplanar backbone and low level of torsional defects. After optimizing, the thermoelectric power factor ($S^2\sigma$) of BBL reached 0.43 $\mu W\ m^{-1}\ K^{-2}$, much higher than those observed for non-ladder P(NDI2OD-T2).

Luscombe and coworkers reported the fabrication of an *n*-type OFET using an NDI-based ladder polymer **25**.[17] OFET device fabrication using **25** from chlorobenzene solution by spin-coating exhibited an average electron mobility of 0.0026 $cm^2\ V^{-1}\ s^{-1}$, which is three orders of magnitude larger than its non-ladder counterparts. The on/off current ratio of the device ($I_{on/off} = 10^4$) was 2 orders of magnitude higher than that of the non-ladder type polymer.

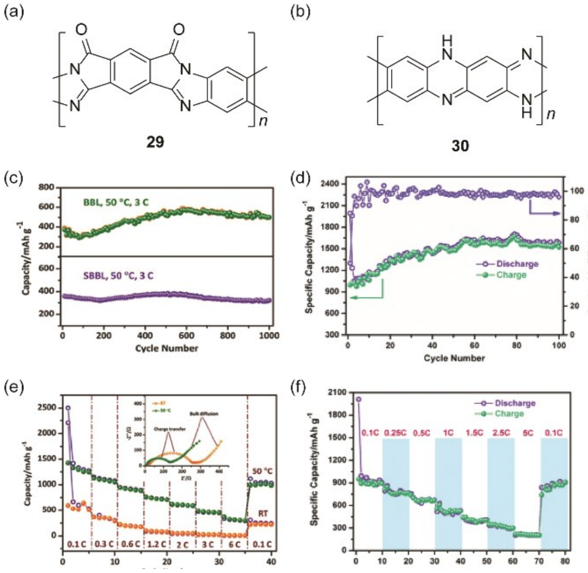

Figure 1.10. Chemical structures of (a) SBBL **29** and (b) PQL **30**. Electrochemical performance of ladder polymer nanoparticles. Cycling performance of (c) BBL **1**, SBBL **29** and (d) PQL **30** nanoparticles showing their superb stability. Rate capability of (e) BBL **1**, SBBL **29** and (f) PQL **30** nanoparticles. Reproduced from refs. 107 and 108 with permission from Wiley-VCH.

Recently, cLPs with a large number of heteroatoms were found to be promising candidates for anode materials of lithium batteries. The prevailing electrodes for lithium batteries in the current market are graphite and $LiCoO_2$. The theoretical capacities of these materials, however, are only about 372 mAh g^{-1} and 140 mAh g^{-1}, respectively.[105] One important strategy to increase the performance is to incorporate redox active heteroatom sites into fused-ring sp^2 systems, such as nitrogen or sulfur. Fan and coworkers synthesized a polysulfur-grafted ladder poly(pyridinopyridine) by heating the precursor poly(acrylonitrile) (PAN) with sulfur at 350 °C.[106] Although the constitutional structure of this ladder polymer is not well-defined, the high percentage of nitrogen and sulfur atoms permits multi-electron states for this polymer to give a high reversible capacity of 1750 mAh g^{-1}. Yan and Zhang and coworkers exploited nanoparticles of BBL **1** and its derivative SBBL **29** as the anode materials of a rechargeable lithium ion battery.[107] These ladder polymers showed a high capacity (1787 mAh g^{-1}, 0.05 C), a good charge rate (317 mAh g^{-1}, 6 C) and an excellent reversibility (1000 cycles, 496 mAh g^{-1}) (Figure 1.10c and e). Inspired by these results, PQL **30** was synthesized to represent a ladder polymer with a large number of nitrogen heteroatoms to serve as the lithium ion insertion sites.[108] At the charge rate of 0.05 C under 50 °C, the lithium half-cell made from PQL **30** nanoparticles exhibited a capacity of 1770 mAh g^{-1} (Figure 1.10d). Moreover, PQL **30** maintained a reversible capacity (above 300 mAh g^{-1}) at a high charge rate of 5 C (Figure 1.10f). The excellent electrochemical performances of cLP materials promise their applications as alternative electrodes for lithium ion batteries.

1.1.4.3. Outlook for potential applications

Despite the aforementioned examples, large-scale applications of cLPs have not been widely established yet, likely due to the synthetic and processing challenges. It is anticipated, however, that these issues can be solved using various chemical and engineering tools. Therefore, advancement along this direction together with the promising properties of cLPs could open up a number of intriguing opportunities for cLP applications.

First of all, cLPs can be viewed as functionalized fragments of single-wall carbon nanotubes (SWCNTs) or graphene nanoribbons. The exceptionally high Young's modulus (> 1 TPa) of SWCNTs and graphene[109, 110] suggest that the simplest linear cLPs, polyacenes, could potentially possess good mechanical properties. DFT calculations on a polyacene resulted in a chain moduli as high as 745 GPa, close to that of (5,5) CNT (1046 GPa).[6] Although polyacenes cannot be synthesized so far due to synthetic challenges and chemical stability issues,[111] cLPs similar to polyacenes can be potentially prepared and should afford comparable mechanical performances.

Furthermore, cLPs are also promising candidates as precursors for high performance carbon fibers. Currently, most high-performance carbon fibers are produced from PAN.[112] Before carbonization, PAN fibers undergo a stabilization process in which they are oxidized to form a ladder polymer-like structure.[113] The progress of the ladderization reaction largely determines the quality of the carbon fiber. Therefore, carbonization of a defect-free ladder polymer with a well-controlled structure could potentially further enhance the mechanical properties of carbon fibers and enrich their functionalities.

Another potential application for cLPs is for organic photovoltaics (OPVs). Step-ladder polymers have been extensively studied for active layer materials in OPVs.[114] For step-ladder polymers, the increase of the conjugation length of the polymer would effectively enhance charge separation and carrier mobility, contributing to a better power conversation efficiency of the OPVs.[115] Compared to step-ladder polymers, cLPs possess an even more planarized structure, rendering a higher electron delocalization, larger charge carrier mobility, and better absorptivity, resulting in a potentially higher photovoltaic efficiency. OPV performances should become optimized as the active polymers approach a fully defect-free conjugated structure. In addition, the promising thermal and photo-stability of cLPs could serve as the key to address the stability issues of OPVs. Of course, potential morphological problems still remain when utilizing these highly rigid polymers in a device setting.

Furthermore, the rigidity and concomitant low disorder of cLPs also make it an ideal platform to study Bose-Einstein condensate (BEC) physics of exciton-polaritons. BECs of exciton-polaritons were normally observed in crystalline materials considering the high level of disorder in the condensed phase. Due to the complexity of crystal growth in the microcavity, investigating BEC physics was challenging. Stoferle and coworkers demonstrated exciton-polaritons' BEC state can be generated in an amorphous MeLPPP **12**, at room temperature, when coupling the polymer thin film to the confined photon mode of a Fabry-Perot microcavity.[116] This study suggests cLPs can provide a new approach to study BEC physics with a simplified experimental condition.

1.1.5 Linear cLP Outlooks

This section summarizes important historical syntheses, examples of processing and applications of cLPs, as well as significant advances in the past decade. The intriguing properties of cLPs promise their future as next generation functional polymer materials. However, in order to maximize the potential of this class of materials, the challenges associated with the synthesis, structural defects, characterization, solubility, and processability of cLPs need to be addressed.

For the synthesis of a well-defined cLP, the development of synthetic strategies in either single-step ladderization or post-polymerization ladderization has seen significant progress. Although the single-step approach is limited by the availability of reactions suitable for the formation of multiple strands of bonds, the idea of using spontaneous intramolecular dynamic bonds enables the possibility of constructing a coplanar ladder-like structure through a single-step polymerization. The stepwise strategy – *i.e.*, polymerization followed by ladderization, – now could afford feasible approach to well-defined cLPs with fewer structural defects. More recently, thermodynamic ring annulation, including RCM, has widened the scope of well-defined cLP synthesis and promises the production of defect-free cLPs.

In order to analyze cLPs' highly rigid structures, analytical and characterization techniques have to evolve alongside the development of synthetic strategies. In contrast with conventional conjugated polymers, the conformation and dynamics of cLPs in solution are significantly different. Therefore, common characterization methods such as SEC with polystyrene standards do not provide accurate depictions of the conformation and molecular weight for cLPs. Several different analytical methods have been applied to overcome the limited effectiveness of SEC. However, the complexity of the instrumentation restricts extensive routine measurements for cLPs. The visualization of rigid ribbon-like structures was also studied by STM. Even though STM displayed detailed conformations of rigid structures at a small scale on solid substrate, it cannot provide an all-encompassing analysis of the entire batch or that in solution. ^{1}H NMR spectroscopy provides rich characterization information of cLPs, but it is often limited by the line broadening and low signal/noise ratio. Hence, the development of accurate characterization methods for cLP characterization is as important as the development of synthetic strategies.

Owing to the limited solubility of cLPs in common organic solvents, only a few successful processing methods were reported before LPPPs were first reported. Because LPPPs are usually soluble in common organic solvents, their electronic and optical properties have been extensively studied. Particularly, MeLPPP **12** has been used for many applications such as OLEDs and OFETs and showed excellent optoelectronic properties. Moreover, the advances made in processing methods allowed processability of insoluble cLPs like BBL **1** through the formation of nanoparticles, leading to devices showing exceptional air stability for multiple years. More recently, cLPs have been applied as electrodes for lithium ion batteries and demonstrated superior capacity and reversibility.

Despite these exciting progresses, the applications of cLPs have not been fully explored yet due to previously mentioned challenges.

Overall, cLPs possess great potential in applications at multiple fronts due to their promising superior properties with remarkable stability. Throughout 50 years of exploration and development, we have seen the promising aspects of cLPs as functional organic materials. We believe, however, that many more thrilling discoveries in this class of materials will be made in the future.

1.2 Crosslinked Ladder Polymer Networks

Porous materials are of a great interest to numerous applications, including chemical storage, separations, catalysis, and energy, among many others, with porous polymers making up a significant subset of such materials.[117] The versatility, modularity, and broad synthetic scope of organic polymer chemistry enables highly tunable, application-directed polymeric materials.[118] A recent area of significant growth revolves around the use of conjugated monomers to form such polymeric systems such as covalent organic frameworks (COFs)[119, 120] or porous polymer networks (PPNs). The latter term, PPN, is herein used to describe amorphous polymer networks comprised of solely conjugated repeating units, while COFs refer to crystalline networks. The rigid backbones of the materials stabilize permanent porosity, often exhibiting high Brunauer-Emmett-Teller (BET) surface areas with different backbone functionalities giving rise to targeted performance for specific applications.[121, 122] As with the previously discussed linear conjugated polymers, ladder polymer chemistries have been applied to crosslinked polymers to achieve improved properties.

The majority of reported crosslinked cLPs rely on the simultaneous creation of both strands of bonds in a single reaction step, though multiple examples of the sequential polymerization–annulation strategy are discussed below. One potential limiting factor for the sequential strategy is that the second annulation step must take place homogeneously within the pores of the initially polymerized network, which may limit diffusion of bulky catalysts, though appropriately sized reagents can still be successful.[123]

Often, reversible reactions such as imine condensation are used to obtain both bonds in a similar manner to early linear cLPs. For example, Jiang and coworkers reported multiple aza-fused π-conjugated microporous frameworks through imine condensation of multifunctional monomers (Scheme 1.12). 1,2,4,5-tetraaminobenzene and triquinoyl hydrate were polymerized to form crosslinked cLP **31** as an amorphous network and later, triphenylene hexamine and *t*-butylpyrene tetrone gave **32** as a crystalline COF.[124, 125] In both cases, the microporous solids possessed a high BET surface area, including up to 1227 m^2 g^{-1} in the case of **31** synthesized at 500 °C. The fused nitrogen sites allowed these networks to be used in energy applications, including for supercapacitive energy storage[124] or for photoenergy conversion and charge transport.[125] Another condensation reaction used to give crosslinked cLPs is the acid-catalyzed trimerization of indole-containing molecules. Scherf and coworkers used various Lewis and Brønsted acids to polymerize three different monomers to obtain cLPs **33-35** with BET surface areas varying from nonporous up to 1165 m^2 g^{-1}.[126] Ruoff and coworkers recently reported the mostly amorphous cLP **36** by ionothermal cyclization of o-cyanoaniline derivatives in the presence of $ZnCl_2$, releasing NH_3 gas as the reaction proceeds.[127] The highly nitrogenous backbone improved CO_2 adsorption, with an uptake capacity of up to 7.16 mmol g^{-1} (at 273K, 1 bar) and a CO_2/N_2 selectivity ratio of over 74.

Other crosslinked ladder polymers have recently been reported using aromatic substitution reactions of strongly electron-deficient perflourinated aromatic monomers (Scheme 1.13). Swager and coworkers reported the concept of using a reversible S_NAr reaction to create fully fused aromatic products.[128] They were able to leverage this reversibility to obtain high yielding small molecules, macrocycles, and an amorphous cLP **37** possessing a BET surface area of 817 m^2 g^{-1}, though the extent of polymerization was relatively low likely on account of poor solubility. It is certainly likely that a greater extent of polymerization could improve the porous characteristics of the material, as evidenced

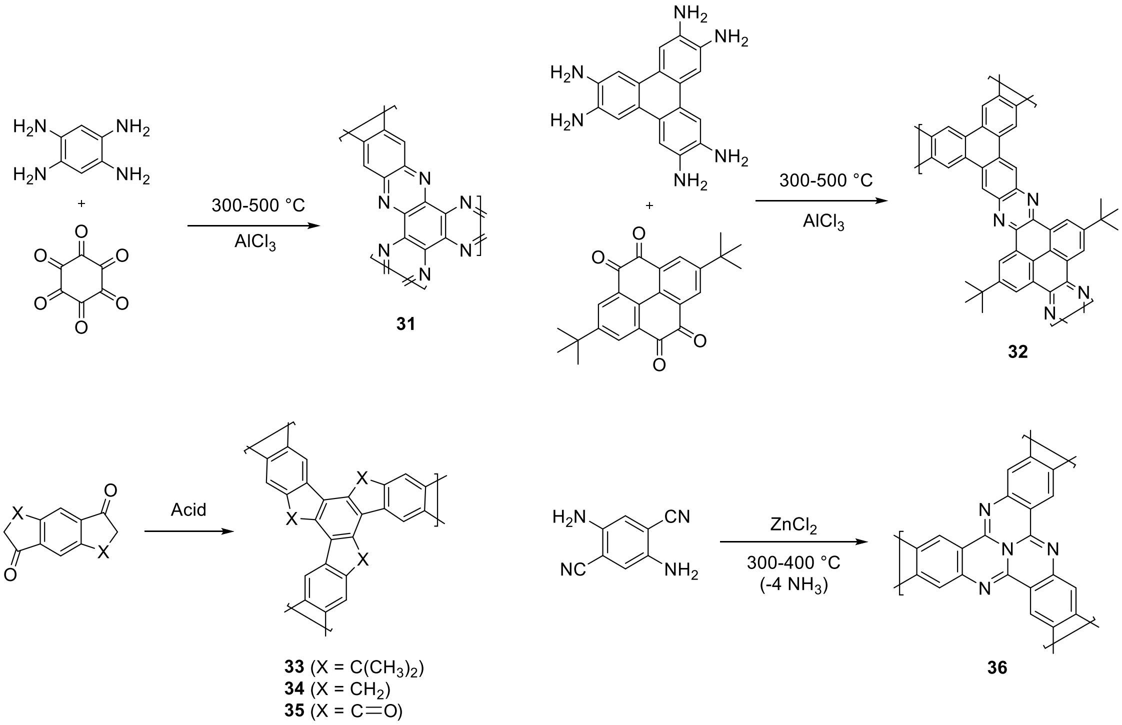

Scheme 1.12. Synthesis of crosslinked cLPs based on one-step condensation polymerizations.

by a similar S_NAr polymerization reported by Qiu. They polymerized tetrafluorinated monomers with hexahydroxyltriphenylene in a base-catalyzed solvothermal reaction to give crystalline, ladder-type COF **38**, which were highly stable in strongly acidic, basic, reducing, and oxidizing environments on account of their poly(aryl ether) backbones.[129]

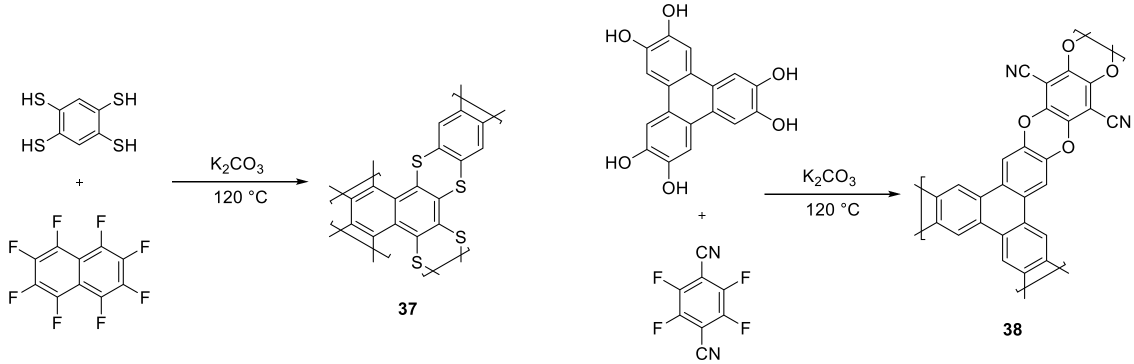

Scheme 1.13. Synthesis of branched cLPs using base-catalyzed nucleophilic aromatic substitution reactions.

In a few cases, branched ladder polymers have been synthesized using the two-step polymerization–annulation strategy.[130, 131] These examples relied on the chemistry used in the synthesis of LPPP, in which an aryl coupling polymerization is followed by a Friedel-Crafts type annulation. Interestingly, these polymers remain soluble after both polymerization and annulation. The molecular weights reported indicate that this solubility may result from a relatively low degree of polymerization. The low degree of polymerization as well as the large sidechains used for solubility of the monomers also mean that these polymers are likely nonporous, though porosity is not discussed in the text. These cases illustrate that solubility is a key challenge in the synthesis and application of crosslinked cLP networks. To date, a porous yet processable crosslinked ladder polymer network has remained an elusive target, motivation for the work presented in Chapter 4.

1.3 X-ray Scattering for Thin Film Morphology Characterization

As significant motivation behind cLP research stems from their potential as applied materials, characterization of their solid-state morphology is important in determining their propensity for different end uses. Because conjugated materials have anisotropic charge transport properties, the manner in which molecules are aligned on a substrate makes certain charge transport directions more favorable than others.[132-135] In some devices, charge transport occurs parallel to the substrate, while in others such as photovoltaic cells and light-emitting diodes, charge transport typically occurs perpendicular to the substrate. Therefore, a reliable method to characterize the solid-state packing of conjugated materials on a substrate is essential.

Grazing-incidence X-ray scattering (GIXS) has emerged as a powerful characterization technique to probe molecular packing and thin film nanostructure.[136-139] A material of interest on a substrate is exposed to an X-ray beam at a very shallow incident angle (α_i), generally below the critical reflective angle (α_c) of the substrate and above that of the studied film. The beam therefore penetrates the film but not the substrate and is subsequently scattered by the electron clouds of the molecules (Figure 1.11). The small α_i creates a long, narrow footprint along the surface, with a width equal to the beam width and length equal to the beam height divided by $\sin(\alpha_i)$, e.g., for a 50 μm diameter circular beam with α_i = 0.15°, this equates to a footprint of 50 μm × 1.9 cm. This means that the observed scattering is averaged over a large distance in the sample, ensuring that the

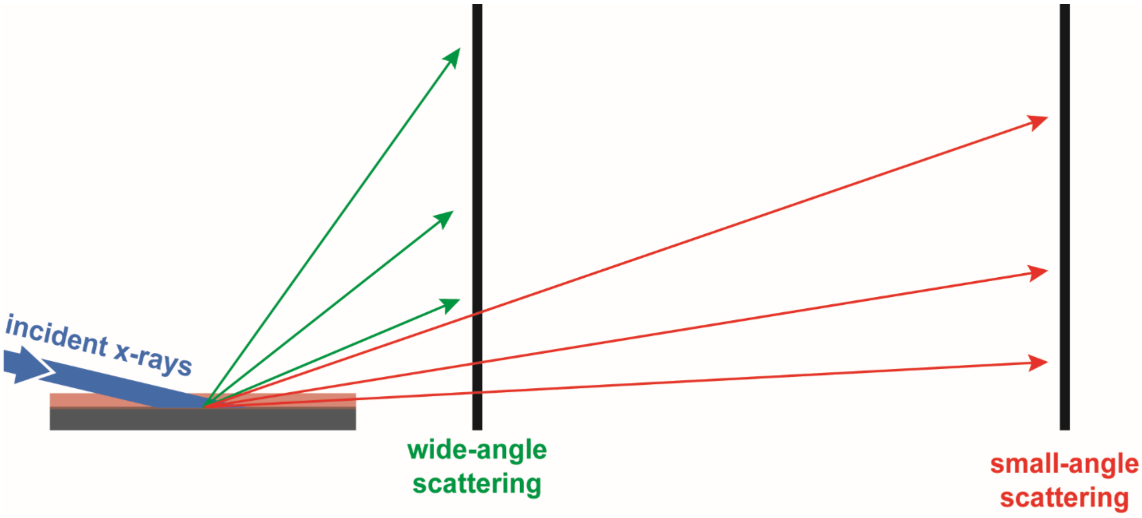

Figure 1.11. Simplified schematic of GIXS setup. Different detector–sample distances are used for different scattering angles which provide information on different length scales in the film.

resulting data is statistically representative of the majority of the film rather than being influenced by local inhomogeneities. Scattering patterns, which arise from constructive interference of repeating features in the film, are monitored by a 2D area detector downstream of the sample. Features from atomic or molecular distances of a few Å up to domains of hundreds of nm can be resolved, with scattering direction and intensity both providing valuable insight to the nature of the film. The scattering peaks themselves represent the intersection of the scattering vector with the Ewald sphere, resulting from momentum transfer of the X-rays upon interaction with the electrons in the molecules. The scattering data is in reciprocal-, or q-, space and can be considered the Fourier transform of the real-space lattice. Real-space distances d can be calculated by the equation $d = \frac{2\pi}{q}$ in order to determine film distances from the scattering data, though corrections are needed to map the spherical scattering vectors to the flat area detector.[140]

Importantly, this inverse relationship means that larger q values correspond to smaller repeating real-space distances and vice versa.

The length scales of observable features are determined by the angle of scattering from the sample, primarily divided into wide-angle (GIWAXS) and small-angle (GISAXS) geometries. These angles are dependent on the sample-detector distance, ranging from tens of centimeters in GIWAXS to multiple meters in GISAXS (Figure 1.11). The larger q values detectable in GIWAXS correspond to atomic or molecular distances of down to a few Å. In cLPs, this is often used to identify interchain distances with a specific emphasis on adjacent π systems due to the importance of through-space conjugation. The longer flightpath for scattered X-rays in GISAXS can resolve smaller scattering angles, corresponding to larger features such as block copolymer phase domains or other nanostructures. Because intermolecular distances are of greater importance to the performance of conjugated molecules and macromolecules, GIWAXS is often a preferential method for characterizing such materials and will be the focus herein.

The direction of the scattering peaks is directly related to the orientation of the repeating features within the film, generally defined as being out-of-plane (q_z axis) or in-plane (q_y axis) with respect to the substrate plane. Out-of-plane scattering therefore results from repeating features perpendicular to the substrate, whereas in-plane scattering indicates features parallel to the substrate plane. For conjugated molecules and macromolecules, correlating the π–π features with the substrate plane gives rise to the two most commonly described packing modes: edge-on and face-on packing. Edge-on packing refers to packing in which the “edges” of the π-system are aligned towards the substrate, and the π-faces are aligned perpendicular to the substrate. In face-on packing, on the other hand, the π-face repeating structures are parallel to the plane of the substrate. It is important to note that these are conventions used to describe the direction of a certain repeating feature and do not necessarily indicate substrate–molecule angles of exactly 90 or 0°. However, these packing geometries have been correlated with changes in device performance due to the direction of charge transport on a substrate.[135] Therefore, they are useful diagnostic tools to report packing geometries of cLPs. Though there are some recent examples of using GIWAXS to characterize thin film morphologies of cLPs,[77, 104, 141, 142] the use of this technique and the knowledge it provides will surely be a significant part of the field as it continues to grow.

CHAPTER II

DONOR–ACCEPTOR LADDER POLYMER VIA AROMATIZATION-DRIVEN THERMODYNAMIC ANNULATION*

2.1 Introduction

Conjugated ladder-type polymers are macromolecules in which the π-conjugated backbone units are connected and fused with multiple strands of covalent bonds (Figure 2.1a). These polymers possess unique properties as a result of their fused constitution, rigid conformation, and lack of torsional disorders.[1, 2, 143-145] Integration of a ladder-type constitution into functional conjugated macromolecules presents an intriguing strategy for enhancing their materials performance. The construction of multiple strands of bonds along the conjugated polymer main-chain in a precise manner, however, remains a major

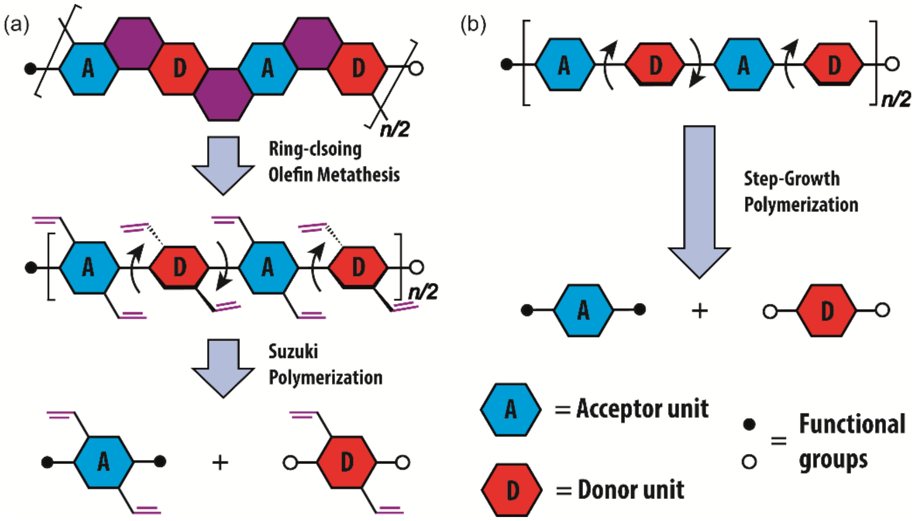

Figure 2.1. General retrosynthesis of (a) a D–A type ladder polymer and (b) a D–A type conjugated polymer. The curved arrows indicate free torsional motions.

---

*Adapted with permission from “Donor–acceptor conjugated ladder polymer *via* aromatization-driven thermodynamic annulation” by Jongbok Lee, Alexander J. Kalin, Chenxu Wang, Julia T. Early, Mohammed Al-Hashimi, and Lei Fang, *Polym. Chem.*, **2018**, *9*, 1603-1609. Copyright 2018 The Royal Society of Chemistry.

synthetic challenge despite significant advances in the past decade. Moreover, the incorporation of structural features that are critical to materials applications imposes additional constraints on the synthesis of functional ladder polymers. It is urgently desirable to overcome these difficulties in order to exploit the promising material properties of conjugated ladder polymers,[5, 15, 97, 98, 107, 108] such as their thermal and chemical stability,[5, 7, 45, 77] high conductivity,[9, 18, 104, 146, 147] and low energy bandgap.[98, 148]

Conjugated polymers with alternating electron-rich donor units and electron-deficient acceptor units (D–A polymers) predominate as active materials in high performance organic photovoltaic devices.[149, 150] Fusing the conjugated main-chain of D–A polymers into a ladder-type constitution can potentially break through the limits of exciton diffusion,[10] inter-chain electronic coupling, and bandgap engineering.[143] The syntheses of D–A ladder polymers, however, are rarely reported[17, 35, 141, 151] due to the combined challenges originating from the electron-deficient monomer in addition to the ladder-type backbone. The electron deficiency of the acceptor monomer makes it difficult to attach functional groups necessary for backbone annulation. Moreover, the electron-poor units often lead to decreased reaction efficiencies on the subsequent postpolymerization annulation, such as the widely used Friedel–Crafts intramolecular cyclization[2, 38, 41, 152] and Scholl oxidation,[35, 98] resulting in structural defects along the polymer chains.[153-155] Scherf and coworkers reported the synthesis of a D–A ladder polymer by Friedel–Crafts annulation,[151] in which the acceptor was prefused with electron-rich units before polymerization, so that the potentially inefficient cyclization was avoided.

Recently, we demonstrated that thermodynamically controlled ring-closing olefin metathesis (RCM) is a powerful tool to annulate conjugated polymers[7] and oligomers in high efficiency.[156] The reversible nature of RCM prevents undesired intermolecular cross-metathesis side products, while the formation of stable aromatic rings facilitates quantitative conversion in the ring annulation step.[7, 54, 156, 157] Furthermore, the mild and neutral reaction conditions allow for a wide substrate scope and excellent functional group tolerance.[158] Although RCM of electron-deficient olefins is still potentially challenging, the aromatization could provide the thermodynamic driving force (e.g., approximately −28 kcal mol^{-1} when converting 2,2′-divinyl-1,1′-biphenyl into phenanthrene[54]) to overcome this problem and lead to an efficient ring annulation. Herein, we report the efficient synthesis of a D–A ladder polymer through RCM annulation. Induced by coplanarity of the ladder polymer backbone, this polymer demonstrated intriguing optical properties.

2.2 Results and discussion

To obtain the desired D–A ladder polymer, a Suzuki coupling polymerization of vinyl-functionalized donor and acceptor monomers can be used to construct a conjugated D–A precursor (**DACP**), similar to the conventional synthesis of nonladder type D–A polymers (Figure 2.1b). Subsequently, it can undergo thermodynamically controlled RCM to afford the D–A ladder polymer (**DALP**) (Figure 2.1a). In this example, 2,1,3-benzothiadizole (BTD) was employed as the acceptor unit due to the following factors: (i) its low-lying molecular orbital energy levels render it sufficiently electron-deficient, (ii) its 4,7-positions are easily functionalized to serve as Suzuki coupling sites, and (iii) its 5,6-positions can be transformed into vinyl groups for RCM from pre-positioned methyl groups. A key factor in the design of the monomers is the requirement for at least one of the monomeric units to be centrosymmetric in order to afford a linear ladder backbone. Due to the non-centrosymmetric nature of BTD, an indolo[3,2-*b*]carbazole derivative with C_{2h} symmetry was selected to serve as the donor unit in order to maintain the desired linear constitution of the resulting rigid polymer.

The donor monomer **ICz-M** was derived from 3,9-dibromoindolo[3,2-*b*]carbazole (Scheme 2.1) as described in the literature.[159] First, α-branched 1-octylnonyl alkyl chains were installed on the *N*-positions to enhance the solubility of the desired D–A ladder polymer by breaking the potentially strong intermolecular π–π interactions.[7] In order to enable RCM of the polymer intermediate, the molecule was functionalized ortho to the bromide groups through Vilsmeier-Haack formylation to give the dialdehyde derivative **S2**. Installation of one strongly electron-withdrawing formyl group onto the indolocarbazole core did not inhibit the second formylation reaction. Vinyl groups for RCM were then installed through Wittig olefination. To provide functional groups for Suzuki coupling, the aryl bromides were lithiated and then converted to boronic esters through substitution with isopropoxypinacolborane to form **ICz-M**. This strategy, per previous optimizations, helps to avoid Heck-type coupling reactions that may occur in Pd-catalyzed borylation.[7]

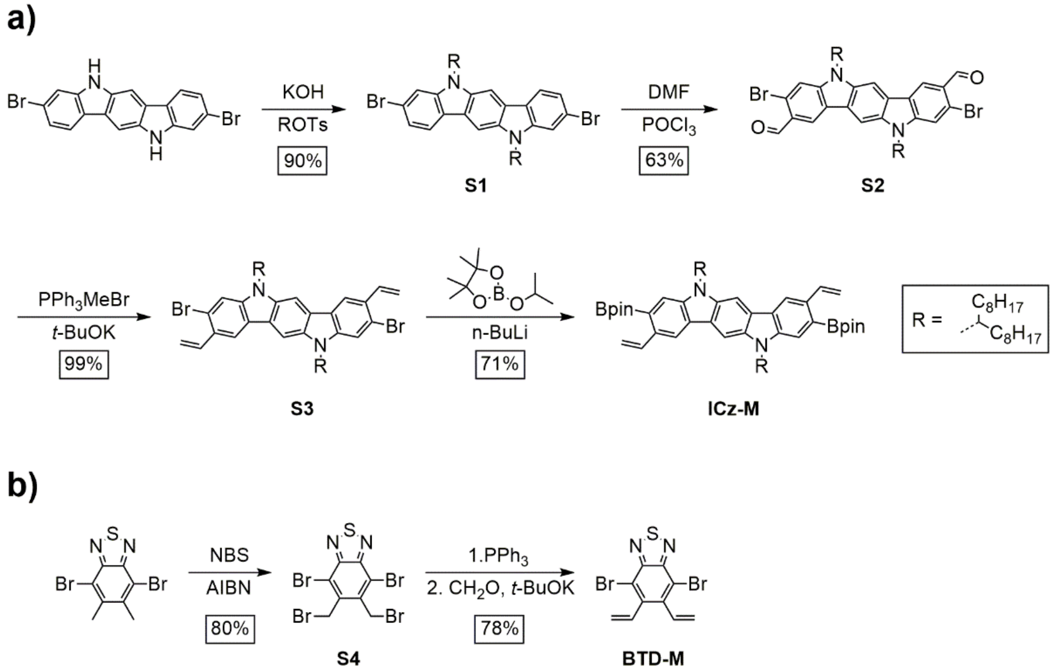

Scheme 2.1. Synthesis of **DALP** monomers from **S1** and **S4**, which were prepared according to references 159 and 160, respectively. (a) synthesis of donor monomer **ICz-M** from 3,9-dibromoindolo[3,2-*b*]carbazole. (b) synthesis of acceptor monomer **BTD-M** from 4,7-dibromo-5,6-dimethyl-2,1,3-benzothiadiazole.

The BTD-derived monomer **BTD-M** was derived from 5,6-dimethyl-2,1,3-benzothiazole (Scheme 2.1b), following reported procedures.[160] The BTD core possesses two aryl bromides for Suzuki coupling polymerization and two methyl groups for installation of the vinyl groups. Direct aromatic functionalization in the same manner as the donor was not possible on the electron-deficient ring, so the prepositioned methyl groups were used in the starting material to provide sites for radical benzylic reactions. The vinyl groups were installed in two steps, with an initial radical bromination using AIBN as a radical initiator to create the bis(bromomethyl) derivative **S4**. Then, **S4** was was converted into the final monomer through Wittig olefination, using PPh_3 and *t*-BuOK to create the phosphonium ylide on the benzothiadiazole unit and reacting with paraformaldehyde, which decomposes to formaldehyde upon heating.

With both monomers in hand, the conjugated D–A ladder polymer was synthesized in two steps (Scheme 2.2). Step-growth Suzuki polymerization between **ICz-M** and **BTD-M** afforded a vinyl-pendant non-ladder type D–A conjugated polymer, which was subsequently end-capped in situ by 2-bromostyrene and 2-vinyl(phenylboronic acid pinacol ester) to give the polymeric intermediate **DACP**. Purification by recycling preparative size exclusion chromatography (SEC) removed lower molecular weight oligomers, affording a batch with a $M_\mathrm{n}^\mathrm{SEC}$ of 43 kg mol^{-1} in a 70% yield. **DACP** was converted into the desired D–A ladder polymer **DALP** in 98% crude yield, with a 66% isolated yield after Soxhlet extraction of the polymer product. The decrease of the molecular weight as well as the isolated yield compared to previously reported RCM annulation steps[7, 156] was mainly due to the low solubility of the high molecular weight material (27%). This lowered solubility is often characteristic of such rigid polymers, necessitating the use of the branched sidechains to interrupt intermolecular packing.

^{1}H NMR spectra showed the conversion of **DACP** into **DALP**, with the peaks associated with the vinyl groups disappearing after RCM, while other peaks shifted further down-field (Figure A6), including peaks downfield shifted beyond 11.0 ppm due to the sterically crowded environments adjacent to the thiadiazoles after ring annulation.[161] Hindered rotation of the two sets of α-branched alkyl chains creates atropisomerism in the monomers and polymers, resulting in distinct peaks of these alkyl chains in ^{1}H and ^{13}C NMR.

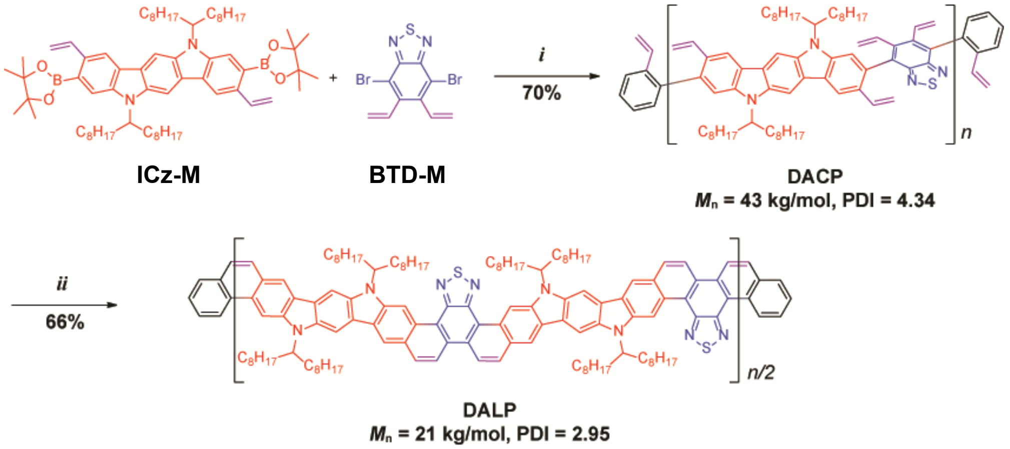

Scheme 2.2. Synthesis of D–A ladder polymer **DACP** and **DALP**. (i) $Pd(PPh_3)_4$, K_2CO_3, aliquat 336, BHT, toluene, H_2O, 100 °C, 24 h; then 2-bromostyrene and 2-vinylphenylboronic acid. (ii) Grubbs' 2nd generation catalyst, toluene, reflux, 6 h.

Optical properties of **DACP** and **DALP** were examined by UV-vis absorption and fluorescence emission spectra in toluene solution (Figure 2.2a). As expected, the absorption edge of **DALP** displayed an approximately 100 nm red-shift compared to that of **DACP**, as well as previously reported ladder polymer **LP** that lacks the D–A architecture.[7] This observation demonstrated that the combined effect of extended π-conjugation in the ladder-type backbone and the alternating donor–acceptor constitution was responsible for the lower bandgap of **DALP**. Furthermore, distinctive vibrational progressions were observed as a result of the highly rigid nature of **DALP**, in contrast to the broad and featureless spectrum of **DACP**. The fluorescence emission spectrum of **DALP** also showed a more structured vibrational progressions and a narrower spectral width than the broad and featureless emission spectrum of **DACP**.[162] Despite its much lower absorption energy, **DALP** emitted at a similar energy (λ_{max} = 569 nm) compared to **DACP** (λ_{max} = 573 nm), resulting in a much smaller Stokes shift (22 nm) than that of

DACP (138 nm). This observation can be attributed to the small energy loss of the rigid ladder-type backbone during excitation and emission. The 22 nm Stokes shift, however, was still much larger[151] than typical ladder-type molecules,[2, 143] suggesting the presence of intramolecular charge transfer (ICT).[163] In order to confirm the ICT process, absorption and emission of **DALP** were recorded in various solvents with different dielectric constants (Figure 2.2b). The absorption spectra in these different solvents displayed no significant change, while the emission spectra maxima red-shifted as the solvent polarity increased from toluene to dichloromethane. Furthermore, the well-structured vibrational progressions of emission observed in toluene became broader in more polar solvents. This broadening and red-shift was caused by dipole moment stabilization of the excited state in polar solvents, corroborating the ICT process.

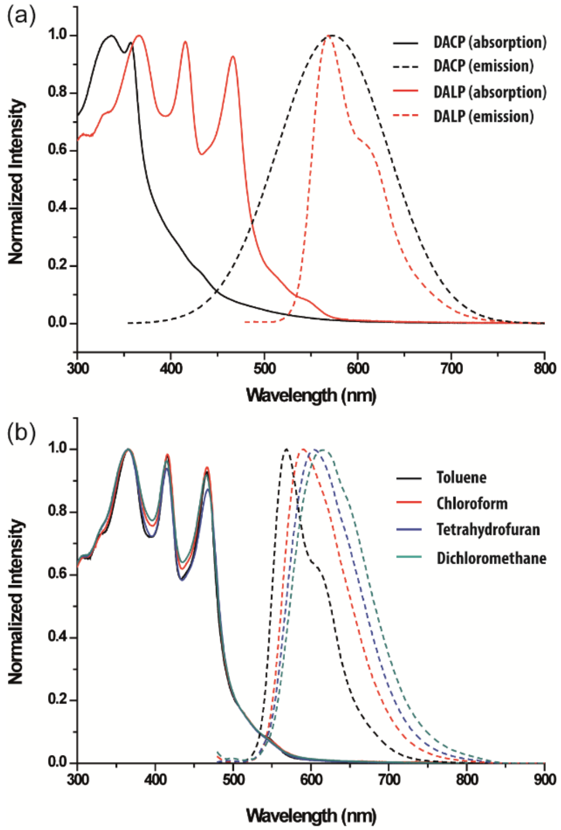

Figure 2.2. (a) UV-vis absorption and fluorescence emission spectra of **DACP** and **DALP** in toluene. (b) UV-vis absorption and fluorescence emission spectra of **DALP** in different solvents.

Solution processability and the resulting solid-state packing are important for practical applications of donor–acceptor polymers. The good solubility of **DALP** allowed for the preparation of uniform thin films on SiO_2 (300 nm)/Si substrates by spin-casting (5 mg mL^{-1} in chloroform). The thin film morphology of **DALP** was then studied using grazing-incidence X-ray wide-angle scattering (GIWAXS) under vacuum to avoid any scattering effects from the air. The amorphous morphology of **DALP** was observed in the as-cast film (Figure A5), which did not change after thermal annealing at 250 °C (Figure 2.3a). The weak ring around $q \approx 1.5$ $Å^{-1}$ was attributed to either scattering from SiO_2 on the substrate surface or from weak amorphous π–π interactions, and the diffuse reflectance peak above the origin is not indicative of any repeating features. However, after thermal annealing the thin film at 500 °C for 30 min, which cleaved the alkyl side-chains, a clear diffraction peak at $q_z \approx 1.68$ Å^{-1} in the out-of-plane direction was observed (Figure 2.3b).[164] 500 °C was chosen as the annealing temperature due to TGA data (Figure 2.3c) which indicated that the alkyl chains were thermally removed between 300–400 °C, and was performed under N_2 to avoid any potential oxidative effects from the air. The newly appeared GIWAXS peak suggested that the rigid and coplanar polymer backbone preferentially reorganized into a face-on orientation with a π–π distance of 3.7 Å after alkyl chain cleavage. Because π-system orientation can have significant impacts on electronic device performance, these data suggested that the reorganization to face-on orientation of **DALP** after thermally induced cleavage of sp^3 carbons may be give the resulting thin film interesting properties for future applications. However, as will be discussed in more detail in Chapter 5, the large size of the ladder polymer leads to only a weakly ordered film, and greater control over thin film morphology may be more easily realized with shorter oligomers or small molecules.

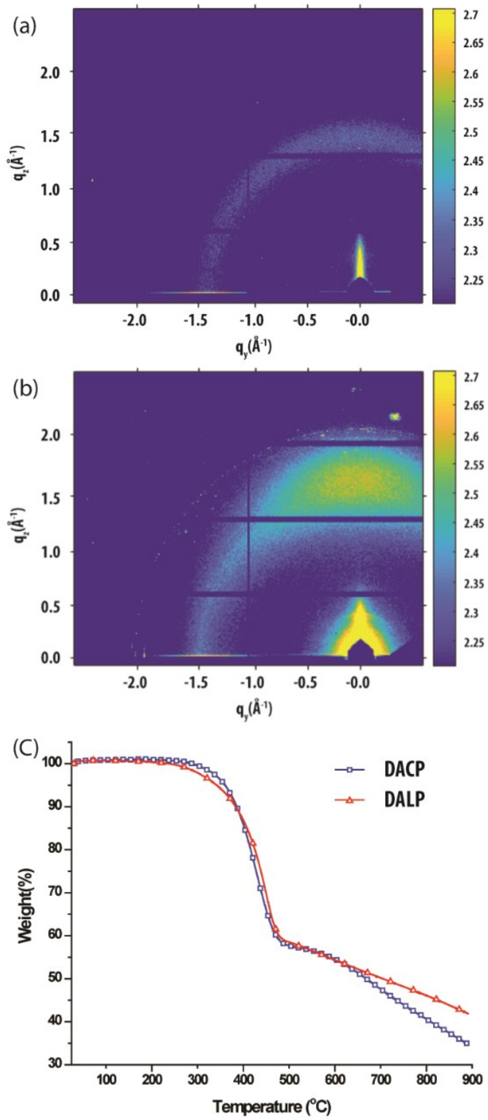

Figure 2.3. (a) GIWAXS image of **DALP** thin film on Si wafer after annealing at 250 °C. (b) GIWAXS image of **DALP** thin film after annealing at 500 °C to cleave alkyl chains. (c) TGA traces of **DALP** and **DACP**.

2.3 Experimental Section

2.3.1 General Information

Starting materials and reagents were purchased from Aldrich, Alfa Aesar, TCI, and Acros, and were used as received without further purification unless specified. Toluene and DMF were dried using Inert Technology pure solvent system (PureSolv-MD-5a) and used without further treatment. Anhydrous THF was distilled with Na/benzophenone before uses. 3,9-dibromo-5,11-dihydro-5,11-di(1-octylnonyl)indolo[3,2-*b*]carbazole (**S1**)[159] and 4,7-dibromo-5,6-bis(bromomethyl)-2,1,3-benzothiadiazole (**S4**)[160] were synthesized according to reported procedures. Analytical thin-layer chromatography (TLC) tests were performed on glass that was precoated with silica gel 60-F_{254} (Sorbtech). Flash column chromatography was carried out using a Biotage® Isolera™ Prime with various sizes of SiO_2 Biotage ZIP® cartridges. UV-visible absorption spectra and fluorescence emission spectra were recorded using a Shimadzu UV-2600 and a Horiba Fluoromax-4 spectrometer, respectively. UV-visible-Near IR spectra were measured on a Hitachi U-4100 spectrometer. ^1H and ^{13}C NMR spectra were obtained on a 500 MHz Varian Inova at room temperature unless specified. Chemical shifts are reported in ppm relative to the signals corresponding to the residual non-deuterated solvents ($CDCl_3$: δ 7.26 for ^1H and 77.16 for ^{13}C at room temperature. Size exclusion chromatography (SEC) was performed on Tosoh EcoSEC (HLC-8320GPC) in THF solution at 40 °C with a flow rate of 0.4 mL/min through TSKgel SuperHM-M and TSKgel SuperH-RC columns. The molecular weights were calculated using a calibration curve based on polystyrene standards. Preparative SEC was performed in chloroform solution at room temperature using a JAI recycling preparative HPLC (LC-92XXII NEXT SERIES). High-resolution Thermal gravimetric analysis (TGA) was recorded under nitrogen atmosphere with heating rate of 10 °C min^{-1} from 25 to 900 °C using TA Q500. For high-resolution mass spectrometry (HRMS), matrix-assisted laser desorption/ionization (MALDI) mass spectra and atmospheric pressure chemical ionization (APCI) mass spectra were measured on Applied Biosystems 4800 MALDI-TOF and a Thermo Scientific LCQ-DECA, respectively.

2.3.2 GIWAXS Preparation and Measurements

GIWAXS measurements were carried out in Sector 8-ID-E at the Advanced Photon Source, Argonne National Laboratory.[165] Beamline 8-ID-E operates at an energy of 10.91 keV and the images were collected from a Pilatus 1MF camera (Dectris), with two exposures for different vertical positions of the detector. Using the GIXSGUI[166] software package for MATLAB (Mathworks), data are corrected for X-ray polarization, detector sensitivity and geometrical solid-angle. The beam size is 0.8 mm × 0.5 mm and the resolution ($\Delta E/E$) is 1×10^{-4}. Sample detector distance is 278 mm. Solid-state samples for GIWAXS were deposited on silicon wafers by spin-casting with the solutions (5 mg/mL in $CHCl_3$) at a spin rate of 1500 rpm and annealed at 250 °C and 500 °C for 30 min. More in-depth explanation of GIWAXS procedures can be found in section 5.5.

2.4 Conclusions

In summary, the efficient synthesis of donor–acceptor ladder polymer **DALP** was achieved by ring-closing olefin metathesis. Donor and acceptor monomers based on indolocarbazole and benzothiadiazole, respectively, were synthesized with Suzuki coupling sites and vinyl groups for RCM. The potential issue of low efficiency in the annulation step caused by electron-deficient acceptor units was addressed by the strong thermodynamic driving force of aromatization, yielding the desired ladder polymer without detectable structural defects. Spectroscopic investigation revealed that **DALP** exhibits a lower energy band gap compared to non-ladder and non D–A analogues. A dipole moment stabilization effect of the excited state in polar solvents confirmed the presence of intramolecular charge transfer. The solid-state packing structure of **DALP** was investigated by GIWAXS, demonstrating its amorphous morphology. However, after the thermally induced alkyl chain cleavage, the residual ladder polymer backbone preferentially reorganized into a face-on orientation with a π–π distance of 3.7 Å. These results provide fundamental understanding of D–A ladder polymers for potential future applications in solid-state electronic and optoelectronic devices.

CHAPTER III

TRUXENE-DERIVED MONOMERS FOR A POROUS LADDER POLYMER NETWORK WITH ENTROPICALLY FAVORABLE GAS ADSORPTION[*]

3.1 Introduction

Porous polymer networks (PPNs) possess multiple beneficial properties for a wide range of next-generation materials, including fields ranging from biomedical applications to energy and beyond.[118, 121, 167] Their high surface areas allow for storage, separation, and delivery of smaller adsorbed molecules, which could play key roles in the ongoing search for innovative and practical energy-related materials. For one example, adsorbed natural gas (ANG) in highly porous materials has emerged as an efficient and safe technology for energy storage. In order to make such adsorption strategies competitive against commercial fuels, high methane storage capacity at room temperature is urgently desired.[168-172] To achieve this, tremendous progress has been made in increasing the surface area of various methane-adsorbing materials.[173, 174] However, an ultrahigh surface area often results in a low material density and lowers the volumetric capacity, which is critical for volume-sensitive applications, such as powering personal vehicles.[175] Therefore, enhancing the overall methane storage capacity by increasing the uptake per unit surface area becomes an important strategy for practical applications. A significant amount of research has focused on increasing the enthalpy gain of the methane adsorption

---

[*] Adapted with permission from "Rigid Ladder-Type Porous Polymer Networks for Entropically Favorable Gas Adsorption" by Sai Che, Jiandong Pang, Alexander J. Kalin, Chenxu Wang, Xiaozhou Ji, Jongbok Lee, Dylan Cole, Jia-Luo Li, Xinman Tu, Qiang Zhang, Hong-Cai Zhou, and Lei Fang, *ACS Materials Lett.* **2020**, *2*, 49-54. Copyright 2020 The American Chemical Society.

process by strengthening the interactions between the adsorbent and methane molecules.[176] However, enthalpic interactions could also potentially lead to incomplete desorption of methane in low-pressure region, impacting the deliverable capacity.[177] An alternative approach to enhance methane uptake per unit surface area is decreasing the entropy penalty of the adsorption process, which is often significant at room temperature. However, such an entropic approach has rarely been employed so far.[178] Therefore, we envisioned that lowering the initial entropy of porous materials could be an efficient strategy to reduce the overall adsorption entropy penalty, not only for adsorbed fuels but for adsorption in porous materials more broadly.

We anticipated that this goal could be achieved by locking the conformation of the organic backbone via the installation of an additional strand of bonds to afford a ladder-type structure.[179] Various synthetic approaches to linear ladder polymers, including a number of scalable and inexpensive ones, have been established in the past three decades.[143, 144] A few examples of porous materials with such ladder-type backbones have been reported.[124, 126-129, 180] Preliminary results indeed showed that extended ladder-type ligands in metal-organic frameworks contributed to higher methane storage performance, although these effects were attributed to enthalpic effects.[181, 182] So far, fully organic porous ladder polymer networks have only been synthesized through a single-step creation of the ladder-type backbone. As discussed in Chapter 1, this strategy typically has a limited synthetic scope, though the use of dynamic covalent chemistry is an efficient strategy to create porous crystalline materials, such as ladder-type COFs. We therefore sought to explore the applicability of the two-step polymerization–annulation strategy in such an organic porous network. Herein, we report a route towards this concept through the design and synthesis of a monomer to create a porous ladder polymer network (**PLAN**) through a PPN intermediate (**PPN-Precursor)**.

3.2 Synthetic Design

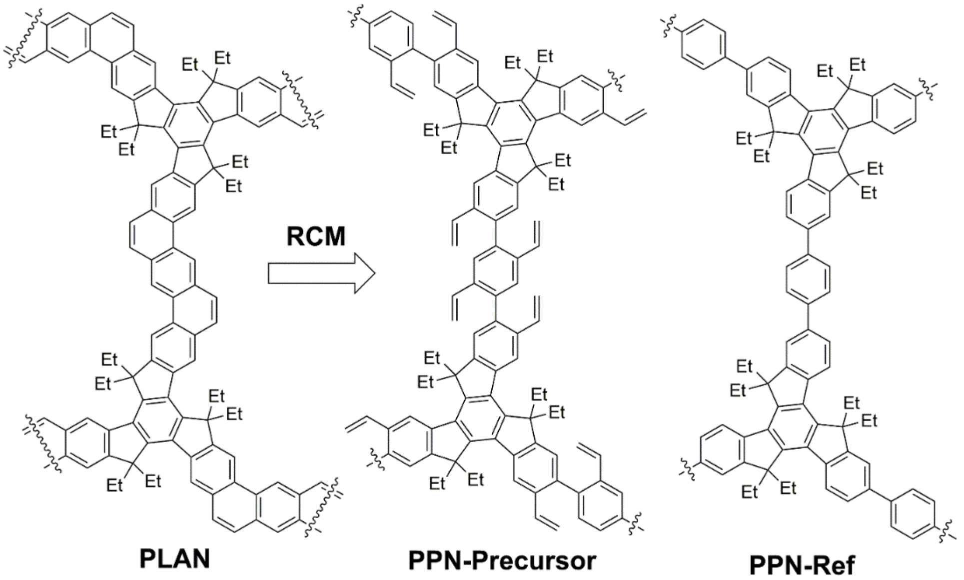

Figure 3.1 Structural formulas of the repeating units of cross-linked porous polymer networks **PLAN**, **PPN-Precursor**, and **PPN-Ref**.

The **PLAN** model was designed to be constructed from rigid monomers through the kinetic formation of covalent bonds, in the same manner as other PPNs (Figure 3.1).[122, 174, 183] In general, PPNs can be imparted with high porosity and superior thermal and chemical stability,[184-188] suitable as a model system for methane storage or other porous material applications. In order to create the crosslinked ladder-type network, we applied reported ladder polymer chemistries to trifunctional and bifunctional comonomers derived from truxene (formally 10,15-dihydro-5*H*-diindeno[1,2-*a*:1',2'-*c*]fluorene) and benzene, respectively (Scheme 3.1). Two sets of monomers were designed: one for the ladder-type

PLAN and another set for a reference material **PPN-Ref** which resembles the constitutional structure of **PLAN** but with a non-ladder type backbone. The fully fused, coplanar, and conjugated trifunctional truxene monomer importantly allows for functionalization with short alkyl chains as well as with aromatic functional groups for polymerization.[189] Pd-catalyzed Suzuki coupling was chosen for the polymerization using conditions previously optimized by our group.[7, 190] For the polymerization, bromide groups were installed on the truxene monomer and boronic esters on the phenylene comonomer.

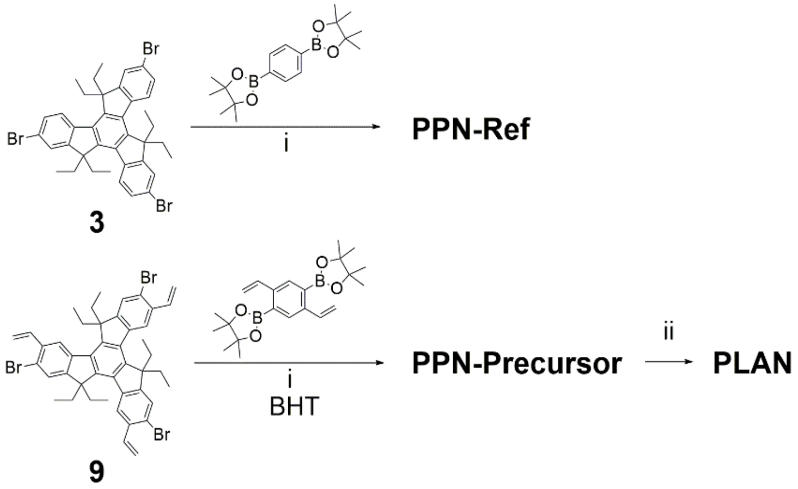

Scheme 3.1. (a) Synthesis of **PPN-Precursor**, **PPN-Ref**, and **PLAN** from truxene-derived monomers. Conditions: (i) $Pd(PPh_3)_4$, K_2CO_3 (ii) Grubbs' 2nd Generation catalyst.

The annulation reaction must be high-yielding and selective towards intrachain annulation rather than intermolecular crosslinking in order to successfully create the ladder-type backbone. Ring-closing olefin metathesis (RCM) was selected to form the ladder-type **PLAN** backbone because it typically gives a highly efficient conversion with few defects under thermodynamic control.[7, 54, 179] Additionally, it has been shown that this reaction can take place heterogeneously in porous solids, which is necessary for the annulation of **PPN-Precursor** to form **PLAN**.[123] To accomplish this, the **PLAN** monomers were functionalized with vinyl groups for the reaction. The monomers for **PPN-Ref** did not require vinyl group functionalization. The synthesis of the monomers, including considerations of the vinyl group installation, is discussed below.

3.3 Synthesis and Discussion

The synthesis of the non-vinyl-functionalized monomer (Scheme 3.2) was accomplished starting from commercially available 3-phenylpropionic acid. Truxene, **1**, was obtained through a single-step, acid-catalyzed reaction which proceeds first through an intramolecular cyclization to form 1-indanone, then undergoes an aldol triple condensation, forming the central aromatic ring. This reaction typically uses polyphosphoric acid (PPA) as solvent and acid catalyst, but the viscosity of PPA (6500 cSt at 25 °C) makes handling inconvenient. We and others have reported similar acid-catalyzed aldol trimerizations of aromatic monomers using the much less viscous methanesulfonic acid (MSA, 7.8 cSt at 25 °C),[126, 191, 192] and so we applied the same strategy to the synthesis of **1**. This made the reaction much easier to perform without any sacrifice of scale or conversion: the MSA-catalyzed trimerization proceeded in high yields (>90%) and the potential isomeric product, isotruxene, was never observed. The low solubility of **1** prevented full solution-phase characterization, but ^{1}H NMR and mass spectrometry matched well with the expected results.

The acidic protons on the methylene bridges of **1** were subsequently deprotonated and nucleophilic substitution of bromoethane gave hexaethyl-substituted **2**, in order to provide sufficient solubility for further functionalization and polymerization without being overly bulky. Though most ladder-type molecules or macromolecules are made soluble with large alkyl chains, those chains may lower the surface area of the final porous network by occupying pore space. Finally, electrophilic bromination installed the aryl bromide groups needed for Suzuki coupling polymerization of the monomer **3**.

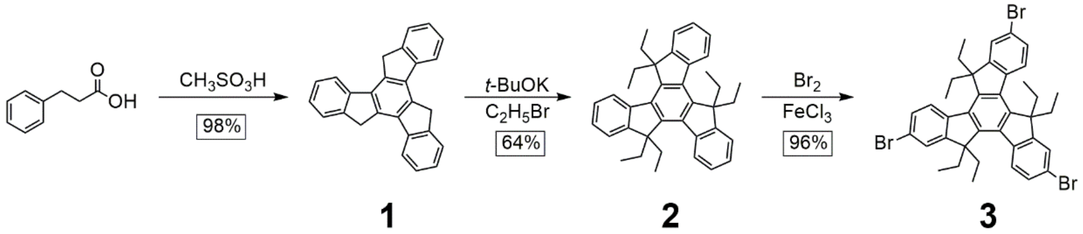

Scheme 3.2. Synthesis of non-vinyl-functionalized monomer **3**.

Previous RCM-based ladder polymers utilized aromatic substitution of carbonyl reagents or radical benzylic bromination as strategies for installing the vinyl groups on the monomers.[7, 190] However, neither strategy was possible on **3** due to the low reactivity of the free ring sites towards aromatic substitution and the lack of any free benzylic positions, so alternate strategies were explored to synthesize the RCM-capable monomer with vinyl groups (Schemes 3.3-4). Commercially available 3-(4-methylphenyl)propionic acid was used as the starting material, giving trimethyltruxene **4** after MSA triple condensation. The methyl groups created benzylic positions on the truxene core, enabling functionalization through radical reactions. Due to the *p*-substitution of the starting material, there is no concern for regioisomer formation in **4** based on the cyclization mechanism.[193] The ethyl chains and aryl bromides were installed in the same manner as previously described to give **5** and **6**, respectively. No difference in reactivity was observed with the methyl substituent.

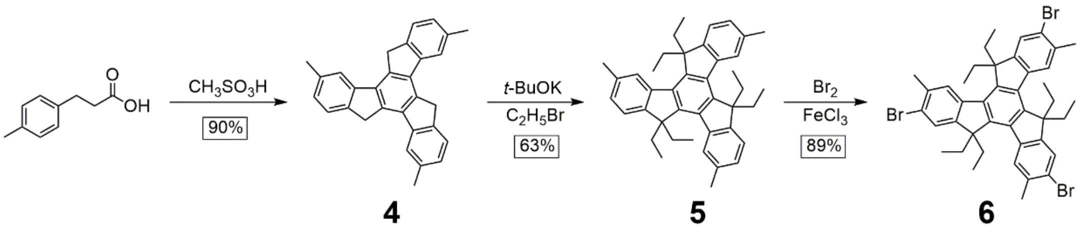

Scheme 3.3. Synthesis of truxene precursor **6**.

To obtain the vinyl groups from **6**, multiple strategies were pursued (Scheme 3.4a). A reported direct oxidation of arylmethanes to benzaldehydes using 2-iodoxybenzoic acid (IBX)[194] was first attempted, but direct oxidation to **8** gave no reaction in multiple attempts. According to discussions regarding reproducibility of this reaction,[195] the active species may be the hydrated form of IBX, and even when accounting for this by adding additional water into the reaction mixture, no reaction was observed. We additionally attempted radical benzylic bromination in the same manner as described previously[54, 156] to monobrominate each methyl group as a precursor to the vinyl groups by using 1 equivalent of NBS for each reaction site. This bromination was not selective to the number of bromines attached at each benzylic position, so the desired product was not able to be isolated from the reaction mixture, which also contained over- and underbrominated species. Instead the benzylic bromination was performed using a large excess of NBS to obtain the fully brominated product **7**. This reaction is known not to proceed to the tribromomethyl product when there is a substituent ortho to the methyl group,[196] thus **7** was the major product of the reaction but some underbrominated products were observed on TLC. The dibromomethyl groups cannot be directly converted into the vinyl groups and so an additional synthetic step is required, but this serves as a suitable alternative to the other strategies.

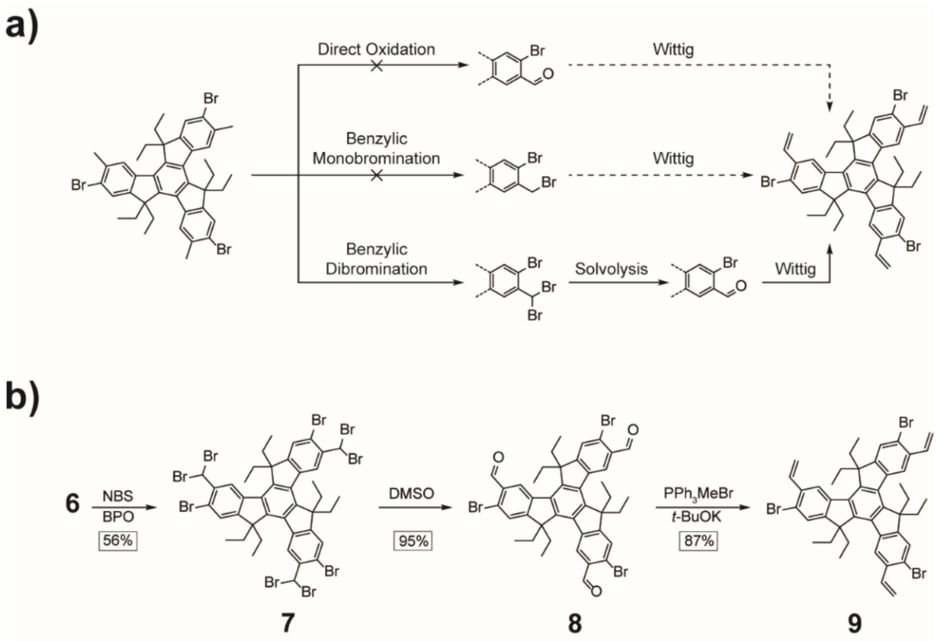

Scheme 3.4. (a) Synthetic strategies explored for vinyl group installation. (b) synthesis of vinyl-functionalized monomer **9**.

7 was then converted to the trialdehyde **8** through oxide transfer from DMSO.[197] This reaction can also be completed by hydrolysis using an aqueous $AgNO_3$ solution, but the simplicity and high yield of the DMSO reaction made exploring other conditions unnecessary. Lastly, **8** was converted through Wittig olefination using a methylphosphonium salt as the carbon source, giving the trivinyl-functionalied final product **9**. Preventing radical polymerization of the vinyl groups was an important key to the success of this reaction. This was primarily accomplished by cooling the reaction to 0 °C to control the temperature of the reaction, though performing the reaction in the dark and adding BHT as a radical scavenger are two additional methods to prevent this. After synthesis of the vinyl-functionalized monomers, a small amount of BHT was added to most monomer solutions when purity was not necessary to prevent radical formation.

The molecules were confirmed by ^{1}H and ^{13}C NMR as well as high-resolution mass spectrometry (Section 3.4 and Appendix C). The addition of the bromines into the monomer precursors could clearly be seen through mass spectrometry (Figure 3.2). The tribromo molecules showed four peaks spaced 2, 4, and 6 m/z units from the [M] or [M+H] peaks, representing the four Br isotope possibilities (3:0, 2:1, 1:2, or 0:3 ratio of ^{79}Br:^{81}Br). This pattern was absent in **5** before aryl bromination. In **7**, which possesses nine Br atoms, the masses corresponding to the extreme ends (greater than 7 of either Br isotope) of the Br ratios were not observed, but a similar 2 unit spacing pattern was still observed, with peaks corresponding to a 4:5 and 5:4 ratio of ^{79}Br:^{81}Br having the highest intensity, matching calculated values.

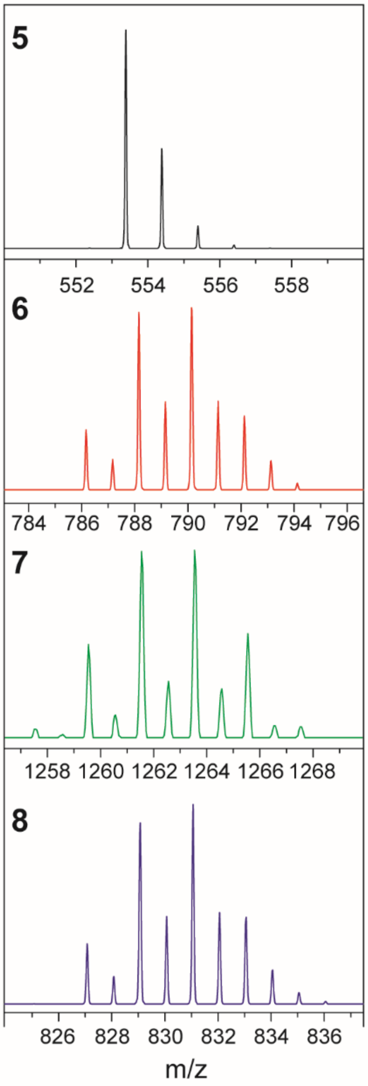

Figure 3.2. Mass spectrometry isotope patterns of the molecular ions of **5**–**8** possessing 0, 3, 9, and 3 Br atoms, respectively.

Using the synthesized monomers, the crosslinked polymer networks **PPN-Precursor** and **PPN-Ref** were obtained through Suzuki coupling polymerization.[198] RCM of **PPN-Precursor** was then performed using Grubbs 2nd Generation catalyst to obtain **PLAN**. The polymers were characterized by solid-state cross-polarization magic angle spinning (CP-MAS) ^{13}C NMR spectroscopy, confirming the full conversion of the RCM reaction. Methane sorption experiments were performed with **PLAN** and **PPN-Ref** to identify the effects of the ladder-type backbone. The conformationally locked backbone imbued **PLAN** with improved thermal and chemical stability over **PPN-Ref** as well as a significant increase in methane adsorption per unit surface area over other reported materials. This improvement was shown to result from the lowered initial entropy of the **PLAN** caused by the ladder-type backbones (Figure 3.3), illustrating the beneficial properties of the rigid backbone in gas adsorption applications.

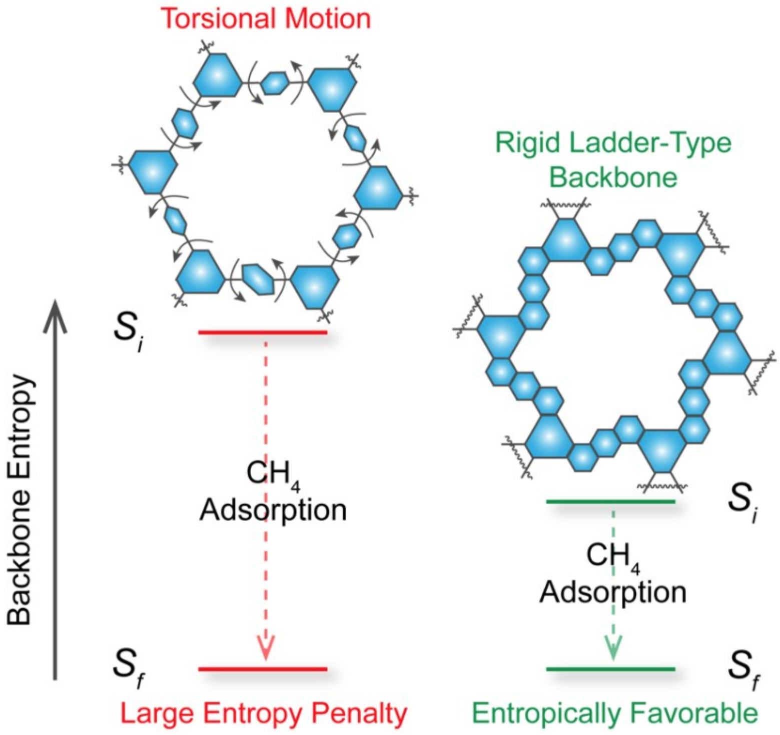

Figure 3.3. Schematic demonstrating the benefits of a ladder-type backbone for gas adsorption by lowering the initial entropy of the system.

3.4 Experimental Section

3.4.1 General Information

Starting materials, reagents, and solvents were purchased from Aldrich, Alfa Aesar, TCI, and Acros, and were used as received without further purification unless otherwise specified. Anhydrous THF was distilled with Na/benzophenone before use. Phenylene monomers 2,2'-(2,5-divinyl-1,4-phenylene)bis(4,4,5,5-tetramethyl-1,3,2-dioxaborolane) and 1,4-bis(4,4,5,5-tetramethyl-1,3,2-dioxaborolan-2-yl)benzene were synthesized and characterized according to reported procedures in literature.[156] Analytical thin-layer chromatography (TLC) tests were performed on glass that was precoated with silica gel 60-F254 (Sorbtech). Flash column chromatography was carried out using a Biotage® Isolera™ Prime. Solution phase ^{1}H and ^{13}C NMR spectra were obtained on Varian Inova 500 MHz and Bruker Ascend 400 MHz spectrometers at room temperature. Chemical shifts are reported in ppm relative to the signals corresponding to the residual non-deuterated solvents (for ^{1}H NMR: $CDCl_3$ $\delta = 7.26$ ppm; for ^{13}C NMR: $CDCl_3$ $\delta = 77.16$ ppm). For high-resolution mass spectrometry (HRMS), atmospheric pressure chemical ionization (APCI) was performed using a Thermo Fisher Scientific Q Exactive Focus. Melting points were taken on an OptiMelt automatic melting point system at a rate of 1 °C/min.

3.4.2 Synthesis

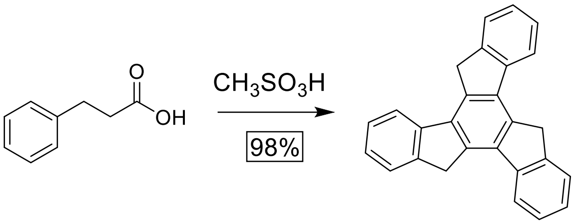

1

Truxene (1): A mixture of 3-phenylpropionic acid (10.1 g, 67.1 mmol) and methanesulfonic acid (50 mL) was heated at 60 °C for 60 min under N_2. Deionized water (1 mL) was then added to the reaction and temperature was raised to 160 °C for 12 h. After the reaction was cooled to room temperature, the mixture was poured into ice water. The precipitate was collected by filtration and washed with water and methanol to yield **1** as a black solid (7.48 g, 21.9 mmol, 98%) and used for next step without further purifications. ^{1}H NMR (400 MHz, $CDCl_3$, RT): δ 7.88 (d, *J* = 7.5 Hz, 3H), 7.65 (d, *J* = 7.3 Hz, 3H), 7.48 (t, *J* = 7.1 Hz, 3H), 7.38 (td, *J* = 7.4, 1.0 Hz, 3H), 4.14 (s, 6H). HRMS (APCI): calcd for $C_{27}H_{18}$ $[M+H]^+$ *m/z*=343.1481; found *m/z*=343.1473.

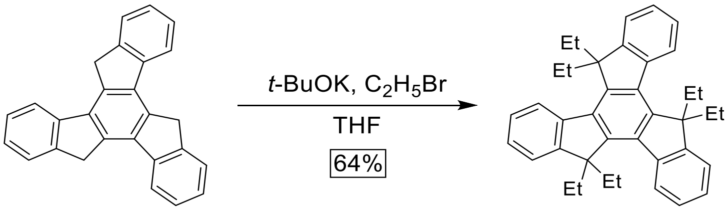

1 **2**

5,5,10,10,15,15-hexaethyltruxene (2): A mixture of **1** (0.885 g, 2.59 mmol) and *t*-BuOK (10.8 g, 96.3 mmol) in dry THF (50 mL) was refluxed for 10 min under N_2 and then cooled to 0 °C. Subsequently, bromoethane (7.0 mL, 94 mmol) was added dropwise using a syringe at 0 °C. The mixture was warmed to room temperature and stirred for 24 h. The reaction mixture was then poured into water and extracted with CH_2Cl_2. The combined organic layer was dried over $MgSO_4$, filtered, and concentrated under reduced pressure. The crude product was purified by column chromatography (SiO_2, 100% hexanes) to yield **2** as a white solid (0.845 g, 1.65 mmol, 64%) with a melting point of 215-219 °C (open capillary). ^{1}H NMR (400 MHz, $CDCl_3$, RT): δ 8.36 (m, 3H), 7.47 (m, 3H), 7.39 (m, 6H), 3.03 (dq, *J* = 14.4, 7.3 Hz, 6H), 2.16 (dq, *J* = 14.6, 7.3 Hz, 6H), 0.21 (t, *J* = 7.3 Hz, 18H). $^{13}C\{^1H\}$ NMR (100 MHz, $CDCl_3$, RT): δ 152.88, 143.91, 140.69, 138.89, 126.50, 126.11, 124.61, 122.31, 56.77, 29.44, 8.56. HRMS (APCI): calcd for $C_{39}H_{42}$ $[M+H]^+$ *m/z*=511.3359; found *m/z*=511.3368.

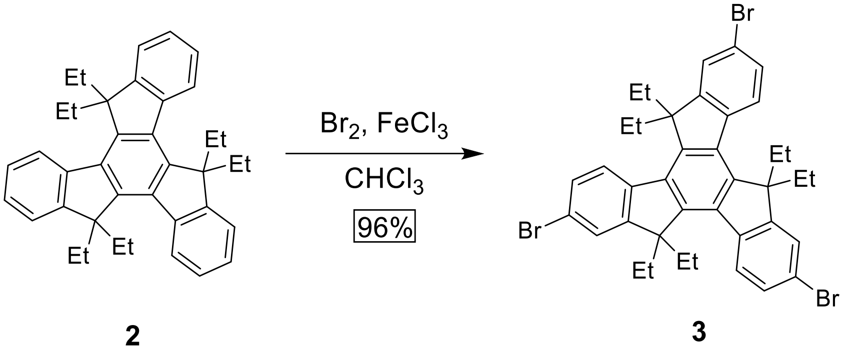

2,7,12-tribromo-5,5,10,10,15,15-hexaethyltruxene (3): A mixture of **2** (0.261 g, 0.511 mmol) and $FeCl_3$ (catalytic amount) in chloroform (10 mL) was cooled to 0 °C under N_2. Br_2 (0.13 mL, 2.5 mmol) was added dropwise. The mixture was warmed to room temperature and stirred for 12 h. The reaction mixture was then poured into a saturated aqueous $NaHSO_3$ solution and extracted with CH_2Cl_2. The combined organic layer was dried over $MgSO_4$, filtered, and concentrated under reduced pressure. The crude product was purified by column chromatography (SiO_2, 100% hexanes) to yield **3** as a white solid (0.367 g, 0.491 mmol, 96%) that decomposes slowly without melting around ~240 °C (open capillary). ^{1}H NMR (400 MHz, $CDCl_3$, RT): δ 8.16 (d, *J* = 8.6 Hz, 3H), 7.57 (d, *J* = 2.0 Hz, 3H), 7.52 (dd, *J* = 8.5, 2.0 Hz, 3H), 2.91 (dq, *J* = 14.4, 7.2 Hz, 6H), 2.10 (dq, *J* = 14.6, 7.4 Hz, 6H), 0.21 (t, *J* = 7.3 Hz, 18H). $^{13}C\{^1H\}$ NMR (100 MHz, $CDCl_3$, RT): δ 155.10, 143.98, 139.17, 138.17, 129.53, 125.90, 125.65, 121.19, 57.13, 29.36, 8.50. HRMS (APCI): calcd for $C_{39}H_{39}Br_3$ $[M]^{+\cdot}$ *m/z*=746.0576; found *m/z*=746.0582.

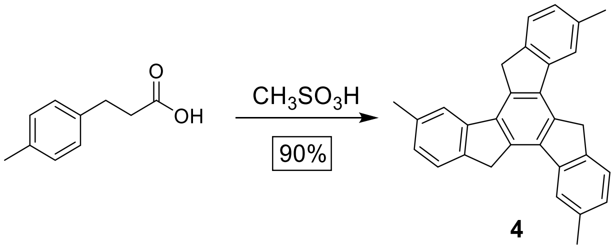

3,8,13-trimethyltruxene (4): A mixture of 3-(4-methylphenyl)propionic acid (4.59 g, 28.0 mmol) and methanesulfonic acid (25 mL) was heated at 60 °C for 60 min under N_2. Water (1 mL) was then added to the reaction and temperature was raised to 160 °C for 12 h. After the reaction was cooled to room temperature, the mixture was poured into ice water. The precipitate was collected by filtration and washed with water and methanol to yield **4** as brown solid (3.22 g, 8.37 mmol, 90%) and used for next step without further purifications. ^{1}H NMR (400 MHz, $CDCl_3$, RT): δ 7.74 (s, 3H), 7.58 (d, *J* = 7.7 Hz, 3H), 7.21 (d, *J* = 7.6 Hz, 3H), 4.22 (s, 6H), 2.55 (s, 9H). HRMS (APCI): calcd for $C_{30}H_{24}$ $[M+H]^+$ *m/z*=385.1951; found *m/z*=385.1942.

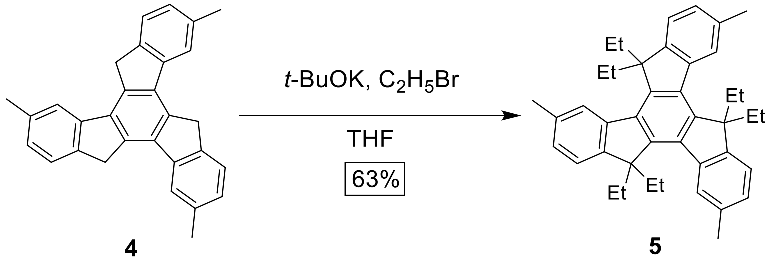

5,5,10,10,15,15-hexaethyl-3,8,13-trimethyltruxene (5): A mixture of **4** (0.72 g, 1.9 mmol) and *t*-BuOK (7.57 g, 67.5 mmol) in dry THF (30 mL) was refluxed for 10 min under N_2 and then cooled to 0 °C. Subsequently, bromoethane (5.04 mL, 67.5 mmol) was added dropwise through a syringe at 0 °C. The mixture was warmed to room temperature and stirred for 24 h. The reaction mixture was then poured into water and extracted with CH_2Cl_2. The combined organic layer was dried over $MgSO_4$, filtered, and concentrated under reduced pressure. The crude product was purified by column chromatography (SiO_2, 100% hexanes) to yield **5** as a white solid (0.65 g, 1.3 mmol, 63%). ^{1}H NMR (500 MHz, $CDCl_3$, RT): δ 8.19 (s, 3H), 7.36 (d, *J* = 7.7 Hz, 3H), 7.22 (d, *J* = 7.7 Hz, 3H), 3.00 (dq, *J* = 14.4, 7.2 Hz, 6H), 2.56 (s, 9H), 2.12 (dq, *J* = 14.6, 7.3 Hz, 6H), 0.25 (t, *J* = 7.3 Hz, 18H). $^{13}C\{^1H\}$ NMR (125 MHz, $CDCl_3$): δ 150.00, 144.03, 140.87, 138.84, 135.22, 127.29, 125.36, 121.84, 56.30, 29.45, 22.06, 8.59. HRMS (APCI): calcd for $C_{42}H_{48}$ $[M+H]^+$ *m/z*=553.3829; found *m/z*=553.3826.

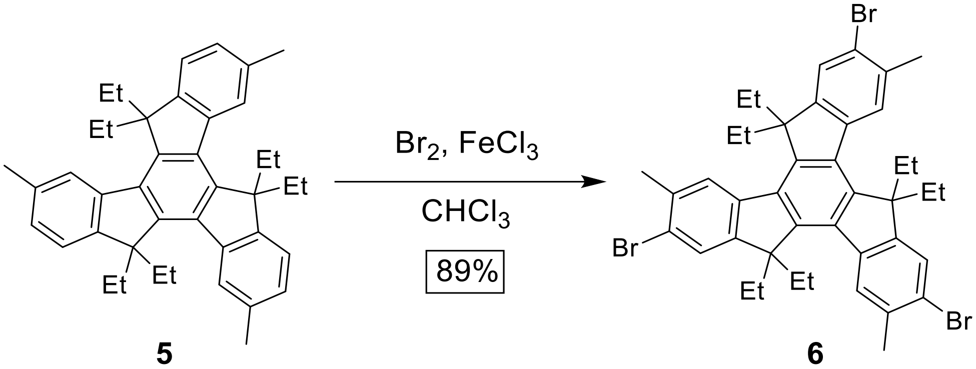

2,7,12-tribromo-5,5,10,10,15,15-hexaethyl-3,8,13-trimethyltruxene (6): A mixture of **5** (0.48 g, 0.87 mmol) and $FeCl_3$ (catalytic amount) in chloroform (50 mL) was cooled to 0 °C under N_2. Br_2 (1.8 mL, 35 mmol) was added dropwise. The mixture was warmed to room temperature and stirred for 12 h. The reaction mixture was subsequently poured into saturated aqueous $NaHSO_3$ solution and extracted with EtOAc. The combined organic layer was dried over $MgSO_4$, filtered, and concentrated under reduced pressure. The crude product was purified by column chromatography (SiO_2, 100% hexanes) to yield **6** as a white solid (0.61 g, 0.77 mmol, 89%) that decomposes slowly without melting around ~300 °C (open capillary). ^{1}H NMR (500 MHz, $CDCl_3$, RT): δ 8.19 (s, 3H), 7.59 (s, 3H), 2.93 (dq, *J* = 14.3, 7.2 Hz, 6H), 2.60 (s, 9H), 2.11 (dq, *J* = 14.6, 7.3 Hz, 6H), 0.25 (t, *J* = 7.3 Hz, 18H). $^{13}C\{^1H\}$ NMR (125 MHz, $CDCl_3$, RT): δ 152.32, 144.05, 139.76, 138.22, 135.21, 126.69, 126.02, 123.62, 56.70, 29.43, 23.71, 8.55. HRMS (APCI): calcd for $C_{42}H_{45}Br_3$ $[M]^{+\cdot}$ *m/z*=788.1045; found *m/z*=788.1034.

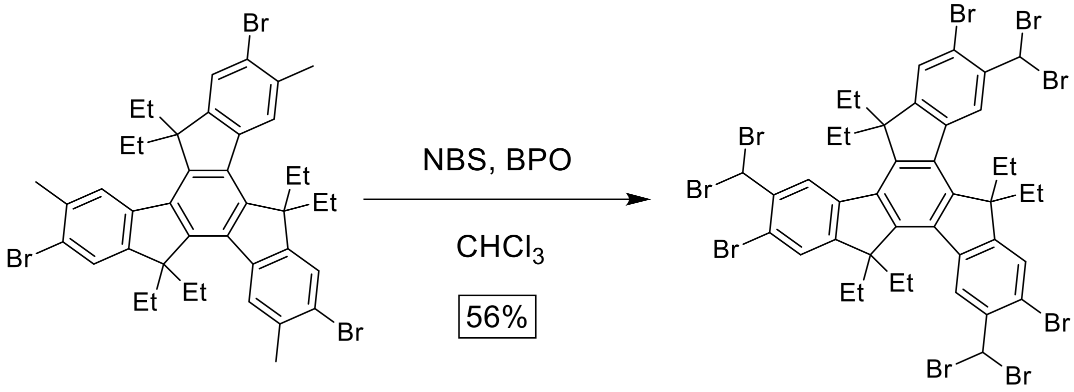

6 **7**

2,7,12-tribromo-3,8,13-tris(dibromomethyl)-5,5,10,10,15,15-hexaethyltruxene (7): A mixture of **6** (0.50 g, 0.64 mmol) and NBS (10 g, 56.2 mmol) in chloroform (30 mL) was stirred at reflux under N_2. BPO (0.15 g, 0.64 mmol) dissolved in chloroform (10 mL) was added for 3 h using syringe pump. The reaction mixture was stirred for an additional 12 h at reflux. Then it was cooled to room temperature, poured into a saturated aqueous $NaHSO_3$ solution, and extracted with CH_2Cl_2. The combined organic layer was dried over $MgSO_4$, filtered, and concentrated under reduce pressure. The crude product was purified by column chromatography (SiO_2, 100% hexanes) to yield **7** as white solid (0.45 g, 0.36 mmol, 56%). ^{1}H NMR (500 MHz, $CDCl_3$, RT): δ 8.98 (s, 3H), 7.60 (s, 3H), 7.24 (s, 3H), 2.99 (dq, J = 14.4, 7.2 Hz, 6H), 2.28 (dq, J = 14.5, 7.3 Hz, 6H), 0.33 (t, J = 7.3 Hz, 18H). $^{13}C\{^1H\}$ NMR (125 MHz, $CDCl_3$, RT): δ 156.58, 145.11, 140.22, 138.74, 137.63, 126.99, 126.18, 118.36, 57.43, 40.76, 29.17, 8.75. HRMS (APCI): calcd for $C_{42}H_{39}Br_9$ $[M]^{+\cdot}$ m/z=1261.5615; found m/z=1261.5549.

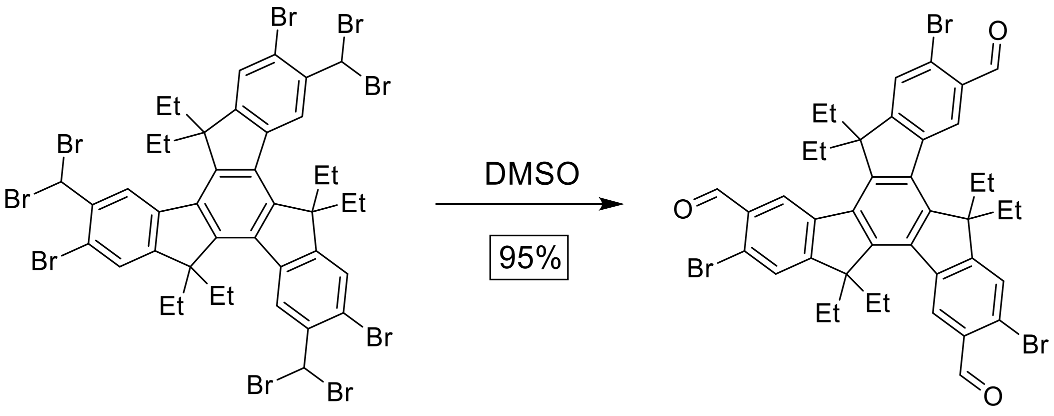

7

8

2,7,12-tribromo-5,5,10,10,15,15-hexaethyltruxene-3,8,13-tricarbaldehyde (8): A mixture of **7** (0.80 g, 0.63 mmol) and DMSO (20 mL) was heated to 100 °C for 24 hours under N_2. Then it was cooled to room temperature, poured into water, and extracted with EtOAc. The combined organic layer was dried over $MgSO_4$, filtered, and concentrated under reduced pressure. The crude product was purified by column chromatography (SiO_2, 5% EtOAc in Hexanes) to yield **8** as a white solid (0.50 g, 0.60 mmol, 95%). ^1H NMR (500 MHz, $CDCl_3$, RT): δ 10.50 (s, 3H), 8.86 (s, 3H), 7.75 (s, 3H), 2.99 (dq, J = 14.4, 7.2 Hz, 6H), 2.24 (dq, J = 14.5, 7.2 Hz, 6H), 0.23 (t, J = 7.3 Hz, 18H). $^{13}C\{^1H\}$ NMR (125 MHz, $CDCl_3$, RT): δ 191.76, 161.18, 145.27, 139.66, 137.47, 132.22, 127.82, 126.65, 125.26, 57.92, 29.15, 8.57. HRMS (APCI): calcd for $C_{42}H_{39}Br_3O_3$ $[M+H]^+$ *m/z*=831.0502; found *m/z*=831.0512.

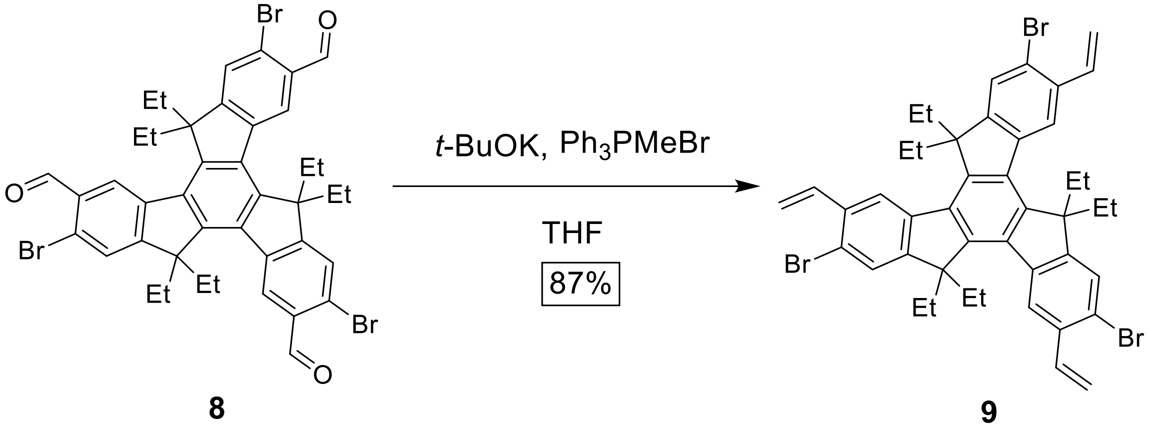

2,7,12-tribromo-5,5,10,10,15,15-hexaethyl-3,8,13-trivinyltruxene (9): A 250 mL 3-neck round bottom flask was charged with triphenylmethylphosphonium bromide (1.38 g, 3.85 mmol) and 150 mL dry THF under N_2. *t*-BuOK (0.41 g, 3.6 mmol) was added to the solution, giving a bright yellow colored suspension. The mixture was cooled to 0 °C before **8** (0.50 g, 0.60 mmol) was added in portions. The yellow color gradually faded away. The mixture was warmed to room temperature and stirred for 12 h in the dark. Subsequently, the reaction mixture was poured into water, and extracted with EtOAc. The combined organic layer was dried over $MgSO_4$, filtered, and concentrated under reduce pressure (low temperature). The crude product was purified by column chromatography (SiO_2, 100% hexanes) to yield **9** as a white solid (0.43 g, 0.52 mmol, 87%). ^{1}H NMR (500 MHz, $CDCl_3$, RT): δ 8.54 (s, 3H), 7.64 (s, 3H), 7.25 (dd, *J* = 17.4, 10.9 Hz, 3H), 5.86 (dd, *J* = 17.4, 0.9 Hz, 3H), 5.50 (dd, *J* = 10.9, 0.9 Hz, 3H), 2.94 (dq, *J* = 14.4, 7.2 Hz, 6H), 2.16 (dq, *J* = 14.5, 7.3 Hz, 6H), 0.29 (t, *J* = 7.3 Hz, 18H). $^{13}C\{^1H\}$ NMR (125 MHz, $CDCl_3$, RT): δ 154.32, 144.36, 139.74, 138.12, 136.61, 135.44, 126.56, 122.68, 122.57, 115.90, 56.98, 29.34, 8.63. HRMS (APCI): calcd for $C_{45}H_{45}Br_3$ $[M+H]^+$ m/z=825.1124; found m/z=825.1113.

3.5 Conclusions

In conclusion, we present here a strategy for the formation of crosslinked ladder polymer networks formed through polymerization–annulation strategy of truxene- and phenylene-derived monomers. The monomers were functionalized with coupling sites for Suzuki coupling polymerization, and the ladder-type backbone was created through RCM of pendant vinyl groups. Various strategies were pursued to install the vinyl groups in order to find a reliable and reproducible synthetic method. The resulting networks showed impressive stability and methane adsorption, showing that this entropic approach may be widely employed in future materials once integrated with scalable synthetic methods and strategies for improved processability. A nanoparticulation strategy to improve the processability of these materials is presented in Chapter 4.

CHAPTER IV

SOLUTION-PROCESSABLE POROUS NANOPARTICLES OF A CONJUGATED LADDER POLYMER NETWORK[*]

4.1 Introduction

Conjugated ladder polymers consist of π-conjugated, fused-ring repeating units, linked together by multiple strands of bonds.[4] Compared to conventional non-ladder type polymers, the additional strand of bonds in ladder polymers induces a significantly higher backbone rigidity.[1, 143, 144] Distinct yet intriguing chemical, optical, and electronic properties arise from the added rigidity, rendering conjugated ladder polymers a promising class of emerging organic materials with unconventional functions.[199] For instance, increased fluorescence intensity and excited state lifetimes in solution can stem from the lack of backbone conformational relaxation.[162] High carrier mobilities in the solid state can arise as a result of better orbital delocalization and lowered reorganization energy.[200-203] Rigid backbones can also render porosity in appropriately designed polymers by stabilizing interchain void space, whether from inefficient solid-state packing of linear ladder polymers[204] or in fully cross-linked networks featuring ladder-type backbones.[124, 126, 128, 129, 205] Although the porosity and optical properties of conjugated ladder polymer networks provide an ideal framework for a number of applications, the lack of

---

[*] Adapted with permission from "Solution-Processable Porous Nanoparticles of a Conjugated Ladder Polymer Network" by Alexander J. Kalin, Sai Che, Chenxu Wang, Anthony U. Mu, E. Meir Duka, and Lei Fang, *Macromolecules*, **2020**, DOI: 10.1021/acs.macromol.9b02635. Copyright 2020 The American Chemical Society.

processability (either from a solution or molten phase into the desired form) limits their practical applications. Therefore, overcoming the obstacle of processability represents a key challenge before one can unlock the potential of ladder-type polymeric materials.

The difficulty associated with solution processability of conjugated ladder polymers, in general, arises from their rigid and often coplanar backbones, which promote strong interchain aggregation. In order to mitigate this issue, they are often decorated with bulky side-chains on the backbone as solubilizing groups.[72, 206] The installation of such bulky side-chains, however, introduces a large fraction of nonactive material into the bulk, lowering the performance that depends on the conjugated backbone.[207] For organic electronic or photovoltaic applications, the insulating side-chains can also interrupt charge/exciton transport pathways in the solid state, adversely impacting the electronic performance.[208] For other applications where high microporosity is desirable, such as sensing,[209, 210] the flexibility of large alkyl side-chains could occupy and block the micropores, exerting a detrimental effect on performance.[211]

Various strategies have been developed to address the issues caused by side-chains. For example, one can install cleavable side-chains to facilitate solution processing of the polymers, which can be subsequently removed in order to restore the desired interchain interactions.[75, 77, 212, 213] Another strategy entails processing soluble precursors into a film, followed by solid-state reactions to afford the ladder-type backbone *in situ*, perhaps best exemplified by on-surface construction of graphene nanoribbons from solution processable monomers through high-temperature polymerization and annulation.[214] This method holds promise for electronic applications but is limited with regards to scalability. In addition, these strategies have been largely only applied to linear ladder polymers, and fewer solutions have been proposed for ladder polymers with different topology.[130, 131] We envisioned that a fully conjugated ladder polymer network can be made porous and solution dispersible without the introduction of excessively large solubilizing groups when nanoparticulated in a carefully designed manner.[107, 108, 215, 216] Herein, we report the successful synthesis of such nanoparticles and their facile solution processability as a proof of concept for practical applications.

4.2 Results and Discussion

4.2.1 Synthetic Design

To achieve the aforementioned goal, we designed porous ladder polymer network nanoparticles (**PLANP**), synthesized from a truxene- and phenylene-derived monomers (**M1–M4**) through a miniemulsion cross-linking polymerization followed by ring-closing olefin metathesis (RCM) annulation (Figure 4.1). The monomers were synthesized as reported and as discussed in Chapter 3, and are relabeled in Figure 4.1 for clarity.[198] For the miniemulsion polymerization, we leveraged reported synthetic strategies of conventional single-stranded conjugated polymer nanoparticles (CPNs), which can be achieved by various polymerization reactions and stabilization mechanisms.[217-221] CPNs can be prepared non-covalently by dispersing pre-synthesized polymers or by performing a dispersed-phase polymerization within a surfactant-stabilized, organic-in-water miniemulsion, which constrains the size of the resulting colloidal particles.[218, 222, 223] If the polymerization yields a fully cross-linked network, the shape-persistent spherical morphology of the CPN can be secured even after surfactants are removed. By this method, normally insoluble polymer networks are rendered solution dispersible while retaining the desired porosity.[224-227] We envisioned that this strategy could then be applied to develop **PLANP** with unprecedented solution processability (Figure 4.1).

We have previously reported a highly efficient annulation method to construct ladder polymers using RCM of a polymer precursor, which can be synthesized by step-growth Suzuki polymerization.[7, 54, 190, 228] The thermodynamically driven RCM reaction is near-quantitative and leads to few backbone defects due to the strong driving force towards aromatization. Both Suzuki and RCM reactions translate well to the designed **PLANP** synthesis: Suzuki coupling is robust toward the aqueous continuous phase[229] and RCM has previously exhibited good conversion on porous precursors, even in a heterogeneous reaction.[123, 198]

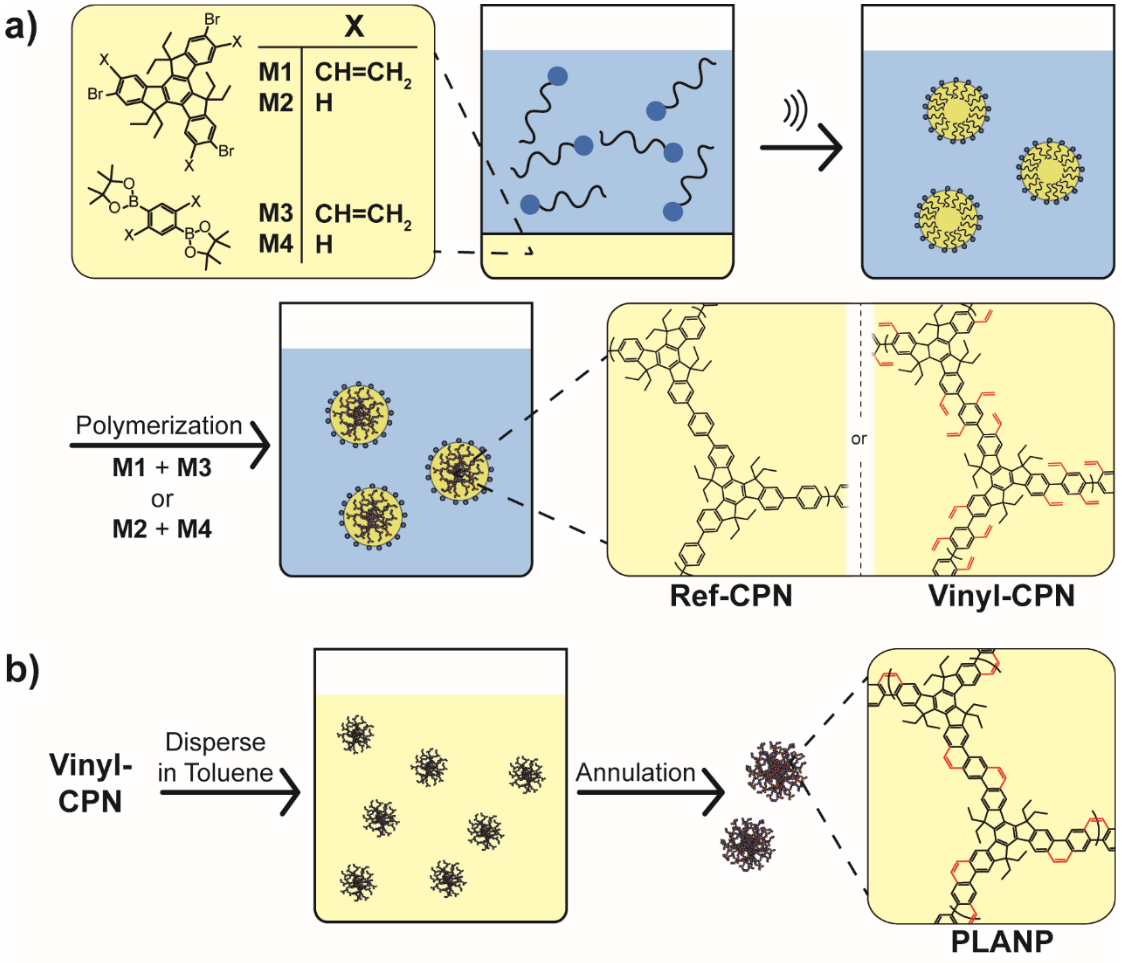

Figure 4.1. General synthetic scheme: (a) miniemulsion polymerization affords nanoparticles **Ref-CPN** and **Vinyl-CPN**; (b) RCM of **Vinyl-CPN** dispersed in organic solvent gives **PLANP**.

4.2.2 Miniemulsion Polymerization

The $A_2 + B_3$ Suzuki coupling polymerization between a trifunctional truxene-derived monomer (**M1** or **M2**) and a difunctional phenylene-derived monomer (**M3** or **M4**) was carried out in a toluene-in-water miniemulsion, generated by sonicating the organic solution mixture with an aqueous sodium dodecylsulfate (SDS) solution (150 mM, 18× critical micelle concentration). Butylated hydroxytoluene (BHT) was added as a radical scavenger to prevent undesired radical addition of the vinyl groups and was dissolved along with the monomers and Pd catalyst in toluene. Through this reaction, the intermediate polymer nanoparticles **Vinyl-CPN** and a control compound **Ref-CPN** were synthesized from **M1** + **M3** (vinyl-functionalized) and **M2** + **M4** (non-vinyl-functionalized), respectively. After the reaction, the anionic SDS was scavenged by a macroreticular basic ion exchange resin, allowing the resulting toluene/water mixture to easily phase separate for extraction and purification. The crude **Ref-CPN** or **Vinyl-CPN** was purified by precipitation into a nonsolvent such as methanol followed by washing. For the RCM annulation to form **PLANP**, **Vinyl-CPN** particles were redispersed into toluene together with Grubbs' 2nd generation catalyst and heated to 100 °C. After the reaction was completed, the product was again purified by precipitation into methanol followed by washing. **Ref-CPN**, **Vinyl-CPN**, and **PLANP** were all isolated as fine powders. **PLANP** was obtained in a 39% overall yield in two steps.

4.2.3 Nanoparticle Characterization

As the key feature of the nanoparticulated polymers, the dispersibility of the particles was investigated. A good dispersion of the particles can be formed in various organic solvents without the use of any surfactants or dispersants, appearing clear with slight Tyndall scattering, and does not show any particle flocculation (Figure 4.2a). N-methylpyrrolidone, the most effective dispersing solvent found for the particles, can disperse 5 mg/mL of **PLANP** and **Ref-CPN** effectively. Chlorinated hydrocarbon solvents such as chloroform and dichloromethane have lower dispersibility of about 1 mg/mL. Above these levels, aggregation and creaming of the particles was observed. The hydrodynamic diameters of the nanoparticles dispersed in chloroform were determined by dynamic light scattering (DLS). The intensity distribution diameters for **PLANP**, **Ref-CPN**, and **Vinyl-CPN** were all approximately 200 nm, indicating the consistent results of the miniemulsion conditions (Table 4.1, Figures C9–C11). All samples also had a similar polydispersity index (PdI) between 0.09 and 0.15. Though size control of the nanoparticles was not part of this study, reports indicate that altering the miniemulsion conditions can potentially lead to larger or smaller nanoparticles, including below 100 nm.[230-232] In this case, using different surfactants such as CTAB, with a critical micelle concentration of 1 mM, or using lower concentrations of SDS, led to a greater amount of oligomeric products. Therefore, the conditions described above were satisfactory to consistently obtain nanoparticles for characterization.

	Diameter (nm)[a]				
Sample	**Intensity Average**	**Volume Average**	**Number Average**	**Z Average**	**PdI**[ab]
Ref-CPN	202 ± 3	209 ± 3	130 ± 7	173 ± 1	0.15 ± 0.01
Vinyl-CPN	191 ± 4	196 ± 5	129 ± 5	169 ± 1	0.11 ± 0.02
PLANP	198 ± 2	203 ± 2	143 ± 2	179 ± 2	0.09 ± 0.01

Table 4.1. Average diameters and PdI of **Ref-CPN**, **Vinyl-CPN**, and **PLANP**. [a]DLS data averaged from three measurements. [b]PdI defined by ISO 22412:2008.

The good colloidal dispersibility allowed for solution processing of these materials into thin films. Spin-casting a chloroform dispersion of **PLANP** onto octadecyltrichlorosilane (OTS)-coated substrates resulted in a smooth thin film, enabling further imaging. Scanning electron microscope (SEM) images of individual nanoparticles and the thin films clearly show the spherical morphology of **PLANP** (Figure 4.2b,c). Larger images confirm that most of the nanoparticles are under 500 nm in diameter and illustrate the dispersity of sizes generated from the miniemulsion polymerization, agreeing with the average size measured by DLS (Figure 4.2c).

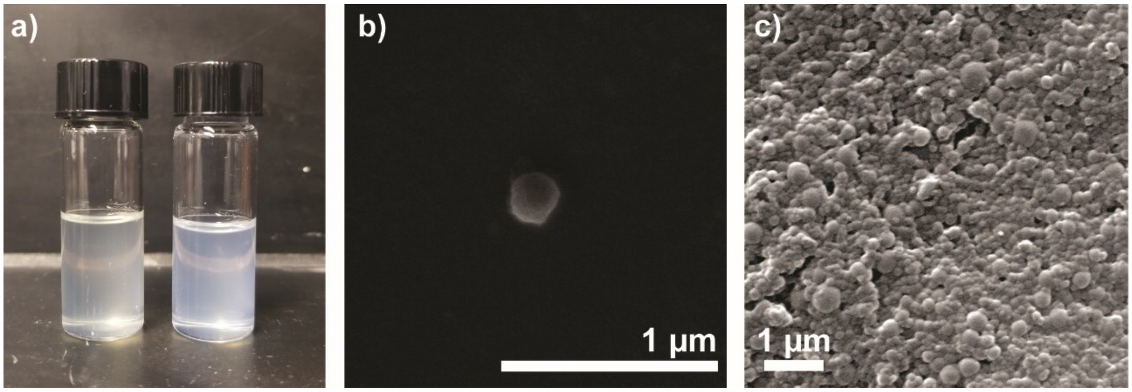

Figure 4.2. (a) Dispersions of **PLANP** (left) and **Ref-CPN** (right) at 2 mg/mL in N-methylpyrrolidone. SEM images of (b) an individual particle of **PLANP** and (c) **PLANP** thin film on OTS-coated Si substrate.

Structural characterization of the nanoparticles was primarily performed by solid-state cross polarization magic angle spinning (CP-MAS) ^{13}C NMR, as conventional solution-phase ^{1}H NMR did not give observable signals due to the large particle size and rigid backbone conformation. In the CP-MAS ^{13}C NMR spectrum, the three sp^3-hybridized carbons corresponding to the truxene methylene bridge and ethyl side-chains could clearly be distinguished (Figure C1), and the signals from the sp^2 carbons of the fused aromatic backbone match well with the previously reported spectrum of the bulk network, which was polymerized and cross-linked in solution as opposed to in miniemulsion.[198] In order to examine the efficiency of the RCM reaction, we synthesized a batch of isotope labeled **Vinyl-CPN**, in which the terminal vinyl $=CH_2$ carbon was labeled with 99% ^{13}C, so that a highly intense ^{13}C signal of the terminal vinyl peak can be used to probe the conversion of the reaction. (Figure C3). After the RCM reaction, the $=CH_2$ peak intensity in the resulting **PLANP** substantially decreases to approximately the same intensity as other carbons on the truxene core. Considering the 99% ^{13}C abundance of the labeled carbon compared to the other carbons with natural abundance (1% ^{13}C), the reaction conversion was estimated to be at least 95%.

Additionally, Fourier-transform infrared (FTIR) spectra of the nanoparticles and relevant precursors were collected with a focus on the aromatic ring substitution patterns of C–H bending peaks in the 950–650 cm^{-1} region (Figures C4–C8).[233, 234] The peaks of interest correspond to the characteristic bending of an "isolated C–H unit" with no H atoms on its neighboring carbons, and to the bending of two adjacent C–H groups.[235] The **Vinyl-CPN** and **PLANP** spectra were mostly similar as expected because the substitution patterns of the phenylene and truxene units do not change after annulation. The only characteristic change observed was a peak at approximately 800 cm^{-1} appearing in the spectrum of **PLANP** (Figure C5), attributed to bending vibrations of the two new adjacent aromatic C–H sites fused into the backbone after RCM. On the other hand, **PLANP** and **Ref-CPN** showed expected differences in relative peak intensity corresponding to the difference in their substitution patterns. The peak corresponding to the isolated C–H bend was more intense in **PLANP**, resulting from the greater number of such sites in its repeating units. The spectrum of **Ref-CPN**, on the other hand, exhibits more intense peaks between 810–840 cm^{-1} (Figure C6) attributed to a greater number of adjacent aromatic C–

H sites. The nanoparticles were also compared to precursors with relevant substitution patterns, and peaks originating from the truxene- and phenylene-derived monomers were represented in the final nanoparticles, further confirming the structural composition of the polymer (Figures C7–C8). Raman spectroscopy was unable to produce spectra of suitable quality for analysis.

Photophysical spectroscopy was employed to further characterize the conjugated ladder-type backbone of **PLANP**. High-quality optical spectra of these samples were collected thanks to the well-dispersed nature of the nanoparticulated polymers in $CHCl_3$. Both UV-visible absorption and fluorescence emission measurements in solution showed significant differences between the spectra of **PLANP** and those of the non-ladder **Vinyl-CPN** and **Ref-CPN** (Figure 4.3). A redshift was observed on both the absorption and emission spectra of **PLANP** compared to those of **Vinyl-CPN** and **Ref-CPN**. Meanwhile, **PLANP** exhibited clear vibrational progressions in both the absorption and emission spectra, while those of **Vinyl-CPN** are broad. **PLANP** also showed an extremely small Stoke shift of <1 nm. These optical properties resembled those observed on previously reported linear conjugated ladder polymers,[7, 35, 36, 236, 237] suggesting that the backbone of **PLANP** was indeed in a fused-ring ladder-type constitution. Specifically, the coplanarity of the ladder-type backbone of **PLANP** rendered a more extended π-conjugation and therefore a red-shifted absorption spectrum. The rigid backbone suppresses vibrational relaxation during photoexcitation, leading to clearly observable vibrational peaks even at room temperature.

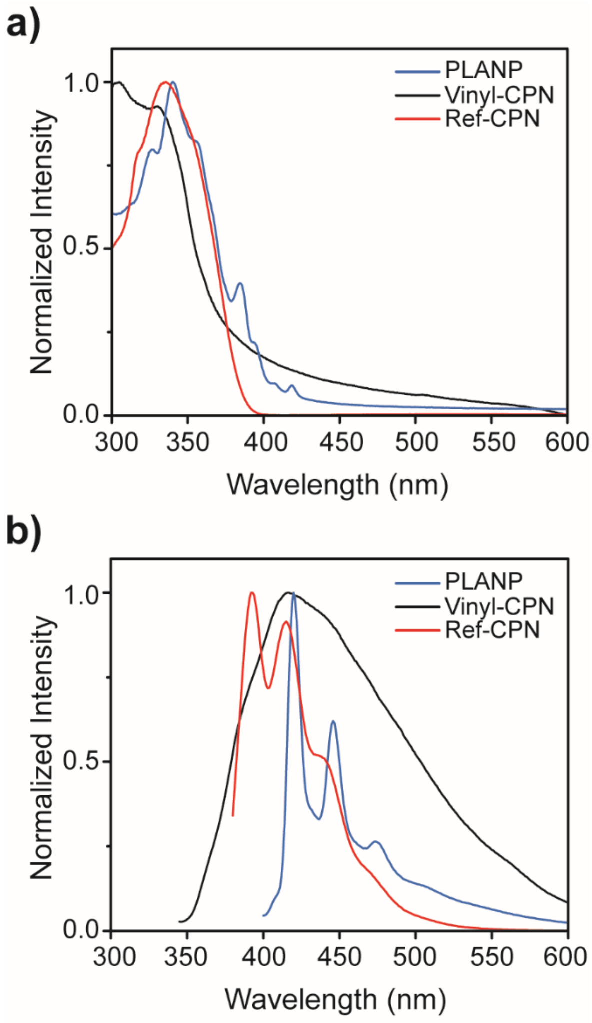

Figure 4.3. UV-visible (a) absorbance and (b) emission spectra of **PLANP**, **Vinyl-CPN**, and **Ref-CPN**.

The crosslinked and rigid backbone of **PLANP** rendered a porous structure, similar to that observed in the bulk network.[198] N_2 sorption measurements were performed to characterize the porosity (Figure 4.4). Prior to RCM, the Brunauer-Emmett-Teller (BET) surface area of **Vinyl-CPN** was 808 m^2 g^{-1}. This value increased to 1096 m^2 g^{-1} for **PLANP**. Increase of surface area was attributed to the prohibited torsional motion of the backbone aromatic units, whereas such motion is possible in **Vinyl-CPN**. Additionally, the loss of the vinyl groups during RCM can contribute to the increase in porosity. The pore size distribution shows that **PLANP** is mostly microporous with pore sizes between 1 and 2 nm with a smaller quantity of larger mesopores (Figure C17). It is noteworthy that **Ref-CPN** has a much lower BET surface area of only 81 m^2 g^{-1}, likely a result of lower steric hindrance due to the lack of the vinyl groups, which allowed for more interpenetration to block the pores.

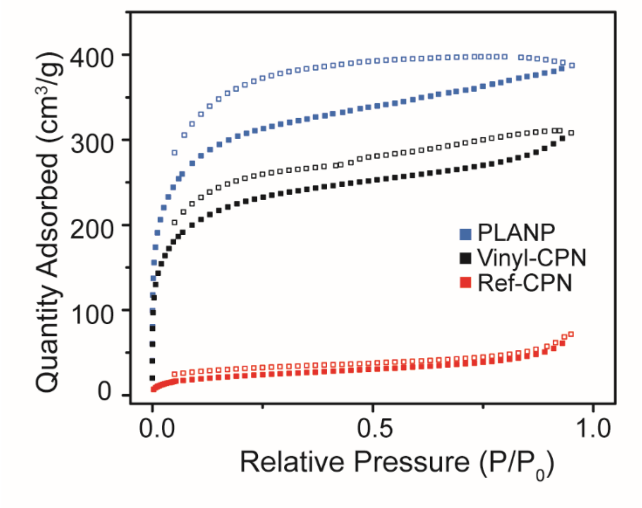

Figure 4.4. N_2 adsorption (filled symbols) and desorption (open symbols) isotherms of **PLANP**, **Vinyl-CPN**, and **Ref-CPN**.

Thermogravimetric analysis (TGA) was performed on the nanoparticles to test their thermal stability (Figure C18). As anticipated, the ladder-type **PLANP** exhibited a higher weight loss onset temperature at 325 °C, compared to 271 °C of **Ref-CPN**. In addition, the carbonization yield of **PLANP** recorded at 900 °C (35%) was approximately double that of **Ref-CPN** (18%). The higher decomposition temperature and carbonization yield indicated that the fused-ring, graphite-like constitution of the **PLANP** backbone is much more thermodynamically stable than the non-ladder constitution of **Ref-CPN**, in agreement with reported examples of linear ladder polymers and polyacrylonitrile.[7, 77, 112, 113, 238, 239]

4.3 Processing

Generally, the fully cross-linked backbones of porous polymer networks render them insoluble, hampering any applications that require good dispersion or solution processing. In the case of **PLANP**, the small size of the nanoparticles enables processing of the porous and fluorescent solids from colloidal organic dispersions, as shown above in the thin film casting of **PLANP**. We sought to demonstrate this advantageous property by fabricating a **PLANP**–polymer composite film.

PLANP was embedded into composite films with polystyrene (PS) as a polymer matrix. PS was dissolved in $CHCl_3$ and **PLANP** was added to the solution and homogenized to form the mixed dispersion. Films could be generated from the mixed dispersion through evaporative film formation on a glass substrate, and then easily delaminated to become freestanding (Figure 4.5). These films retained the characteristic fluorescence of **PLANP** (Figure 4.5a) with negligible differences between the film and solution-phase spectra (Figure 4.5b). Confocal laser microscopy was used to probe the dispersion of **PLANP** in the composite by visualizing the fluorescence of the particles. Blue emission from **PLANP** could clearly be seen distributed throughout the entire film, clustered into grains on the order of 10s of μm. This image indicated that the nanoparticles were well-dispersed in the polymer matrix, with only a moderate level of aggregation

(Figure 4.5c). **PLANP** was also able to be fabricated into PS films containing multiwalled carbon nanotubes to introduce a conductive element to the films (Appendix C). The maintained dispersibility of the nanoparticles in the solid state enables their future employment in functional composite applications.

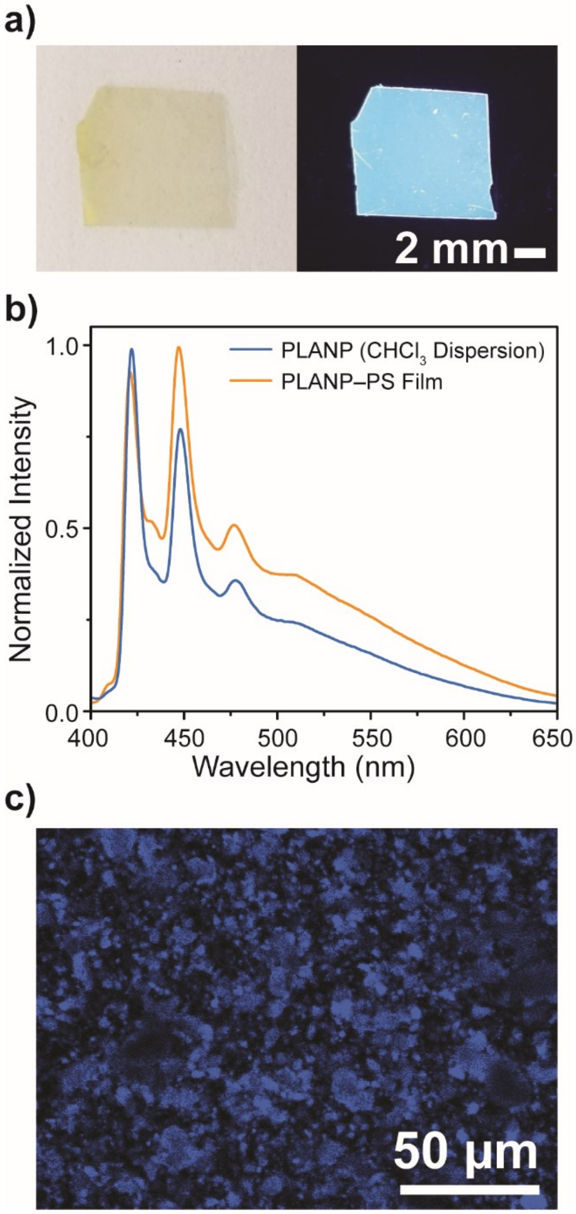

Figure 4.5. Freestanding **PLANP**–PS composite films. (a) macroscopic images of film sample under ambient (left) and 365 nm UV light (right). (b) Fluorescence spectra comparison of film and $CHCl_3$ dispersion. (c) Confocal fluorescence microscope image.

4.4 Experimental Section

4.4.1 General information

Nanomaterials can pose significant health and safety hazards, and appropriate exposure precautions should be taken. Starting materials, reagents, and solvents were purchased from Aldrich, Alfa Aesar, TCI, and Acros, and were used as received without further purification unless otherwise specified. Monomers **M1**~**M4** were synthesized according to literature reports.[156, 198] Monomers **M1** and **M3** were purified prior to polymerization by preparative size-exclusion chromatography on a JAI recycling HPLC with SEC columns; **M2** and **M4** were purified by recrystallization. All other reagents were used as purchased. Toluene was dried by an Inert Technology PureSolv-MD-5a solvent purification system. Miniemulsions were generated with a Heischler UP50H probe sonicator. Solid-state proton-decoupled ^{13}C NMR spectra were obtained on a Bruker Avance 400 MHz spectrometer with 4 mm CP/MAS probes and MAS rates of 10 kHz at room temperature. Peaks were assigned in accordance with literature.[198] Field-emission scanning electron microscopic (SEM) images were collected using a FEI Quanta 600 FE-SEM at 20 kV. Samples were sputter coated in gold prior to imaging. Spin-coating of thin films was performed using an SCS spin coater from $CHCl_3$ dispersions at 0.5 mg/mL of the nanoparticles onto octadecyltrichlorosilane (OTS)-coated SiO_2/Si wafers.

4.4.2 Synthesis

Vinyl-CPN (Miniemulsion Polymerization): DI water (50 mL) was added to a two-necked round bottom flask and degassed by bubbling N_2. Sodium dodecyl sulfate (2.178 g, 150 mM) was added under N_2 and stirred until dissolved. **M1** (0.222 g, 0.269 mmol, 2 eq), **M3** (0.154 g, 0.403 mmol, 3 eq), $Pd(PPh_3)_4$ (0.032 g, 0.027 mmol), and BHT (60 mg) were dissolved in degassed, dry toluene (5 mL) and further degassed by three cycles of freeze–pump–thaw. The organic phase was injected into the aqueous surfactant solution under a high rate of stirring. Keeping the flask under nitrogen, a Heischler UP50 probe sonicator was used to sonicate the mixture for 10 minutes, until a homogeneous miniemulsion was formed. K_2CO_3 (0.379 g, 2.74 mmol) was added to the emulsion, which was resealed and heated to 80 °C for 24h. Subsequently, 2-bromostyrene (0.1 mL) as an end-capping agent was added and allowing to react for an additional 6h, before repeating the end-capping process with 2-vinylphenylboronic acid pinacol ester (0.2 mL). After cooling to room temperature, Amberlyst IRA-900 was added and stirred for 2h. The resin beads were filtered out and the resulting biphasic mixture was transferred to a separatory funnel where the organic products were extracted with CH_2Cl_2. The combined organic solution was dried over $MgSO_4$ before the solvent was removed by rotary evaporation, to give the **Vinyl-CPN** product (355 mg, 0.228 mmol, 85% crude yield). The product was used for RCM without further purification. Solid-state $^{13}C\{^1H\}$ NMR: δ 151.11, 142.96, 138.17, 135.03, 126.32, 111.22, 55.90, 28.45, 6.85. FTIR (cm^{-1}): 3070.68, 2962.66, 2918.30, 2873.94, 2848.86, 1471.69, 987.55, 893.04, 748.38, 692.44.

PLANP (Ring-Closing Metathesis): Vinyl-CPN (355 mg, 0.228 mmol) and Grubbs' 2nd Generation catalyst (0.015 g, 0.018 mmol) were dispersed in toluene (5 mL) and heated to 100 °C in a flask shielded from light. An additional portion of Grubbs 2nd generation catalyst (0.045 g, 0.053 mmol) was dissolved in toluene (10 mL) and added via syringe pump over 3 hr. The reaction was stirred overnight, then cooled and concentrated by rotary evaporation. The product was precipitated into methanol followed by filtration using a 0.5 μm membrane filter to give **PLANP** as a dark solid (0.139 g, 0.100 mmol, 39% two-step yield). Solid-state $^{13}C\{^{1}H\}$ NMR: δ 151.72, 145.06, 139.60, 131.07, 126.73, 115.61, 57.64, 30.19, 7.90. FTIR (cm^{-1}): 2962.66, 292.01, 2873.94, 2848.86, 1456.26, 1377.17, 887.26, 794.67, 746.45, 692.44.

Ref-CPN: Through the same minimemulsion polymerization described above using **M2** (0.209 g, 0.280 mmol) and **M4** (0.139 g, 0.421 mmol), **Ref-CPN** was isolated as a pale solid (172 mg, 0.138 mmol, 49 %). Solid-state $^{13}C\{^{1}H\}$ NMR: δ 152.25, 138.46, 125.58, 55.70, 28.43, 6.33. FTIR (cm^{-1}): 3030.17, 2962.66, 2929.87, 2872.01, 1473.62, 1458.18, 1375.25, 887.26, 831.32, 806.25, 758.02, 696.30.

4.5 Conclusions

In conclusion, we successfully synthesized porous ladder polymer network nanoparticles, using a dispersed-phase miniemulsion polymerization and subsequent RCM annulation in organic solvent. The well-defined nanoscale spherical morphology enabled excellent dispersibility of these materials in common organic solvents. Compared to the non-ladder type analogue, the ladder-type backbone imbued the particles with a significant increase in porosity, strongly structured vibrational optical spectra, and increased thermal stability. The particles were solution processed into freestanding composite films with retained optical properties. This work offers a proof of concept of processing typically highly insoluble, cross-linked ladder polymer networks. The integrated porosity, optical signal output, and processability of these materials promise their utility for future application in vapor sensing and stimuli-responsive functional materials.

CHAPTER V

GRAZING INCIDENCE X-RAY SCATTERING (GIXS) OF LADDER MOLECULE AND MACROMOLECULE THIN FILMS

5.1 Introduction

Ladder-type molecules and macromolecules are promising candidates for thin film electronic devices due to their beneficial electronic properties and wide scope of potential synthetic and processing strategies.[143, 144, 240] The orientation of the molecules within the film is fundamental to the performance of an organic electronic device, due to the inherent electronic anisotropy of conjugated π-systems.[241, 242] Reliable control over the overlap and orientation of π-systems is therefore essential for bulk intermolecular charge transport in the direction of the desired device geometry. GIXS from a high brilliance synchrotron light source enables high resolution characterization of this molecular morphology within the film.[137, 165] A properly chosen grazing incident angle allows X-rays to penetrate the film but not the substrate, reducing background signal to ensure scattering is primarily caused by the material of interest. The scattered X-ray beams result in scattering peaks corresponding to repeating features in the film. By observing different scattering angles, different length scales can be probed in the film, ranging from atomic or molecular distances up to hundreds of nm. Grazing incidence wide-angle X-ray scattering (GIWAXS) is the technique of focus in this chapter as it probes smaller real-space distances (3–30 Å) relating to intermolecular distances and orientation, of great importance in forming charge transport pathways.

In addition to characterizing the film, the ability to control thin film morphology either through molecular design, processing methods, or external stimuli presents a significant opportunity to improve the functionality of the materials. The primary method of controlling morphology after processing is thermal annealing, which provides rearrangement energy to the molecules in the solid-state, enabling the film to achieve a more thermodynamically favorable packing. The nature of this rearrangement can provide information about intermolecular interactions within the film by studying the morphology before and after annealing.

Ladder-type small molecules often exhibit a large degree of crystallinity and long-range order in thin films due to their small size and well-defined structure. Electronic devices with mobilities of up to 10 $cm^2\ V^{-1}\ s^{-1}$ have been generated with fused-ring molecules such as acenes or heteroacenes,[240, 243, 244] including functionalized pentacenes[245] or benzothieno[3,2-*b*]benzothiophenes (BTBT).[246, 247] Molecular engineering of their ladder-type coplanar backbones facilitates solid-state packing structures which maximize π-system overlap to create charge transport pathways. BTBT and pentacene derivatives have served as model compounds for fundamental X-ray scattering explorations into thin film behaviors of ladder-type molecules. Such experiments have advanced understanding of thin film crystallization,[248, 249] including substrate-induced phases[250-252] or the effects of post-processing treatments like thermal[253] or solvent vapor annealing.[254] The wealth of knowledge in this area therefore provides a strong foundation on which to continue to study novel ladder-type small molecules with unique functionalities, pushing further towards high performance devices.

On the other hand, extended ladder-type macromolecules often lack a significant degree of crystallinity, translating to either isotropic scattering peaks or featureless images.[77, 141, 142] The large size of the backbone inhibits the solid-state reorganization needed to undergo crystallization within the film, and the disperse molecular weight prevents regularly repeating features. Additionally, the large sidechains needed for solubility often disrupt interchain interactions between the large π-faces. The relative lack of GIXS studies of longer ladder-type macromolecules indicates the need for further research into their solid-state interactions to improve understanding of their thin film behaviors.

Herein, we report various examples of controllable thin-film morphology, illustrated by different classes of molecules and macromolecules, ranging from fully conjugated ladder polymers to fused oligomers and small molecules. Both thermal and solvent vapor annealing were used to effect different changes in the films by controlling inter- and intramolecular interactions.

5.2 Thermally Induced Morphology Changes of Ladder Polymers[*]

First, the thermal annealing-induced rearrangement of donor-acceptor ladder polymer **DALP** provides valuable information as to the behavior of extended fully conjugated ladder polymers in thin films (Figure 5.1). As discussed in Chapter 2, the good solubility of **DALP** allowed for the preparation of uniform thin films on Si substrates by

---

[*] Section 5.2 adapted with permission from "Donor–acceptor conjugated ladder polymer *via* aromatization-driven thermodynamic annulation" by Jongbok Lee, Alexander J. Kalin, Chenxu Wang, Julia T. Early, Mohammed Al-Hashimi, and Lei Fang, *Polym. Chem.*, **2018**, *9*, 1603-1609. Copyright 2018 The Royal Society of Chemistry

spin-casting from chloroform solution. However, the as-cast film showed no scattering features due to the completely amorphous morphology of **DALP** (Figure A5), even after thermal annealing at 250 °C (Figure 5.1a). Based on the large polarizable π-faces as well as the electron-rich donors and electron-deficient acceptors, **DALP** should be expected to organize into a π-π stacking orientation, leading to improved order in the film.[255, 256] The lack of this phenomenon in the GIWAXS image indicates that the large α-branched side chains that are necessary for the good solubility of **DALP** also provide enough steric hindrance to limit efficient ordering of the films in the solid-state.

However, thermal annealing of the film at 500 °C for 30 min cleaved the alkyl side-chains, leading to a clear out-of-plane scattering peak (Figure 5.1b) resulting from a face-on orientation with a π–π distance of 3.7 Å.[164] These data suggested that thermally induced cleavage of sp^3 carbons may provide a powerful, if irreversible, tool to induce rearrangement by restoring interactions between adjacent π systems. As charge transport is facilitated by π system overlap, this strategy may be an efficient method of imbuing solution processability into ladder polymers without sacrificing performance. More thermally labile side chains have been used in other reported systems,[75, 77] and so continued development of such chemistries will improve the feasibility of this method. However, even after the restoration of the interchain packing, the large size and disperse molecular weights of the polymer lead to relatively weak ordering in the film. This is consistent with many other reported ladder polymers[77, 141, 142] and this is a key limitation of using polymers to study solid-state morphology of ladder-type materials.

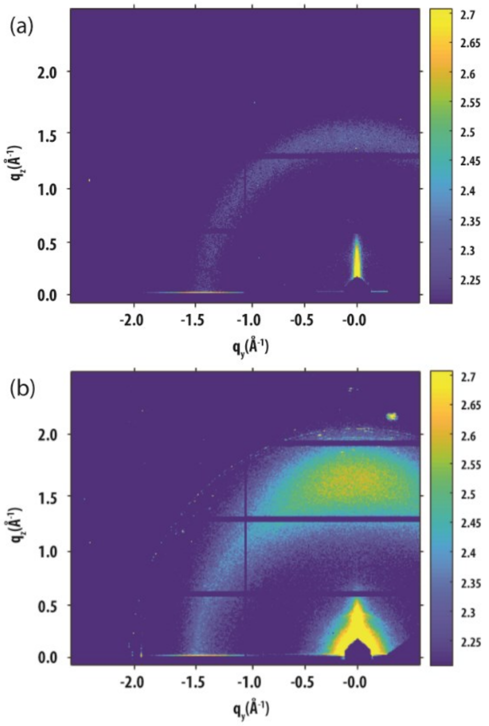

Figure 5.1. a) GIWAXS scattering image of DALP after 250 °C thermal annealing. b) Scattering image after 500 °C thermal annealing to cleave alkyl sidechains.

5.3 Solid-State Dynamics of Ladder-type Oligomers[*]

Due to the weak ordering of conjugated ladder polymers, we anticipated that GIWAXS measurements of a series of oligomers would help bridge the gap between small molecules and polymers in order to better explain size-dependent solid-state properties, aiding future molecular design efforts. To study this, thermally induced solid-state rearrangements were explored in a series of fused polycyclic aromatic hydrocarbon

---

[*] Section 5.3 adapted with permission from “Extended Ladder-Type Benzo[k]tetraphene-Derived Oligomers” by Jongbok Lee, Haunbin Li, Alexander J. Kalin, Tianyu Yuan, Chenxu Wang, Troy Olson, Hanying Li, and Lei Fang, *Angew. Chem. Int. Ed.*, **2017**, *56*, 13727-13731. Copyright 2017 Wiley-VCH Verlag GmbH & Co. KGaA, Weinheim.

oligomers based on benzo[*k*]tetraphene (BTp). Access to this series of oligomers with extended conjugation enabled an unprecedented, precise correlation of oligomer size with solid-state crystallization dynamics. Establishment of such a correlation is crucial for solid-state processing and device performances of *sp*^{2} carbon-based materials, and is important to better understand crystallization of macromolecules.[257]

The series of BTp oligomers were synthesized from vinyl-functionalized oligo-*p*-phenylenes (Figure 5.2) through RCM. The BTp derivatives contained from 5 fused rings (**BTp-5**) up to 13 fused rings (**BTp-13**), all with branched alkoxy sidechains on their terminal rings. The oligomers **BTp-5~BTp-11** were soluble in common organic solvents at room temperature while **BTp-13** was only slightly soluble at room temperature and highly soluble at 90 °C in 1,2-dichlorobenzene, thus allowing solution-phase processing into organic thin films through spin-coating. The oligomers were cast into thin films on Si wafers and annealed at 250 °C under N_2. Absorption spectra and GIWAXS images were

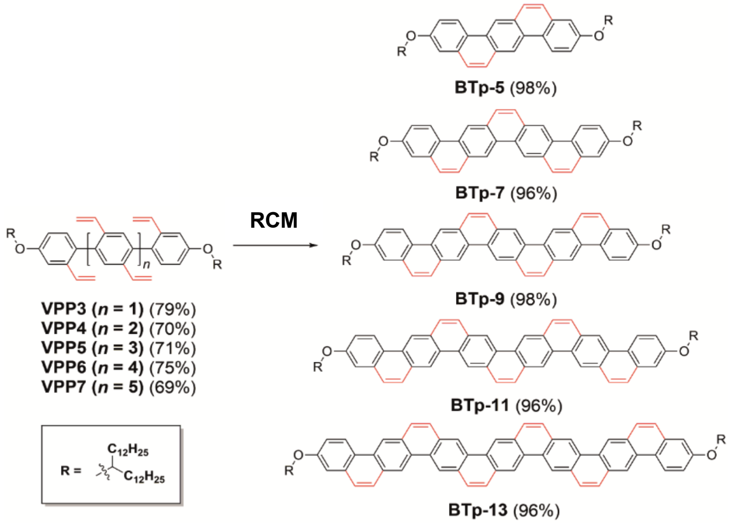

Scheme 5.1. Synthesis of BTp oligomers from vinyl-functionalized oligo-p-phenylenes (VPPs).

used to explore morphology and intermolecular interactions before and after annealing. Changes in intermolecular aggregation in the thin film were observed as shifted absorbance spectra from the solution-phase as well as in the GIWAXS scattering peaks.

For **BTp-5,** the solid-state absorption spectrum of the as-cast film was identical to that in the solution phase, indicating that (*i*) the molecular conformation remained persistent as a result of the fused-ring rigidity and (*ii*) there was no significant intermolecular electronic coupling due to the small *π*-face and relatively bulky solubilizing chains (Figure D1a). The GIWAXS pattern of **BTp-5** showed only moderately ordered face-on and edge-on packing, and no significant change before and after annealing (Figure 5.3a), suggesting that the film was already in a thermodynamically stable, weakly crystalline state as cast at room temperature. For **BTp-7** and **9**, the solid-state spectra were bathochromically shifted while maintaining well-structured vibrational progression (Figure D1b and D1c), indicating the presence of intermolecular electronic coupling in an ordered packing mode due to the large *π*-faces. Indeed, in GIWAXS, the as-cast film of **BTp-7** afforded highly crystalline scattering peaks with out-of-plane lamellar packing and edge-on *π*-*π* stacking at room temperature (Figure 5.3b). However, the as-cast film of **BTp-9** afforded less crystalline scattering peaks than **BTp-7** at room temperature and became less characteristic upon annealing (Figure 5.3c). For larger oligomer such as **BTp-11**, however, solid-state absorption of the as-cast film showed a broad and featureless spectrum, indicative of a kinetically trapped amorphous phase as a result of low molecular mobility and over-strengthened intermolecular interaction originating from the larger *π*-faces (Figure D1d).[258] GIWAXS of the as-cast sample of **BTp-11** demonstrated weak crystallinity and only face-on π-π stacking. After annealing at 250 °C, however, the absorption spectrum of **BTp-11** regained a well-defined vibrational progression, as a result of a thermally induced crystallization process that gave back the highly ordered packing mode. GIWAXS of the annealed sample demonstrated well-resolved and highly crystalline scattering peaks with out-of-plane lamellar packing and edge-on π-π stacking (Figure 5.3d). Such phenomena were also observed in the more extreme case of **BTp-13**, but the annealing process gave less profound molecular reorganization due to the prohibitively large π-systems, hence low reorganization dynamics. It is worth noting that it was difficult to obtain good quality thin films of **BTp-13** due to its low solubility.

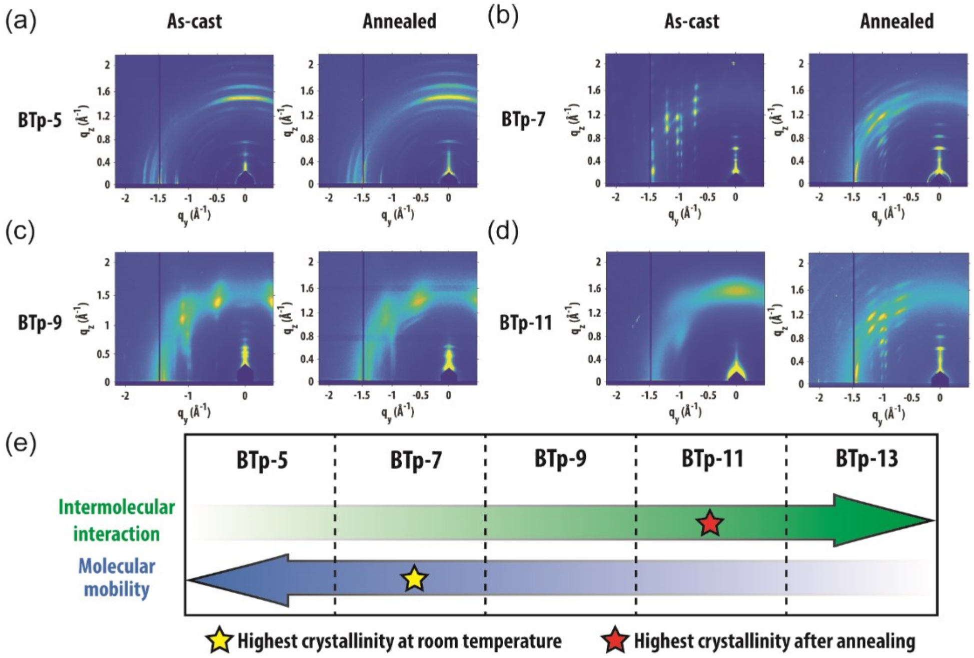

Figure 5.2. GIWAXS images of (a) **BTp-5**, (b) **BTp-7**, (c) **BTp-9**, and (d) **BTp-11** thin films as-cast and after annealing. (e) Correlation chart between intermolecular interaction and molecular mobility based on the relative size of building block to the alkyl chain.

These results suggested that the balance between molecular mobility and intermolecular interaction was crucial in obtaining highly crystalline solid-state packing for ladder-type BTp-derived materials. Larger π-systems facilitated stronger intermolecular interaction but also rendered lower molecular mobility for crystallization. These two counteractive factors must be optimally balanced to achieve good crystallinity at a certain temperature. The BTp oligomers with fine-tuned size differences enabled a unique opportunity to strike this balance. The best ordered solid-state packing from room temperature casting was seen on the somewhat smaller **BTp-7**, while after annealing, the highest crystallinity thin film was observed on the larger **BTp-11** (Figure 5.3e).

Though these results and those of **DALP** both rely on thermally induced rearrangements, being able to control morphology with milder and less energetically intensive conditions is desirable for the stability of the materials by avoiding unwanted chemical decomposition. For this reason, the use of shorter ladder-type molecules may be of greater interest than of extended polymers. As other reports have shown, the properties of ladder-type molecules do not increase above a certain chain length, including band gaps and charge transfer.[156, 200] The data from the BTp oligomer scattering may potentially corroborate that longer chains are not always better by showing the potential upper size limit to high degrees of ordering in ladder-type chains.

5.4 Characterization of B–N Fused Small Molecules and Solvent Vapor Morphology Control

Though thermal annealing is a commonly used method to effect solid state rearrangements, we also sought to explore other possible stimuli that could create morphological changes in small molecules. Full control over morphology requires a dynamic component, thereby allowing for reversible changes. In the case of the previously mentioned molecules, there is a lack of reversibility in the morphological changes, as the post-annealing packing is representative of a thermodynamically favorable end state. Previously, we have reported systems possessing noncovalent interactions that could be reversibly controlled,[32, 259, 260] and we therefore anticipated that a thin film possessing such interactions would be susceptible to external control.

To test this, molecules were designed with intramolecular noncovalent B–N bonds between an electron-rich indolocarbazole core and electron-deficient benzothiazole arms (Figure 5.4). The B–N bonds provide rigidity to the molecules by locking the conformation of the central aromatic units. This locked conformation promotes charge- and spin-delocalization, allowing for extraordinary redox processes between the oxidation-active core and reduction-active arms.[259] Importantly, these B–N bonds are dynamic and can be reversibly broken with competing Lewis acidic or basic reagents to disrupt the intramolecular interactions. The molecules possess either phenylene (Ph) or thiophene (Th) linkages to branched alkyl sidechains to provide good solubility while tuning the electron density of the donor core. Additionally, the benzothiazole units were synthesized both with (**Ph-Cl**; **Th-Cl**) and without chlorine (**Ph**; **Th**) substituents in order to increase the electron deficiency of the arms. The good solubility of these molecules allowed for efficient processing into thin films from chloroform solutions. Thermal annealing at 160 °C was also used to obtain the thermodynamically favorable packing structure of the molecules in the films.

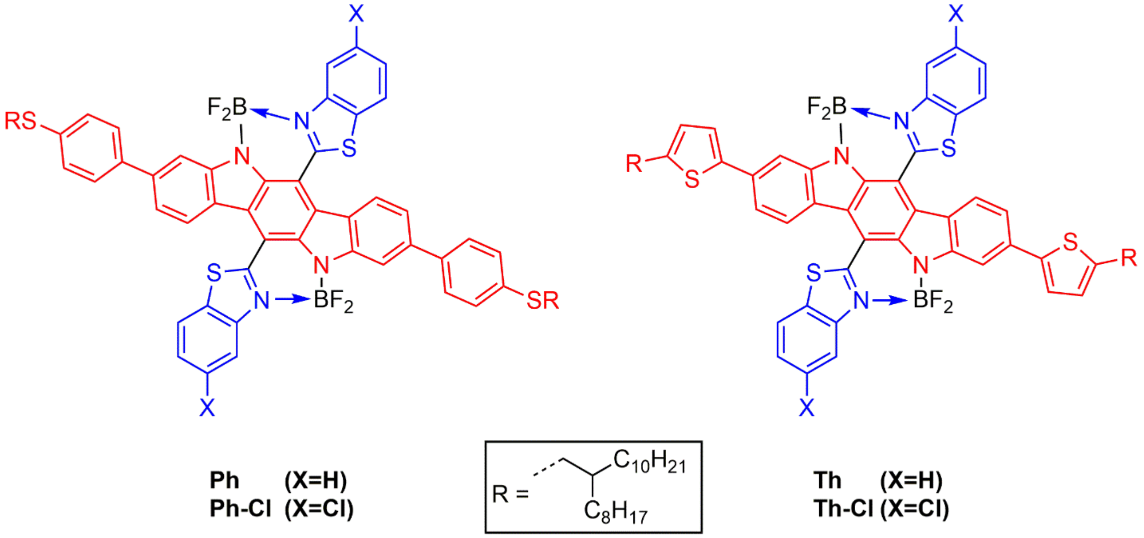

Ph **(X=H)**
Ph-Cl **(X=Cl)**

Th **(X=H)**
Th-Cl **(X=Cl)**

Figure 5.3. Acceptor-donor-acceptor molecules conformationally locked by B–N noncovalent bonds.

GIWAXS images were taken of **Ph**, **Ph-Cl**, **Th**, and **Th-Cl** both before and after thermal annealing at 110 °C to compare the effects of different structures on thin film morphology. The thiophene-appended molecule **Th** shows moderate ordering in the as-cast film, with weak crystalline scattering peaks and several intense out-of-plane lamellar peaks, which become sharper after annealing. When chlorinated, **Th-Cl** shows only one strong out-of-plane lamellar peak after spin-coating but annealing causes numerous lamellar peaks and weak crystalline scattering peaks to arise. For **Ph**, the as-cast film showed several out-of-plane lamellar peaks. After annealing, the lamellar peaks became sharper and more intense and weak crystalline peaks emerged. In the chlorinated case of **Ph-Cl**, the as-cast film showed a more amorphous morphology, with only one strong lamellar out-of-plane peak. After annealing, however, the film was highly crystalline, with numerous sharp diffraction peaks.

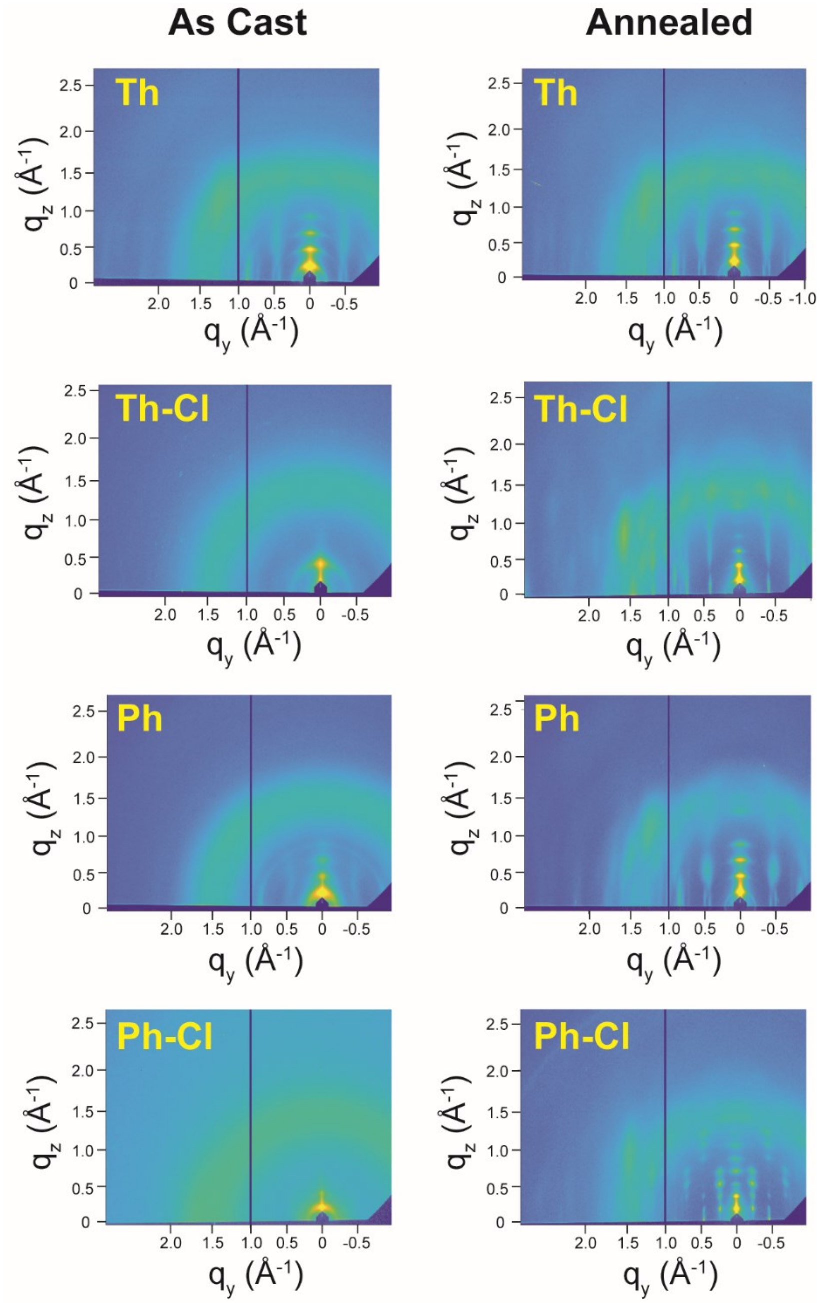

Figure 5.4. GIWAXS images of B-N fused molecules before (left column) and after (right column) thermal annealing.

The similar behavior of these molecules indicates that the structural difference between a thiophene and benzene ring attached to the indolocarbazole core does not cause significant changes in the behavior of these molecules in a thin film. The addition of chlorines on the benzothiazole arms may disrupt packing at ambient conditions but appears to enable stronger crystallinity after annealing. In all cases, the film after annealing is more ordered after annealing, indicating that efficient packing is thermodynamically favorable for these molecules. These results are promising for tunable molecules for organic electron applications, by ensuring that small structural changes that alter molecular orbital energy levels do not prevent efficient solid-state packing. This facilitates the creation of specifically tuned energy levels to obtain a desired performance without sacrificing film quality.

As previously stated, the key feature of these B–N fused ladder molecules is the dynamic nature of the noncovalent bond, enabling Lewis acidic or basic reagents to compete with the B–N interaction.[32] We anticipated that if such a competing reagent were added in situ during a GIWAXS experiment, the torsion of the benzothiazole arms after breaking this interaction would disrupt the ordered packing within the thin film (Figure 5.6a), which could then be observed in near real-time by changes in the GIWAXS images. We therefore took advantage of a sample chamber which could be connected to a solvent vapor flow line in order to test this hypothesis. The solvents chosen for this experiment were methanol and chloroform. Both should be able to compete with the B–N bond to some extent, but the molecules also have good solubility in chloroform and almost none in methanol. This helps to rule out effects that a good solvent might have on the film, such as swelling. Additionally, a Filmetrics film thickness analyzer was used to measure the film thickness during the experiment.

Th-Cl was chosen for this experiment because of its highly ordered thin film with clearly distinguishable lamellar stacking peaks. The scattering image of **Th-Cl** after annealing (Figure 5.5) in the ultrahigh vacuum sample chamber was used as a control for the experiment. As expected, the scattering peaks observed in the control image were no longer visible after exposure to methanol. The film thickness changed less than 1%, indicating that this loss of scattering peaks was not due to swelling of the films. Interestingly, after removing the film from the methanol environment and letting dry, the ordered scattering peaks reappeared (Figure 5.6b). The out-of-plane lamellar peaks were less pronounced, and some in-plane and amorphous lamellar scattering was observed in the reformed film. This indicates that the dynamic nature of these bonds which control molecular conformation can be reversibly disrupted and reformed. Through further study, we believe that this may lead to a "turn-off" effect of certain properties of the molecules or the film such as transistor performance or changes in optical spectra, which could be then correlated specifically to the change in morphology. This would then enable full control over the morphology of similar molecules that possess dynamic intramolecular interactions.

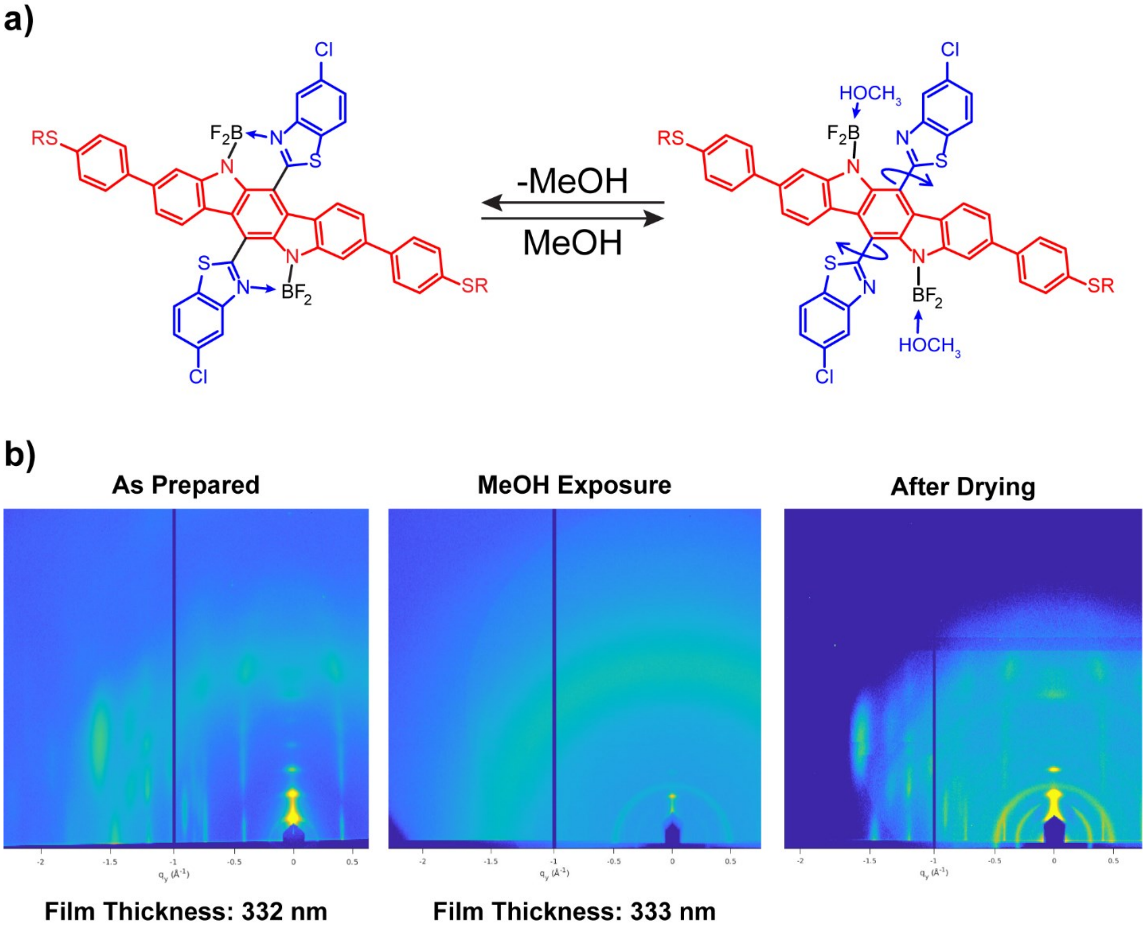

Figure 5.5. a) Competing reagents such as MeOH can break B-N noncovalent interactions, which are then restored when the competing reagent is removed. b) the clear scattering peaks in the film can be reversibly disrupted and reformed without a measurable change in film thickness.

5.5 Experimental Section

5.5.1 General Information

Solvents for sample solutions were purchased from Aldrich, Alfa Aesar, TCI, and Acros, and were used as received without further purification unless otherwise specified. All measurements were performed at the Advanced Photon Source (APS) at Argonne

National Laboratory on beamline 8-ID-E.[165] Beamline 8-ID-E operates at an energy of 10.91 keV and the images were collected from a Pilatus 1MF camera (Dectris), with two exposures for different vertical positions of the detector. Software developed at the beamline provides a GUI for processing data and performing calculations based on the scattering images.[166, 261] The X-ray beam is approximately 100 µm wide and 50 µm and was set to an incident angle of 0.15°. An ultrahigh vacuum chamber was used for standard GIWAXS measurements in order to avoid diffuse scattering effects from the air. For solvent vapor annealing experiments, a PTFE sample chamber was used. To introduce solvent vapor to the chamber, N_2 was bubbled through a solvent reservoir, connected by tubing to the chamber. The rate of N_2 flow was controlled using a mass flow controller.

5.5.2 Sample Preparation

Si wafers (1×2 cm) were cleaned with a UV-ozone cleaner for 15 minutes before creating films. Wafers were spin coated with a Specialty Coating Systems G3 spin coater and annealed in an N_2 glovebox. Spin rate, solution concentration and solvent, and annealing temperature were chosen dependent on sample. Sample solution was drop cast onto the wafer in the spin coater, then the spin coating procedure was run to form the film. The wafers were then left to dry overnight. Thermal annealing was performed in an N_2 glovebox, typically at 150 °C for 2h, unless stated otherwise.

5.5.3 Measurement Procedures

In a typical experiment, a sample is first aligned, followed by as many scattering measurements as is necessary. Samples were vertically aligned so as to have the surface of the film centered in the beam, and the angle of the sample was aligned to be horizontal with respect to the beam. The samples were then set to the incident angle and a test exposure was taken to ensure proper alignment. The gathered data was then taken from other areas on the film in order to avoid any decomposition effect that might have happened during alignment. Unless specifically stated otherwise, 4 exposures were taken on each film in 4 different spots. The images showing the fewest scattering artifacts were chosen for presentation.

5.6 Conclusion & Outlook

The previously discussed experiments have shown the potential for controllable thin film morphology in ladder-type molecules and macromolecules. Thermal energy was used in a donor-acceptor ladder polymer, a series of conjugated oligomers, and noncovalently fused molecules to induce favorable morphological rearrangements, while solvent vapor annealing could reliably disrupt noncovalent interactions. Importantly, we were able to compare ladder-type macromolecules of different lengths, showing that controllable morphology is more effective with smaller molecules, but also that intermolecular interactions of extended π faces can be much stronger than their shorter counterparts. For these reasons, it is vital that the backbone size be central to molecular design in order to fully take advantage of the properties of conjugated ladder-type systems.

These experiments have helped to build a portfolio of experimental techniques, which can now be applied to other fundamental studies or used in more functional applications. With the ability to control thin film morphology, more complex experiments can be designed to combine multiple stimuli to provide additional structure-property correlations. An additional tool not explored thus far in our research is the ability to connect the GIWAXS sample measurement chamber to a source measure unit, allowing for electric voltage and current measurement. On its own, electronic control of a thin film can be used to drive solid-state redox processes, which should cause conformational changes in the molecules. Further, combining electronic monitoring with the other methods described here would allow real-time correlation of electronic device performance with morphological changes brought on by external stimuli, something that to our knowledge is unexplored in such conjugated ladder molecule systems.

We also anticipate that combinations of external stimuli can be applied to larger functional devices which would be outside the GIWAXS measurement regime. However, the modularity of modern beamline equipment makes switching to a small-angle geometry trivial. This would enable explorations of features at length scales up to hundreds of nm, enabling characterization of scalable devices. By expanding these experiments towards multifunctional systems, such morphological characterizations could play a key role in advancing and accelerating the next generation of functional organic materials.

CHAPTER VI

CONCLUSIONS

In conclusion, this dissertation discussed various aspects of conjugated ladder-type backbones in organic molecules and macromolecules. The importance of these materials stems from their rigidity and stability from a secondary strand of backbone bonds, making them prime candidates for various applications, but requiring new synthetic strategies to solve the challenges of reliable multiple bond creation. Based on historical precedents, we advanced the field by developing efficient chemistries for creation of conjugated ladder polymers with different functionalities. We showed that thermodynamically controlled RCM can be applicable to challenging substrates, and in doing so we could explore the properties offered by such systems.

In Chapter II, donor and acceptor monomers were synthesized and polymerized to form an alternating donor–acceptor ladder polymer **DALP** was constructed using RCM annulation, therefore avoiding difficult intramolecular cyclization with an electron-deficient backbone. **DALP** showed lower energy optical absorption and emission due to its lowered bandgap, as well as highly structured optical spectra, and was fabricated into ordered thin films using thermal annealing.

In Chapter III, truxene-derived monomers were synthesized in order to apply RCM to another challenging substrate, a crosslinked ladder polymer network (**PLAN).** Various strategies were explored to add the vinyl groups necessary for RCM. **PLAN** provided unprecedentedly high methane adsorption per unit surface area due to the lessened initial entropy of the rigidified ladder-type backbone, as well as being chemically and thermally more stable than a single-stranded counterpart.

In Chapter IV, the truxene-based network was made solution-processable using a miniemulsion polymerization, affording porous ladder polymer network nanoparticles (**PLANP**). The nanoparticles were consistently measured to be approximately 200 nm in diameter with a narrow PdI of 0.1. **PLANP** retained the valuable porosity of the crosslinked network with a BET surface area of 1097 m^2 g^{-1}. The colloidally sized nanoparticles were easily dispersed in organic solvents for solution-phase optical characterization. **PLANP** possessed highly structured optical spectra due to the lack of conformational relaxation of the rigid backbones. Importantly, the nanoparticle processability allowed for implementation of the porous and fluorescent framework into various applications, and we showed that freestanding films could be generated that retained the **PLANP** properties in a polystyrene matrix.

In Chapter V, we studied a series of ladder-type molecules and macromolecules using GIWAXS to explore thin film morphology. We were able to show that multiple external stimuli could be used to control morphology. In the case of a conjugated ladder polymer and oligomers, thermal annealing improved packing in the films by improving interactions between the backbone π-faces either through side-chain cleavage or by providing energy for solid-state reorganization driven by length-dependent intermolecular interactions. Additionally, solvent vapor exposure was shown to reversibly compete with noncovalent intramolecular bonds, increasing molecular torsion and disrupting thin film packing.

Overall, this dissertation highlighted several strategies that could tackle the challenges posed by rigid, fully conjugated ladder-type backbones. RCM is capable of creating the double-stranded backbone highly efficiently due to the thermodynamic driving force of aromatization, even with electron-deficient backbones or within a porous solid. The success of these methods establishes RCM as a valuable tool to be applied in further syntheses of unique ladder-type substrates, and the use of a dispersed-phase system in order to create processable ladder polymers provides an alternative strategy for solution processing without relying on long alkyl side-chains. These two approaches will help to efficiently combine design, synthesis, and processing in order to expand the scope of conjugated ladder polymers within the rapidly developing field of functional organic materials.

REFERENCES

1. Yu, L.; Chen, M.; Dalton, L. R., Ladder polymers: recent developments in syntheses, characterization, and potential applications as electronic and optical materials. *Chem. Mater.* **1990**, *2*, 649-659.

2. Scherf, U., Ladder-type materials. *J. Mater. Chem.* **1999**, *9*, 1853-1864.

3. Grimsdale, A. C.; Müllen, K., Oligomers and Polymers Based on Bridged Phenylenes as Electronic Materials. *Macromol. Rapid Commun.* **2007**, *28*, 1676-1702.

4. Jones, R. G.; Wilks, E. S.; Metanomski, W. V.; Kahovec, J.; Hess, M.; Stepto, R.; Kitayama, T., *Compendium of Polymer Terminology and Nomenclature (IUPAC Recommendations 2008)*. RSC Publications: Cambridge, 2009.

5. Wu, Y.; Zhang, J.; Fei, Z.; Bo, Z., Spiro-Bridged Ladder-Type Poly(p-phenylene)s: Towards Structurally Perfect Light-Emitting Materials. *J. Am. Chem. Soc.* **2008**, *130*, 7192-7193.

6. Zeng, S. Z.; Jin, N. Z.; Zhang, H. L.; Hai, B.; Chen, X. H.; Shi, J. L., High-modulus all-carbon ladder polymer of hydroquinone and formaldehyde that bridges the gap between single-strand polymers and graphene nanoribbons. *RSC Adv.* **2014**, *4*, 18676-18682.

7. Lee, J.; Rajeeva, B. B.; Yuan, T.; Guo, Z.-H.; Lin, Y.-H.; Al-Hashimi, M.; Zheng, Y.; Fang, L., Thermodynamic synthesis of solution processable ladder polymers. *Chem. Sci.* **2016**, *7*, 881-889.

8. Grozema, F. C.; van Duijnen, P. T.; Berlin, Y. A.; Ratner, M. A.; Siebbeles, L. D. A., Intramolecular Charge Transport along Isolated Chains of Conjugated Polymers: Effect of Torsional Disorder and Polymerization Defects. *J. Phys. Chem. B* **2002**, *106*, 7791-7795.

9. Prins, P.; Grozema, F. C.; Schins, J. M.; Patil, S.; Scherf, U.; Siebbeles, L. D. A., High intrachain hole mobility on molecular wires of ladder-type poly(p-phenylenes). *Phys. Rev. Lett.* **2006**, *96*, 146601.

10. Samiullah, M.; Moghe, D.; Scherf, U.; Guha, S., Diffusion length of triplet excitons in organic semiconductors. *Phys. Rev. B* **2010**, *82*, 205211.

11. Bjorgaard, J. A.; Köse, M. E., Theoretical Study of Torsional Disorder in Poly(3-alkylthiophene) Single Chains: Intramolecular Charge-Transfer Character and Implications for Photovoltaic Properties. *J. Phys. Chem. A* **2013**, *117*, 3869-3876.

12. Van Deusen, R. L., Benzimidazo-benzophenanthroline polymers. *J. Polym. Sci. B Polym. Lett.* **1966**, *4*, 211-214.

13. Schlüter, A.-D., Ladder Polymers: The new generation. *Adv. Mater.* **1991**, *3*, 282-291.

14. Grem, G.; Leising, G., ELECTROLUMINESCENCE OF WIDE-BANDGAP CHEMICALLY TUNABLE CYCLIC CONJUGATED POLYMERS. *Synth. Met.* **1993**, *57*, 4105-4110.

15. Leising, G.; Tasch, S.; Meghdadi, F.; Athouel, L.; Froyer, G.; Scherf, U., Blue electroluminescence with ladder-type poly (para-phenylene) and para-hexaphenyl. *Synth. Met.* **1996**, *81*, 185-189.

16. Piok, T.; Gamerith, S.; Gadermaier, C.; Plank, H.; Wenzl, F. P.; Patil, S.; Montenegro, R.; Kietzke, T.; Neher, D.; Scherf, U.; Landfester, K.; List, E. J. W., Organic Light-Emitting Devices Fabricated from Semiconducting Nanospheres. *Adv. Mater.* **2003**, *15*, 800-804.

17. Durban, M. M.; Kazarinoff, P. D.; Segawa, Y.; Luscombe, C. K., Synthesis and Characterization of Solution-Processable Ladderized n-Type Naphthalene Bisimide Copolymers for OFET Applications. *Macromolecules* **2011**, *44*, 4721-4728.

18. Babel, A.; Jenekhe, S. A., High electron mobility in ladder polymer field-effect transistors. *J. Am. Chem. Soc.* **2003**, *125*, 13656-13657.

19. Chen, X. L.; Bao, Z.; Schön, J. H.; Lovinger, A. J.; Lin, Y.-Y.; Crone, B.; Dodabalapur, A.; Batlogg, B., Ion-modulated ambipolar electrical conduction in thin-film transistors based on amorphous conjugated polymers. *Appl. Phys. Lett.* **2001**, *78*, 228-230.

20. Babel, A.; Jenekhe, S. A., Electron transport in thin-film transistors from an n-type conjugated polymer. *Adv. Mater.* **2002**, *14*, 371-374.

21. Briseno, A. L.; Mannsfeld, S. C. B.; Shamberger, P. J.; Ohuchi, F. S.; Bao, Z.; Jenekhe, S. A.; Xia, Y., Self-Assembly, Molecular Packing, and Electron Transport in n-Type Polymer Semiconductor Nanobelts. *Chem. Mater.* **2008**, *20*, 4712-4719.

22. Stille, J. K.; Mainen, E. L., Ladder polyquinoxalines. *J. Polym. Sci. B Polym. Lett.* **1966**, *4*, 39-41.

23. Stille, J. K.; Mainen, E. L., Ladder polyquinoxalines. *J. Polym. Sci. B Polym. Lett.* **1966**, *4*, 665-667.

24. Kim, O.-K., Electrical conductivity of heteroaromatic ladder polymers. 3. Phenothiazine and the structurally related ladder polymers. *J. Polym. Sci. Polym. Lett. Ed.* **1985**, *23*, 137-139.

25. Schluter, A. D.; Loffler, M.; Enkelmann, V., Synthesis of a fully unsaturated all-carbon ladder polymer. *Nature* **1994**, *368*, 831-834.

26. Schlicke, B.; Schirmer, H.; Schlüter, A. D., Unsaturated ladder polymers: Structural variations and improved molecular weights. *Adv. Mater.* **1995**, *7*, 544-546.

27. Delnoye, D. A. P.; Sijbesma, R. P.; Vekemans, J. A. J. M.; Meijer, E. W., π-Conjugated Oligomers and Polymers with a Self-Assembled Ladder-like Structure. *J. Am. Chem. Soc.* **1996**, *118*, 8717-8718.

28. Pieterse, K.; Vekemans, J. A. J. M.; Kooijman, H.; Spek, A. L.; Meijer, E. W., Ladderlike Oligomers; Intramolecular Hydrogen Bonding, Push–Pull Character, and Electron Affinity. *Chem. Eur. J.* **2000**, *6*, 4597-4603.

29. Vetrichelvan, M.; Valiyaveettil, S., Intramolecular Hydrogen-Bond-Assisted Planarization of Asymmetrically Functionalized Alternating Phenylene–Pyridinylene Copolymers. *Chem. Eur. J.* **2005**, *11*, 5889-5898.

30. Tian, Y.-H.; Kertesz, M., Low-Bandgap Pyrazine Polymers: Ladder-Type Connectivity by Intramolecular S···N(sp2) Interactions and Hydrogen Bonds. *Macromolecules* **2009**, *42*, 2309-2312.

31. Wakamiya, A.; Taniguchi, T.; Yamaguchi, S., Intramolecular B–N Coordination as a Scaffold for Electron-Transporting Materials: Synthesis and Properties of Boryl-Substituted Thienylthiazoles. *Angew. Chem. Int. Ed.* **2006**, *45*, 3170-3173.

32. Zhu, C.; Guo, Z.-H.; Mu, A. U.; Liu, Y.; Wheeler, S. E.; Fang, L., Low Band Gap Coplanar Conjugated Molecules Featuring Dynamic Intramolecular Lewis Acid–Base Coordination. *J. Org. Chem.* **2016**, *81*, 4347-4352.

33. Crossley, D. L.; Cade, I. A.; Clark, E. R.; Escande, A.; Humphries, M. J.; King, S. M.; Vitorica-Yrezabal, I.; Ingleson, M. J.; Turner, M. L., Enhancing electron affinity and tuning band gap in donor-acceptor organic semiconductors by benzothiadiazole directed C-H borylation. *Chem. Sci.* **2015**, *6*, 5144-5151.

34. Scherf, U.; Müllen, K., Polyarylenes and poly(arylenevinylenes), 7. A soluble ladder polymer via bridging of functionalized poly(p-phenylene)-precursors. *Makromol. Chem., Rapid Commun.* **1991**, *12*, 489-497.

35. Yuan, Z.; Xiao, Y.; Yang, Y.; Xiong, T., Soluble Ladder Conjugated Polymer Composed of Perylenediimides and Thieno[3,2-b]thiophene (LCPT): A Highly Efficient Synthesis via Photocyclization with the Sunlight. *Macromolecules* **2011**, *44*, 1788-1791.

36. Kass, K. J.; Forster, M.; Scherf, U., Incorporating an Alternating Donor-Acceptor Structure into a Ladder Polymer Backbone. *Angew. Chem. Int. Ed.* **2016**, *55*, 7816-7820.

37. Nehls, B. S.; Füldner, S.; Preis, E.; Farrell, T.; Scherf, U., Microwave-Assisted Synthesis of 1,5- and 2,6-Linked Naphthylene-Based Ladder Polymers. *Macromolecules* **2005**, *38*, 687-694.

38. Patil, S. A.; Scherf, U.; Kadashchuk, A., New Conjugated Ladder Polymer Containing Carbazole Moieties. *Adv. Funct. Mater.* **2003**, *13*, 609-614.

39. Forster, M.; Annan, K. O.; Scherf, U., Conjugated Ladder Polymers Containing Thienylene Units. *Macromolecules* **1999**, *32*, 3159-3162.

40. Fiesel, R.; Huber, J.; Scherf, U., Synthesis of an Optically Active Poly(para-phenylene) Ladder Polymer. *Angew. Chem. Int. Ed. Engl.* **1996**, *35*, 2111-2113.

41. Scherf, U.; Müllen, K., Polyarylenes and poly(arylenevinylene)s: 8. The first soluble ladder polymer with 1,4-benzoquinone-bismethide subunits. *Polymer* **1992**, *33*, 2443-2446.

42. Cho, S. Y.; Grimsdale, A. C.; Jones, D. J.; Watkins, S. E.; Holmes, A. B., Polyfluorenes without Monoalkylfluorene Defects. *J. Am. Chem. Soc.* **2007**, *129*, 11910-11911.

43. List, E. J. W.; Guentner, R.; Freitas, P. S. d.; Scherf, U., The Effect of Keto Defect Sites on the Emission Properties of Polyfluorene-Type Materials. *Adv. Mater.* **2002**, *14*, 374-378.

44. Scherf, U.; List, E. J. W., Semiconducting Polyfluorenes—Towards Reliable Structure–Property Relationships. *Adv. Mater.* **2002**, *14*, 477-487.

45. Qiu, S.; Lu, P.; Liu, X.; Shen, F.; Liu, L.; Ma, Y.; Shen, J., New Ladder-Type Poly(p-phenylene)s Containing Fluorene Unit Exhibiting High Efficient Electroluminescence. *Macromolecules* **2003**, *36*, 9823-9829.

46. Chen, Y.; Huang, W.; Li, C.; Bo, Z., Synthesis of Fully Soluble Azomethine-Bridged Ladder-Type Poly(p-phenylenes) by Bischler−Napieralski Reaction. *Macromolecules* **2010**, *43*, 10216-10220.

47. Chmil, K.; Scherf, U., A simple two-step synthesis of a novel, fully aromatic ladder-type polymer. *Makromol. Chem., Rapid Commun.* **1993**, *14*, 217-222.

48. Chmil, K.; Scherf, U., Conjugated all-carbon ladder polymers: improved solubility and molecular weights. *Acta Polym.* **1997**, *48*, 208-211.

49. Goldfinger, M. B.; Swager, T. M., Fused Polycyclic Aromatics via Electrophile-Induced Cyclization Reactions: Application to the Synthesis of Graphite Ribbons. *J. Am. Chem. Soc.* **1994**, *116*, 7895-7896.

50. Debad, J. D.; Bard, A. J., Electropolymerization of Acenaphtho[1,2-k]fluoranthene Derivatives: Formation of a New Conductive Electroactive Electrochromic Hydrocarbon Ladder Polymer. *J. Am. Chem. Soc.* **1998**, *120*, 2476-2477.

51. Zou, Y.; Yuan, T.; Yao, H.; Frazier, D. J.; Stanton, D. J.; Sue, H.-J.; Fang, L., Solution-Processable Core-Extended Quinacridone Derivatives with Intact Hydrogen Bonds. *Org. Lett.* **2015**, *17*, 3146-9.

52. Rowan, S. J.; Cantrill, S. J.; Cousins, G. R. L.; Sanders, J. K. M.; Stoddart, J. F., Dynamic covalent chemistry. *Angew. Chem. Int. Ed.* **2002**, *41*, 898-952.

53. Tour, J. M.; Lamba, J. J. S., Synthesis of planar poly(p-phenylene) derivatives for maximization of extended pi-conjugation. *J. Am. Chem. Soc.* **1993**, *115*, 4935-4936.

54. Bonifacio, M. C.; Robertson, C. R.; Jung, J.-Y.; King, B. T., Polycyclic Aromatic Hydrocarbons by Ring-Closing Metathesis. *J. Org. Chem.* **2005**, *70*, 8522-8526.

55. Tsai, F. C.; Chang, C. C.; Liu, C. L.; Chen, W. C.; Jenekhe, S. A., New thiophene-linked conjugated poly(azomethine)s: Theoretical electronic structure, synthesis, and properties. *Macromolecules* **2005**, *38*, 1958-1966.

56. Streifel, B. C.; Peart, P. A.; Martínez Hardigree, J. F.; Katz, H. E.; Tovar, J. D., Torsional Influences within Disordered Organic Electronic Materials Based upon Non-Benzenoid 1,6-Methano[10]annulene Rings. *Macromolecules* **2012**, *45*, 7339-7349.

57. Wood, S.; Kim, J. H.; Hwang, D. H.; Kim, J. S., Effects of Fluorination and Side Chain Branching on Molecular Conformation and Photovoltaic Performance of Donor-Acceptor Copolymers. *Chem. Mater.* **2015**, *27*, 4196-4204.

58. Wang, Q.; Zhang, B.; Liu, L.; Chen, Y.; Qu, Y.; Zhang, X.; Yang, J.; Xie, Z.; Geng, Y.; Wang, L.; Wang, F., Effect of End Groups on Optoelectronic Properties of Poly(9,9-dioctylfluorene): A Study with Hexadecylfluorenes as Model Polymers. *J. Phys. Chem. C* **2012**, *116*, 21727-21733.

59. Asaoka, S.; Takeda, N.; Iyoda, T.; Cook, A. R.; Miller, J. R., Electron and Hole Transport To Trap Groups at the Ends of Conjugated Polyfluorenes. *J. Am. Chem. Soc.* **2008**, *130*, 11912-11920.

60. Koldemir, U.; Puniredd, S. R.; Wagner, M.; Tongay, S.; McCarley, T. D.; Kamenov, G. D.; Müllen, K.; Pisula, W.; Reynolds, J. R., End Capping Does Matter: Enhanced Order and Charge Transport in Conjugated Donor–Acceptor Polymers. *Macromolecules* **2015**, *48*, 6369-6377.

61. Grisorio, R.; Piliego, C.; Striccoli, M.; Cosma, P.; Fini, P.; Gigli, G.; Mastrorilli, P.; Suranna, G. P.; Nobile, C. F., Influence of Keto Groups on the Optical, Electronic, and Electroluminescent Properties of Random Fluorenone-Containing Poly(fluorenylene-vinylene)s. *J. Phys. Chem. C* **2008**, *112*, 20076-20087.

62. Lupton, J. M., On-chain defect emission in conjugated polymers - Comment on 'Exciton dissociation dynamics in a conjugated polymer containing aggregate states' - A. Haugeneder, U. Lemmer, U. Scherf, Chem. Phys. Lett. 351 (2002) 354. *Chem. Phys. Lett.* **2002**, *365*, 366-368.

63. Liu, L.; Yang, B.; Zhang, H.; Tang, S.; Xie, Z.; Wang, H.; Wang, Z.; Lu, P.; Ma, Y., Role of Tetrakis(triphenylphosphine)palladium(0) in the Degradation and Optical Properties of Fluorene-Based Compounds. *J. Phys. Chem. C* **2008**, *112*, 10273-10278.

64. Adachi, T.; Vogelsang, J.; Lupton, J. M., Unraveling the Electronic Heterogeneity of Charge Traps in Conjugated Polymers by Single-Molecule Spectroscopy. *J. Phys. Chem. Lett.* **2014**, *5*, 573-577.

65. Becker, K.; Lupton, J. M.; Feldmann, J.; Nehls, B. S.; Galbrecht, F.; Gao, D. Q.; Scherf, U., On-Chain Fluorenone Defect Emission from Single Polyfluorene Molecules in the Absence of Intermolecular Interactions. *Adv. Funct. Mater.* **2006**, *16*, 364-370.

66. Wang, B.; Forster, M.; Preis, E.; Wang, H.; Ma, Y.; Scherf, U., Simplified synthesis of spiro-bridged ladder-type poly(p-phenylene). *J. Polym. Sci., Part A: Polym. Chem.* **2009**, *47*, 5137-5143.

67. Simpson, C. D.; Brand, J. D.; Berresheim, A. J.; Przybilla, L.; Rader, H. J.; Mullen, K., Synthesis of a giant 222 carbon graphite sheet. *Chem. Eur. J.* **2002**, *8*, 1424-1429.

68. Narita, A.; Feng, X.; Hernandez, Y.; Jensen, S. A.; Bonn, M.; Yang, H.; Verzhbitskiy, I. A.; Casiraghi, C.; Hansen, M. R.; Koch, A. H. R.; Fytas, G.; Ivasenko,

O.; Li, B.; Mali, K. S.; Balandina, T.; Mahesh, S.; De Feyter, S.; Müllen, K., Synthesis of structurally well-defined and liquid-phase-processable graphene nanoribbons. *Nat. Chem.* **2014**, *6*, 126-132.

69. Kang, E.-H.; Lee, I.-H.; Choi, T.-L., Brush Polymers Containing Semiconducting Polyene Backbones: Graft-Through Synthesis via Cyclopolymerization and Conformational Analysis on the Coil-to-Rod Transition. *ACS Macro Lett.* **2012**, *1*, 1098-1102.

70. Liu, L.; Han, T.; Wu, X.; Qiu, S.; Wang, B.; Hanif, M.; Xie, Z.; Ma, Y., Aggregation Behaviors of Ladder-Type Poly(p-phenylene) in Dilute Solutions and Spin-Coated Films. *J. Phys. Chem. C* **2015**, *119*, 11833-11838.

71. Lee, J.; Han, A. R.; Yu, H.; Shin, T. J.; Yang, C.; Oh, J. H., Boosting the Ambipolar Performance of Solution-Processable Polymer Semiconductors via Hybrid Side-Chain Engineering. *J. Am. Chem. Soc.* **2013**, *135*, 9540-9547.

72. Lei, T.; Dou, J.-H.; Pei, J., Influence of Alkyl Chain Branching Positions on the Hole Mobilities of Polymer Thin-Film Transistors. *Adv. Mater.* **2012**, *24*, 6457-6461.

73. Lei, T.; Wang, J.-Y.; Pei, J., Design, Synthesis, and Structure–Property Relationships of Isoindigo-Based Conjugated Polymers. *Acc. Chem. Res.* **2014**, *47*, 1117-1126.

74. Mei, J.; Bao, Z., Side chain engineering in solution-processable conjugated polymers. *Chem. Mater.* **2013**, *26*, 604-615.

75. Guo, Z.-H.; Ai, N.; McBroom, C. R.; Yuan, T.; Lin, Y.-H.; Roders, M.; Zhu, C.; Ayzner, A. L.; Pei, J.; Fang, L., A side-chain engineering approach to solvent-resistant semiconducting polymer thin films. *Polym. Chem.* **2016**, *7*, 648-655.

76. Smith, Z. C.; Meyer, D. M.; Simon, M. G.; Staii, C.; Shukla, D.; Thomas, S. W., Thiophene-Based Conjugated Polymers with Photolabile Solubilizing Side Chains. *Macromolecules* **2015**, *48*, 959-966.

77. Zou, Y.; Ji, X.; Cai, J.; Yuan, T.; Stanton, D. J.; Lin, Y.-H.; Naraghi, M.; Fang, L., Synthesis and Solution Processing of a Hydrogen-Bonded Ladder Polymer. *Chem* **2017**, *2*, 139-152.

78. Godt, A.; Schlüter, A.-D., End group identification and molecular weight determination of a Diels-Alder ladder polymer. *Makromol. Chem.* **1992**, *193*, 501-506.

79. Hickl, P.; Ballauff, M.; Scherf, U.; Müllen, K.; Lindner, P., Characterization of a Ladder Polymer by Small-Angle X-ray and Neutron Scattering. *Macromolecules* **1997**, *30*, 273-279.

80. Wong, M.; Hollinger, J.; Kozycz, L. M.; McCormick, T. M.; Lu, Y.; Burns, D. C.; Seferos, D. S., An Apparent Size-Exclusion Quantification Limit Reveals a Molecular Weight Limit in the Synthesis of Externally Initiated Polythiophenes. *ACS Macro Lett.* **2012**, *1*, 1266-1269.

81. März, K.; Lindner, P.; Urban, G.; Ballauff, M.; Kugler, J.; Fischer, E. W., Conformation and shape of rigid-rod polyesters substituted with flexible side chains as revealed by small-angle neutron scattering. *Acta Polym.* **1993**, *44*, 139-147.

82. Liu, T.; Xiao, Z., Dynamic Light Scattering of Rigid Rods – A Universal Relationship on the Apparent Diffusion Coefficient as Revealed by Numerical Studies and Its Use for Rod Length Determination. *Macromol. Chem. Phys.* **2012**, *213*, 1697-1705.

83. Trachtenberg, S.; Hammel, I., Determining the persistence length of biopolymers and rod-like macromolecular assemblies from electron microscope images and deriving some of their mechanical properties. In *Microscopy: Science, Technology, Applications, and Education*, Méndez-Vilas, A. D., J. , Ed. 2010; Vol. 3, pp 1690-1695.

84. Shetty, A. M.; Wilkins, G. M. H.; Nanda, J.; Solomon, M. J., Multiangle Depolarized Dynamic Light Scattering of Short Functionalized Single-Walled Carbon Nanotubes. *J. Phys. Chem. C* **2009**, *113*, 7129-7133.

85. Su, W.-F., Polymer Size and Polymer Solutions. In *Principles of Polymer Design and Synthesis*, Springer Berlin Heidelberg: Berlin, Heidelberg, 2013, pp 9-26.

86. Ebdon, J. R., *Introduction to polymers*. 2nd ed.; John Wiley & Sons, Ltd: London, 1992; Vol. 27, p 207-208.

87. Striegel, A. M., Viscometric Detection in Size-Exclusion Chromatography: Principles and Select Applications. *Chromatographia* **2016**, *79*, 945-960.

88. Vanhee, S.; Rulkens, R.; Lehmann, U.; Rosenauer, C.; Schulze, M.; Köhler, W.; Wegner, G., Synthesis and Characterization of Rigid Rod Poly(p-phenylenes). *Macromolecules* **1996**, *29*, 5136-5142.

89. Molina, R.; Gómez-Ruiz, S.; Montilla, F.; Salinas-Castillo, A.; Fernández-Arroyo, S.; Ramos, M. d. M.; Micol, V.; Mallavia, R., Progress in the Synthesis of

Poly(2,7-Fluorene-alt-1,4-Phenylene), PFP, via Suzuki Coupling. *Macromolecules* **2009**, *42*, 5471-5477.

90. Cotts, P. M.; Swager, T. M.; Zhou, Q., Equilibrium Flexibility of a Rigid Linear Conjugated Polymer. *Macromolecules* **1996**, *29*, 7323-7328.

91. Gao, B.; Wang, M.; Cheng, Y.; Wang, L.; Jing, X.; Wang, F., Pyrazine-Containing Acene-Type Molecular Ribbons with up to 16 Rectilinearly Arranged Fused Aromatic Rings. *J. Am. Chem. Soc.* **2008**, *130*, 8297-8306.

92. Collison, C. J.; Rothberg, L. J.; Treemaneekarn, V.; Li, Y., Conformational Effects on the Photophysics of Conjugated Polymers: A Two Species Model for MEH−PPV Spectroscopy and Dynamics. *Macromolecules* **2001**, *34*, 2346-2352.

93. Dudenko, D.; Kiersnowski, A.; Shu, J.; Pisula, W.; Sebastiani, D.; Spiess, H. W.; Hansen, M. R., A Strategy for Revealing the Packing in Semicrystalline π-Conjugated Polymers: Crystal Structure of Bulk Poly-3-hexyl-thiophene (P3HT). *Angew. Chem. Int. Ed.* **2012**, *51*, 11068-11072.

94. Chen, L.; Hernandez, Y.; Feng, X.; Müllen, K., From Nanographene and Graphene Nanoribbons to Graphene Sheets: Chemical Synthesis. *Angew. Chem. Int. Ed.* **2012**, *51*, 7640-7654.

95. Han, M. Y.; Özyilmaz, B.; Zhang, Y.; Kim, P., Energy Band-Gap Engineering of Graphene Nanoribbons. *Phys. Rev. Lett.* **2007**, *98*, 206805.

96. Grimsdale, A. C.; Chan, K. L.; Martin, R. E.; Jokisz, P. G.; Holmes, A. B., Synthesis of Light-Emitting Conjugated Polymers for Applications in Electroluminescent Devices. *Chem. Rev.* **2009**, *109*, 897-1091.

97. Kallinger, C.; Hilmer, M.; Haugeneder, A.; Perner, M.; Spirkl, W.; Lemmer, U.; Feldmann, J.; Scherf, U.; Müllen, K.; Gombert, A.; Wittwer, V., A Flexible Conjugated Polymer Laser. *Adv. Mater.* **1998**, *10*, 920-923.

98. Tsuda, A.; Osuka, A., Fully Conjugated Porphyrin Tapes with Electronic Absorption Bands That Reach into Infrared. *Science* **2001**, *293*, 79-82.

99. Tanaka, T.; Osuka, A., Conjugated porphyrin arrays: synthesis, properties and applications for functional materials. *Chem. Soc. Rev.* **2015**, *44*, 943-969.

100. Jenekhe, S. A.; Tibbetts, S. J., Ion implantation doping and electrical properties of high-temperature ladder polymers. *J. Polym. Sci., Part B: Polym. Phys.* **1988**, *26*, 201-209.

101. Bao, Z., Materials and Fabrication Needs for Low-Cost Organic Transistor Circuits. *Adv. Mater.* **2000**, *12*, 227-230.

102. Briseno, A. L.; Kim, F. S.; Babel, A.; Xia, Y. N.; Jenekhe, S. A., n-Channel polymer thin film transistors with long-term air-stability and durability and their use in complementary inverters. *J. Mater. Chem.* **2011**, *21*, 16461-16466.

103. Bornoz, P.; Prévot, M. S.; Yu, X.; Guijarro, N.; Sivula, K., Direct Light-Driven Water Oxidation by a Ladder-Type Conjugated Polymer Photoanode. *J. Am. Chem. Soc.* **2015**, *137*, 15338-15341.

104. Wang, S.; Sun, H.; Ail, U.; Vagin, M.; Persson, P. O. Å.; Andreasen, J. W.; Thiel, W.; Berggren, M.; Crispin, X.; Fazzi, D.; Fabiano, S., Thermoelectric Properties of Solution-Processed n-Doped Ladder-Type Conducting Polymers. *Adv. Mater.* **2016**, *28*, 10764-10771.

105. Xie, J.; Rui, X.; Gu, P.; Wu, J.; Xu, Z. J.; Yan, Q.; Zhang, Q., Novel Conjugated Ladder-Structured Oligomer Anode with High Lithium Storage and Long Cycling Capability. *ACS Appl. Mater. Interfaces* **2016**, *8*, 16932-16938.

106. Wang, L.; He, X.; Sun, W.; Li, J.; Gao, J.; Tian, G.; Wang, J.; Fan, S., Organic polymer material with a multi-electron process redox reaction: towards ultra-high reversible lithium storage capacity. *RSC Adv.* **2013**, *3*, 3227-3231.

107. Wu, J.; Rui, X.; Wang, C.; Pei, W.-B.; Lau, R.; Yan, Q.; Zhang, Q., Nanostructured Conjugated Ladder Polymers for Stable and Fast Lithium Storage Anodes with High-Capacity. *Adv. Energy Mater.* **2015**, *5*, 1402189.

108. Wu, J.; Rui, X.; Long, G.; Chen, W.; Yan, Q.; Zhang, Q., Pushing Up Lithium Storage through Nanostructured Polyazaacene Analogues as Anode. *Angew. Chem. Int. Ed.* **2015**, *54*, 7354-7358.

109. Treacy, M. M. J.; Ebbesen, T. W.; Gibson, J. M., Exceptionally high Young's modulus observed for individual carbon nanotubes. *Nature* **1996**, *381*, 678-680.

110. Lee, C.; Wei, X. D.; Kysar, J. W.; Hone, J., Measurement of the elastic properties and intrinsic strength of monolayer graphene. *Science* **2008**, *321*, 385-388.

111. Tonshoff, C.; Bettinger, H. F., Photogeneration of Octacene and Nonacene. *Angew. Chem. Int. Ed.* **2010**, *49*, 4125-4128.

112. Nataraj, S. K.; Yang, K. S.; Aminabhavi, T. M., Polyacrylonitrile-based nanofibers A state-of-the-art review. *Prog. Polym. Sci.* **2012**, *37*, 487-513.

113. Dalton, S.; Heatley, F.; Budd, P. M., Thermal stabilization of polyacrylonitrile fibres. *Polymer* **1999**, *40*, 5531-5543.

114. Wu, J. S.; Cheng, S. W.; Cheng, Y. J.; Hsu, C. S., Donor-acceptor conjugated polymers based on multifused ladder-type arenes for organic solar cells. *Chem. Soc. Rev.* **2015**, *44*, 1113-1154.

115. Li, Y. X.; Yao, K.; Yip, H. L.; Ding, F. Z.; Xu, Y. X.; Li, X. S.; Chen, Y.; Jen, A. K. Y., Eleven-Membered Fused-Ring Low Band-Gap Polymer with Enhanced Charge Carrier Mobility and Photovoltaic Performance. *Adv. Funct. Mater.* **2014**, *24*, 3631-3638.

116. Plumhof, J. D.; Stoferle, T.; Mai, L.; Scherf, U.; Mahrt, R. F., Room-temperature Bose-Einstein condensation of cavity exciton-polaritons in a polymer. *Nat. Mater.* **2014**, *13*, 247-52.

117. Das, S.; Heasman, P.; Ben, T.; Qiu, S., Porous Organic Materials: Strategic Design and Structure–Function Correlation. *Chem. Rev.* **2017**, *117*, 1515-1563.

118. Wu, J.; Xu, F.; Li, S.; Ma, P.; Zhang, X.; Liu, Q.; Fu, R.; Wu, D., Porous Polymers as Multifunctional Material Platforms toward Task-Specific Applications. *Adv. Mater.* **2019**, *31*, 1802922.

119. Lohse, M. S.; Bein, T., Covalent Organic Frameworks: Structures, Synthesis, and Applications. *Adv. Funct. Mater.* **2018**, *28*, 1705553.

120. Feng, X.; Ding, X.; Jiang, D., Covalent organic frameworks. *Chem. Soc. Rev.* **2012**, *41*, 6010-6022.

121. Mittal, V., *Porous Polymer Networks*. Central West Publishing: 2019.

122. Lu, W.; Yuan, D.; Zhao, D.; Schilling, C. I.; Plietzsch, O.; Muller, T.; Bräse, S.; Guenther, J.; Blümel, J.; Krishna, R.; Li, Z.; Zhou, H.-C., Porous Polymer Networks:

Synthesis, Porosity, and Applications in Gas Storage/Separation. *Chem. Mater.* **2010**, *22*, 5964-5972.

123. Vermeulen, N. A.; Karagiaridi, O.; Sarjeant, A. A.; Stern, C. L.; Hupp, J. T.; Farha, O. K.; Stoddart, J. F., Aromatizing Olefin Metathesis by Ligand Isolation inside a Metal– Organic Framework. *J. Am. Chem. Soc.* **2013**, *135*, 14916-14919.

124. Kou, Y.; Xu, Y.; Guo, Z.; Jiang, D., Supercapacitive Energy Storage and Electric Power Supply Using an Aza-Fused π-Conjugated Microporous Framework. *Angew. Chem. Int. Ed.* **2011**, *50*, 8753-8757.

125. Guo, J.; Xu, Y.; Jin, S.; Chen, L.; Kaji, T.; Honsho, Y.; Addicoat, M. A.; Kim, J.; Saeki, A.; Ihee, H.; Seki, S.; Irle, S.; Hiramoto, M.; Gao, J.; Jiang, D., Conjugated organic framework with three-dimensionally ordered stable structure and delocalized π clouds. *Nat. Commun.* **2013**, *4*, 2736.

126. Sprick, R. S.; Thomas, A.; Scherf, U., Acid catalyzed synthesis of carbonyl-functionalized microporous ladder polymers with high surface area. *Polym. Chem.* **2010**, *1*, 283-285.

127. Buyukcakir, O.; Yuksel, R.; Jiang, Y.; Lee, S. H.; Seong, W. K.; Chen, X.; Ruoff, R. S., Synthesis of Porous Covalent Quinazoline Networks (CQNs) and Their Gas Sorption Properties. *Angew. Chem. Int. Ed.* **2019**, *58*, 872-876.

128. Ong, W. J.; Swager, T. M., Dynamic self-correcting nucleophilic aromatic substitution. *Nat. Chem.* **2018**, *10*, 1023-1030.

129. Guan, X.; Li, H.; Ma, Y.; Xue, M.; Fang, Q.; Yan, Y.; Valtchev, V.; Qiu, S., Chemically stable polyarylether-based covalent organic frameworks. *Nat. Chem.* **2019**, *11*, 587-594.

130. Wu, Y.; Hao, X.; Wu, J.; Jin, J.; Ba, X., Pure Blue-Light-Emitting Materials: Hyperbranched Ladder-Type Poly(p-phenylene)s Containing Truxene Units. *Macromolecules* **2010**, *43*, 731-738.

131. Bai, L.; Li, D.; Lu, H.; Wu, Y.; Ba, X.; Bo, Z., Facile Synthesis of Linear and Hyperbranched Ladder Poly(p-Phenylene)s without Structural Defects. *Macromol. Rapid Commun.* **2012**, *33*, 1787-1790.

132. Salleo, A., Charge transport in polymeric transistors. *Mater. Today* **2007**, *10*, 38-45.

133. Coropceanu, V.; Cornil, J.; da Silva Filho, D. A.; Olivier, Y.; Silbey, R.; Brédas, J.-L., Charge Transport in Organic Semiconductors. *Chem. Rev.* **2007**, *107*, 926-952.

134. Salomon, A.; Cahen, D.; Lindsay, S.; Tomfohr, J.; Engelkes, V. B.; Frisbie, C. D., Comparison of Electronic Transport Measurements on Organic Molecules. *Adv. Mater.* **2003**, *15*, 1881-1890.

135. Sirringhaus, H.; Brown, P. J.; Friend, R. H.; Nielsen, M. M.; Bechgaard, K.; Langeveld-Voss, B. M. W.; Spiering, A. J. H.; Janssen, R. A. J.; Meijer, E. W.; Herwig, P.; de Leeuw, D. M., Two-dimensional charge transport in self-organized, high-mobility conjugated polymers. *Nature* **1999**, *401*, 685-688.

136. Renaud, G.; Lazzari, R.; Leroy, F., Probing surface and interface morphology with Grazing Incidence Small Angle X-Ray Scattering. *Surf. Sci. Rep.* **2009**, *64*, 255-380.

137. Hexemer, A.; Muller-Buschbaum, P., Advanced grazing-incidence techniques for modern soft-matter materials analysis. *IUCrJ* **2015**, *2*, 106-125.

138. Müller-Buschbaum, P., A Basic Introduction to Grazing Incidence Small-Angle X-Ray Scattering. In *Applications of Synchrotron Light to Scattering and Diffraction in Materials and Life Sciences*, Gomez, M.; Nogales, A.; Garcia-Gutierrez, M. C.; Ezquerra, T. A., Eds. Springer Berlin Heidelberg: Berlin, Heidelberg, 2009, pp 61-89.

139. Richter, L. J.; DeLongchamp, D. M.; Amassian, A., Morphology Development in Solution-Processed Functional Organic Blend Films: An In Situ Viewpoint. *Chem. Rev.* **2017**, *117*, 6332-6366.

140. Baker, J. L.; Jimison, L. H.; Mannsfeld, S.; Volkman, S.; Yin, S.; Subramanian, V.; Salleo, A.; Alivisatos, A. P.; Toney, M. F., Quantification of Thin Film Crystallographic Orientation Using X-ray Diffraction with an Area Detector. *Langmuir* **2010**, *26*, 9146-9151.

141. Bheemireddy, S. R.; Hautzinger, M. P.; Li, T.; Lee, B.; Plunkett, K. N., Conjugated Ladder Polymers by a Cyclopentannulation Polymerization. *J. Am. Chem. Soc.* **2017**, *139*, 5801-5807.

142. Kraner, S.; Koerner, C.; Leo, K.; Bittrich, E.; Eichhorn, K. J.; Karpov, Y.; Kiriy, A.; Stamm, M.; Hinrichs, K.; Al-Hussein, M., Dielectric function of a poly(benzimidazobenzophenanthroline) ladder polymer. *Phys. Rev. B* **2015**, *91*, 195202.

143. Lee, J.; Kalin, A. J.; Yuan, T.; Al-Hashimi, M.; Fang, L., Fully conjugated ladder polymers. *Chem. Sci.* **2017**, *8*, 2503-2521.

144. Teo, Y. C.; Lai, H. W. H.; Xia, Y., Synthesis of Ladder Polymers: Developments, Challenges, and Opportunities. *Chem. Eur. J.* **2017**, *23*, 14101-14112.

145. Zhu, C.; Fang, L., Locking the Coplanar Conformation of π-Conjugated Molecules and Macromolecules Using Dynamic Noncovalent Bonds. *Macromol. Rapid Commun.* **2018**, *39*, 1700241.

146. Son, Y.-W.; Cohen, M. L.; Louie, S. G., Half-metallic graphene nanoribbons. *Nature* **2006**, *444*, 347-349.

147. Li, X.; Wang, X.; Zhang, L.; Lee, S.; Dai, H., Chemically Derived, Ultrasmooth Graphene Nanoribbon Semiconductors. *Science* **2008**, *319*, 1229.

148. Yang, W.; Lucotti, A.; Tommasini, M.; Chalifoux, W. A., Bottom-Up Synthesis of Soluble and Narrow Graphene Nanoribbons Using Alkyne Benzannulations. *J. Am. Chem. Soc.* **2016**, *138*, 9137-9144.

149. Cheng, Y.-J.; Yang, S.-H.; Hsu, C.-S., Synthesis of Conjugated Polymers for Organic Solar Cell Applications. *Chem. Rev.* **2009**, *109*, 5868-5923.

150. Lu, L.; Zheng, T.; Wu, Q.; Schneider, A. M.; Zhao, D.; Yu, L., Recent Advances in Bulk Heterojunction Polymer Solar Cells. *Chem. Rev.* **2015**, *115*, 12666-12731.

151. Kass, K.-J.; Forster, M.; Scherf, U., Incorporating an Alternating Donor–Acceptor Structure into a Ladder Polymer Backbone. *Angew. Chem. Int. Ed.* **2016**, *55*, 7816-7820.

152. Dierschke, F.; Grimsdale, A. C.; Müllen, K., Novel Carbazole-Based Ladder-Type Polymers for Electronic Applications. *Macromol. Chem. Phys.* **2004**, *205*, 1147-1154.

153. Zhai, L.; Shukla, R.; Wadumethrige, S. H.; Rathore, R., Probing the Arenium-Ion (ProtonTransfer) versus the Cation-Radical (Electron Transfer) Mechanism of Scholl Reaction Using DDQ as Oxidant. *J. Org. Chem.* **2010**, *75*, 4748-4760.

154. Hayashi, R.; Cook, G. R., Remarkably Mild and Efficient Intramolecular Friedel−Crafts Cyclization Catalyzed by In(III). *Org. Lett.* **2007**, *9*, 1311-1314.

155. Bandini, M.; Tragni, M.; Umani-Ronchi, A., Iron(III)-Catalyzed Intramolecular Friedel–Crafts Alkylation of Electron-Deficient Arenes with π-Activated Alcohols. *Adv. Synth. Catal.* **2009**, *351*, 2521-2524.

156. Lee, J.; Li, H.; Kalin, A. J.; Yuan, T.; Wang, C.; Olson, T.; Li, H.; Fang, L., Extended Ladder-Type Benzo[k]tetraphene-Derived Oligomers. *Angew. Chem. Int. Ed.* **2017**, *56*, 13727-13731.

157. Iuliano, A.; Piccioli, P.; Fabbri, D., Ring-Closing Olefin Metathesis of 2,2‘-Divinylbiphenyls: A Novel and General Approach to Phenanthrenes. *Org. Lett.* **2004**, *6*, 3711-3714.

158. Trnka, T. M.; Grubbs, R. H., The Development of L2X2RuCHR Olefin Metathesis Catalysts: An Organometallic Success Story. *Acc. Chem. Res.* **2001**, *34*, 18-29.

159. Li, Y.; Wu, Y.; Gardner, S.; Ong, B. S., Novel Peripherally Substituted Indolo[3,2-b]carbazoles for High-Mobility Organic Thin-Film Transistors. *Adv. Mater.* **2005**, *17*, 849-853.

160. Yoon, K.-J.; Park, J. S.; Lee, S.-J.; Song, M.; Shin, I. A.; Lee, J. W.; Gal, Y.-S.; Jin, S.-H., Synthesis and characterization of fluorene-based copolymers containing

benzothiadiazole derivative for light-emitting diodes applications. *J. Polym. Sci., Part A: Polym. Chem.* **2008**, *46*, 6762-6769.

161. Kumar, S.; Saravanan, S.; Reuben, P.; Kumar, A., Synthesis of trans-dihydrodiol derivatives of phenanthro[3,4-b]-thiophene and phenanthro[4,3-b]thiophene. *J. Heterocycl. Chem.* **2005**, *42*, 1345-1355.

162. Hollingsworth, W. R.; Lee, J.; Fang, L.; Ayzner, A. L., Exciton Relaxation in Highly Rigid Conjugated Polymers: Correlating Radiative Dynamics with Structural Heterogeneity and Wavefunction Delocalization. *ACS Energy Lett.* **2017**, *2*, 2096-2102.

163. Dutta, T.; Woody, K. B.; Parkin, S. R.; Watson, M. D.; Gierschner, J., Conjugated Polymers with Large Effective Stokes Shift: Benzobisdioxole-Based Poly(phenylene ethynylene)s. *J. Am. Chem. Soc.* **2009**, *131*, 17321-17327.

164. Oh, J. H.; Lee, W.-Y.; Noe, T.; Chen, W.-C.; Könemann, M.; Bao, Z., Solution-Shear-Processed Quaterrylene Diimide Thin-Film Transistors Prepared by Pressure-Assisted Thermal Cleavage of Swallow Tails. *J. Am. Chem. Soc.* **2011**, *133*, 4204-4207.

165. Jiang, Z.; Li, X.; Strzalka, J.; Sprung, M.; Sun, T.; Sandy, A. R.; Narayanan, S.; Lee, D. R.; Wang, J., The dedicated high-resolution grazing-incidence X-ray scattering beamline 8-ID-E at the Advanced Photon Source. *J. Synchotron Rad.* **2012**, *19*, 627-636.

166. Jiang, Z., GIXSGUI: a MATLAB toolbox for grazing-incidence X-ray scattering data visualization and reduction, and indexing of buried three-dimensional periodic nanostructured films. *J. Appl. Crystallogr.* **2015**, *48*, 917-926.

167. Wu, D.; Xu, F.; Sun, B.; Fu, R.; He, H.; Matyjaszewski, K., Design and Preparation of Porous Polymers. *Chem. Rev.* **2012**, *112*, 3959-4015.

168. Peng, Y.; Krungleviciute, V.; Eryazici, I.; Hupp, J. T.; Farha, O. K.; Yildirim, T., Methane storage in metal-organic frameworks: current records, surprise findings, and challenges. *J. Am. Chem. Soc.* **2013**, *135*, 11887-11894.

169. Li, B.; Wen, H.-M.; Zhou, W.; Xu, Jeff Q.; Chen, B., Porous Metal-Organic Frameworks: Promising Materials for Methane Storage. *Chem* **2016**, *1*, 557-580.

170. Mason, J. A.; Oktawiec, J.; Taylor, M. K.; Hudson, M. R.; Rodriguez, J.; Bachman, J. E.; Gonzalez, M. I.; Cervellino, A.; Guagliardi, A.; Brown, C. M.; Llewellyn, P. L.; Masciocchi, N.; Long, J. R., Methane storage in flexible metal-organic frameworks with intrinsic thermal management. *Nature* **2015**, *527*, 357-361.

171. Zhang, Y. B.; Furukawa, H.; Ko, N.; Nie, W.; Park, H. J.; Okajima, S.; Cordova, K. E.; Deng, H.; Kim, J.; Yaghi, O. M., Introduction of functionality, selection of topology, and enhancement of gas adsorption in multivariate metal-organic framework-177. *J. Am. Chem. Soc.* **2015**, *137*, 2641-2650.

172. Rowland, C. A.; Lorzing, G. R.; Gosselin, E. J.; Trump, B. A.; Yap, G. P. A.; Brown, C. M.; Bloch, E. D., Methane Storage in Paddlewheel-Based Porous Coordination Cages. *J. Am. Chem. Soc.* **2018**, *140*, 11153-11157.

173. Jia, J.; Chen, Z.; Jiang, H.; Belmabkhout, Y.; Mouchaham, G.; Aggarwal, H.; Adil, K.; Abou-Hamad, E.; Czaban-Jóźwiak, J.; Tchalala, M. R.; Eddaoudi, M., Extremely Hydrophobic POPs to Access Highly Porous Storage Media and Capturing Agent for Organic Vapors. *Chem* **2019**, *5*, 180-191.

174. Yuan, D.; Lu, W.; Zhao, D.; Zhou, H. C., Highly stable porous polymer networks with exceptionally high gas-uptake capacities. *Adv. Mater.* **2011**, *23*, 3723-3725.

175. Wilmer, C. E.; Leaf, M.; Lee, C. Y.; Farha, O. K.; Hauser, B. G.; Hupp, J. T.; Snurr, R. Q., Large-scale screening of hypothetical metal-organic frameworks. *Nat. Chem.* **2011**, *4*, 83-89.

176. Guo, Z.; Wu, H.; Srinivas, G.; Zhou, Y.; Xiang, S.; Chen, Z.; Yang, Y.; Zhou, W.; O'Keeffe, M.; Chen, B., A metal-organic framework with optimized open metal sites and pore spaces for high methane storage at room temperature. *Angew. Chem. Int. Ed.* **2011**, *50*, 3178-3181.

177. Jiang, J.; Furukawa, H.; Zhang, Y. B.; Yaghi, O. M., High Methane Storage Working Capacity in Metal-Organic Frameworks with Acrylate Links. *J. Am. Chem. Soc.* **2016**, *138*, 10244-10251.

178. Savage, M.; da Silva, I.; Johnson, M.; Carter, J. H.; Newby, R.; Suyetin, M.; Besley, E.; Manuel, P.; Rudic, S.; Fitch, A. N.; Murray, C.; David, W. I.; Yang, S.; Schroder, M., Observation of Binding and Rotation of Methane and Hydrogen within a Functional Metal-Organic Framework. *J. Am. Chem. Soc.* **2016**, *138*, 9119-9127.

179. Zhu, C.; Kalin, A. J.; Fang, L., Covalent and Noncovalent Approaches to Rigid Coplanar pi-Conjugated Molecules and Macromolecules. *Acc. Chem. Res.* **2019**, *52*, 1089-1100.

180. DeBlase, C. R.; Dichtel, W. R., Moving Beyond Boron: The Emergence of New Linkage Chemistries in Covalent Organic Frameworks. *Macromolecules* **2016**, *49*, 5297-5305.

181. Ma, S.; Sun, D.; Simmons, J. M.; Collier, C. D.; Yuan, D.; Zhou, H. C., Metal-organic framework from an anthracene derivative containing nanoscopic cages exhibiting high methane uptake. *J. Am. Chem. Soc.* **2008**, *130*, 1012-1016.

182. Düren, T.; Sarkisov, L.; Yaghi, O. M.; Snurr, R. Q., Design of New Materials for Methane Storage. *Langmuir* **2004**, *20*, 2683-2689.

183. Lu, W.; Wei, Z.; Yuan, D.; Tian, J.; Fordham, S.; Zhou, H.-C., Rational Design and Synthesis of Porous Polymer Networks: Toward High Surface Area. *Chem. Mater.* **2014**, *26*, 4589-4597.

184. Ben, T.; Ren, H.; Ma, S.; Cao, D.; Lan, J.; Jing, X.; Wang, W.; Xu, J.; Deng, F.; Simmons, J. M.; Qiu, S.; Zhu, G., Targeted synthesis of a porous aromatic framework with high stability and exceptionally high surface area. *Angew. Chem. Int. Ed.* **2009**, *48*, 9457-9460.

185. Dawson, R.; Stevens, L. A.; Drage, T. C.; Snape, C. E.; Smith, M. W.; Adams, D. J.; Cooper, A. I., Impact of water coadsorption for carbon dioxide capture in microporous polymer sorbents. *J. Am. Chem. Soc.* **2012**, *134*, 10741-10744.

186. Zhu, Y.; Yang, H.; Jin, Y.; Zhang, W., Porous Poly(aryleneethynylene) Networks through Alkyne Metathesis. *Chem. Mater.* **2013**, *25*, 3718-3723.

187. Ma, L.; Liu, Y.; Liu, Y.; Jiang, S.; Li, P.; Hao, Y.; Shao, P.; Yin, A.; Feng, X.; Wang, B., Ferrocene-Linkage-Facilitated Charge Separation in Conjugated Microporous Polymers. *Angew. Chem. Int. Ed.* **2019**, *58*, 4221-4226.

188. Lee, J.; Buyukcakir, O.; Kwon, T. W.; Coskun, A., Energy Band-Gap Engineering of Conjugated Microporous Polymers via Acidity-Dependent in Situ Cyclization. *J. Am. Chem. Soc.* **2018**, *140*, 10937-10940.

189. Goubard, F.; Dumur, F., Truxene: a promising scaffold for future materials. *RSC Adv.* **2015**, *5*, 3521-3551.

190. Lee, J.; Kalin, A. J.; Wang, C.; Early, J. T.; Al-Hashimi, M.; Fang, L., Donor-acceptor conjugated ladder polymer via aromatization-driven thermodynamic annulation. *Polym. Chem.* **2018**, *9*, 1603-1609.

191. Wang, C.; Li, C.; Rutledge, E. R. C.; Che, S.; Lee, J.; Kalin, A. J.; Zhang, C.; Zhou, H.-C.; Guo, Z.-H.; Fang, L., Aromatic porous polymer network membranes for organic solvent nanofiltration under extreme conditions. *J. Mater. Chem. A* **2019**, 10.1039/C9TA10190J.

192. Guo, Z.-H.; Wang, C.; Zhang, Q.; Che, S.; Zhou, H.-C.; Fang, L., Cost-effective synthesis and solution processing of porous polymer networks through methanesulfonic acid-mediated aldol triple condensation. *Mater. Chem. Front.* **2018**, *2*, 396-401.

193. Amick, A. W.; Scott, L. T., Trisannulated Benzene Derivatives by Acid Catalyzed Aldol Cyclotrimerizations of Cyclic Ketones. Methodology Development and Mechanistic Insight. *J. Org. Chem.* **2007**, *72*, 3412-3418.

194. Nicolaou, K. C.; Montagnon, T.; Baran, P. S.; Zhong, Y. L., Iodine(V) Reagents in Organic Synthesis. Part 4. o-Iodoxybenzoic Acid as a Chemospecific Tool for Single Electron Transfer-Based Oxidation Processes. *J. Am. Chem. Soc.* **2002**, *124*, 2245-2258.

195. Blog Syn #003: Benzylic Oxidation of Arylmethanes by IBX. http://blog-syn.blogspot.com/2013/02/blog-syn-003-benzylic-oxidation-of_18.html (accessed December 20).

196. Shuntaro, M.; Guo-Bin, L.; Tsuyoshi, S.; Masayoshi, K.; Masashi, T., Photothermal Side-Chain Bromination of Methyl-, Dimethyl-, and Trimethylbenzenes with N-Bromosuccinimide. *Bull. Chem. Soc. Jpn.* **1994**, *67*, 1113-1119.

197. Li, W.; Li, J.; DeVincentis, D.; Mansour, T. S., Oxygen transfer from sulfoxide: formation of aromatic aldehydes from dihalomethylarenes. *Tetrahedron Lett.* **2004**, *45*, 1071-1074.

198. Che, S.; Pang, J.; Kalin, A. J.; Wang, C.; Ji, X.; Lee, J.; Cole, D.; Li, J.-L.; Tu, X.; Zhang, Q.; Zhou, H.-C.; Fang, L., Rigid Ladder-Type Porous Polymer Networks for Entropically Favorable Gas Adsorption. *ACS Materials Lett.* **2019**, *2*, 49-54.

199. Zhu, C.; Kalin, A. J.; Fang, L., Covalent and Noncovalent Approaches to Rigid Coplanar π-Conjugated Molecules and Macromolecules. *Acc. Chem. Res.* **2019**, *52*, 1089-1100.

200. Jin, Y.; Qiao, J.-A.; Liu, C.; Luo, L.; Chi, X.; Zhang, Y.; Zeng, M.-H., Charge Transfer and Delocalization in Ladder-Type Fused Bithiophene Imide Oligomers. *J. Phys. Chem. C* **2019**, *123*, 20093-20104.

201. Lu, Y.; Yu, Z.-D.; Zhang, R.-Z.; Yao, Z.-F.; You, H.-Y.; Jiang, L.; Un, H.-I.; Dong, B.-W.; Xiong, M.; Wang, J.-Y.; Pei, J., Rigid Coplanar Polymers for Stable n-Type Polymer Thermoelectrics. *Angew. Chem. Int. Ed.* **2019**, *58*, 11390-11394.

202. Sui, Y.; Deng, Y.; Du, T.; Shi, Y.; Geng, Y., Design strategies of n-type conjugated polymers for organic thin-film transistors. *Mater. Chem. Front.* **2019**, *3*, 1932-1951.

203. Wang, Y.; Guo, H.; Ling, S.; Arrechea-Marcos, I.; Wang, Y.; López Navarrete, J. T.; Ortiz, R. P.; Guo, X., Ladder-type Heteroarenes: Up to 15 Rings with Five Imide Groups. *Angew. Chem. Int. Ed.* **2017**, *56*, 9924-9929.

204. McKeown, N. B.; Budd, P. M., Polymers of intrinsic microporosity (PIMs): organic materials for membrane separations, heterogeneous catalysis and hydrogen storage. *Chem. Soc. Rev.* **2006**, *35*, 675-683.

205. Zhang, B.; Wei, M.; Mao, H.; Pei, X.; Alshmimri, S. A.; Reimer, J. A.; Yaghi, O. M., Crystalline Dioxin-Linked Covalent Organic Frameworks from Irreversible Reactions. *J. Am. Chem. Soc.* **2018**, *140*, 12715-12719.

206. Lei, T.; Wang, J.-Y.; Pei, J., Roles of Flexible Chains in Organic Semiconducting Materials. *Chem. Mater.* **2014**, *26*, 594-603.

207. Lin, C. F.; Su, W. F.; Wu, C. I.; Cheng, I. C., *Organic, Inorganic and Hybrid Solar Cells: Principles and Practice*. Wiley-IEEE Press: 2012.

208. Nagamatsu, S.; Pandey, S. S.; Takashima, W.; Endo, T.; Rikukawa, M.; Kaneto, K., Photocarrier transport in processable poly(3-alkylthiophene). *Synth. Met.* **2001**, *121*, 1563-1564.

209. Liu, X.; Xu, Y.; Jiang, D., Conjugated Microporous Polymers as Molecular Sensing Devices: Microporous Architecture Enables Rapid Response and Enhances

Sensitivity in Fluorescence-On and Fluorescence-Off Sensing. *J. Am. Chem. Soc.* **2012**, *134*, 8738-8741.

210. Novotney, J. L.; Dichtel, W. R., Conjugated Porous Polymers For TNT Vapor Detection. *ACS Macro Lett.* **2013**, *2*, 423-426.

211. Chaoui, N.; Trunk, M.; Dawson, R.; Schmidt, J.; Thomas, A., Trends and challenges for microporous polymers. *Chem. Soc. Rev.* **2017**, *46*, 3302-3321.

212. Liu, C.; Dong, S.; Cai, P.; Liu, P.; Liu, S.; Chen, J.; Liu, F.; Ying, L.; Russell, T. P.; Huang, F.; Cao, Y., Donor–Acceptor Copolymers Based on Thermally Cleavable Indigo, Isoindigo, and DPP Units: Synthesis, Field Effect Transistors, and Polymer Solar Cells. *ACS Appl. Mater. Interfaces* **2015**, *7*, 9038-9051.

213. Zhang, H.; Yang, K.; Chen, Y.-M.; Bhatta, R.; Tsige, M.; Cheng, S. Z. D.; Zhu, Y., Polymers Based on Benzodipyrrolidone and Naphthodipyrrolidone with Latent Hydrogen-Bonding on the Main Chain. *Macromol. Chem. Phys.* **2017**, *218*, 1600617.

214. Narita, A.; Chen, Z.; Chen, Q.; Müllen, K., Solution and on-surface synthesis of structurally defined graphene nanoribbons as a new family of semiconductors. *Chem. Sci.* **2019**, *10*, 964-975.

215. Janietz, S.; Sainova, D., Significant Improvement of the Processability of Ladder-Type Polymers by Using Aqueous Colloidal Dispersions. *Macromol. Rapid Commun.* **2006**, *27*, 943-947.

216. Teo, Y. C.; Lai, H. W. H.; Xia, Y., Arm-degradable star polymers with crosslinked ladder-motif cores as a route to soluble microporous nanoparticles. *Polym. Chem.* **2019**, *11*, 265-269.

217. Feng, X.; Lv, F.; Liu, L.; Tang, H.; Xing, C.; Yang, Q.; Wang, S., Conjugated Polymer Nanoparticles for Drug Delivery and Imaging. *ACS Appl. Mater. Interfaces* **2010**, *2*, 2429-2435.

218. Tuncel, D.; Demir, H. V., Conjugated polymer nanoparticles. *Nanoscale* **2010**, *2*, 484-494.

219. Chen, J.-T.; Hsu, C.-S., Conjugated polymer nanostructures for organic solar cell applications. *Polym. Chem.* **2011**, *2*, 2707-2722.

220. Li, K.; Liu, B., Polymer-encapsulated organic nanoparticles for fluorescence and photoacoustic imaging. *Chem. Soc. Rev.* **2014**, *43*, 6570-6597.

221. Cai, X.; Bandla, A.; Chuan, C. K.; Magarajah, G.; Liao, L.-D.; Teh, D. B. L.; Kennedy, B. K.; Thakor, N. V.; Liu, B., Identifying glioblastoma margins using dual-targeted organic nanoparticles for efficient in vivo fluorescence image-guided photothermal therapy. *Mater. Horiz.* **2019**, *6*, 311-317.

222. Slomkowski, S.; Alemán José, V.; Gilbert Robert, G.; Hess, M.; Horie, K.; Jones Richard, G.; Kubisa, P.; Meisel, I.; Mormann, W.; Penczek, S.; Stepto Robert, F. T., Terminology of polymers and polymerization processes in dispersed systems (IUPAC Recommendations 2011). *Pure Appl. Chem.* **2011**, *83*, 2229.

223. Pecher, J.; Mecking, S., Nanoparticles of Conjugated Polymers. *Chem. Rev.* **2010**, *110*, 6260-6279.

224. Pallavi, P.; Bandyopadhyay, S.; Louis, J.; Deshmukh, A.; Patra, A., A soluble conjugated porous organic polymer: efficient white light emission in solution, nanoparticles, gel and transparent thin film. *Chem. Commun.* **2017**, *53*, 1257-1260.

225. Deshmukh, A.; Bandyopadhyay, S.; James, A.; Patra, A., Trace level detection of nitroanilines using a solution processable fluorescent porous organic polymer. *J. Mater. Chem. C* **2016**, *4*, 4427-4433.

226. Bandyopadhyay, S.; Pallavi, P.; Anil, A. G.; Patra, A., Fabrication of porous organic polymers in the form of powder, soluble in organic solvents and nanoparticles: a unique platform for gas adsorption and efficient chemosensing. *Polym. Chem.* **2015**, *6*, 3775-3780.

227. Patra, A.; Koenen, J.-M.; Scherf, U., Fluorescent nanoparticles based on a microporous organic polymer network: fabrication and efficient energy transfer to surface-bound dyes. *Chem. Commun.* **2011**, *47*, 9612-9614.

228. Kalin, A. J.; Lee, J.; Fang, L., Annulation Reactions for Conjugated Ladder-Type Oligomers. *Synlett* **2018**, *29*, 993-998.

229. Hoffmann, I.; Blumenröder, B.; Onodi neé Thumann, S.; Dommer, S.; Schatz, J., Suzuki cross-coupling in aqueous media. *Green Chem,* **2015**, *17*, 3844-3857.

230. Xu, Y.; Wu, X.; Chen, Y.; Hang, H.; Tong, H.; Wang, L., Fiber-optic detection of nitroaromatic explosives with solution-processable triazatruxene-based hyperbranched conjugated polymer nanoparticles. *Polym. Chem.* **2016**, *7*, 4542-4548.

231. Li, H.; Wu, X.; Xu, Y.; Tong, H.; Wang, L., Dicyanovinyl-functionalized fluorescent hyperbranched conjugated polymer nanoparticles for sensitive naked-eye cyanide ion detection. *Polym. Chem.* **2014**, *5*, 5949-5956.

232. Li, H.; Wu, X.; Xu, B.; Tong, H.; Wang, L., Solution-processible hyperbranched conjugated polymer nanoparticles with tunable particle sizes by Suzuki polymerization in miniemulsion. *RSC Adv.* **2013**, *3*, 8645-8648.

233. Thompson, J. M., *Infrared Spectroscopy*. Pan Stanford Publishing: Milton, United Kingdom, 2018.

234. Stuart, B. H., *Infrared Spectroscopy: Fundamentals and Applications*. John Wiley & Sons, Incorporated: Hoboken, United Kingdom, 2004.

235. Larkin, P., *Infrared and Raman Spectroscopy: Principles and Spectral Interpretation*. Elsevier: Saint Louis, United States, 2017.

236. Stampfl, J.; Graupner, W.; Leising, G.; Scherf, U., Photoluminescence and UV-VIS absorption study of poly (para-phenylene)-type ladder-polymers. *J. Lumin.* **1995**, *63*, 117-123.

237. Shen, X.; Wu, Y.; Bai, L.; Zhao, H.; Ba, X., Microwave-assisted synthesis of 4,9-linked pyrene-based ladder conjugated polymers. *J. Polym. Sci., Part A: Polym. Chem.* **2017**, *55*, 1285-1288.

238. Xue, T. J.; McKinney, M. A.; Wilkie, C. A., The thermal degradation of polyacrylonitrile. *Polym. Degrad. Stab.* **1997**, *58*, 193-202.

239. Liu, F.; Wu, Y.; Wang, C.; Ma, J.; Wu, F.; Zhang, Y.; Ba, X., Synthesis and Characterization of Fully Conjugated Ladder Naphthalene Bisimide Copolymers. *Polymers* **2018**, *10*, 790.

240. Wu, W.; Liu, Y.; Zhu, D., π-Conjugated molecules with fused rings for organic field-effect transistors: design, synthesis and applications. *Chem. Soc. Rev.* **2010**, *39*, 1489-1502.

241. Locklin, J.; Roberts, M. E.; Mannsfeld, S. C. B.; Bao, Z., Optimizing the Thin Film Morphology of Organic Field-Effect Transistors: The Influence of Molecular Structure and Vacuum Deposition Parameters on Device Performance. *Journal of Macromolecular Science, Part C* **2006**, *46*, 79-101.

242. Puniredd, S. R.; Pisula, W.; Müllen, K., 2 - Influence of film morphology on optical and electronic properties of organic materials. In *Handbook of Organic Materials for Optical and (Opto)electronic Devices*, Ostroverkhova, O., Ed. Woodhead Publishing: 2013, pp 83-101.

243. Xue, Z.; Chen, S.; Gao, N.; Xue, Y.; Lu, B.; Watson, O. A.; Zang, L.; Xu, J., Structural Design and Applications of Stereoregular Fused Thiophenes and Their Oligomers and Polymers. *Polymer Reviews* **2019**, 10.1080/15583724.2019.1673404.

244. Anthony, J. E., Functionalized Acenes and Heteroacenes for Organic Electronics. *Chem. Rev.* **2006**, *106*, 5028-5048.

245. Payne, M. M.; Parkin, S. R.; Anthony, J. E.; Kuo, C.-C.; Jackson, T. N., Organic Field-Effect Transistors from Solution-Deposited Functionalized Acenes with Mobilities as High as 1 cm2/V·s. *J. Am. Chem. Soc.* **2005**, *127*, 4986-4987.

246. Ebata, H.; Izawa, T.; Miyazaki, E.; Takimiya, K.; Ikeda, M.; Kuwabara, H.; Yui, T., Highly Soluble [1]Benzothieno[3,2-b]benzothiophene (BTBT) Derivatives for

High-Performance, Solution-Processed Organic Field-Effect Transistors. *J. Am. Chem. Soc.* **2007**, *129*, 15732-15733.

247. Iino, H.; Usui, T.; Hanna, J.-i., Liquid crystals for organic thin-film transistors. *Nat. Commun.* **2015**, *6*, 6828.

248. Pachmajer, S.; Werzer, O.; Mennucci, C.; Buatier de Mongeot, F.; Resel, R., Biaxial growth of pentacene on rippled silica surfaces studied by rotating grazing incidence X-ray diffraction. *J. Cryst. Growth* **2019**, *519*, 69-76.

249. Spreitzer, H.; Kaufmann, B.; Ruzié, C.; Röthel, C.; Arnold, T.; Geerts, Y. H.; Teichert, C.; Resel, R.; Jones, A. O. F., Alkyl chain assisted thin film growth of 2,7-dioctyloxy-benzothienobenzothiophene. *J. Mater. Chem. C* **2019**, *7*, 8477-8484.

250. Jones, A. O. F.; Chattopadhyay, B.; Geerts, Y. H.; Resel, R., Substrate-Induced and Thin-Film Phases: Polymorphism of Organic Materials on Surfaces. *Adv. Funct. Mater.* **2016**, *26*, 2233-2255.

251. Chung, H.; Diao, Y., Polymorphism as an emerging design strategy for high performance organic electronics. *J. Mater. Chem. C* **2016**, *4*, 3915-3933.

252. Lee, W. H.; Park, J.; Sim, S. H.; Lim, S.; Kim, K. S.; Hong, B. H.; Cho, K., Surface-Directed Molecular Assembly of Pentacene on Monolayer Graphene for High-Performance Organic Transistors. *J. Am. Chem. Soc.* **2011**, *133*, 4447-4454.

253. Wang, S.; Wei, Z.; Yang, Y.; Zhao, X.; Tang, Q.; Tong, Y.; Liu, Y., Low surface energy interface-derived low-temperature recrystallization behavior of organic thin films for boosting carrier mobility. *J. Mater. Chem. C* **2019**, *7*, 13778-13785.

254. Ullah Khan, H.; Li, R.; Ren, Y.; Chen, L.; Payne, M. M.; Bhansali, U. S.; Smilgies, D.-M.; Anthony, J. E.; Amassian, A., Solvent Vapor Annealing in the Molecular Regime Drastically Improves Carrier Transport in Small-Molecule Thin-Film Transistors. *ACS Appl. Mater. Interfaces* **2013**, *5*, 2325-2330.

255. Grimme, S., Do Special Noncovalent π–π Stacking Interactions Really Exist? *Angew. Chem. Int. Ed.* **2008**, *47*, 3430-3434.

256. Martinez, C. R.; Iverson, B. L., Rethinking the term “pi-stacking”. *Chem. Sci.* **2012**, *3*, 2191-2201.

257. Ober, C. K.; Cheng, S. Z. D.; Hammond, P. T.; Muthukumar, M.; Reichmanis, E.; Wooley, K. L.; Lodge, T. P., Research in Macromolecular Science: Challenges and Opportunities for the Next Decade. *Macromolecules* **2009**, *42*, 465-471.

258. Krotzky, S.; Morchutt, C.; Vyas, V. S.; Lotsch, B. V.; Gutzler, R.; Kern, K., Thermodynamics of the Segregation of a Kinetically Trapped Two-Dimensional Amorphous Metal–Organic Network. *J. Phys. Chem. C* **2016**, *120*, 4403-4409.

259. Zhu, C.; Ji, X.; You, D.; Chen, T. L.; Mu, A. U.; Barker, K. P.; Klivansky, L. M.; Liu, Y.; Fang, L., Extraordinary Redox Activities in Ladder-Type Conjugated Molecules Enabled by B ← N Coordination-Promoted Delocalization and Hyperconjugation. *J. Am. Chem. Soc.* **2018**, *140*, 18173-18182.

260. Zhang, W.; Ji, X.; Peng, B.-J.; Che, S.; Ge, F.; Liu, W.; Al-Hashimi, M.; Wang, C.; Fang, L., High-Performance Thermoresponsive Dual-Output Dye System for Smart Textile Application. *Adv. Funct. Mater.*, 1906463.

261. Sinha, S. K.; Sirota, E. B.; Garoff, S.; Stanley, H. B., X-ray and neutron scattering from rough surfaces. *Phys. Rev. B* **1988**, *38*, 2297-2311.

APPENDIX A

SUPPLEMENTARY DATA FOR CHAPTER II

A1. Synthesis

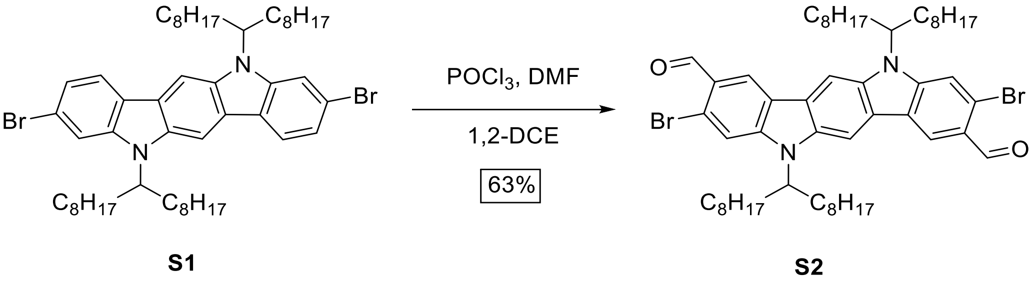

3,9-dibromo-5,11-dihydro-5,11-di(1-octylnonyl)indolo[3,2-*b*]carbazole-2,8-dicarbaldehyde (S2): In a 150 mL sealed tube, DMF (8.7 mL, 110 mmol) was added in anhydrous 1,2-dichloroethane (30 mL) and cooled to 0 °C under N_2. To the mixture was added phosphorus oxychloride (10.5 mL, 113 mmol) dropwise at 0 °C. After the reaction mixture was warmed to room temperature, compound **S1** (4.0 g, 4.5 mmol) was added into the flask, and the mixture was stirred at 95 °C for 48 h. The reaction was cooled to room temperature and quenched with water. The aqueous mixture was basified to pH = 7 by 2M KOH solution. The mixture was extracted with CH_2Cl_2 (3 × 50 mL), and the combined organic layer was dried over $MgSO_4$, filtered through Celite, and concentrated under reduced pressure. The residue was purified by flash column chromatography (SiO_2, hexane:CH_2Cl_2 = 100:0 to 50:50) to give the product **S2** (2.7 g, 2.9 mmol, 63%) as a yellow solid. ^{1}H NMR (500 MHz, $CDCl_3$): δ 10.46 (s, 2H), 8.83, 8.81 (two s[*], 2H), 8.27,

---

[*] NMR data marked with * in Appendix A indicate that multiple peaks were observed in the spectra due to atropisomerism from hindered rotation of the alkyl sidechains.

8.24, 8.13, 8.10 (four s*, 2H), 7.86, 7.77 (two s*, 2H), 4.68, 4.55 (two quint*, 2H), 2.40, 2.26 (two m*, 4H), 2.05 (m, 4H), 1.13 (m, 46H), 0.78 (t, J = 7.0 Hz, 12H). $^{13}C\{^1H\}$ NMR* (125 MHz, $CDCl_3$): δ 191.98, 147.06, 143.82, 139.06, 138.93, 135.15, 125.15, 124.68, 124.36, 124.32, 123.72, 123.30, 123.11, 122.97, 122.76, 122.41, 122.04, 121.69, 104.08, 13.68, 103.39, 103.00, 100.96, 100.59, 57.94, 57.59, 33.77, 33.44, 31.84, 29.44, 29.23, 27.36, 26.99, 26.66, 22.70, 14.48, 14.19, 13.84. HRMS (MALDI): calcd for $C_{54}H_{78}Br_2N_2O_2$ $[M+H]^+$ $m/z = 947.4488$; found $m/z = 947.4431$.

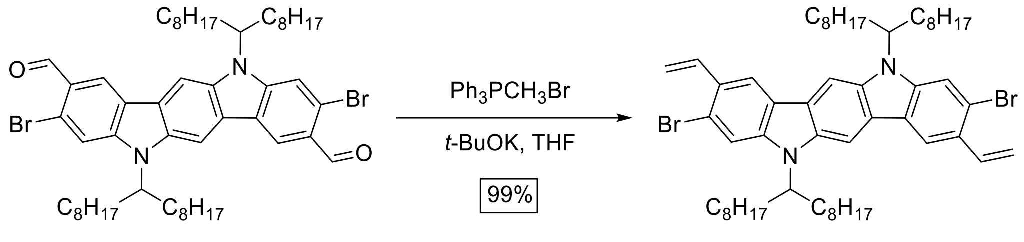

S2 **S3**

3,9-dibromo-2,8-diethenyl-5,11-dihydro-5,11-di(1-octylnonyl)indolo[3,2-*b*]carbazole (S3): To a mixture of methyltriphenylphosphonium bromide (4.0 g, 11 mmol) in THF (80 mL) was added *t*-BuOK (1.18 g, 10.5 mmol) in small portions over 10 min at room temperature. Compound **S2** (2.5 g, 2.6 mmol) was added into the flask with several crystals of 2,6-di-t-butyl-4-methylphenol (BHT). The mixture was stirred in the dark at reflux for 6 h. The reaction was quenched with water and diluted with CH_2Cl_2. The mixture was extracted with CH_2Cl_2 (3 × 30 mL) and the combined organic layer was dried over $MgSO_4$, filtered through Celite, and concentrated under reduced pressure. The residue was purified by flash column chromatography (SiO_2, hexane) to give the product **S3** (2.5 g, 2.6 mmol, 99%) as a yellow solid. ^1H NMR (500MHz, $CDCl_3$): δ 8.38, 8.35 (two s*, 2H), 8.14, 8.10, 8.00, 7.97 (four s*, 2H), 7.75, 7.59 (two s*, 1H), 7.26 (dd, J = 17.5 Hz, 11.0

Hz, 2H), 5.82 (dd, *J* = 17.5 Hz, 11.0 Hz, 2H), 5.34 (d, *J* = 11.0 Hz, 2H), 4.67, 4.48 (two br*, 2H), 2.42, 2.26 (two m*, 4H), 2.00 (m, 4H), 1.13 (m, 46H), 0.79 (t, *J* = 7.0 Hz, 12H). $^{13}C\{^1H\}$ NMR (125 MHz, $CDCl_3$): δ 143.69, 142.79, 140.14, 138.25, 137.34, 137.12, 136.60, 136.36, 134.40, 127.47, 123.83, 123.55, 122.41, 122.17, 121.51, 120.92, 117.96, 117.78, 117.60, 114.77, 114.55, 113.85, 113.22, 112.49, 112.31, 105.12, 102.25, 101.95, 99.47, 99.26, 57.38, 57.02, 56.43, 33.88, 33.64, 31.88, 29.58, 29.46, 29.31, 27.04, 22.72, 14.21, 14.16. HRMS (MALDI): calcd for $C_{56}H_{82}Br_2N_2$ $[M+H]^+$ *m/z* = 944.4923; found *m/z* = 944.4905.

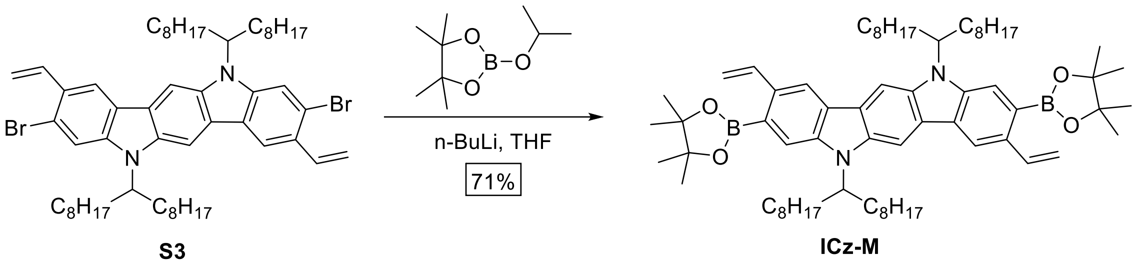

2,8-diethenyl-3,9-bis(4,4,5,5-tetramethyl-1,3,2-dioxaborolan-2-yl)-5,11-dihydro-5,11-di(1-octylnonyl)indolo[3,2-*b*]carbazole (ICz-M): To the mixture of compound **S3** (1.1 g, 1.1 mmol) in anhydrous THF (20 mL) at –78 °C was added *n*-BuLi (1.4 mL, 2.3 mmol, 1.6 M in hexane) dropwise over 1 h and stirred for another 1h at –78 °C. 2-isopropoxy-4,4,5,5-tetramethyl-1,3,2-dioxaborolane (0.53 mL, 2.6 mmol) was added into the mixture, and the mixture was allowed to room temperature and stirred for 24 h. The reaction was quenched with water and diluted with CH_2Cl_2. The mixture was extracted with CH_2Cl_2 (3 × 30 mL) and the combined organic layer was dried over $MgSO_4$, filtered through Celite, and concentrated under reduced pressure. The residue was purified by flash column chromatography (SiO_2, hexane:CH_2Cl_2 = 100:0 to 50:50) to give the product **ICz-**

M (0.81g, 0.78 mmol, 71%) as a yellow solid. ^{1}H NMR (500MHz, CDCl$_3$): δ 8.46 (m, 2H), 8.20 (m, 2H), 8.17, 8.05 (two s*, 1H), 8.01 (s, 1H), 7.85 (s, 1H), 7.76 (dd, *J* = 17.0 Hz, 11.0 Hz, 2H), 5.85 (d, *J* = 17.0 Hz, 2H), 5.25 (d, *J* = 11.0 Hz, 2H), 4.71 (bs, 2H), 2.44, 2.37 (two m*, 4H), 2.02 (m, 4H), 1.43 (s, 24H), 1.14 (m, 46H), 0.80 (t, *J* = 7.0 Hz, 12H). ^{13}C{^{1}H} NMR* (125 MHz, CDCl$_3$): 151.67, 142.52, 138.76, 134.70, 133.83, 126.38, 125.67, 125.02, 124.16, 118.46, 116.21, 116.06, 115.88, 111.45, 102.36, 101.98, 99.55, 99.19, 83.73, 56.88, 56.39, 34.09, 33.77, 31.91, 29.69, 29.51, 29.38, 27.12, 26.98, 25.10, 22.73, 14.18. HRMS (MALDI): calcd for $C_{68}H_{106}B_2N_2O_4$ [M+H]$^+$ *m/z* = 1037.8417; found *m/z* = 1037.8499.

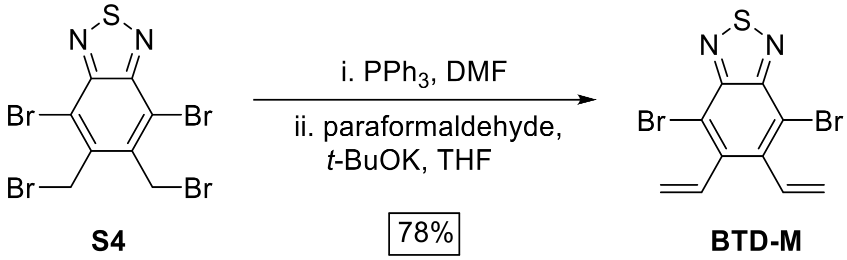

4,7-dibromo-5,6-diethenyl-2,1,3-benzothiadiazole (BTD-M): A mixture of compound **S4** (3.0 g, 6.3 mmol) and PPh$_3$ (4.1 g, 16 mmol) in DMF (40 mL) was stirred at 80 °C for 18 h. After being cooled to room temperature, the reaction mixture was concentrated under reduced pressure. The residue and paraformaldehyde (4.3 g) were suspended in THF (70 mL) under N$_2$. While stirring, *t*-BuOK (2.1 g, 19 mmol) was added in small portions over 10 min. After 30 min, the reaction was quenched with water and extracted with CH$_2$Cl$_2$ (3 × 30 mL). The combined organic layer was dried over MgSO$_4$, filtered through Celite, and concentrated under reduced pressure. The residue was purified by flash column chromatography (SiO$_2$, hexane) to give the product **BTD-M** (1.7 g, 4.9 mmol, 78%) as a white solid. ^{1}H NMR (500 MHz, $CDCl_3$): δ 6.70 (dd, *J* = 17.5 Hz, 12.0 Hz, 2H), 5.76 (d, *J* = 12.0 Hz, 1.5 Hz, 2H), 5.61 (dd, *J* = 17.5 Hz, 1.5 Hz, 2H). $^{13}C\{^1H\}$ NMR (125 MHz, $CDCl_3$): δ 152.31, 140.56, 134.42, 124.49, 113.72. HRMS (APCI): calcd for $C_{10}H_6Br_2N_2S$ $[M+H]^+$ *m/z* = 346.87; found *m/z* = 346.93.

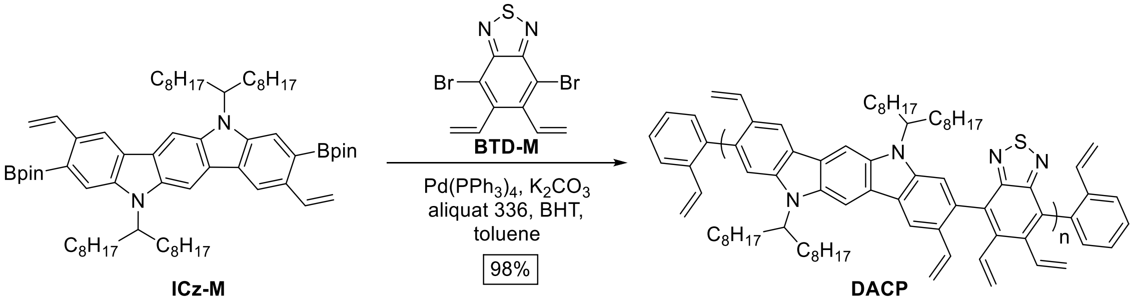

DACP: Under N_2, degassed toluene (4 mL) and water (0.8 mL) was added to a mixture of **ICz-M** (99.6 mg, 0.096 mmol), **BTD-M** (33.2 mg, 0.096 mmol), $Pd(PPh_3)_4$ (11 mg, 9.5×10^{-6} mol), K_2CO_3 (80 mg, 0.6 mmol), a drop of aliquat 336, and several crystals of BHT. The solution was further degassed for 3 times by freeze–pump–thaw. The reaction mixture was stirred at 100 °C for 24 h in the dark, before it was cooled to room temperature. 2-bromostyrene (50 μL, 0.38 mmol) was added into the flask at room temperature, and the mixture was heated again to 100 °C and stirred for 24 h. Subsequently, 2-vinylphenylboronic acid (110 mg, 0.77 mmol) was added into the flask, and the mixture was stirred at 100 °C for another 24 h. The resulting product was precipitated from methanol, filtered, and washed with acetone. The solid was dried under vacuum to afford **DACP** (91 mg, 0.094 mmol, 98%, M_n = 28 kg mol^{-1}, PDI = 5.16 by SEC). **DACP** was further purified by preparative recycling SEC to remove lower molecular weight oligomers to afford a batch with higher M_n and lower PDI (65 mg, 70%,

M_n = 43 kg mol^{-1}, PDI = 4.34 by SEC). ^{1}H NMR (500 MHz, $CDCl_3$): δ 8.64 (bs, 2H), 8.27, 8.15 (two m, 2H), 7.52, 7.36 (two m*, 2H), 6.78 (m, 2H), 6.58 (m, 2H), 5.90 (m, 2H), 5.32 (m, 4H), 5.10 (m, 2H), 4.79, 4.62 (two bs*, 2H), 2.55, 2.33 (two m, 4H), 1.98 (m, 4H), 1.18 (m, 46H), 0.82 (m, 12H).

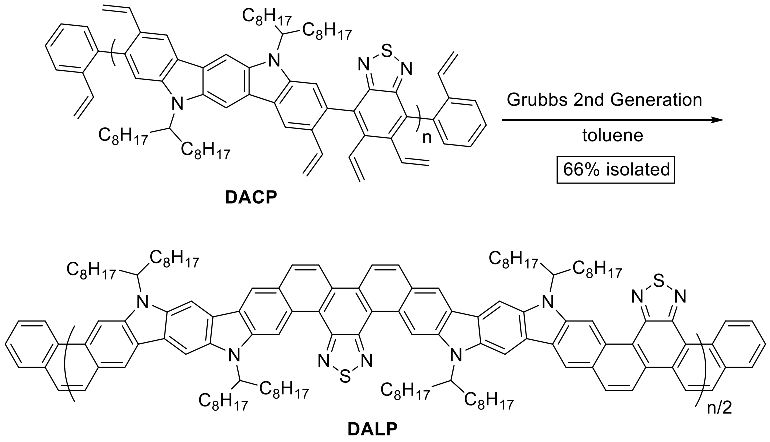

DALP: To a 50 mL Schlenk flask was added **DACP** (126 mg, 0.13 mmol) and Grubbs' 2nd generation catalyst (6 mg, 5 mol%) under N_2. Subsequently, degassed toluene (12 mL) was added, and the reaction mixture was heated to reflux while stirring. At this point, additional solution of Grubbs' 2nd generation catalyst (16 mg, 15 mol%) in degassed toluene (8 mL) was injected into the reaction mixture slowly using syringe pump over the course of 4 h. The reaction was kept running for an additional 2 h at reflux temperature before cooling to room temperature. The resulting product was precipitated from methanol and filtered. The crude solid was washed via Soxhlet extraction with acetone and hexane, before being extracted by chloroform. The chloroform solution was filtered and condensed under reduced pressure. The desired **DALP** product was precipitated from methanol and isolated by filtration and drying under vacuum (73 mg, 0.086 mmol, 66%, M_n = 21 kg mol^{-1}, PDI = 2.95 by SEC). The insoluble high molecular weight fraction left over as a solid in the Soxhlet extractor was also collected and dried under vacuum (30 mg, 0.04 mmol, 27%). ^{1}H NMR (500 MHz, $CDCl_3$): δ 11.21, 11.05 (two bs, 2H), 8.97 (m, 3H), 8.82 (m, 1H), 8.54 (m, 4H), 5.33, 5.01 (two bs*, 2H), 2.94, 2.76 (two m*, 4H), 2.30 (m, 4H), 1.10 (m, 46H), 0.70 (m, 12H).

A2. Size Exclusion Chromatography (SEC)

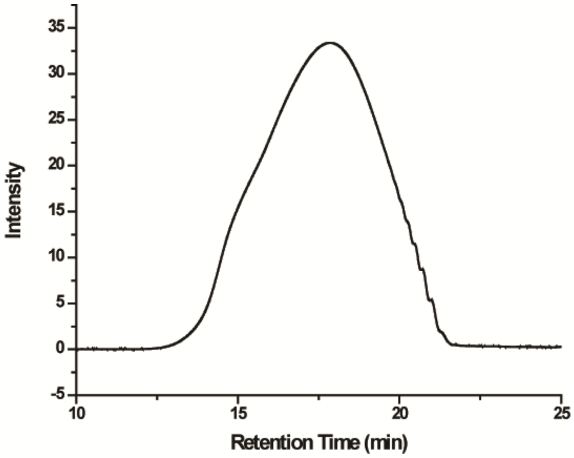

Figure A1. Size exclusion chromatogram of **DACP** after purification by preparative recycling SEC. M_n^{SEC} = 43 kg/mol, PDI = 4.34. An aggregation feature was observed as a shoulder peak in the high molecular weight region.

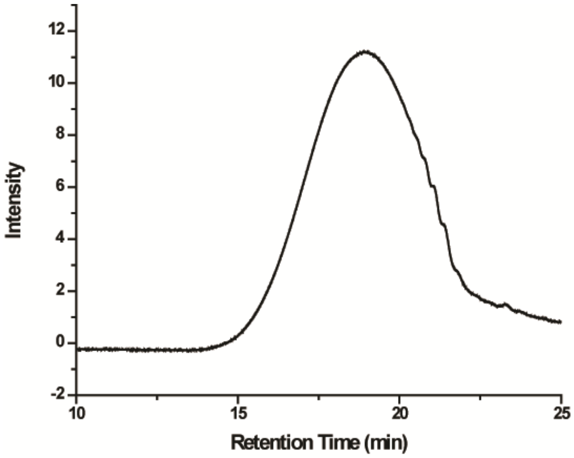

Figure A2. Size exclusion chromatogram of **DALP** after Soxhlet extraction from CHCl₃. M_n^{SEC} = 21 kg/mol, PDI = 2.95.

A3. Lippert-Mataga Solvatochromism Plot

The positive solvatochromism of **DALP** was demonstrated by a Lippert-Mataga plot using the Lippert-Mataga equation (1).

$$\bar{\nu}_A - \bar{\nu}_E = \frac{2(\mu_G - \mu_E)^2}{hca^3}\Delta f + c \qquad (1)$$

Herein, ν_A and ν_E are the absorption maximum and emission maximum in wavenumbers, μ_g and μ_E are, respectively, the ground and excited state dipole moments, *h* is Planck's constant, *c* is the speed of light in vacuum, *a* is the Onsager cavity radius, and Δf is the orientation polarizability. Stokes shift is generally described by the difference of absorption maximum and emission maximum. However, since **DALP** exhibits optically weak HOMO-LUMO transitions in the absorption spectrum, the Stokes shift of **DALP** represents the difference of the weak HOMO-LUMO absorption and the emission maximum. Unfortunately, it was difficult to obtain an accurate wavelength of the weak HOMO-LUMO absorptions in various solvents because the weak absorption shoulder (468 nm) observed in toluene became less characteristic in more polar solvents. Although the difference between absorption maxima and emission maxima does not depicts Stokes shift of **DALP**, the difference, which is more apparent, was plotted as a function of Δf, which is defined as the equation (2).

$$\Delta f = \left(\frac{\varepsilon - 1}{2\varepsilon + 1}\right) - \left(\frac{n^2 - 1}{2n^2 + 1}\right) \qquad (2)$$

where, ε is dielectric constant, and n is refractive index of a solvent.

Table A1. Summary of dielectric constants (ε),[6] refractive indices (n),[6] orientation polarizabilities (Δf), absorptions, emissions, and the difference between the absorptions and emissions in various solvents.

	ε	n	Δf	λ_{abs} (nm)	λ_{em} (nm)	Δv (cm^{-1})
Toluene	2.38	1.4969	0.013	468	569	3792
Chlorobenzene	5.62	1.5248	0.143	469	591	4401
Chloroform	4.81	1.4459	0.148	467	590	4464
1,2-Dichlorobenzene	9.93	1.5514	0.186	470	608	4829
Tetrahydrofuran	7.58	1.4072	0.210	468	604	4811
Dichloromethane	8.93	1.4242	0.217	466	616	5225
1,2-Dichloroethane	10.37	1.4448	0.221	466	618	5278

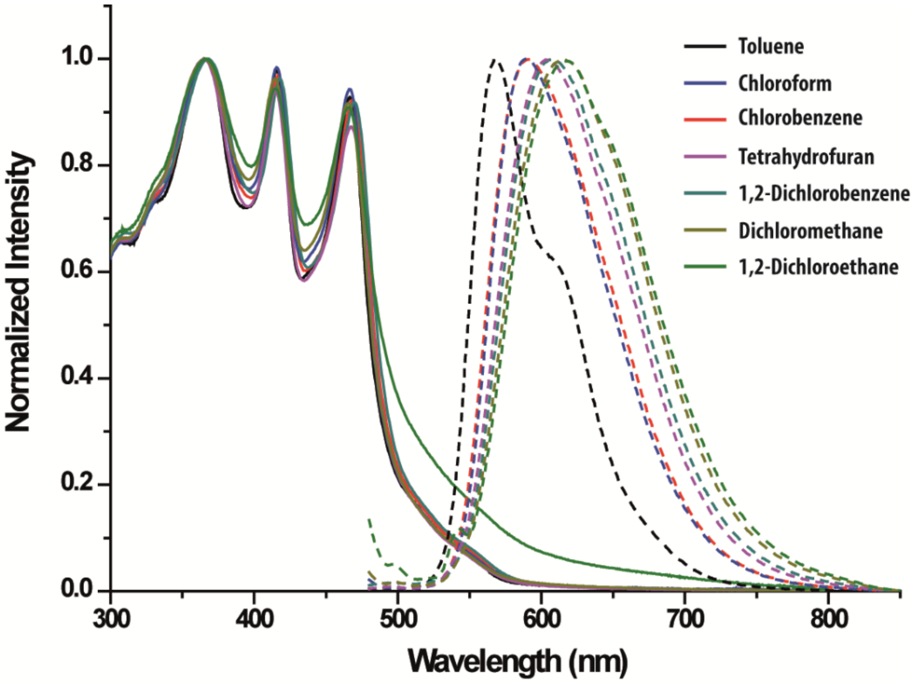

Figure A3. UV-vis absorption and fluorescence emission spectra of **DALP** in different solvents.

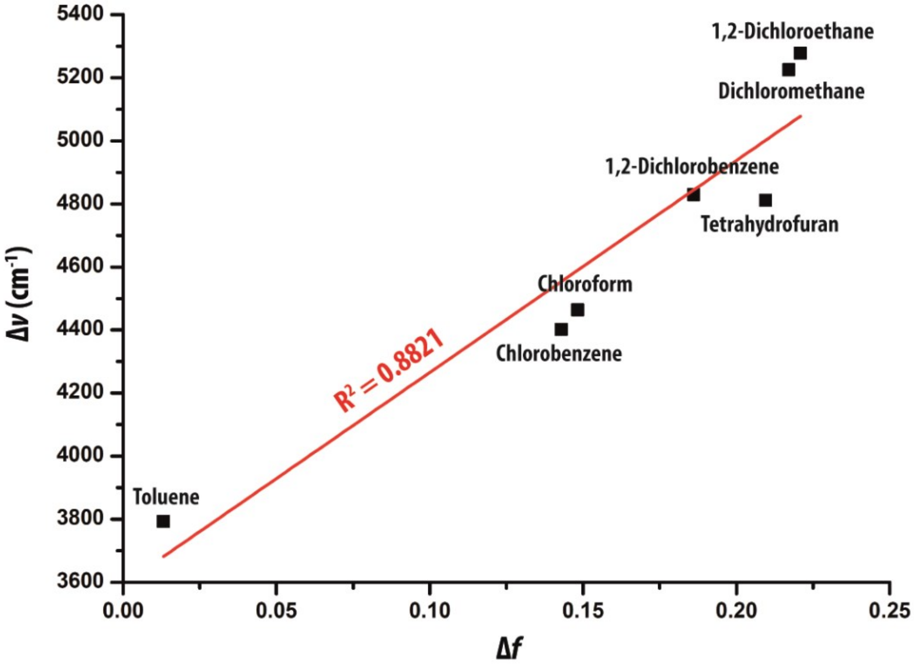

Figure A4. Lippert-Mataga plot of **DALP**. The red line represents the linear fit (R^2 = 0.8821).

A5. Grazing Incidence Wide-Angle X-ray Scattering (GIWAXS)

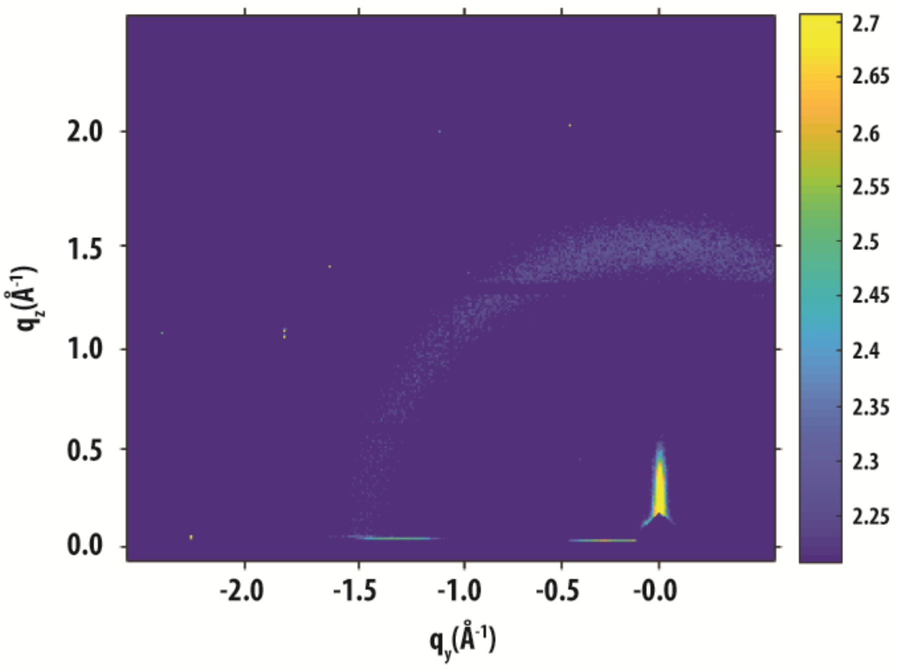

Figure A5. GIWAXS image of as-cast film of **DALP**. Weak ring around q = 1.5 Å^{-1} likely due to either SiO_2 scattering or weak amorphous π–π interactions.

A6. ^{1}H and ^{13}C NMR Spectra

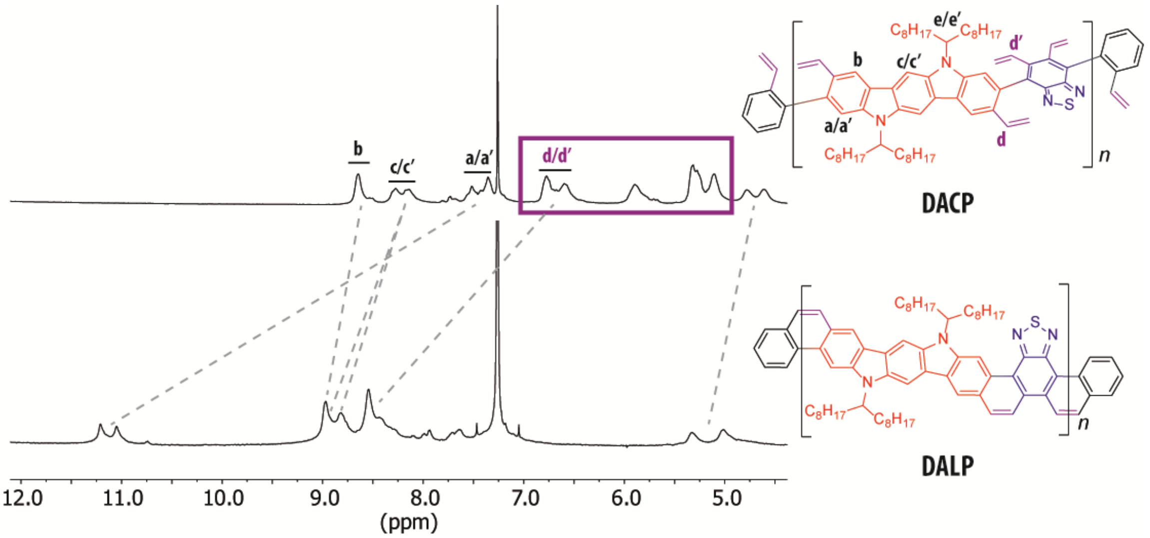

Figure A6. Partial ^{1}H NMR spectra of **DACP** and **DALP**. Dotted lines represent the change of chemical shifts of each resonance peak after RCM. Proton resonance peaks for the vinyl groups in the box all disappeared after RCM. Multiple sets of peaks result from atropisomerism caused by the hindered rotation of the side chains.

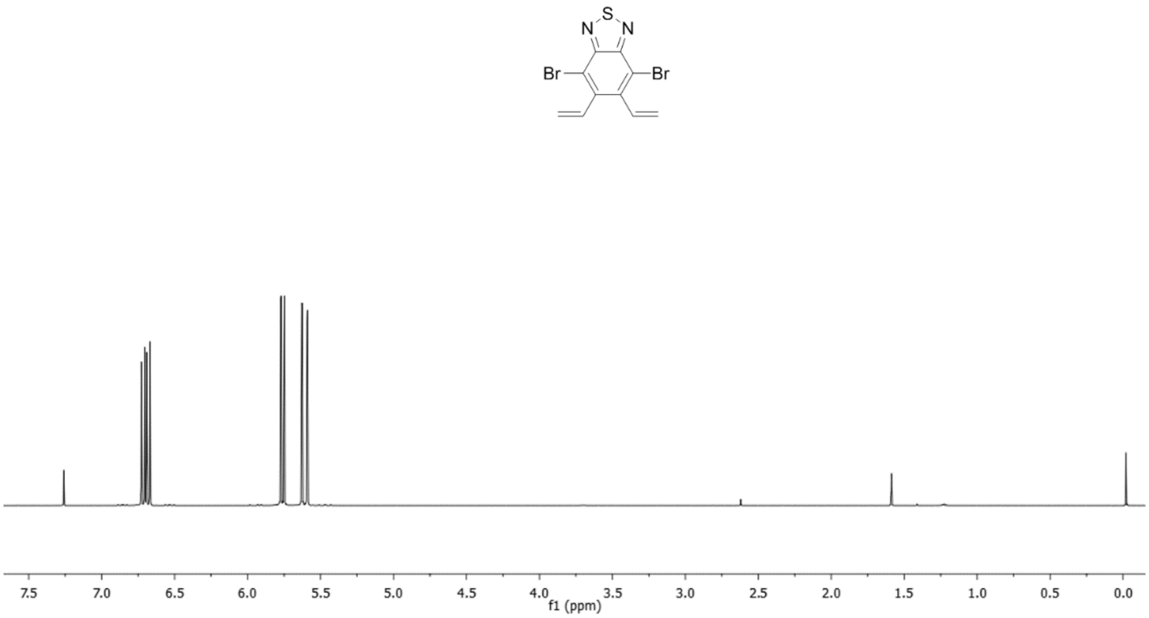

Figure A7. ^{1}H NMR of **S4** (500 MHz, $CDCl_3$, RT).

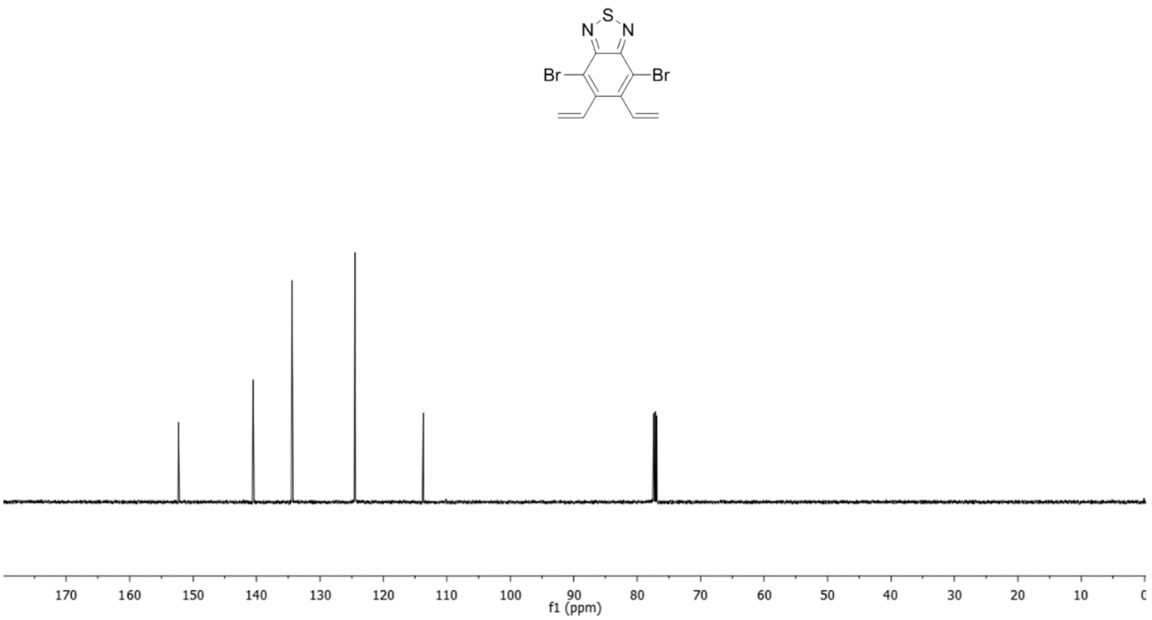

Figure A8. $^{13}C\{^1H\}$ NMR of **S4** (125 MHz, $CDCl_3$, RT).

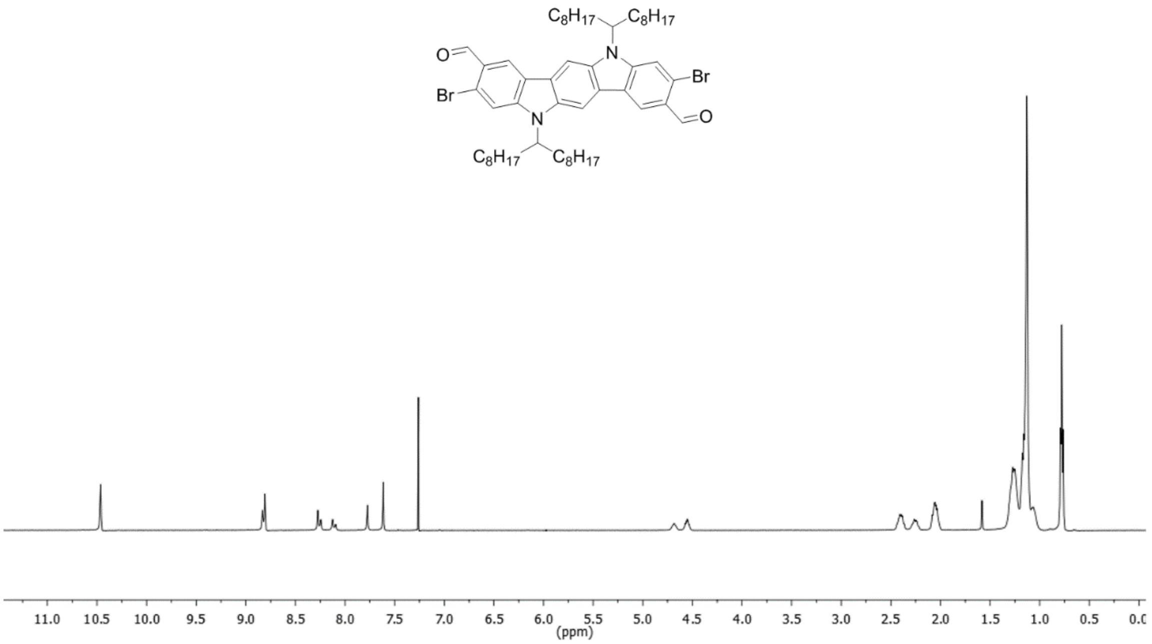

Figure A9. ^1H NMR of **S1** (500 MHz, $CDCl_3$, RT).

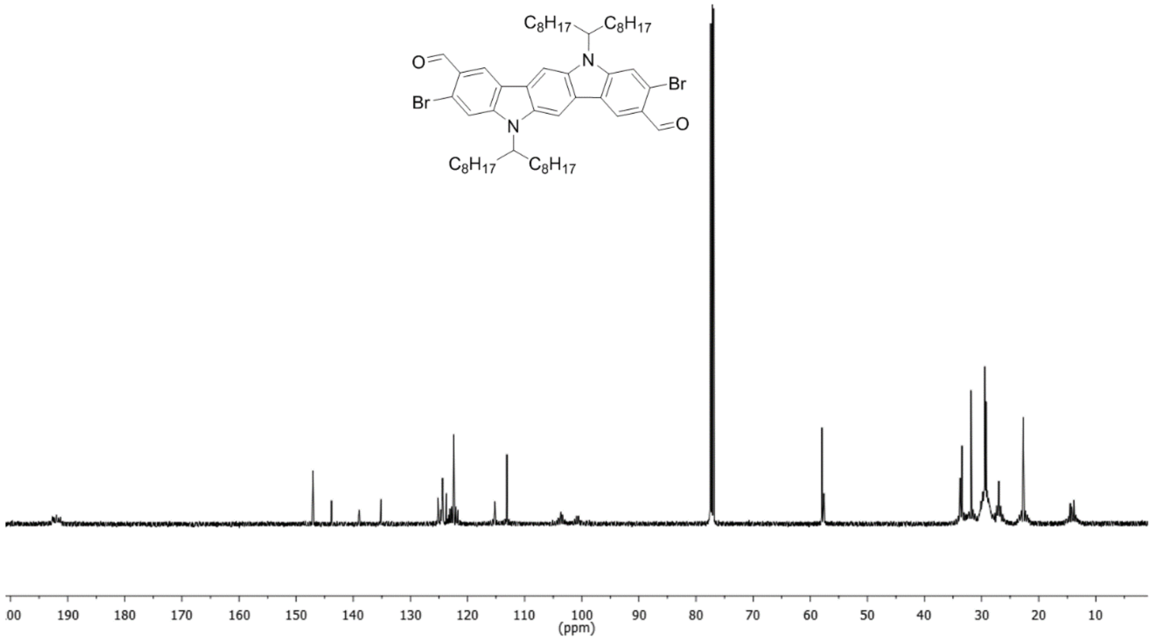

Figure A10. $^{13}C\{^{1}H\}$ NMR of **S1** (125 MHz, CDCl$_3$, RT).

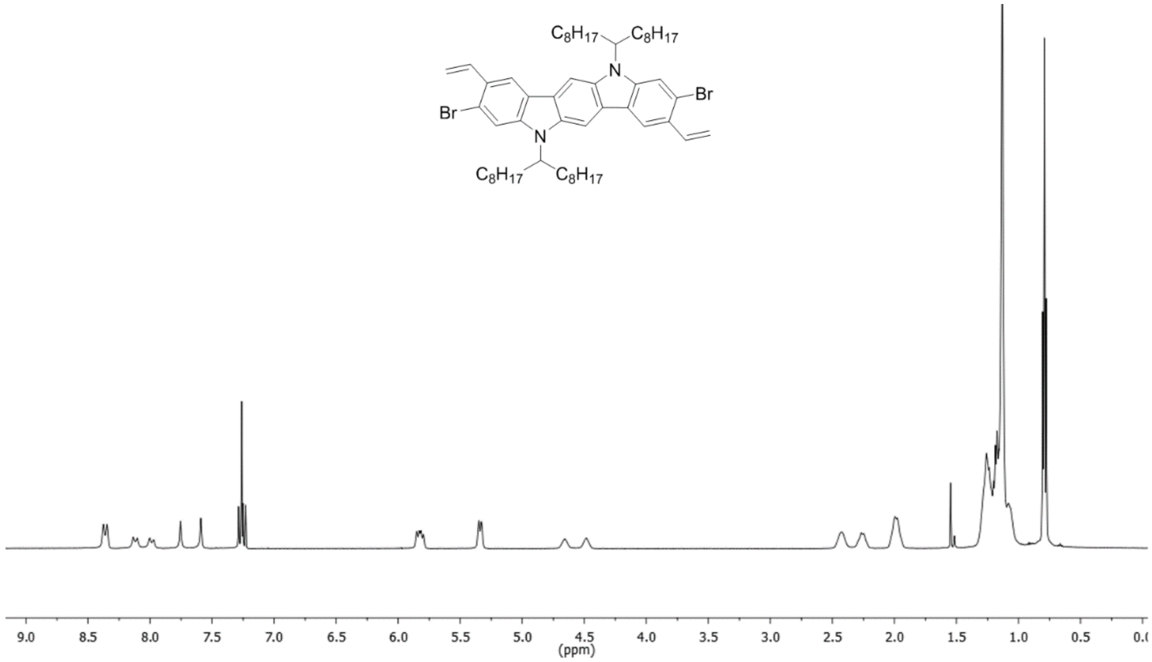

Figure A11. ^{1}H NMR of **S2** (500 MHz, CDCl$_3$, RT).

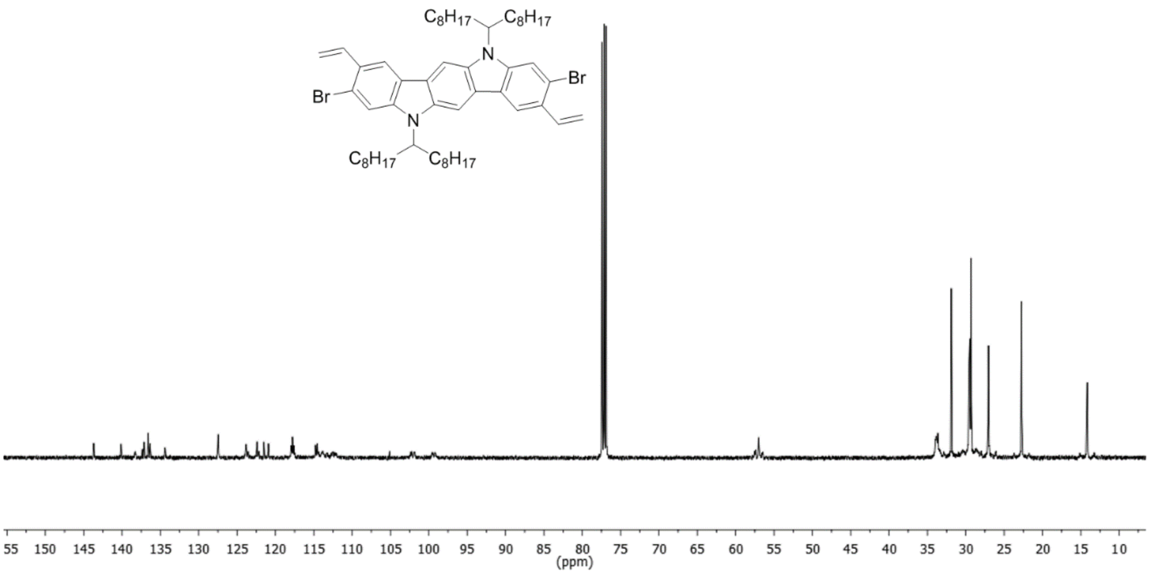

Figure A12. $^{13}C\{^{1}H\}$ NMR of **S2** (125 MHz, $CDCl_3$, RT).

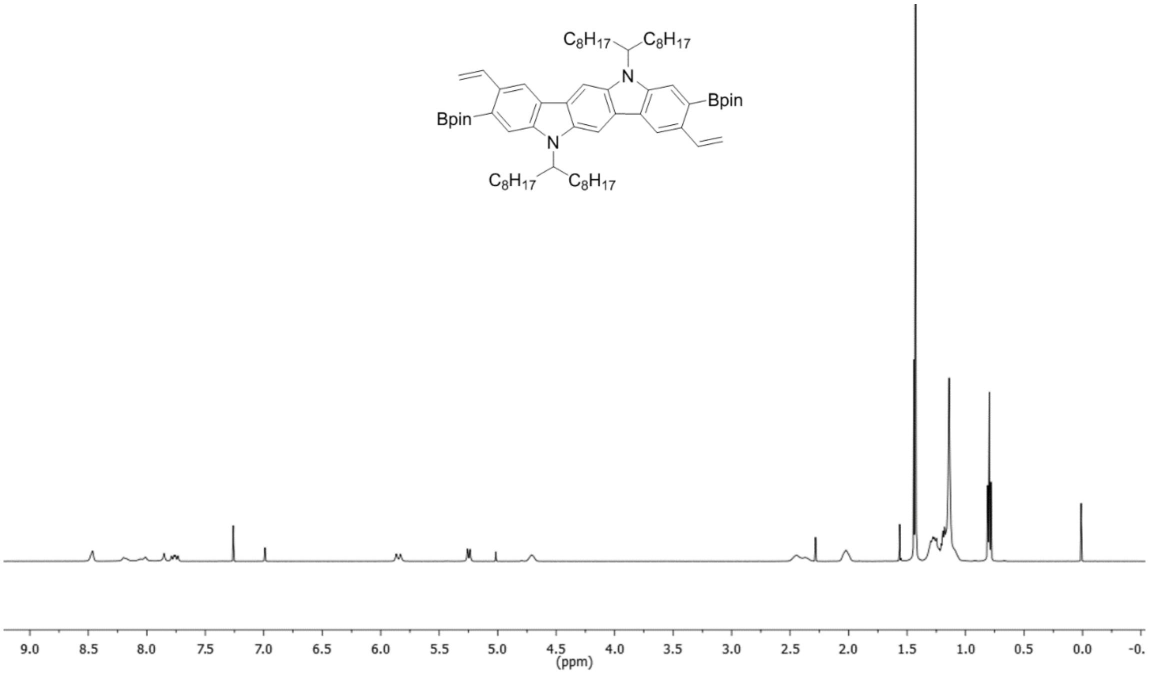

Figure A13. ^{1}H NMR of **ICz-M** (500 MHz, $CDCl_3$, RT).

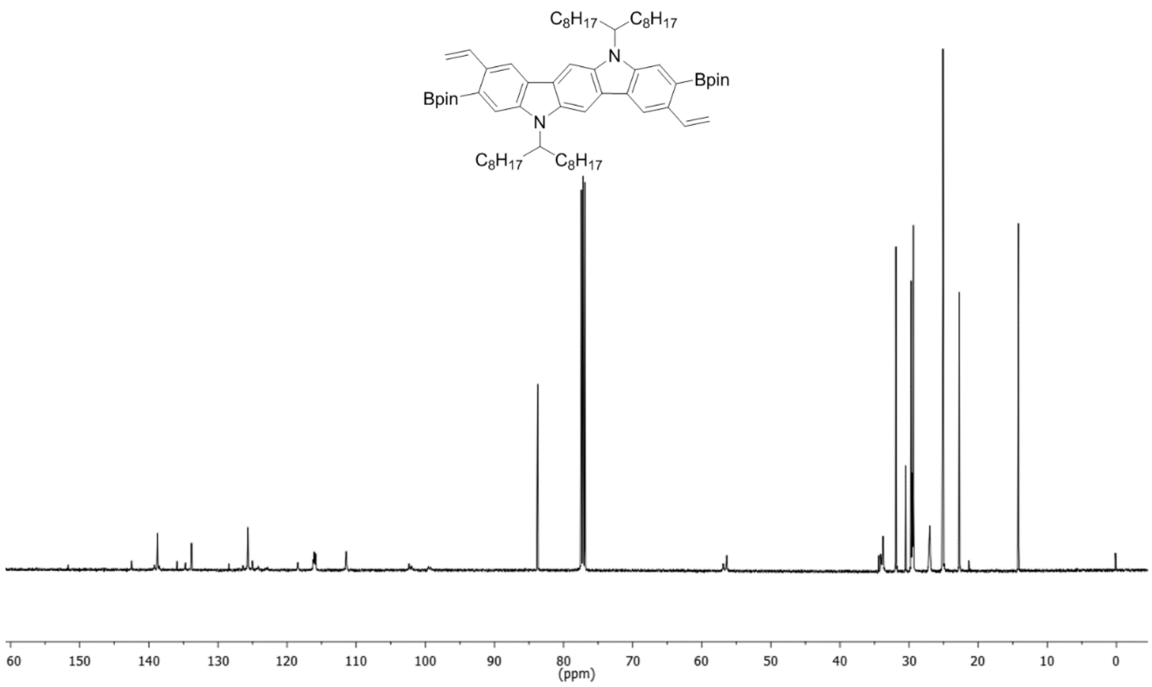

Figure A14. $^{13}C\{^{1}H\}$ NMR of **ICz-M** (125 MHz, $CDCl_3$, RT).

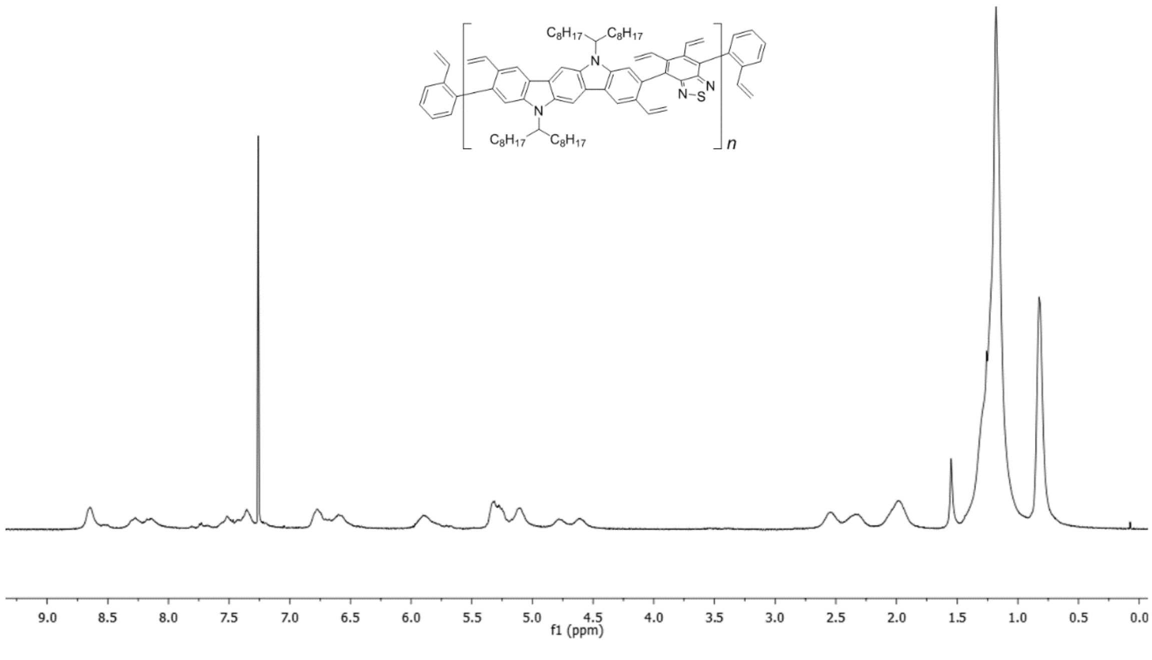

Figure A15. ^{1}H NMR of **DACP** (500 MHz, $CDCl_3$, RT).

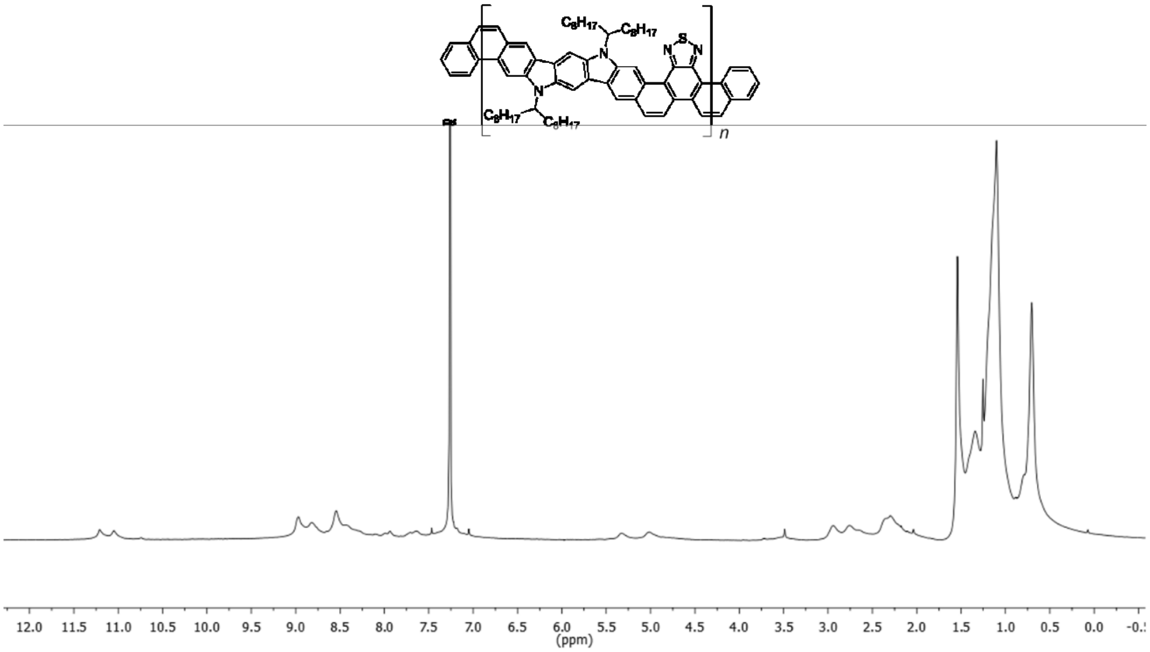

Figure A16. ^{1}H NMR of **DALP** (500 MHz, $CDCl_3$, RT).

APPENDIX B

SUPPLEMENTARY DATA FOR CHAPTER III

B1. ^{1}H and ^{13}C NMR Spectra

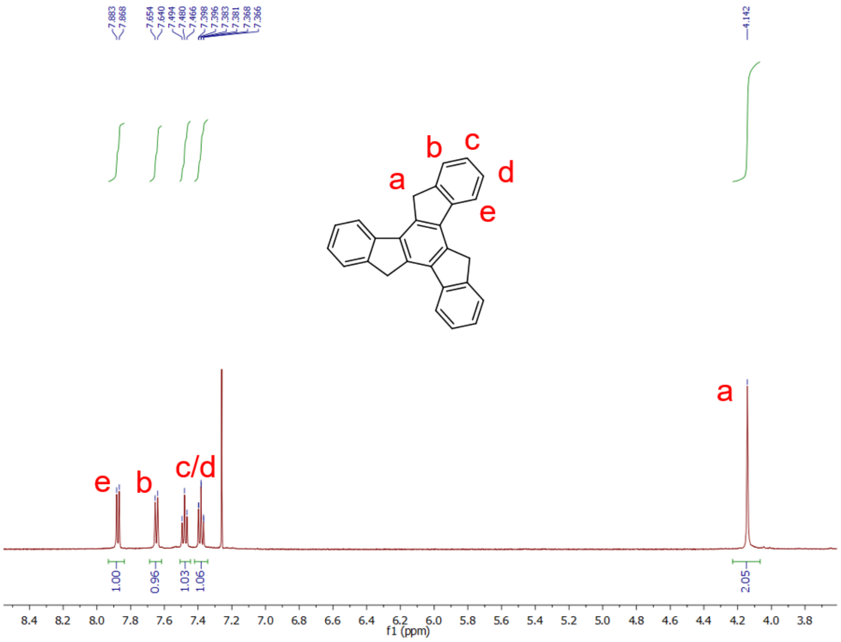

Figure B1. ^{1}H NMR of **1** (400 MHz, $CDCl_3$, RT).

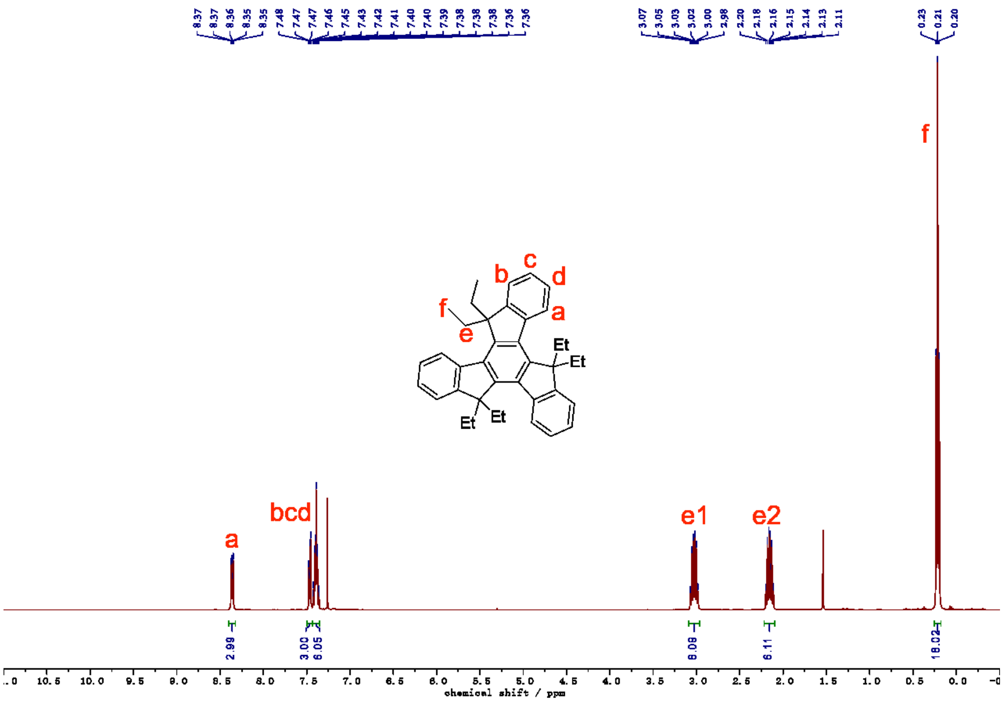

Figure B2. ^{1}H NMR of **2** (400 MHz, CDCl$_3$, RT).

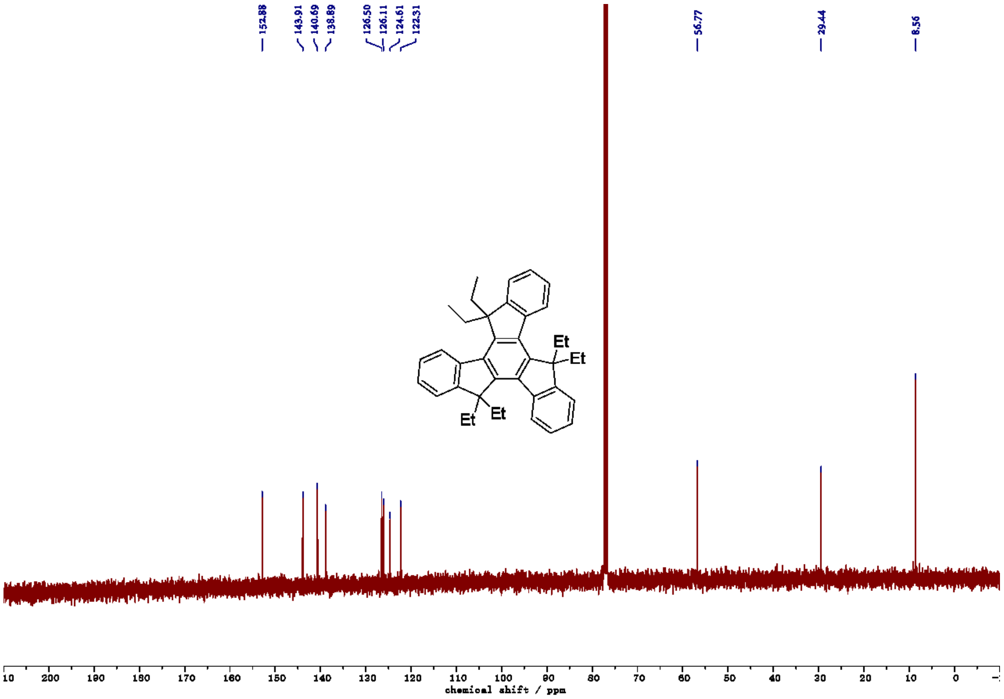

Figure B3. ^{13}C{^{1}H} NMR of **2** (100 MHz, CDCl$_3$, RT).

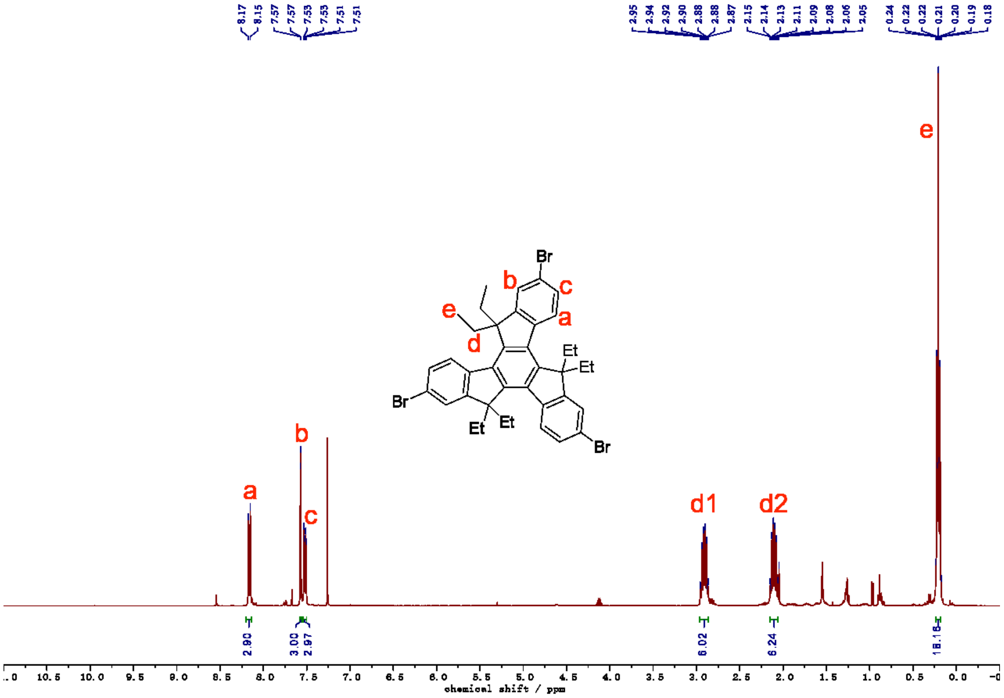

Figure B4. ^{1}H NMR of **3** (400 MHz, CDCl$_3$, RT).

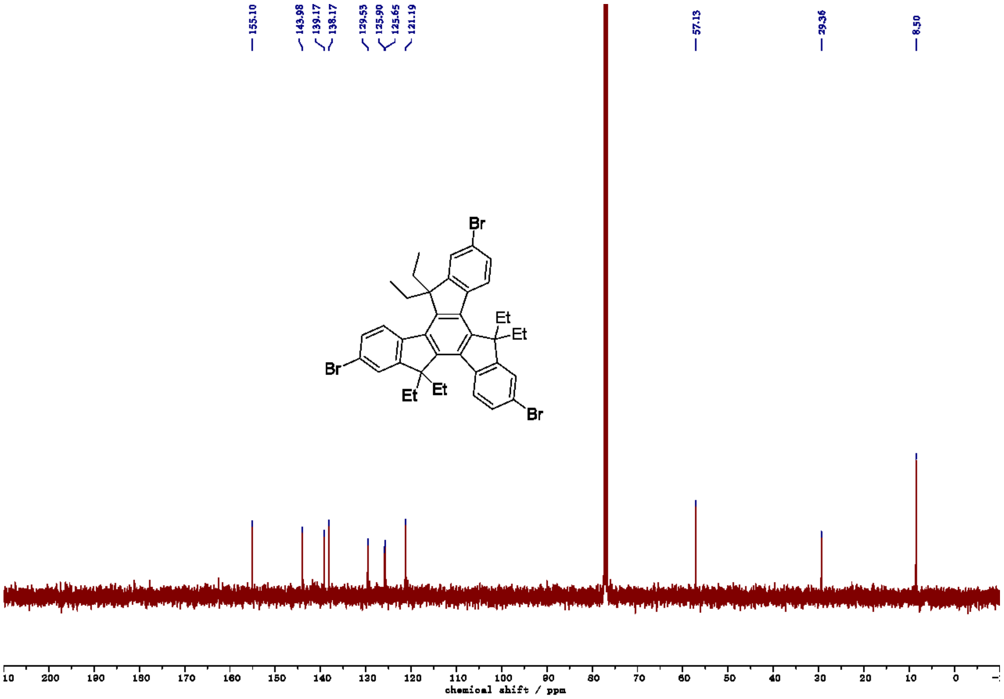

Figure B5. ^{13}C{^{1}H} NMR of **3** (100 MHz, CDCl$_3$, RT).

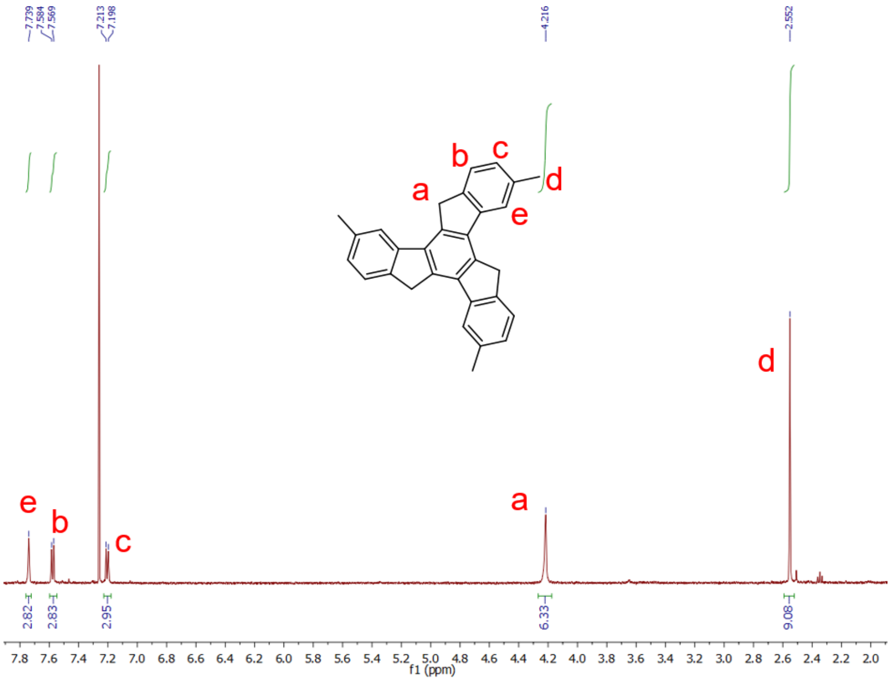

Figure B6. ^{1}H NMR of **4** (500 MHz, CDCl$_3$, RT).

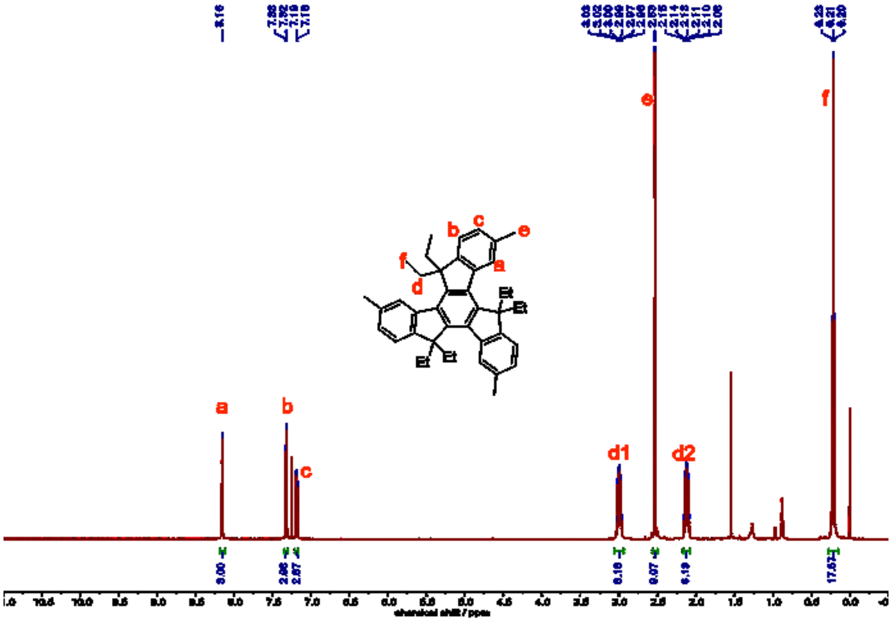

Figure B7. ^{1}H NMR of **5** (500 MHz, CDCl$_3$, RT).

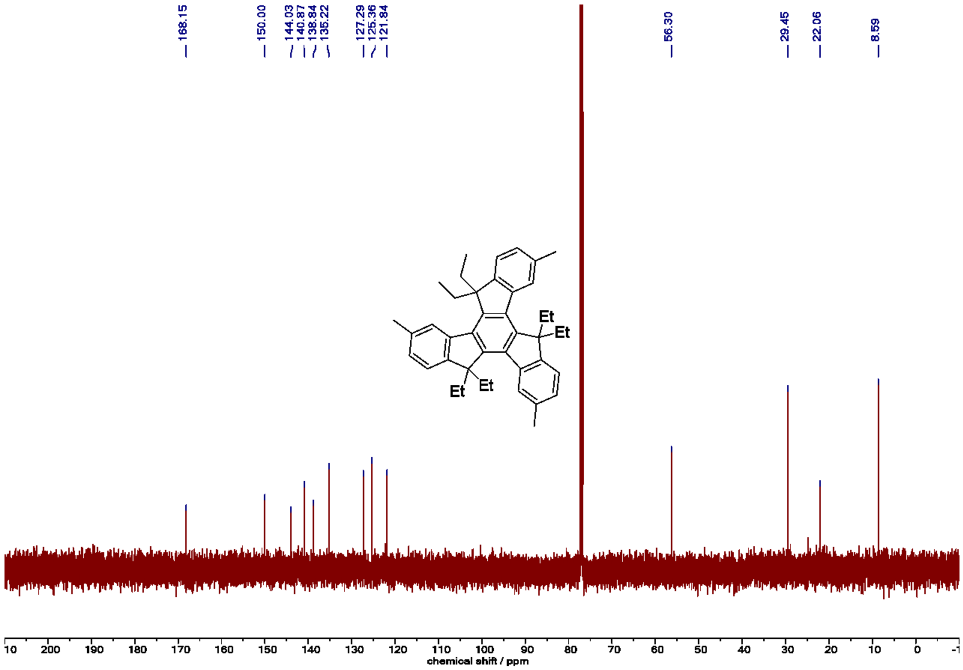

Figure B8. $^{13}C\{^{1}H\}$ NMR of **5** (125 MHz, $CDCl_3$, RT).

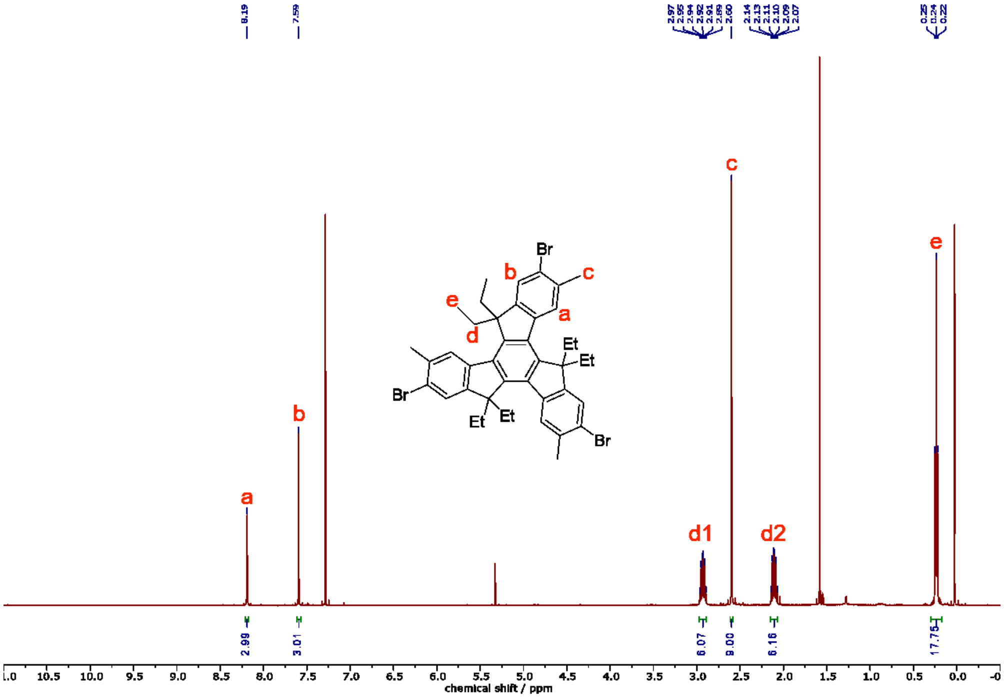

Figure B9. ^{1}H NMR of **6** (500 MHz, $CDCl_3$, RT).

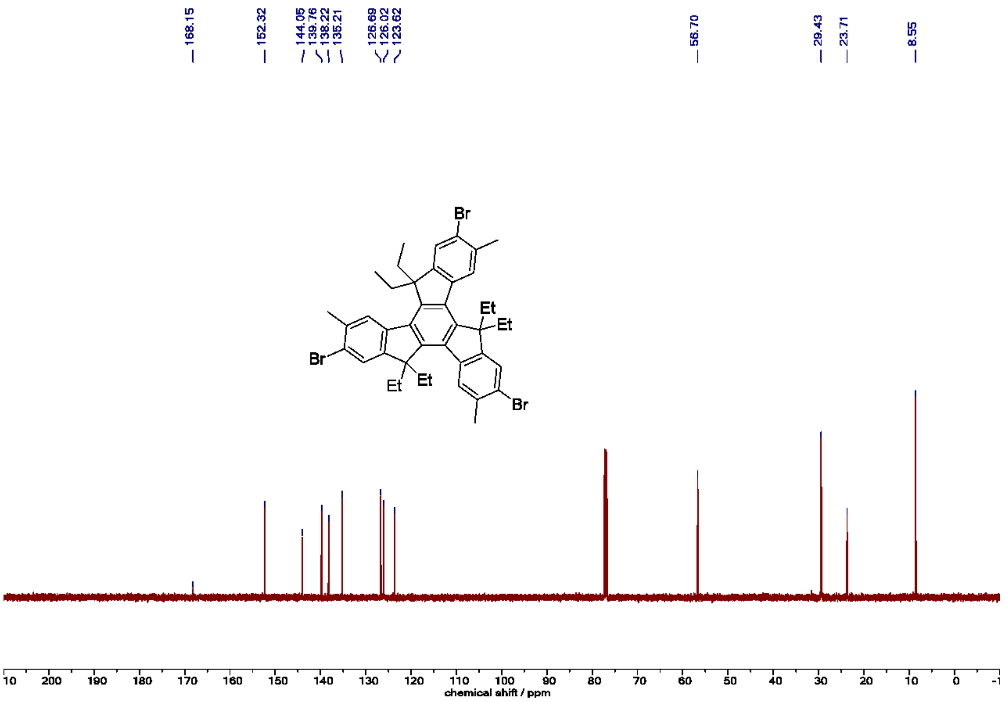

Figure B10. $^{13}C\{^{1}H\}$ NMR of **6** (125 MHz, $CDCl_3$, RT).

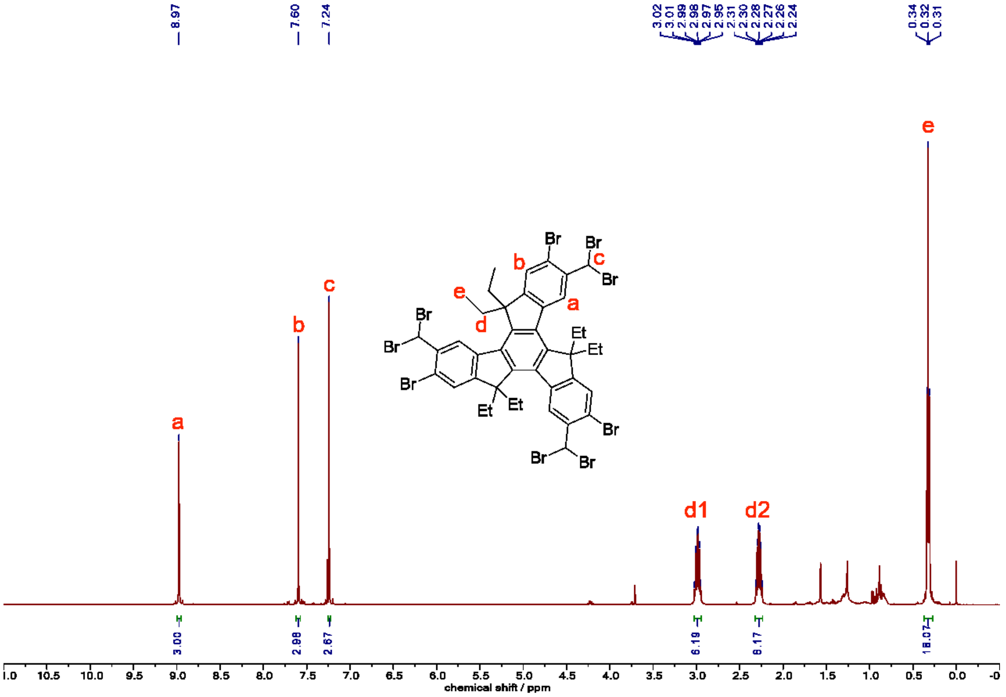

Figure B11. ^{1}H NMR of **7** (500 MHz, $CDCl_3$, RT).

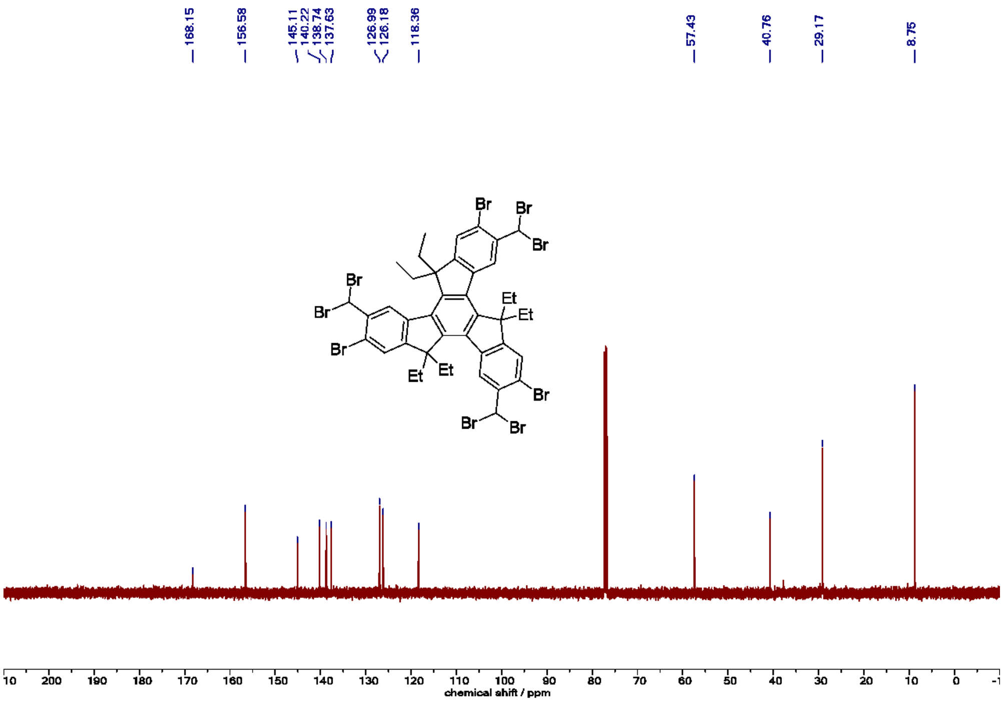

Figure B12. $^{13}C\{^{1}H\}$ NMR of **7** (125 MHz, $CDCl_3$, RT).

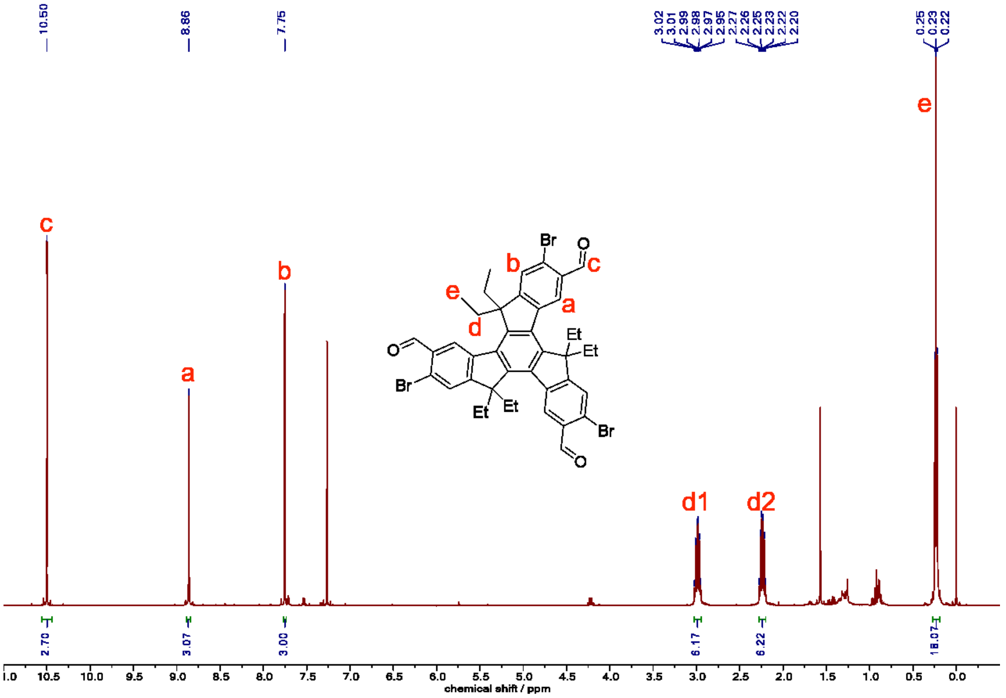

Figure B13. ^{1}H NMR of **8** (500 MHz, $CDCl_3$, RT).

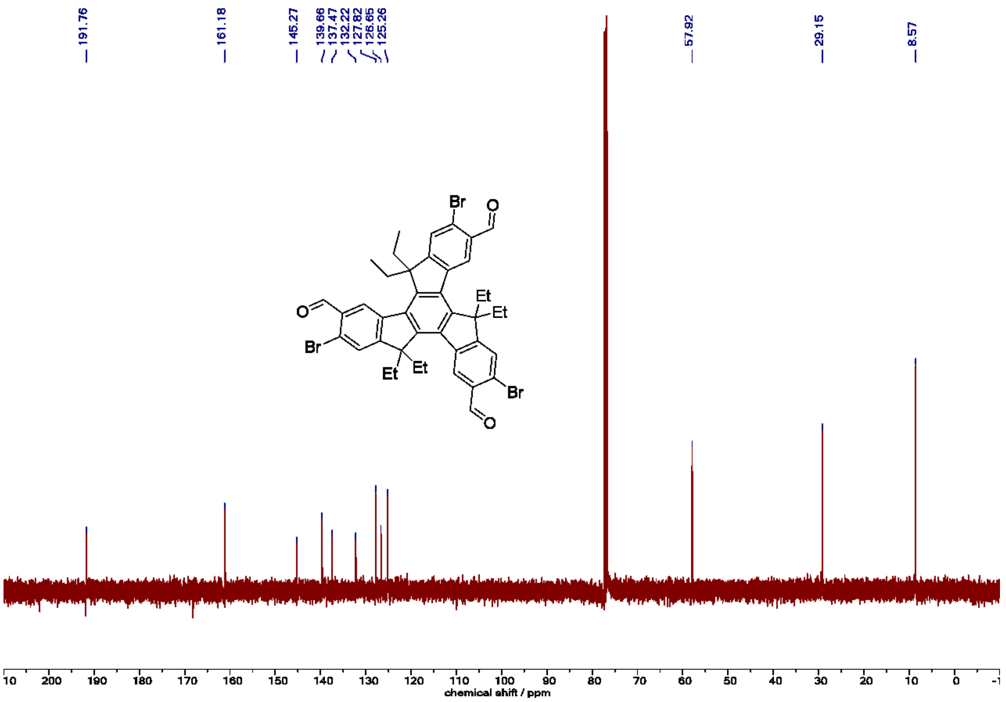

Figure B14. $^{13}C\{^{1}H\}$ NMR of **8** (125 MHz, $CDCl_3$, RT).

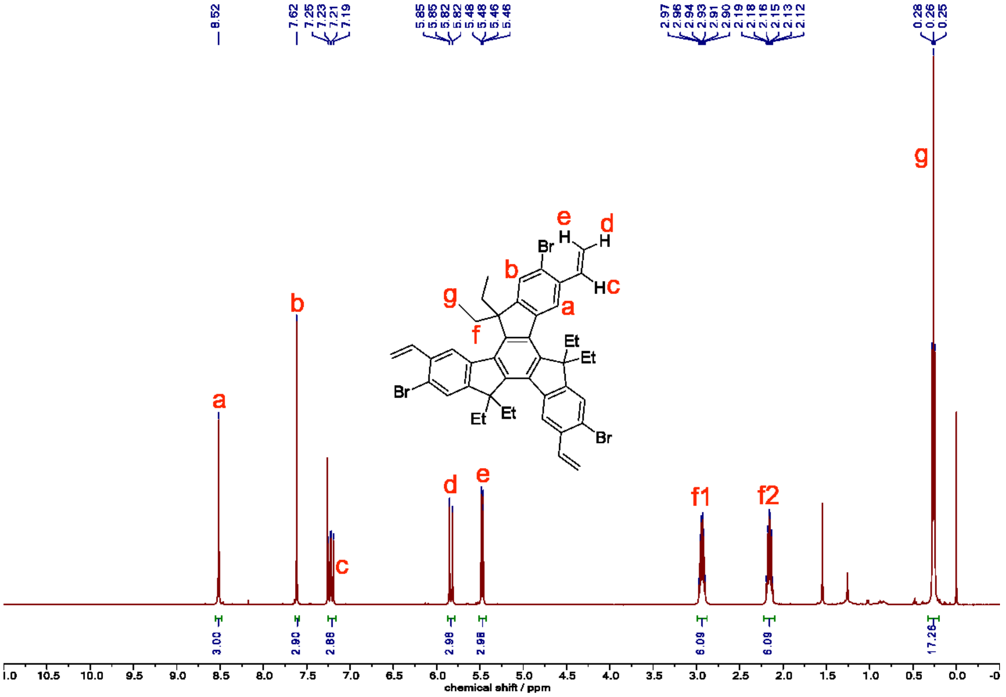

Figure B15. ^{1}H NMR of **9** (500 MHz, $CDCl_3$, RT).

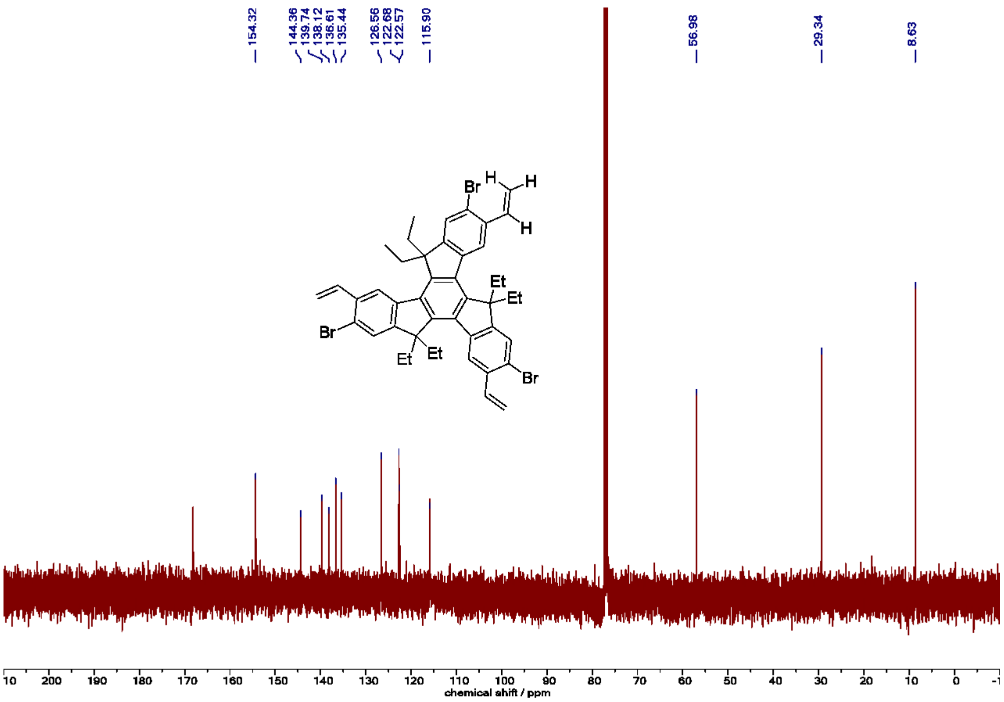

Figure B16. $^{13}C\{^{1}H\}$ NMR of **9** (125 MHz, $CDCl_3$, RT).

B2. High Resolution Mass Spectrometry

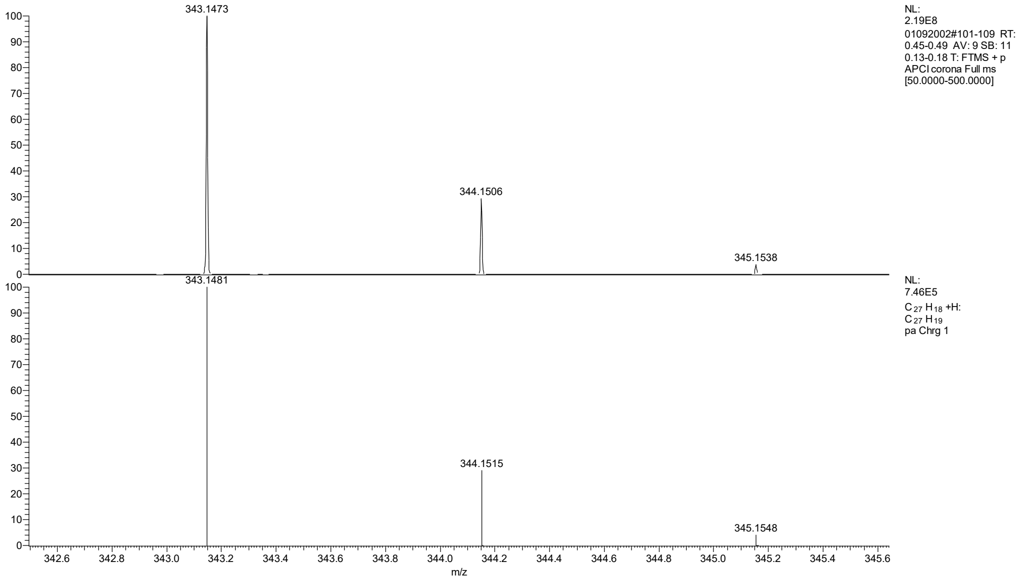

Figure B17. HRMS experimental (top) and calculated (bottom) spectra of **1**.

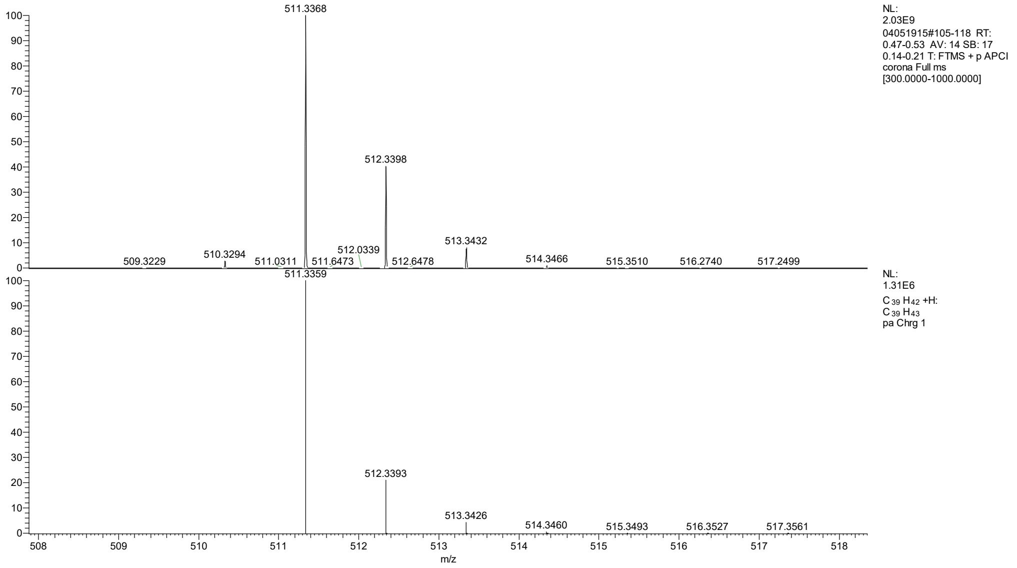

Figure B18. HRMS experimental (top) and calculated (bottom) spectra of **2**.

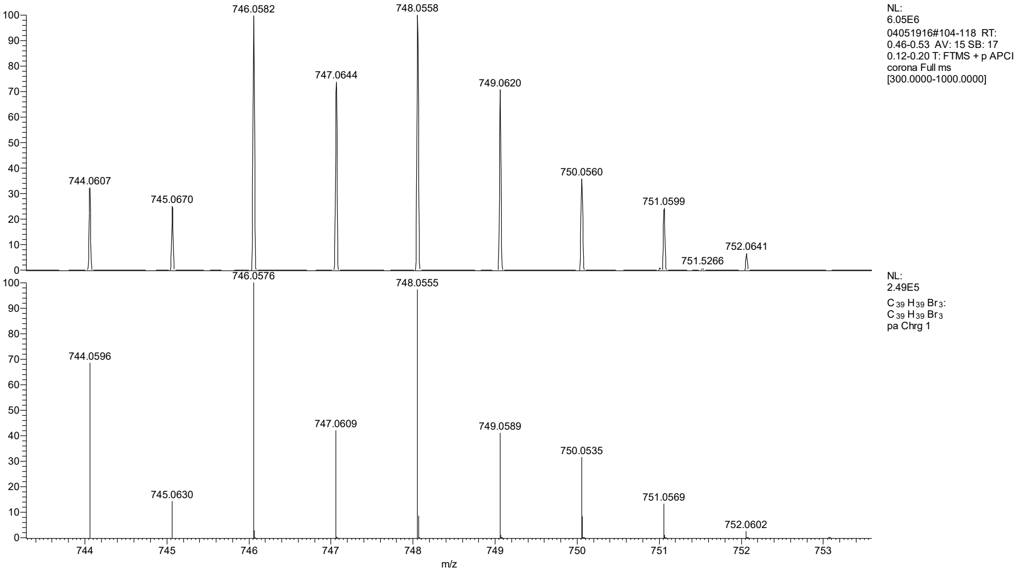

Figure B19. HRMS experimental (top) and calculated (bottom) spectra of **3**.

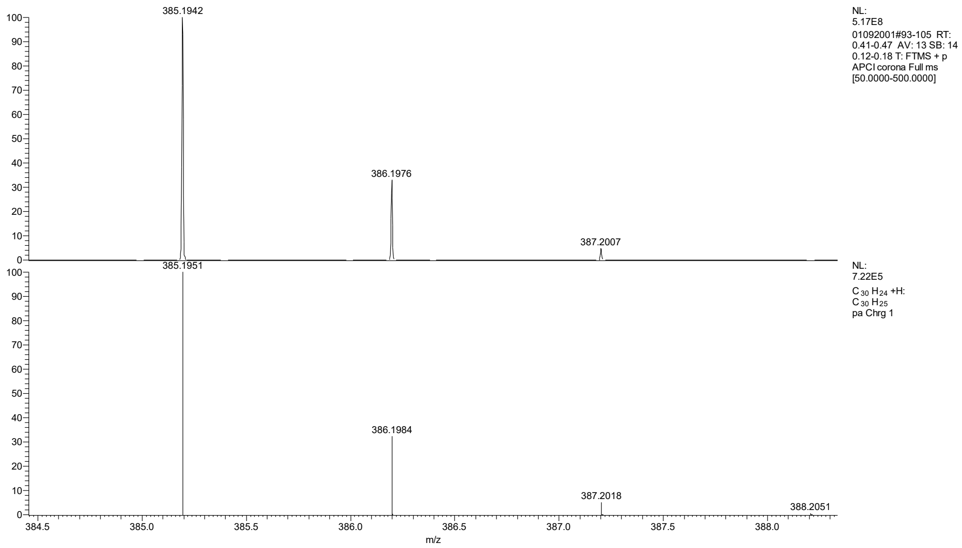

Figure B20. HRMS experimental (top) and calculated (bottom) spectra of **4**.

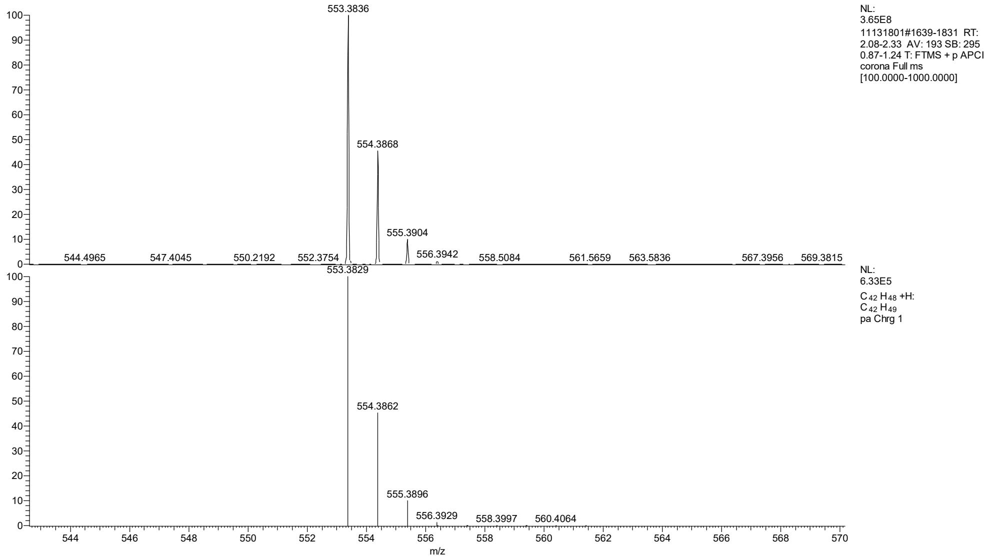

Figure B21. HRMS experimental (top) and calculated (bottom) spectra of **5**.

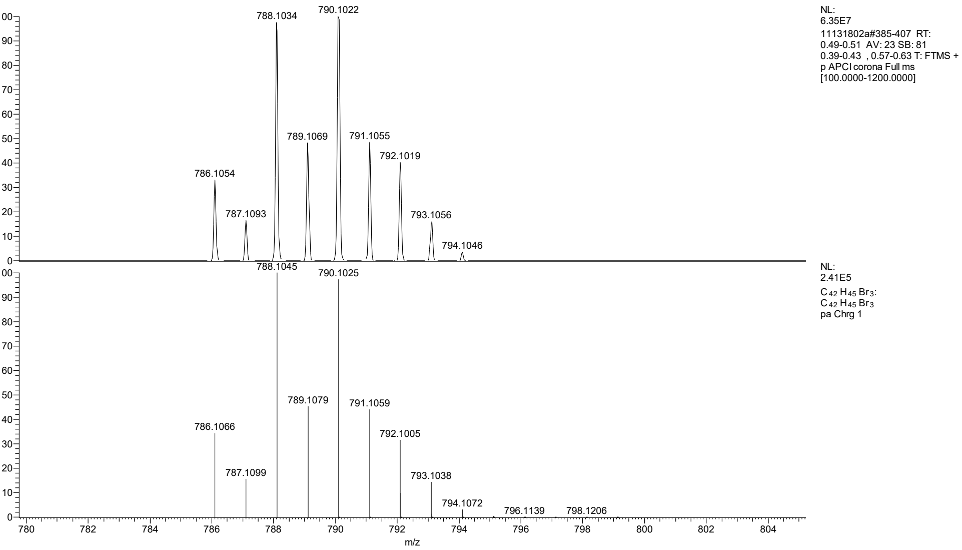

Figure B22. HRMS experimental (top) and calculated (bottom) spectra of **6**.

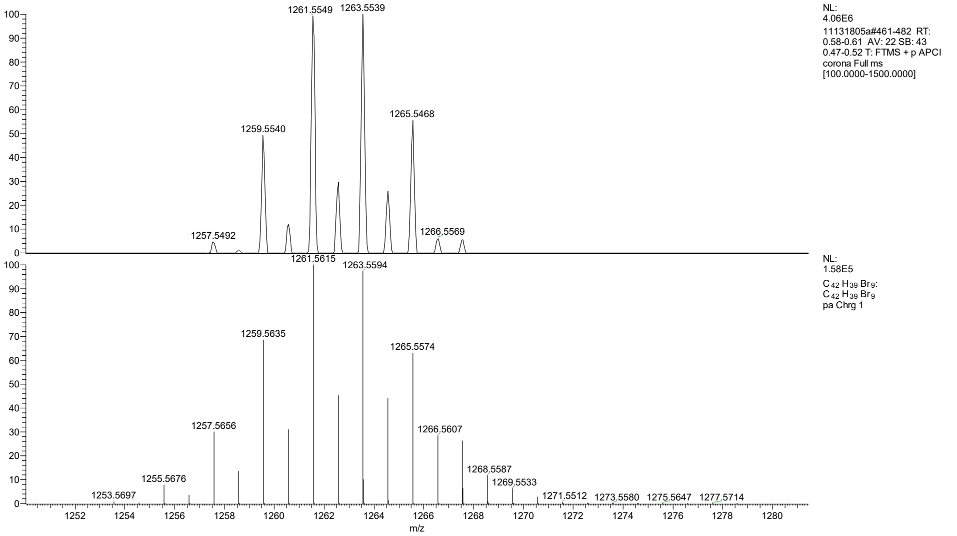

Figure B23. HRMS experimental (top) and calculated (bottom) spectra of **7**.

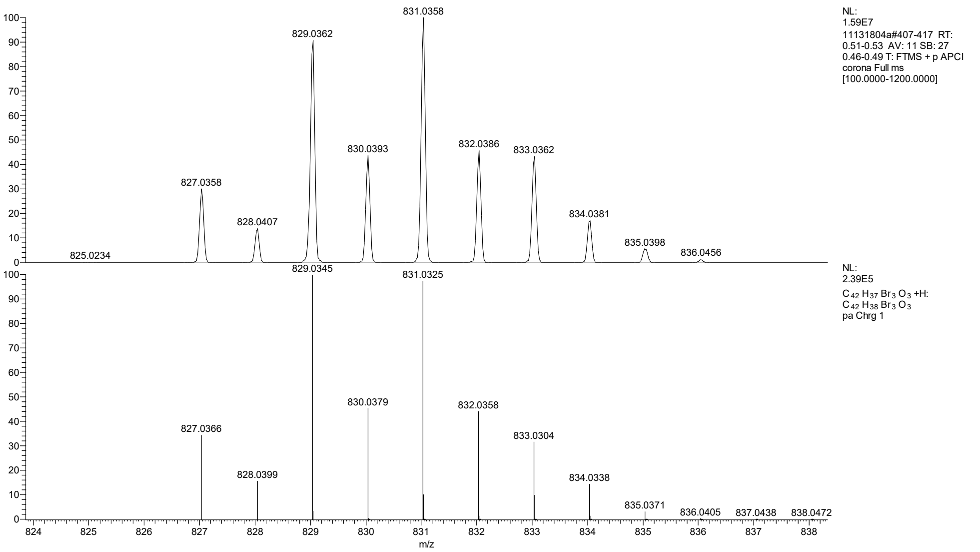

Figure B24. HRMS experimental (top) and calculated (bottom) spectra of **8**.

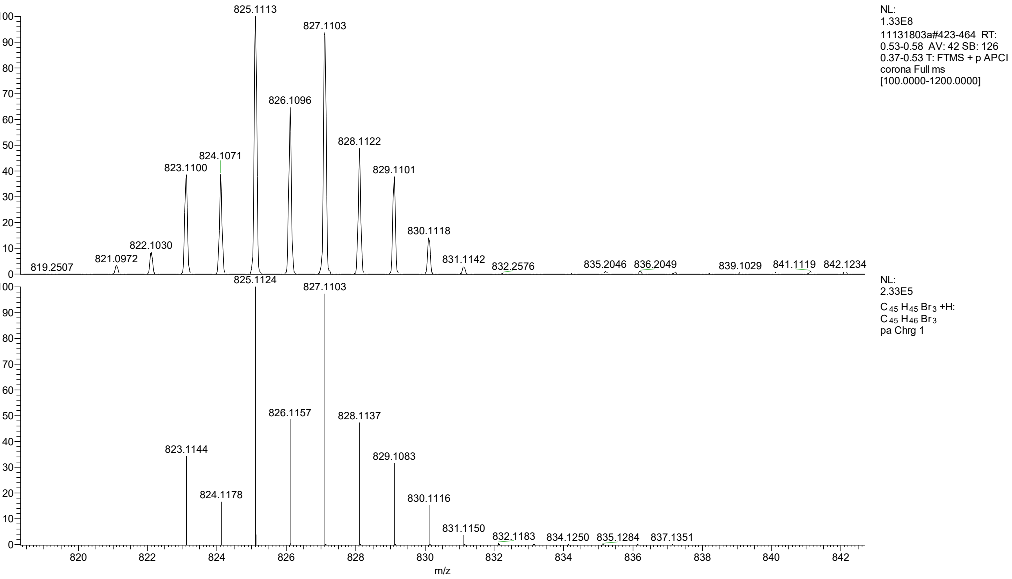

Figure B25. HRMS experimental (top) and calculated (bottom) spectra of **9**.

B3. FTIR Spectra

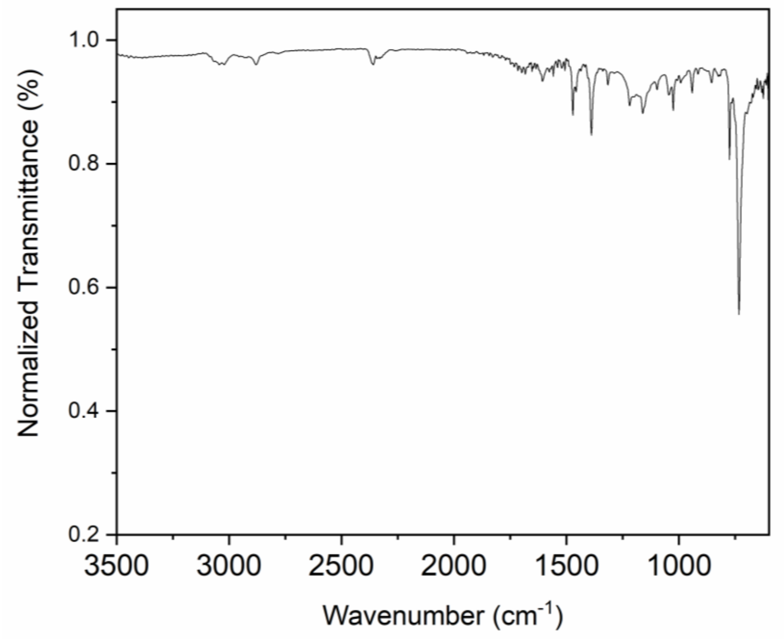

Figure B26. FTIR spectrum of **1**.

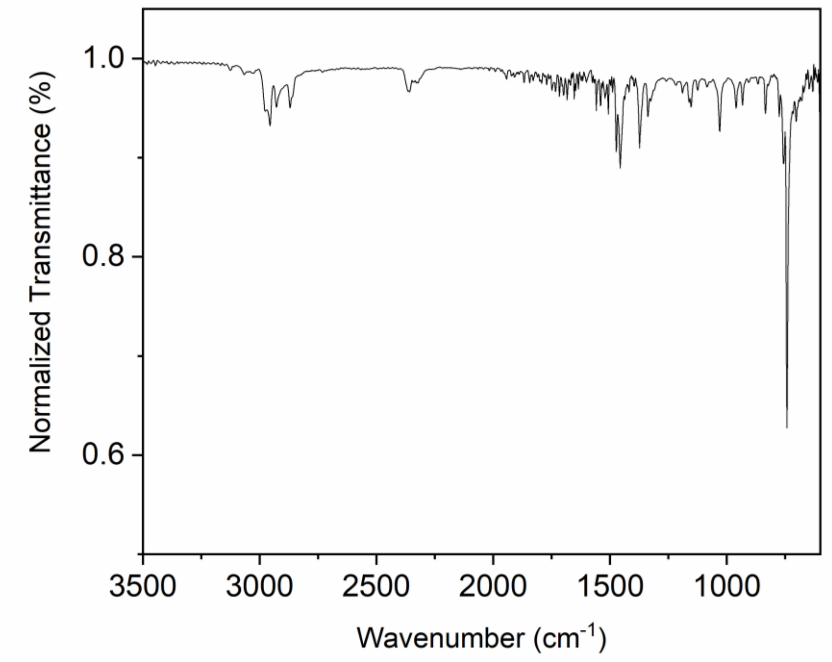

Figure B27. FTIR spectrum of **2**.

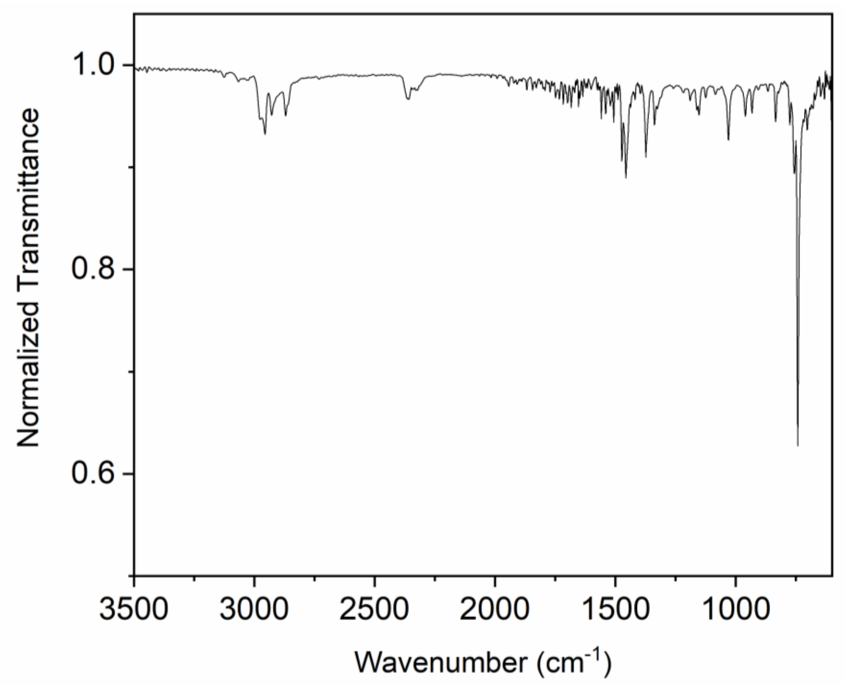

Figure B28. FTIR spectrum of **3**.

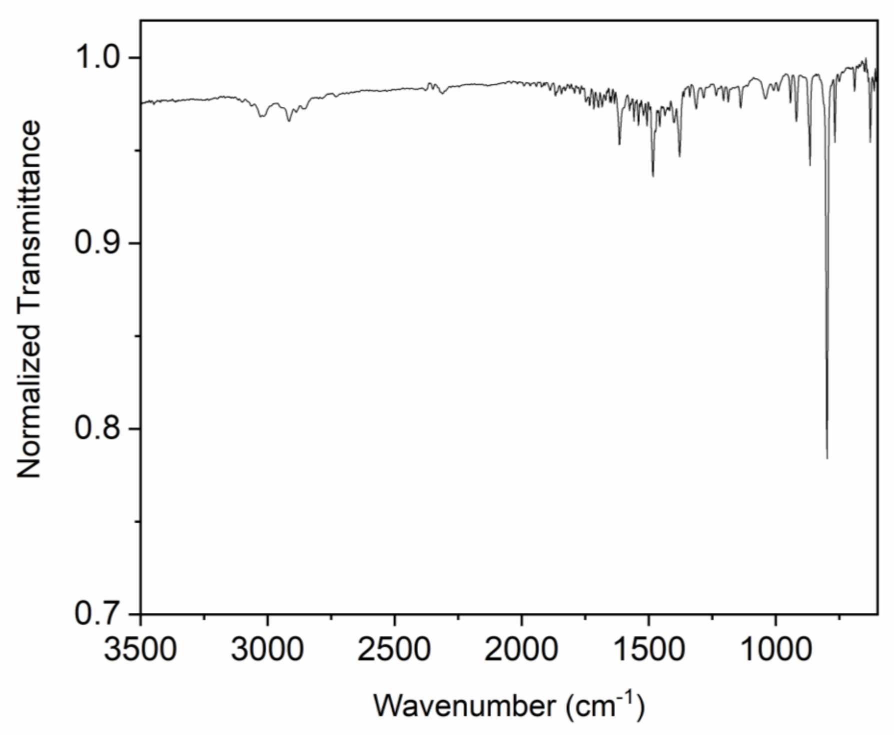

Figure B29. FTIR spectrum of **4**.

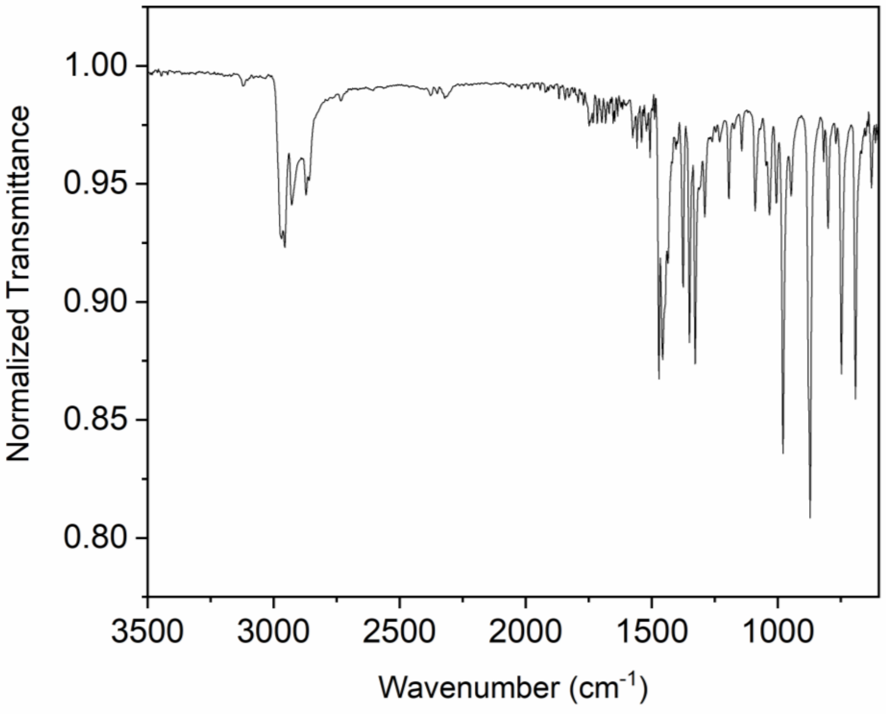

Figure B30. FTIR spectrum of **6.**

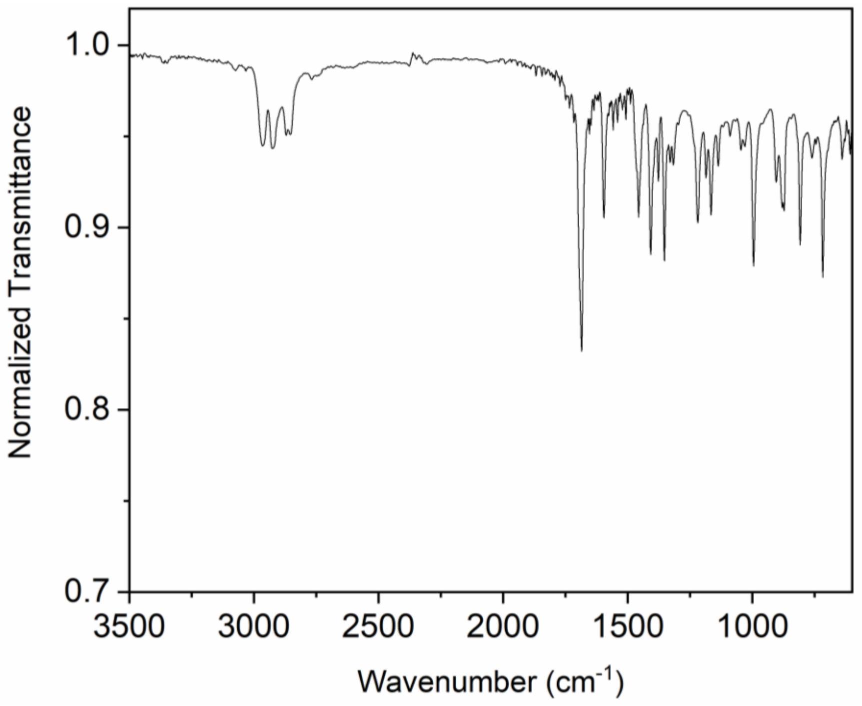

Figure B31. FTIR spectrum of **8.**

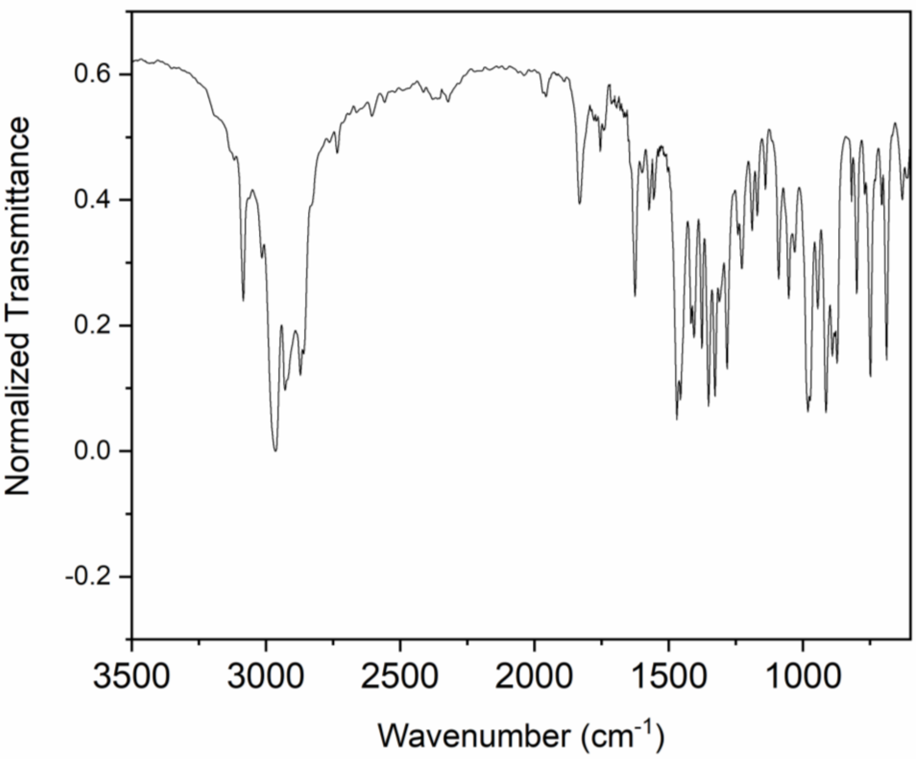

Figure B32. FTIR spectrum of **9.**

APPENDIX C

SUPPLEMENTARY DATA FOR CHAPTER IV

C1. ^{13}C Nuclear Magnetic Resonance

Solid-state NMR spectra were obtained on a Bruker Avance 400 MHz spectrometer with 4 mm CP-MAS probes and MAS rates of 10 kHz at room temperature. Peaks were assigned in accordance with literature.[198]

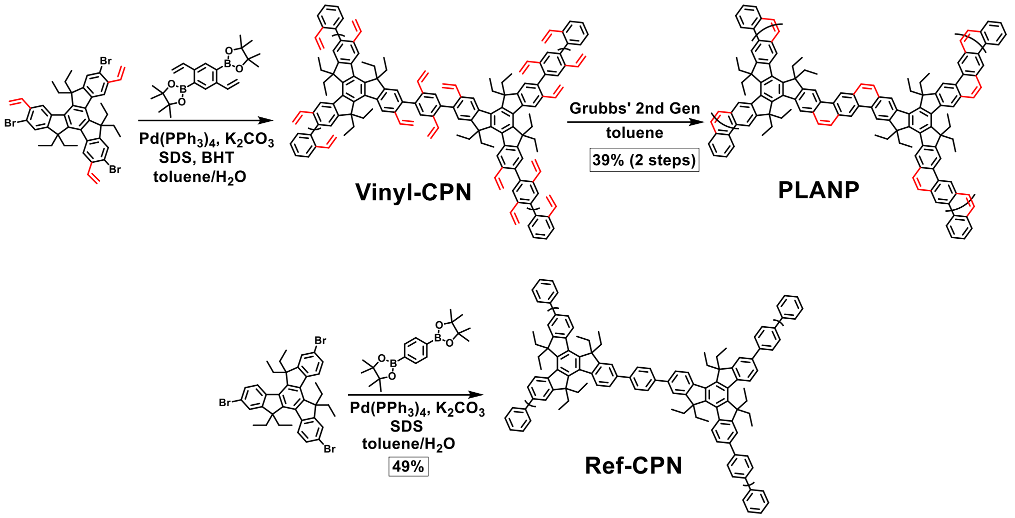

Scheme C1. Polymerization and annulation conditions for **Vinyl-CPN**, **PLANP**, and **Ref-CPN**.

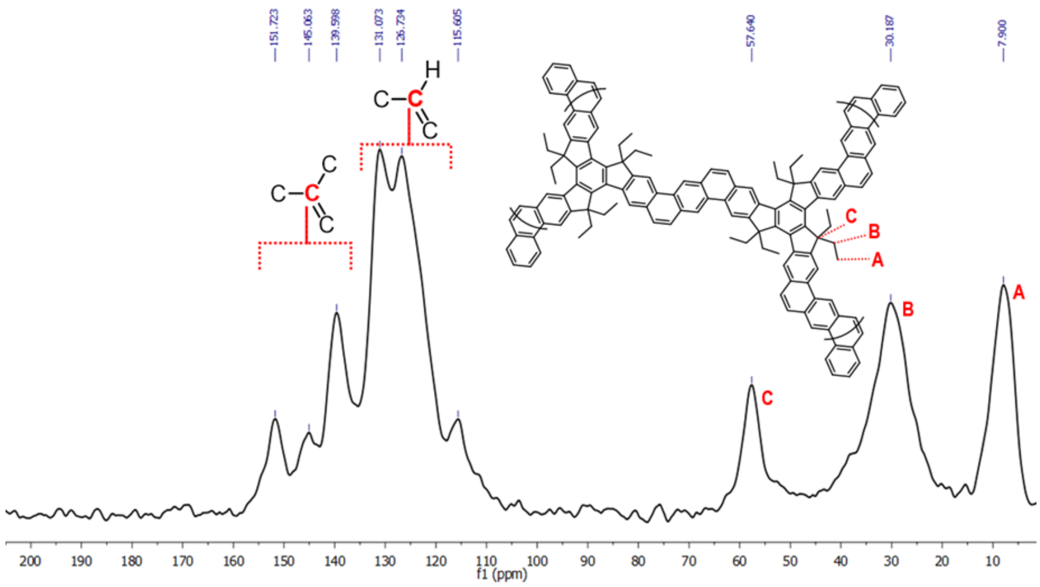

Figure C1. ^{13}C{^{1}H} CP-MAS NMR Spectrum of **PLANP**.

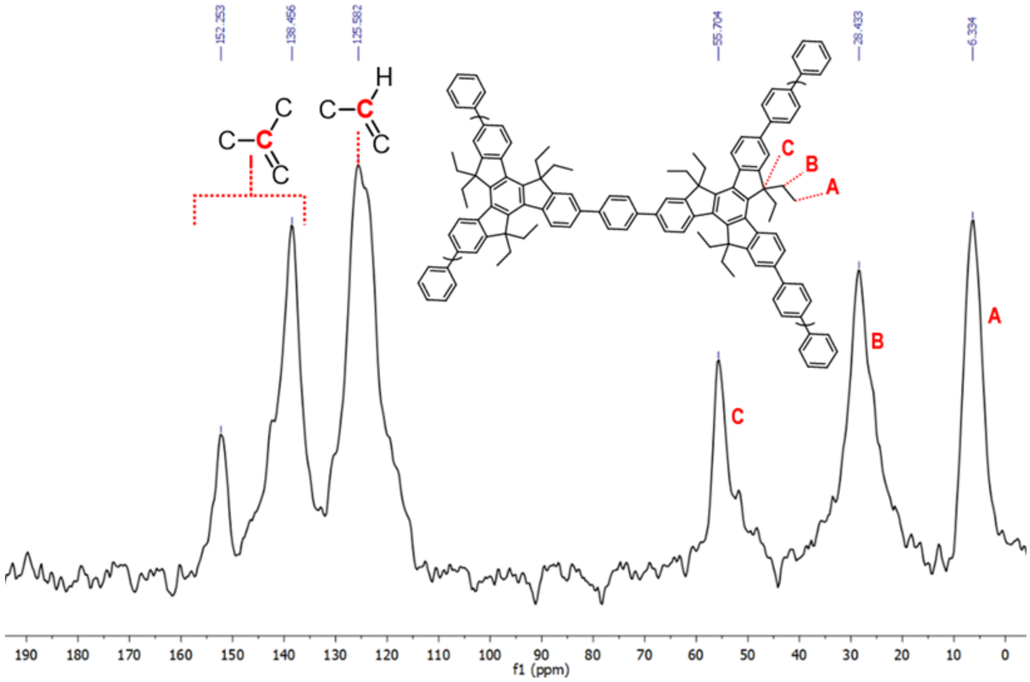

Figure C2. ^{13}C{^{1}H} CP-MAS NMR Spectrum of **Ref-CPN**.

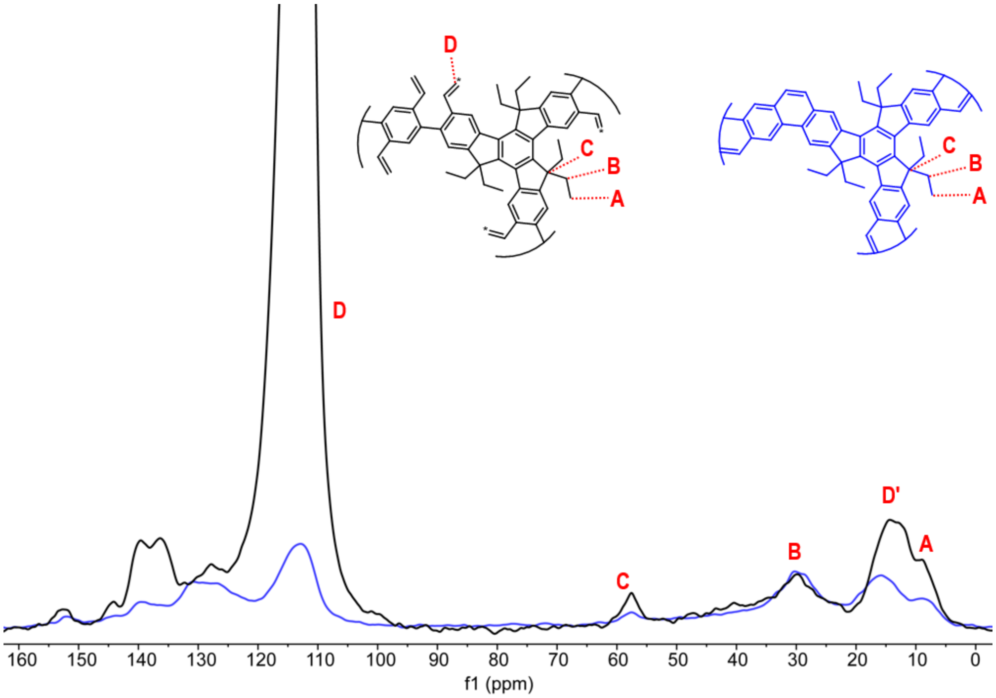

Figure C3. $^{13}C\{^{1}H\}$ CP-MAS NMR spectra of ^{13}C-labeled **Vinyl-CPN** (labeled carbon marked with asterisk) and spectra of **PLANP** after RCM. D′ is the side band of the ^{13}C isotope labeled carbon.

C2. FTIR Spectra

Fourier transform infrared spectroscopy (FT-IR) spectra were recorded by ZnSe attenuated total reflection with a Shimadzu IRAffinity-1S spectrometer. Powders of the samples were tested with no prior preparation. All nanoparticles showed sp^3 (moderate intensity) and sp^2 (weak to negligible) C–H stretches at 2900-3100 cm^{-1}, aromatic C=C stretching around 1500 cm^{-1}, and C–H bending peaks between 650-950 cm^{-1}. As aromatic C–H bends were used for structural comparisons, precursors for fingerprint region comparisons were chosen for having the same aromatic substitution patterns as the polymers.

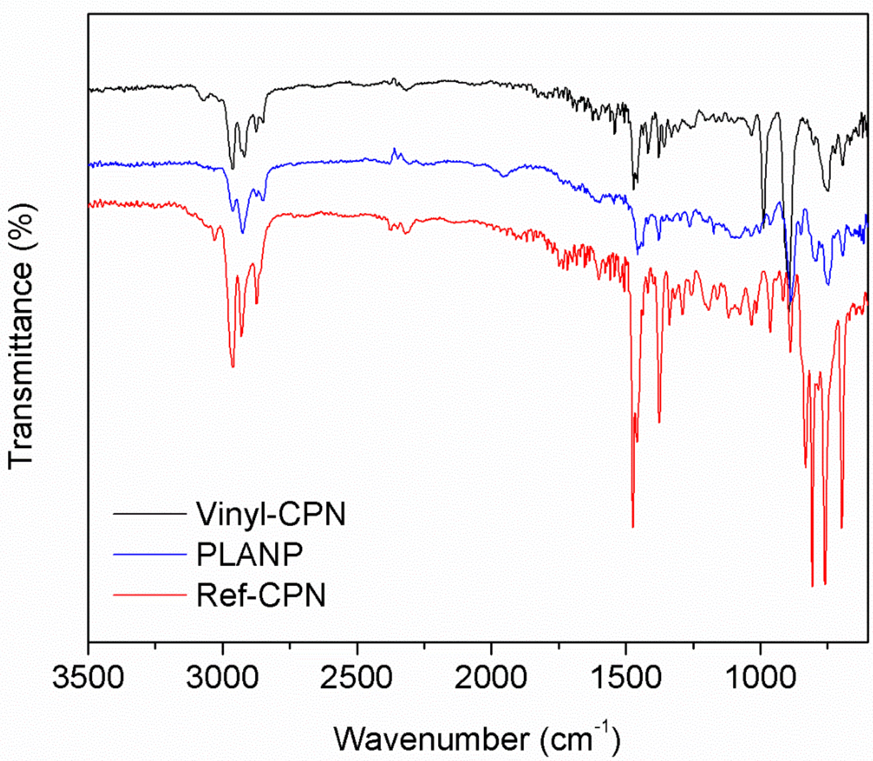

Figure C4. FTIR Spectra of **Vinyl-CPN**, **PLANP**, and **Ref-CPN**.

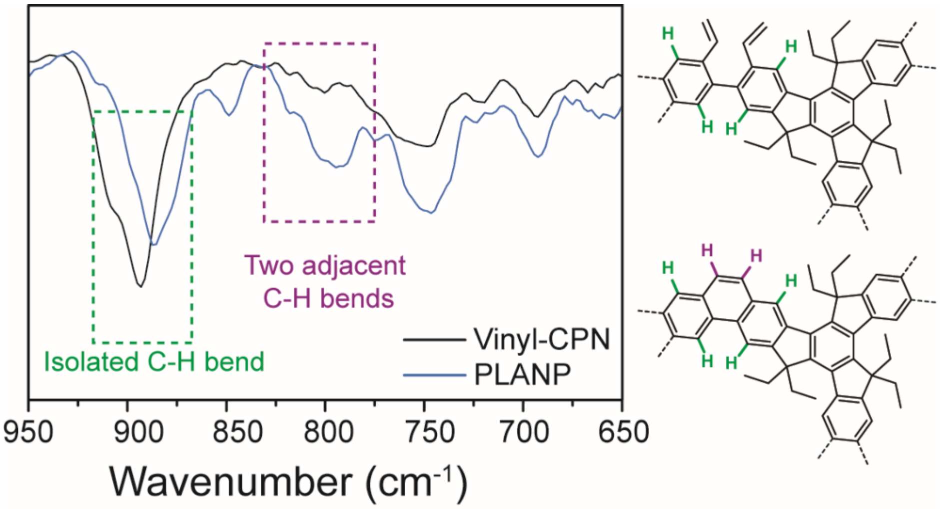

Figure C5. FTIR fingerprint region of **PLANP** and **Ref-CPN**, with peaks highlighted according to corresponding structures.

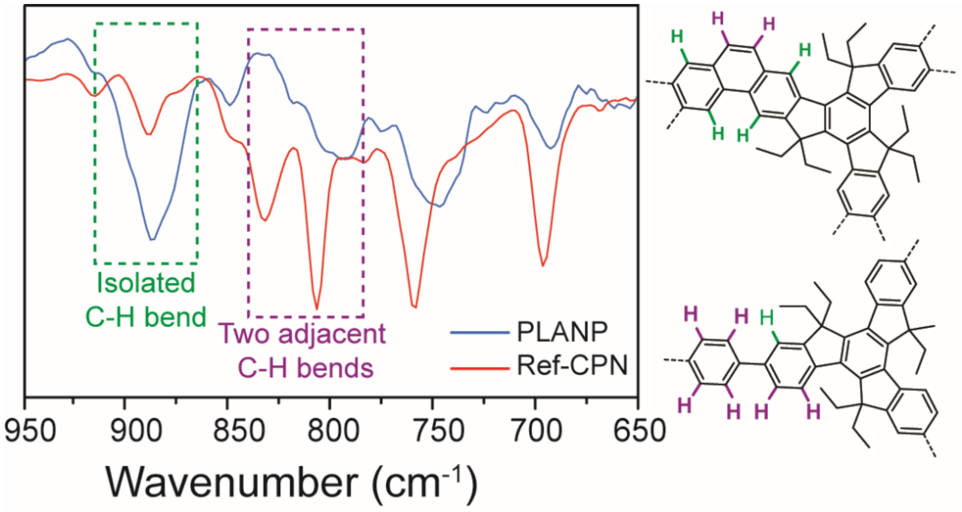

Figure C6. FTIR fingerprint region of **PLANP** and **Ref-CPN**, with peaks highlighted according to corresponding structures.

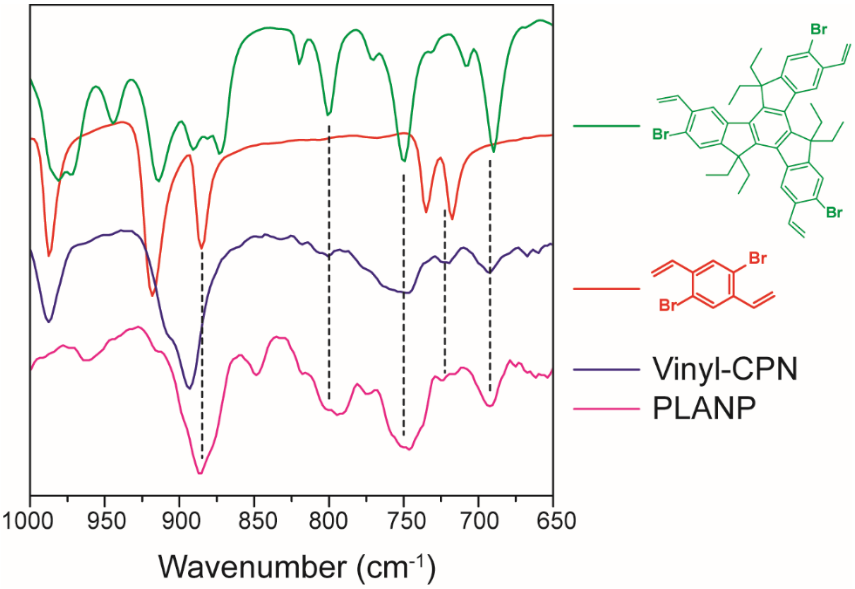

Figure C7. FTIR fingerprint region of **PLANP**, **Vinyl-CPN**, and truxene and phenylene precursors.

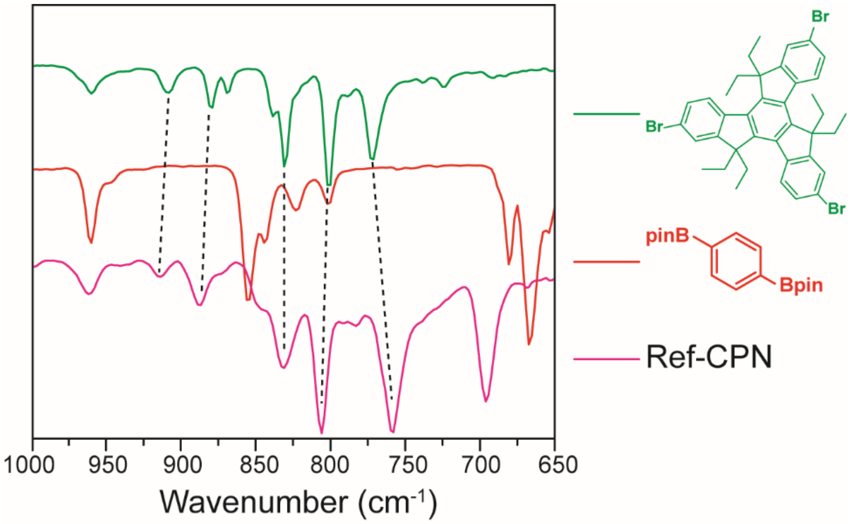

Figure C8. FTIR fingerprint region of **PLANP**, **Vinyl-CPN**, and truxene and phenylene precursors.

C3. Dynamic Light Scattering of Nanoparticle Suspensions

DLS data of nanoparticle dispersions was obtained on a Malvern Zetasizer Nano ZS. Nanoparticles were dispersed into $CHCl_3$ at approximately 0.5 mg/mL and measured in a quartz cuvette. Data from three measurements runs for each sample were averaged together by the Malvern software package, giving the values in Table 4.1.

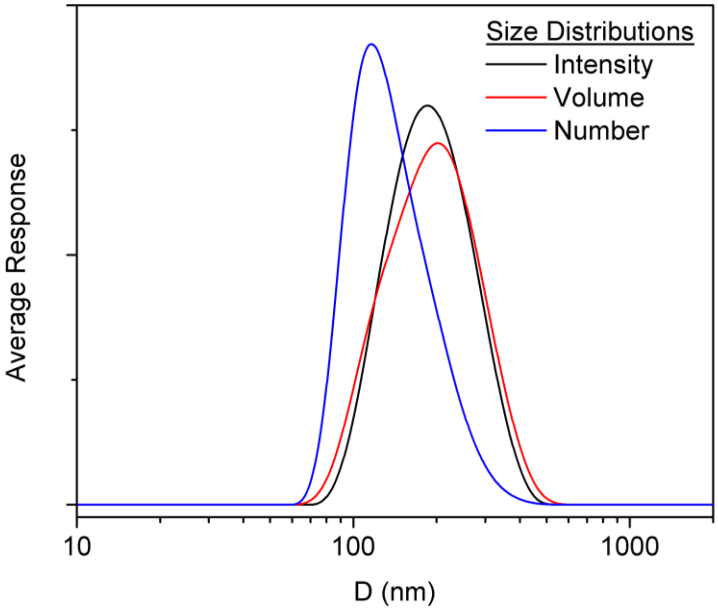

Figure C9. DLS size distributions of **PLANP**.

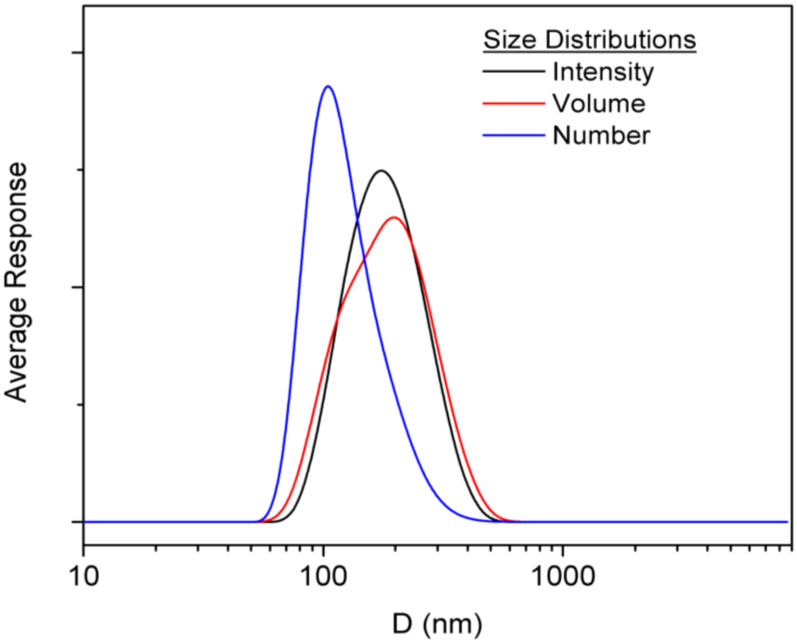

Figure C10. DLS size distributions of **Ref-CPN**.

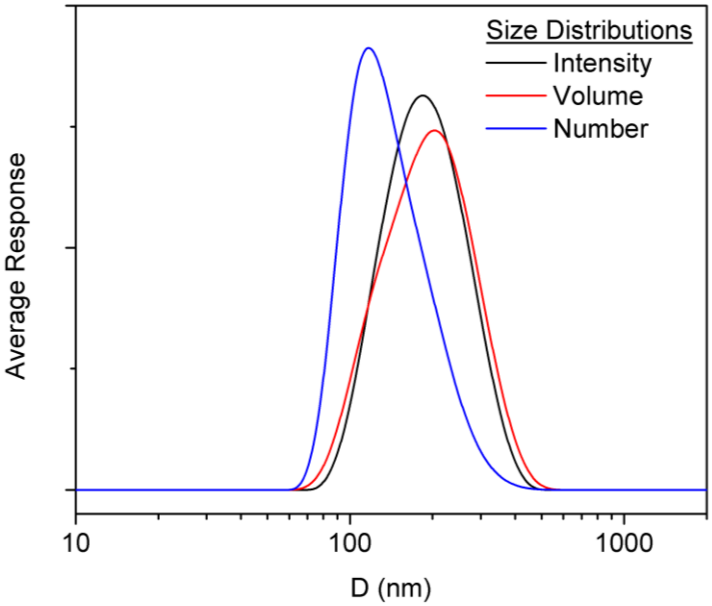

Figure C11. DLS size distributions of **Vinyl-CPN**.

C3. Optical Spectra

UV-Visible absorption spectroscopy was performed on a Shimadzu UV-2600 and fluorescence emissions were measured on a Horiba Fluoromax-4. Nanoparticles were dispersed in $CHCl_3$ at low concentrations (0.5–1.5 mg/L) to prevent detector saturation and spectra were measured in quartz cuvettes. Emission measurements were performed with 5 nm slit widths. Excitation wavelengths (λ_{ex}) are noted below each figure.

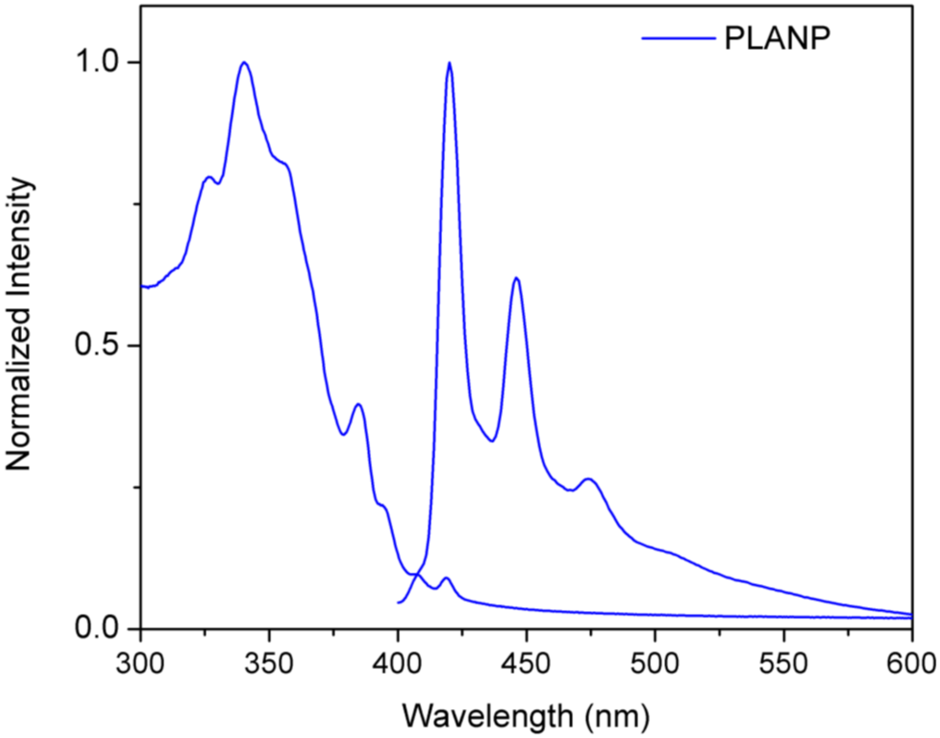

Figure C12. UV-Vis absorbance and emission ($\lambda_{ex} = 385$ nm) spectra of **PLANP**. The Stokes shift between the weak lowest energy absorbance peak and the highest energy emission peak is <1 nm.

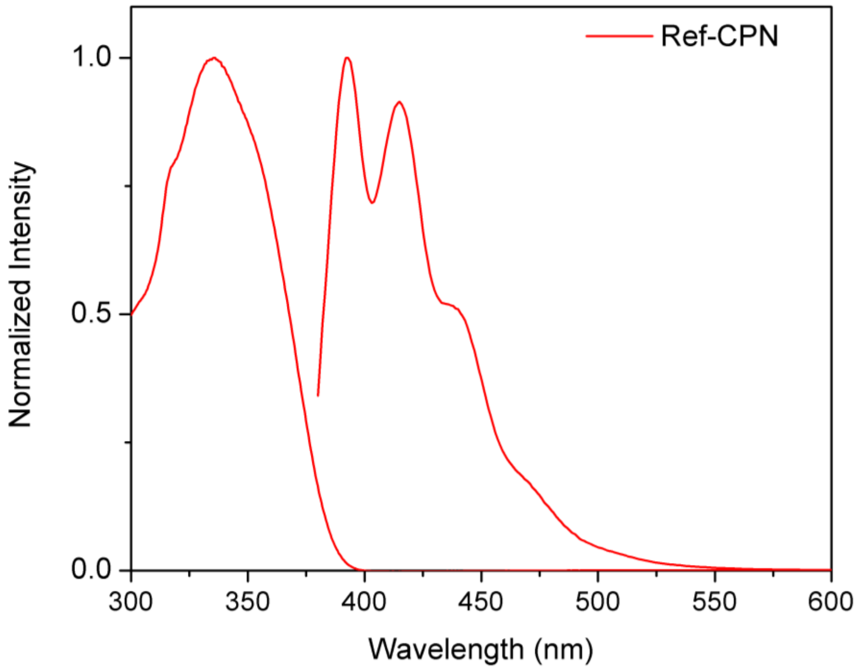

Figure C13. UV-Vis absorbance and emission (λ_{ex} = 365 nm) spectra of **Ref-CPN**. Ref-CPN possesses a slightly lower λ_{max} than **PLANP**, with a Stokes shift of 57 nm.

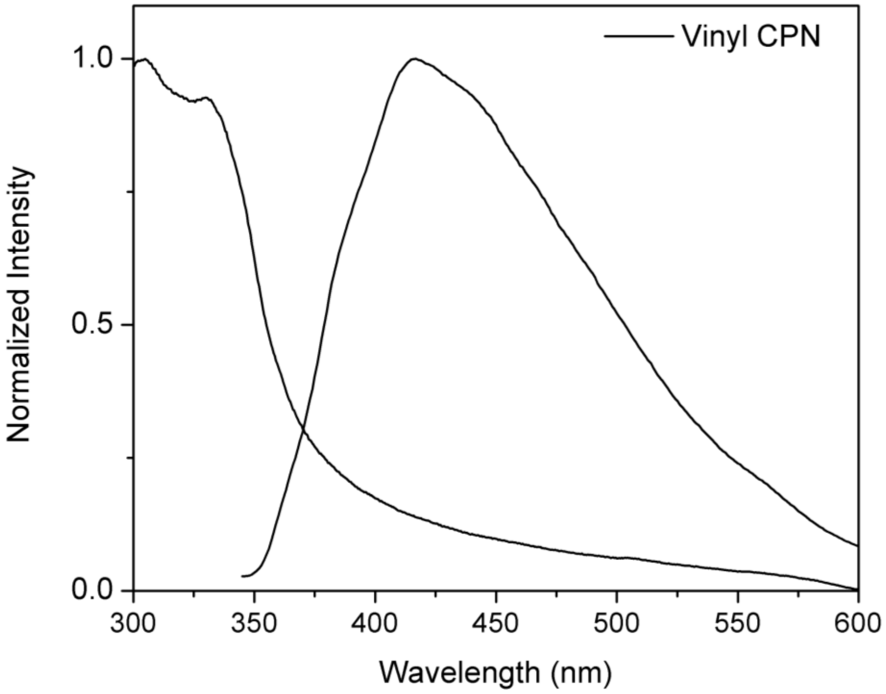

Figure C14. UV-Vis absorbance and emission (λ_{ex} = 350 nm) spectra of **Vinyl-CPN**. Similar to **Ref-CPN**, **Vinyl-CPN** exhibits broad spectra, with a Stokes shift of 87 nm.

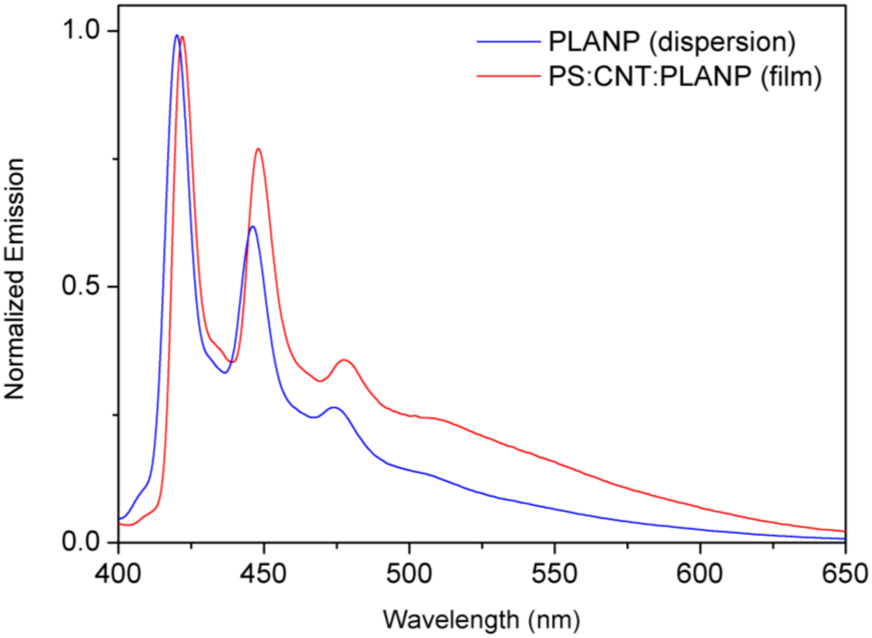

Figure C15. Fluorescence emission (λ_{ex} = 385 nm) spectra of **PLANP** in dispersion and polystyrene/carbon nanotube film.

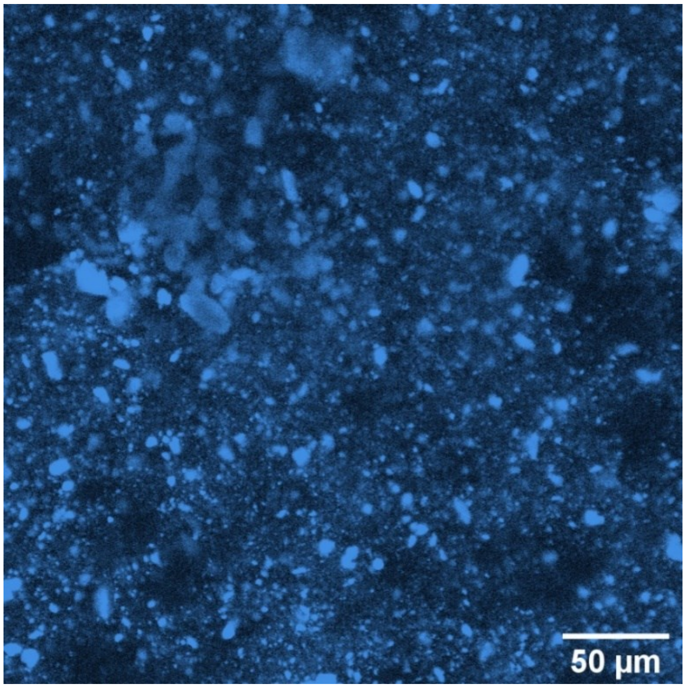

Figure C16. Fluorescence Confocal Microscopy image of PS:CNT:**PLANP** film. A 405 nm laser was used for excitation during these measurements as the highest energy option available on the instrument.

C4. N_2 sorption data

N_2 sorption measurements were performed on a Micromeritics ASAP 2020 surface area and pore size analyzer. Prior to the gas adsorption measurements, the sample was degassed for 10 h at 120 °C. Pore size distribution data were calculated from the N_2 sorption isotherms based on the Nonlocal Density Functional Theory (NLDFT) method in the Micromeritics ASAP 2020 software package (assuming slit pore geometry).

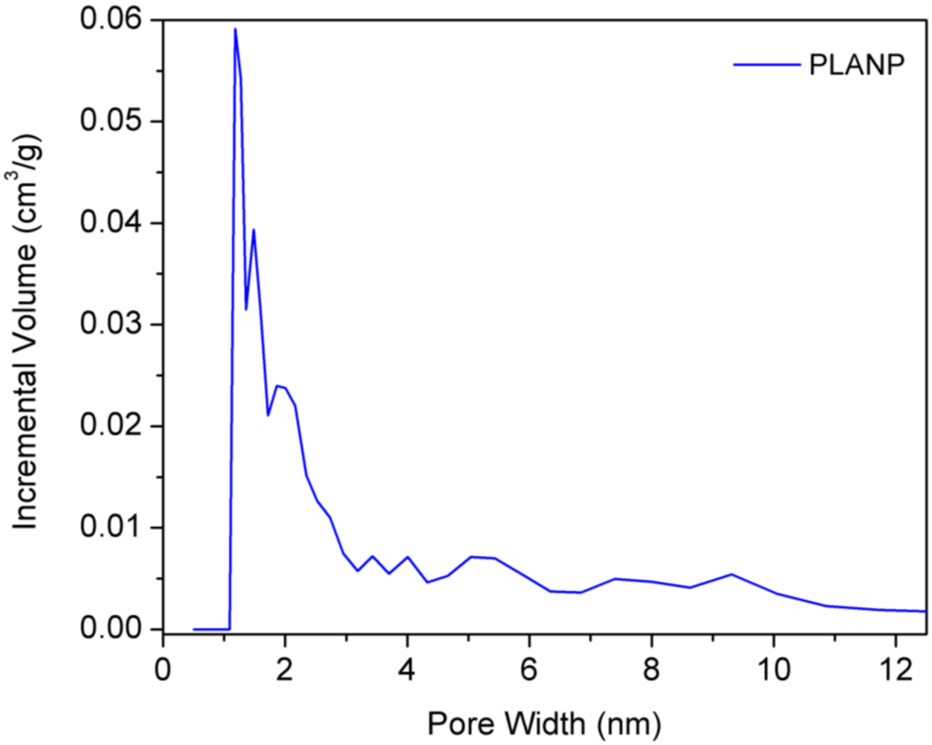

Figure C17. Pore size distribution of **PLANP**.

C5. Thermogravimetric Analysis

Thermogravimetric analysis (TGA) data were collected on Mettler-Toledo TGA-DSC-1 at a heating rate of 20 °C min^{-1} from 30 °C to 900 °C under an N_2 atmosphere. Decomposition temperature was calculated as the temperature at which 5% mass loss occurred.

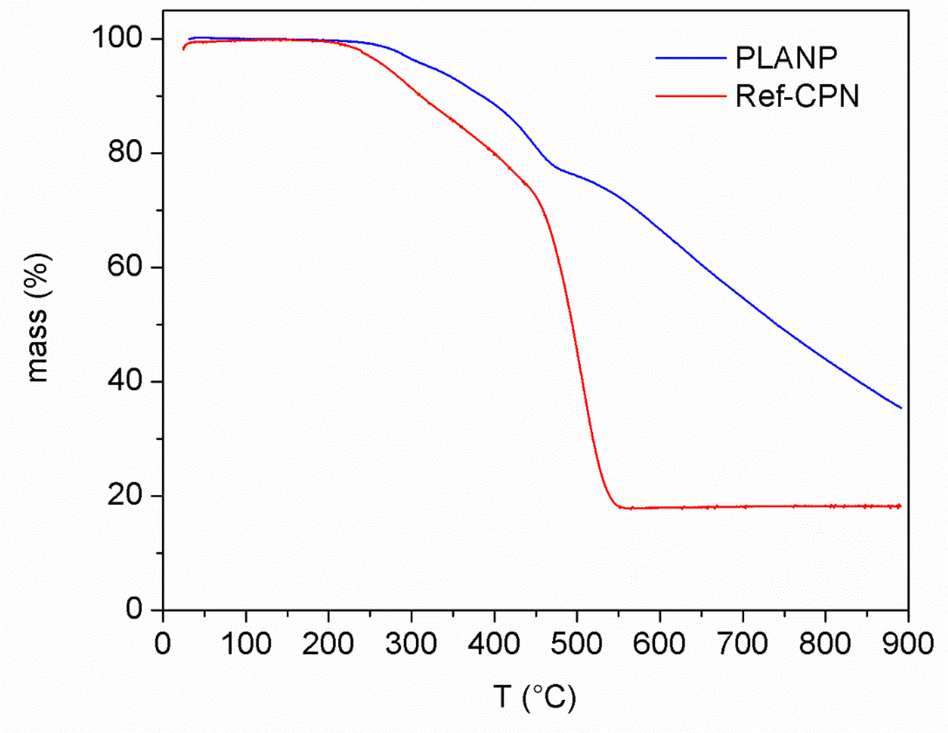

Figure C18. TGA traces of **PLANP** and **Ref-CPN**.

C6. Measurements of PS:CNT:PLANP Film Properties

To form the PS:CNT:PLANP dispersions, polystyrene (60 mg) was dissolved in $CHCl_3$ (10 g). To this, multiwalled carbon nanotubes (5 wt% of PS) were added and sonicated until a black dispersion was formed. Any remaining particulates were removed through centrifugation, leaving a PS:CNT dispersion with no visible solids. To this, **PLANP** (5 wt% of PS) was added and sonicated to homogenize to form the final dispersion. From these dispersions, films could be formed by drop casting onto a glass slide, or by evaporation from a vial. The films were left to dry overnight and then delaminated from the glass surface for measurements. Conductivity measurements were performed under vacuum using a Keithley source measure unit in a two-point geometry.

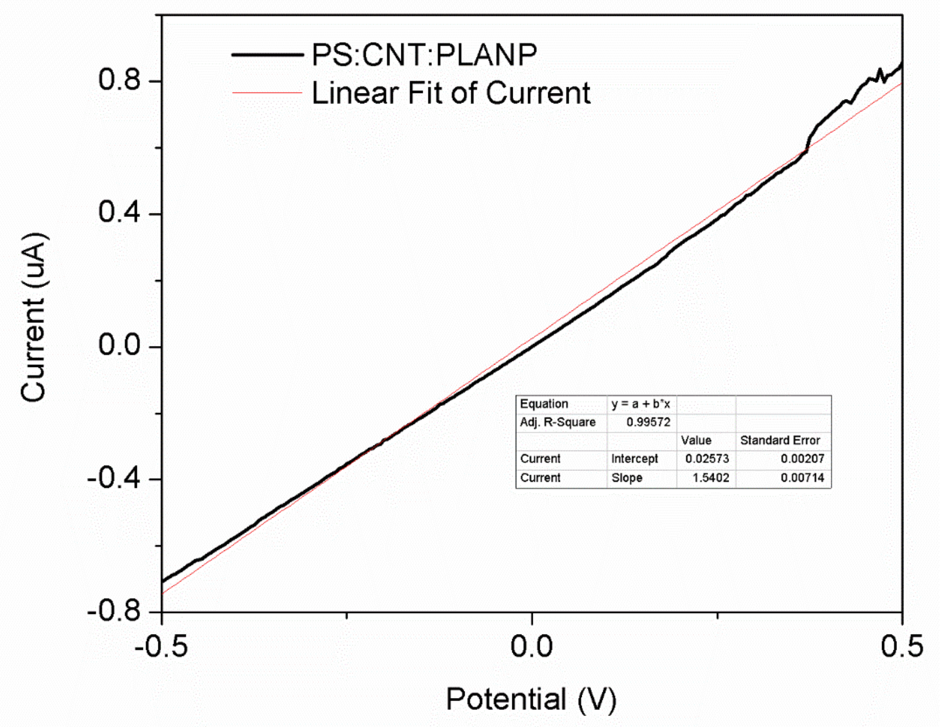

Equation	y = a + b*x		
Adj. R-Square	0.99572		
		Value	Standard Error
Current	Intercept	0.02573	0.00207
Current	Slope	1.5402	0.00714

Figure C19. I-V curve of PS:CNT:**PLANP** film.

APPENDIX D

SUPPLEMENTARY DATA FOR CHAPTER V

D1. Absorbance Spectra of BTp Oligomers

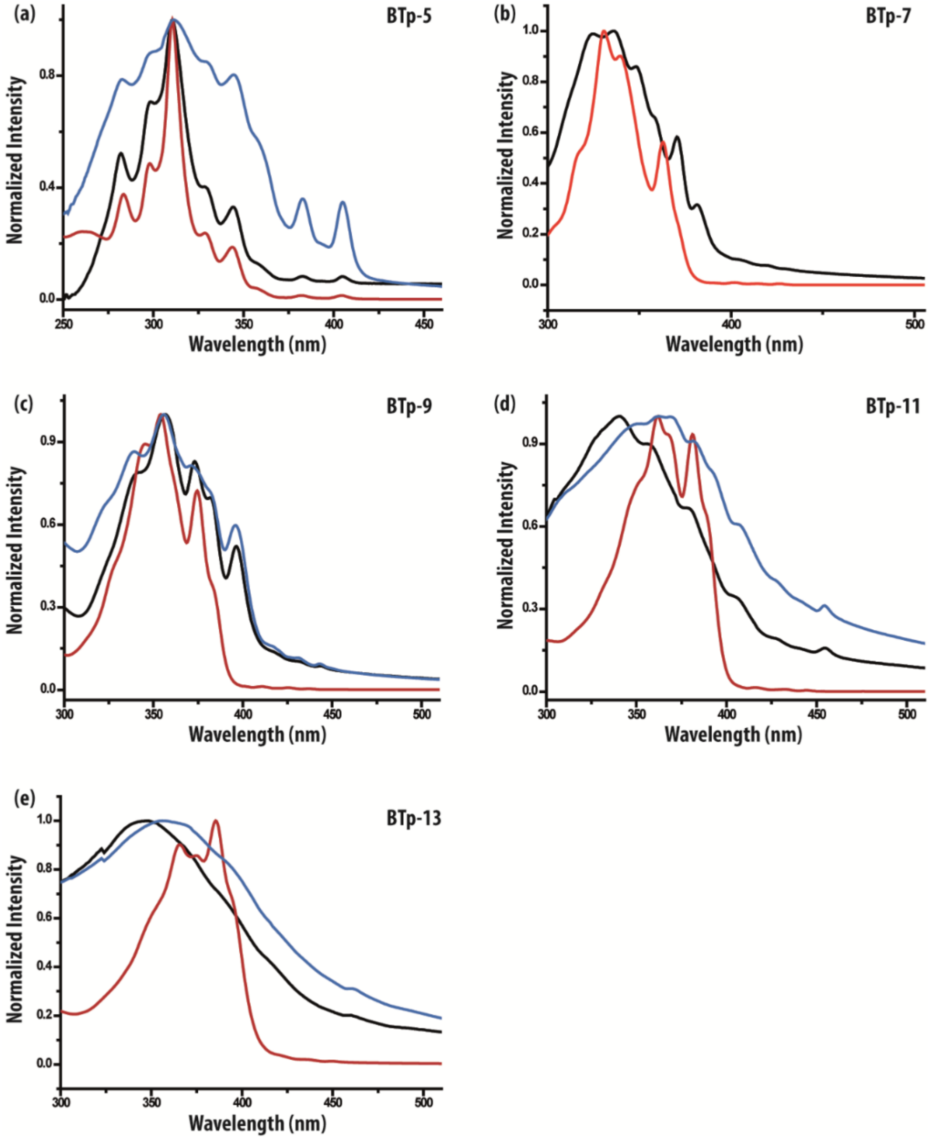

Figure D1. UV-vis spectra of **BTp-5**, **BTp-7**, **BTp-9**, **BTp-11**, and **BTp-13** in $CHCl_3$ (red), as-cast thin film (black), and annealed thin film at 250 °C (blue). **BTp-7** showed good crystallinity even before annealing, but it was not able to observe a good quality UV-vis absorption after annealing due to the small grain size of the crystals and phase segregation on the substrate.